

Model hierarchies for chemical process design

Habilitationsschrift

von Dr.-Ing. Peter Heidebrecht

geboren am 5.5.1975 in Frunse

zur Verleihung des akademischen Grades

Doktor-Ingenieur habitatus (Dr.-Ing. habil.)

genehmigt von der Fakultät für Verfahrens- und Systemtechnik
der Otto-von-Guericke-Universität Magdeburg am 1.11.2011.

Gutachter:

Prof. Dr.-Ing. habil. Kai Sundmacher, Universität Magdeburg

Prof. Lorenz T. Biegler, Carnegie Mellon University, Pittsburgh

Prof. Dr. Dr. h.c. Frerich Keil, Universität Hamburg-Harburg

Forschungsberichte aus dem Max-Planck-Institut
für Dynamik komplexer technischer Systeme

Band 31

Peter Heidebrecht

Model hierarchies for chemical process design

Shaker Verlag
Aachen 2011

Bibliographic information published by the Deutsche Nationalbibliothek

The Deutsche Nationalbibliothek lists this publication in the Deutsche Nationalbibliografie; detailed bibliographic data are available in the Internet at <http://dnb.d-nb.de>.

Zugl.: Magdeburg, Univ., Habil.-Schr., 2011

Copyright Shaker Verlag 2011

All rights reserved. No part of this publication may be reproduced, stored in a retrieval system, or transmitted, in any form or by any means, electronic, mechanical, photocopying, recording or otherwise, without the prior permission of the publishers.

Printed in Germany.

ISBN 978-3-8440-0638-4

ISSN 1439-4804

Shaker Verlag GmbH • P.O. BOX 101818 • D-52018 Aachen

Phone: 0049/2407/9596-0 • Telefax: 0049/2407/9596-9

Internet: www.shaker.de • e-mail: info@shaker.de

Danksagung

Diese Arbeit spiegelt den Kern meiner wissenschaftlichen Tätigkeit am Max-Planck-Institut und an der Otto-von-Guericke-Universität in Magdeburg während der letzten 6½ Jahre wider. Die Möglichkeit hierzu verdanke ich Prof. Kai Sundmacher, der mir nicht nur bestmögliche Arbeitsumstände geboten und meine Arbeit begleitet hat, sondern vor allem einige seiner Mitarbeiter meiner Obhut anvertraut hat.

Daß am Ende dieses Weges tatsächlich eine Habilitation stehen würde, haben manche immer für selbstverständlich gehalten. Ich nicht. Daß ich dieses Ziel erreicht habe, verdanke ich zu einem guten Teil anderen.

Mein zutiefst empfundener Dank hierfür gilt meiner Frau Alexandra, die immer um mich war und deren moralischer Beitrag für diese Arbeit absolut entscheidend war; und unserer Tochter Rebekka, die mit einer Geste jeden Schatten wegwischt. Die Kinder dieser Welt sind es, für die sich jeder Weg lohnt.

Herrn Prof. Frerich Keil und Herrn Prof. Lorenz T. Biegler danke ich nicht nur für die Übernahme der Gutachterrollen in meinem Verfahren, sondern vor allem für ihr stetes Interesse an meiner Arbeit, das mir immer Auftrieb war. Herrn Biegler und dem DAAD danke ich zudem für eine großartige Zeit an der Carnegie Mellon University, die noch lange nachwirken wird.

Ein großes Dankeschön geht an meine Habilitandenkollegen, insbesondere an Richard Hanke-Rauschenbach und Hannsjörg Freund, für viele fachliche Diskussionen. Und für ihre Offenheit in noch zahlreicheren persönlichen Gesprächen. Es gibt Dinge, die man nur mit solchen Weggefährten teilen kann.

Danke auch allen Mitgliedern meines Teams, Matthias Pfafferodt, Christoph Hertel, Benny Hartono, Silvia Piewek, André Sommer und Wenjing Wang. Die Worte „mein Team“ machen mich immer stolz – nicht wegen des ersten Wortes, sondern wegen des zweiten. Und weil es mir immer Freude und Ehre war, meine Doktoranden ein Stück auf ihrem Weg zu begleiten.

Schließlich möchte ich all jenen Kollegen in unserer Arbeitsgruppe danken, die eben nicht nur ihre Arbeit tun, sondern mit Hingabe dabei sind, zum Beispiel Nancy Jirsack, die selbst im Chaos noch den Überblick behält und weiterhilft; Bianka Stein, die stets mehr leistet, als nur Meßdaten aufzunehmen und weiterzugeben; Torsten Schröder, der auf vielen Baustellen Lösungen findet; Robert Rehner, der auch bei dummen User-Fragen gelassen bleibt ... die Liste ließe sich noch lange fortsetzen.

“Es braucht ein ganzes Dorf, um ein Kind großzuziehen” lautet ein afrikanisches Sprichwort. Das ist wahr, und es gilt nicht nur für Kinder. Auch ich hatte hier ein ganzes Dorf um mich. Danke dafür.

Contents

Zusammenfassung.....	3
1 Introduction.....	7
1.1 Boundary conditions of process modelling.....	7
1.2 Requirements for models in process design.....	9
1.3 Model hierarchies.....	10
2 Cyclic Water Gas Shift Reactor.....	12
2.1 Working principle of the Cyclic Water Gas Shift Reactor (CWGSR).....	12
2.2 The Reference Model.....	14
2.3 The Single Reaction Model.....	20
2.4 The Front Model.....	21
2.5 Summary.....	24
3 Structured reforming reactor.....	25
3.1 The Indirect Internal Reforming Reactor (IIR).....	25
3.2 The Detailed Model.....	27
3.3 The Zone Model.....	31
3.4 The Phase Model.....	33
3.5 Summary.....	37
4 Optimal design of TPR experiments.....	39
4.1 The Temperature Programmed Reduction (TPR) method.....	39
4.2 The Complete Problem.....	40
4.3 The Reduced Problem.....	44
4.4 Summary.....	46
5 Mass integration of high temperature fuel cell systems.....	47
5.1 Introduction.....	47
5.2 Equilibrium Models.....	48
5.3 Stoichiometric Model.....	50
5.4 Summary.....	53
6 Concluding remarks.....	54
References.....	57
Selected publications from the author.....	61

Zusammenfassung

Die mathematische Modellierung ist ein unverzichtbares Werkzeug für den Entwurf chemischer Prozesse. Sowohl bei der Auslegung etablierter Prozesse als auch bei der Entwicklung neuer Systeme werden Modelle für eine große Vielfalt von Anwendungen benötigt. Da jede Anwendung individuelle Forderungen an die zu verwendenden Modelle stellt, ist ein ähnlich breites Spektrum an Modellen für die Entwicklung eines Prozesses notwendig. Die Herleitung, Implementierung und Validierung dieser Modelle bedeutet einen nicht zu unterschätzenden Aufwand.

Der Fokus der chemischen Prozessentwicklung hat sich in den letzten beiden Jahrzehnten zu Systemen verlagert, die ein hohes Maß an Komplexität aufweisen. Diese Komplexität kann zum Beispiel auf die Integration mehrerer Prozesse, auf inhärent dynamischen Betrieb oder auf die Realisierung einer gezielten Prozessführung zurückzuführen sein. Einerseits ist die Entwicklung solcher Systeme ohne die Hilfe mathematischer Modellierung nicht denkbar. Andererseits steigt aber der Modellierungsaufwand mit der Komplexität der Systeme. Hinzu kommt eine immer stärker werdende Integration von unterschiedlichen Größen- und Zeitskalen im Prozessentwurf, beispielsweise wenn das Reaktorverhalten mit Hilfe der Mikrostrukturierung des Katalysators optimiert werden soll. Dies erfordert die Verknüpfung von Modellen auf verschiedenen Größenskalen.

Eine sinnvolle Strategie zur effizienten Modellierung komplexer Systeme stellen Modellhierarchien dar. Deren grundlegende Idee ist, Modelle für unterschiedliche Verwendungszwecke nicht unabhängig von einander zu erstellen, sondern mit Hilfe von Methoden der Modellreduktion von einander abzuleiten. Auf diese Weise wird nicht nur der Modellierungsaufwand verringert, sondern darüber hinaus hängen die resultierenden Modelle zusammen, da sie auf ähnlichen Annahmen basieren. Dadurch können Ergebnisse, die mit einem Modell erzielt werden, auf andere Modelle der gleichen Hierarchie übertragen werden. In der vorliegenden Arbeit wird das Konzept der Modellhierarchien angewendet, um Modelle für den Entwurf von vier unterschiedlichen Prozessen zu entwickeln.

Die Modellhierarchie für den zyklischen Wassergas-Shiftreaktor (Cyclic Water Gas Shift Reactor, CWGSR) umfasst drei unterschiedliche Modelle. Ausgehend vom Referenzmodell werden die anderen beiden Modelle durch zusätzliche Annahmen hinsichtlich des Reaktionssystems beziehungsweise der Reaktionsrate hergeleitet. Sie decken ein breites Spektrum an Einsatzzwecken ab. Das Einzelreaktionsmodell ermöglicht grundlegende Entscheidungen im Entwurfsprozess, etwa zur Umkehr der Strömungsrichtung oder zur ungefähren Phasendauer dieses zyklischen Prozesses.

Das Frontenmodell stellt ausgehend von den Befunden des Einzelreaktionsmodells den isothermen Grenzfall unter chemischen Gleichgewichtsbedingungen dar. Aufgrund seiner mathematisch sehr einfachen Struktur eignet es sich hervorragend zur Abschätzung maximal erreichbarer Leistungsparameter des CWGSR unter gegebenen Randbedingungen und zur Identifikation sinnvoller Fenster von Betriebsparametern. Das Referenzmodell stellt die detaillierteste Stufe in dieser Modellhierarchie dar und ist zur Optimierung von Betriebs- und Auslegungsparametern, zur Entwicklung von Wärmeintegrationskonzepten und Anfahrstrategien geeignet. Diese Modellhierarchie ist auch auf ähnliche, zyklisch betriebene reaktive Festbettreaktoren übertragbar.

Der systematische Entwurf strukturierter Reaktoren, insbesondere solche mit geordneten Strukturen, ist der Mittelpunkt der zweiten Modellhierarchie. Diese umfasst drei Modelle, welche den Prozess auf unterschiedlichen Größenskalen beschreiben. Das Detailmodell spiegelt die Phänomene in den wiederkehrenden Struktureinheiten des Reaktors wider. Die mit diesem Modell ermittelten Parameter finden unter anderem direkte Verwendung im Zonenmodell, welches ausgehend von den Ergebnissen des Detailmodells von diesem mit Hilfe physikalisch-chemischer Vereinfachungen abgeleitet wurde. Mit dem Zonenmodell können Entscheidungen auf der Reaktorskala getroffen werden, wie beispielsweise die gestufte Anordnung unterschiedlicher Strukturen im Reaktor. Das dritte Modell in der Hierarchie, das Phasenmodell, wird durch zusätzliche Annahmen und mathematische Mittelungsmethoden von dem Zonenmodell abgeleitet. Es ermöglicht die modellbasierte Auslegung der Integration des strukturierten Reaktors mit anderen Einheiten. In dieser Arbeit werden Anwendungen aller drei Modelle am Beispiel eines Indirekten Internen Reformierungsreaktors (IIR) vorgestellt.

Der optimale Entwurf von Temperaturprogrammierten Reduktionsexperimenten (TPR) ist Gegenstand der dritten Modellhierarchie. Da es sich bei TPR um dynamische Versuche handelt, führt diese Aufgabe zu Optimalsteuerungsproblemen. Die numerische Lösung dieser Probleme ist nicht trivial und erfordert daher Expertenwissen. Allerdings weisen die optimalen Kontrollprofile für unterschiedliche Parameterkombinationen starke Ähnlichkeiten auf. Darauf basierend werden in dieser Arbeit reduzierte Optimalsteuerungsprobleme mit deutlich weniger Freiheitsgraden entworfen. Die Reduktion geht in diesem Fall darauf zurück, dass die Kontrollprofile als abschnittsweise konstant definiert werden. Die Ergebnisse der reduzierten Probleme stimmen gut mit denen der vollständigen Probleme überein und lassen sich darüber hinaus zuverlässig, schnell und weitgehend automatisiert lösen.

Die stoffliche Integration von Brennstoffaufschluß und Hochtemperaturbrennstoffzelle in Kraftwerkssystemen steht im Mittelpunkt der vierten Modellhierarchie. Dabei geht es um

die Idee, Anodenabgase zurückzuführen und als Oxidationsmittel im Reformierungs- oder Vergasungsprozess einzusetzen. Die Machbarkeit dieses Konzepts wurde mittels zweier verschiedener Modellsätze untersucht. Mit Hilfe von Modellen, die im Wesentlichen auf Gleichgewichtsannahmen beruhen und zudem Kohlenstoffablagerung und systemweite Wärmeintegration berücksichtigen, wurden geeignete Rückführungsverhältnisse ermittelt. Sie deuten darauf hin, dass das Konzept insbesondere für Brennstoffzellen mit hohen Temperaturen wie der SOFC für ein breites Spektrum an Brennstoffen funktioniert. Das reduzierte Modell geht von stöchiometrischen Einsatzverhältnissen und Umsätzen aus. Es stimmt für SOFC-Systeme sehr gut mit dem komplexeren Gleichgewichtsmodell überein und erlaubt eine Abschätzung der notwendigen Rückführungsraten mit Hilfe einer einzigen algebraischen Gleichung.

Die in dieser Arbeit gezeigten Modellhierarchien sind Beispiele für die Entwicklung physikalisch-chemisch motivierter Modelle mit einer klaren Anwendungsorientierung. Die Verwendungszwecke der Modelle sind klar definiert und von einander abgegrenzt. Die Kompatibilität der Modelle wird durch die Übertragung von Ergebnissen innerhalb einer Hierarchie in mehreren Beispielen belegt. Die meisten der Methoden zur Modellreduktion, die Modelle und deren Anwendungen sind auf andere Systeme übertragbar. Somit geht der Nutzen der hier gezeigten Modelle deutlich über die hier präsentierten Anwendungen hinaus.

1 Introduction

1.1 Boundary conditions of process modelling

Mathematical modelling is a part of almost all aspects of chemical process design ([1]-[4]). The increasing necessity to develop more efficient, economically and ecologically sustainable processes has lead to new ideas in chemical engineering which are summarised under the term “process intensification”. One of the novelties of process intensification compared to traditional chemical engineering concepts is the integration of all aspects on different time and length scales in process design ([5]). Ideally, this means that catalyst development and system design should be executed simultaneously, or at least in an iterative, closed loop process. This is an ambitious aim, and it requires models for a wide spectrum of purposes.

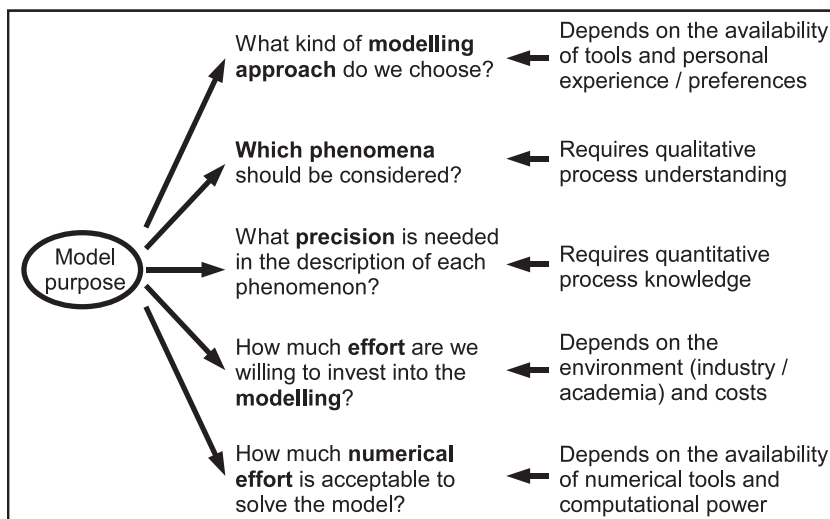


Figure 1: Factors influencing the outcome of a modelling process.

The process of model development is conducted under certain conditions, which ultimately determine the mathematical form and the dimension of a model. Figure 1 lists five important questions regarding the modelling process and indicates which factors influence the answers to these questions:

- The purpose of the model influences the modelling approach¹ that is chosen. This decision also strongly depends on the availability of numerical tools that allow to apply certain modelling approaches². In addition, this decision is often made against the background of the personal experience and preferences of the modeller. This is not necessarily bad, as long as the modeller does not reject approaches that are significantly better than his preferred ones.
- An important part of the model development is to decide which physical and chemical phenomena to include in the model. As a general rule, all phenomena should be considered which contribute significantly to the process behaviour which is in the focus of the model purpose³. According to the principle of parsimony (also known as 'Ockham's razor', [7]), the simplest possible model should be used, so irrelevant phenomena should be excluded from the model⁴. Of course, this requires sufficient qualitative knowledge about the relevant phenomena, as the modeller must be able to decide whether or not a phenomenon is relevant for the purpose. If the process knowledge is insufficient, this may result in a failure of the modelling process.
- Also the level of precision needed in the description of the relevant physical and chemical phenomena depends on the model purpose. A sufficiently precise description also requires adequate quantitative knowledge about the process⁵. Very often, a lack of quantitative knowledge in process modelling is overcome by 'fitting' model parameters to data from an experimental realisation of the process.
- Model development can be a very laborious task. The effort one is going to take to set up a model depends on the model purpose and its importance. Only important purposes justify complex models.
- At the end of the modelling process, the mathematical model needs to be solved. The effort that is considered acceptable for this depends on the purpose of the

1 Examples for modelling approaches are continuum models, population balance models or stochastic models.

2 E.g., one would not choose to set up a computational fluid dynamics model unless one has access to a numerical CFD package.

3 E.g., electrostatic effects on the surfaces of particles in a fixed bed are negligible if the purpose of the model is to describe the pressure distribution in this reactor. However, if the model is supposed to predict the spatial distribution of adhesive particles in the reactor, they may be of high importance.

4 A much more poetic and illustrative formulation of this criterion goes back to Antoine de Saint-Exupéry ([6]): "Il semble que la perfection soit atteinte non quand il n'y a plus rien à ajouter, mais quand il n'y a plus rien à retrancher." (It would seem that perfection is attained not when no more can be added, but when no more can be removed).

5 Quantitative knowledge includes kinetic expressions and kinetic parameters, material properties as well as thermodynamic models and parameters.

model⁶. Depending on the availability of numerical tools and computational power, this limits the numerical complexity of a model.

This short discussion shows that among all the boundary conditions, the model purpose has the strongest impact on the outcome of the modelling process ([8]). This conclusion can be inverted: A good model is not necessarily a model that describes many details of a process in excellent precision; a good model is a model which is appropriate for its purpose.

1.2 Requirements for models in process design

In process design, models are required for a wide range of applications, for example to roughly estimate a reactor's performance or to identify zones of educt maldistribution in a stirred tank reactor with a complex geometry. According to the previous chapter, this multitude of purposes demands a large number of different models.

Figure 2 shows three pairs of examples for different model purposes to illustrate the span of requirements that one encounters when designing a stirred tank reactor, for example:

- The conceptual design of the reactor requires models that can be solved within seconds, preferably analytically or even graphically⁷. In opposite to that, calculation times of one week or more may be considered acceptable for the analysis of the spatially distributed reactor behaviour during start-up, because the model needs to be solved only a few times.
- Depending on the model purpose, different physical phenomena may be relevant. The analysis of processes on the catalyst surface calls for models on the molecular scale, while the integration of the reactor in a multi-step synthesis plant applies spatially lumped models on a far larger length scale.
- The models may also differ with respect to the time constants involved; to design a temperature controller, a model needs to include relevant phenomena on the characteristic time constant of the energy balance, but a model describing the degradation of the catalyst neglects the dynamics of such fast processes.

6 A short cut model, for example, should be solved very quickly, preferably manually. For a process optimisation, a detailed model is required which can be solved within about one minute.

7 Examples for graphical solutions are the design of a cascade of adiabatic reactors as shown for example by Baerns, Hofmann and Renken (Chapter 10.1.4 in [9]), and the Mc-Cabe-Thiele diagram ([10]).

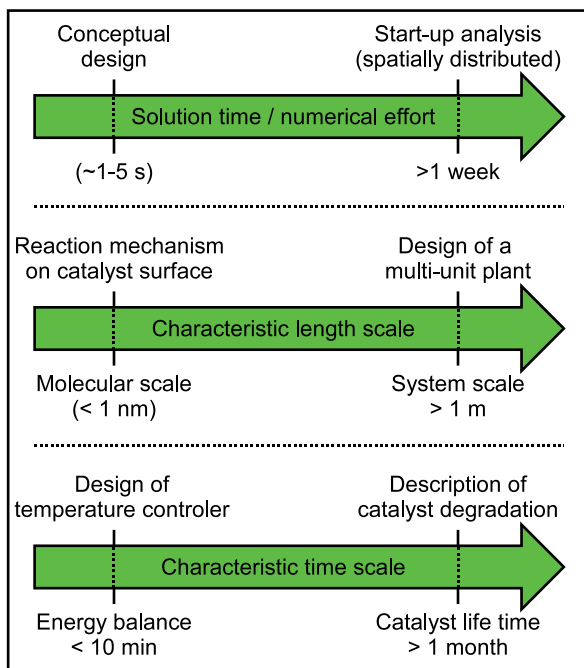


Figure 2: Examples of model purposes in the design process of a stirred tank reactor.

1.3 Model hierarchies

The previous discussion indicates that a large number of different models is needed to design a process, which gives rise to two problems. Firstly, the development (and the implementation, numerical solution and experimental validation) of so many models is a time-consuming task. Secondly, if the individual models are derived independently, they are most likely not compatible to each other. Chances are high that models apply different – even contradicting – approaches, for example with regard to reaction kinetics. That means that results obtained with one model, for example estimates of parameters, can not be transferred to another model.

The application of model hierarchies in the model development process can solve or at least alleviate these two problems. The basic idea of this concept is that models are not derived individually, but most of them are derived from others. This is illustrated in Figure 3, where reduced models are derived from a reference model by some reduction

technique. This simplifies the modelling process, because most of the reference model equations only need to be modified for the reduced model instead of being derived again from the start. Except for those assumptions that are changed in the reduction process, all of the characteristics of the reference model are transferred to the reduced model, so they are compatible to a certain degree. Therefore, the model hierarchy can be referred to as coherent.

A model hierarchy may not only contain three models as shown in Figure 3, but more reduced models can be generated from the reference model by applying different sets of additional assumptions to it, or from already reduced models. Each of the elements of the hierarchy can be tailored for one specific purpose or for several purposes that pose similar boundary conditions on the modelling process. Figuratively speaking, a model hierarchy is a tool box for designing a certain process, whose tools are specialised for different tasks, but they all have been forged in the same smithy.

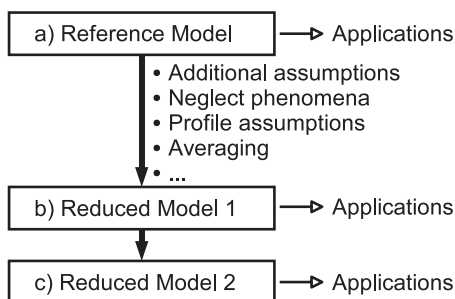


Figure 3: Principle of a model hierarchy.

In the subsequent chapters, several examples of model hierarchies for the design of four different processes are shown. The shape and size of the models are briefly outlined and the approach for model reductions is explained. In addition, exemplary results and applications are shown. In the last chapter, some general remarks regarding model hierarchies and model reduction are made.

2 Cyclic Water Gas Shift Reactor

2.1 Working principle of the Cyclic Water Gas Shift Reactor (CWGSR)

The idea of the CWGSR dates back to the beginning of the 20th century, when it was patented by Messerschmitt ([11]). Its principle is illustrated in Figure 4. A gas mixture containing hydrogen and carbon monoxide, for example from a gasification or reforming process, is used to reduce a fixed bed of iron oxide at temperatures of about 600-800 °C. This temperature range is very similar to typical temperatures of the mentioned fuel conversion processes, so a combination of them with the CWGSR is advantageous from an energetic point of view. The gaseous product during the reduction phase contains steam and carbon dioxide as well as a remainder of hydrogen and carbon monoxide. Once the bed is reduced to a sufficient extent, the gas feed is switched to steam, which then oxidises the iron to iron oxide. During this oxidation phase, the gaseous product is a mixture of steam and hydrogen, which contains no carbon monoxide. It is suitable for low temperature fuel cells such as the PEMFC. The net reaction over a complete cycle is the water gas shift reaction. Thus, the CWGSR can be applied to replace the sequence of shift reactors which is traditionally used to remove carbon monoxide in low temperature fuel cell systems.

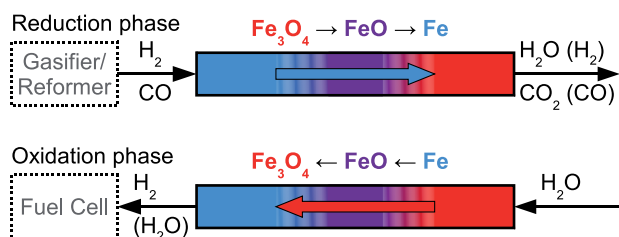


Figure 4: Working principle of the Cyclic Water Gas Shift Reactor (CWGSR).

Despite its early invention, this reactor has not yet been applied commercially. Only during the last decade, with the foreseeable demand for clean hydrogen and the necessity for alternative routes for the water gas shift process, research groups have started to investigate it again. Its principle has been realised as a stirred tank reactor ([12]-[15]) and as a chemical looping process ([16]-[19]). However, because these

options can only achieve lower efficiencies⁸, this chapter is focused on fixed bed reactors with a high length-to-diameter-ratio (as shown in Figure 4).

There are many questions to answer in the course of designing a CWGSR, for example:

- Is the application of periodic flow reversal (as indicated in Figure 4) beneficial?
- What is the qualitative system behaviour?
- What are the optimal durations of the oxidation and the reduction phase with respect to fuel efficiency?
- What does the axial temperature profile look like?
- Are there easily measurable states that can be used for process control?

These questions can be answered with the help of the model hierarchy illustrated in Figure 5. It comprises three models: the Reference Model, the Single Reaction Model and the Front Model, which are discussed in the following sections.

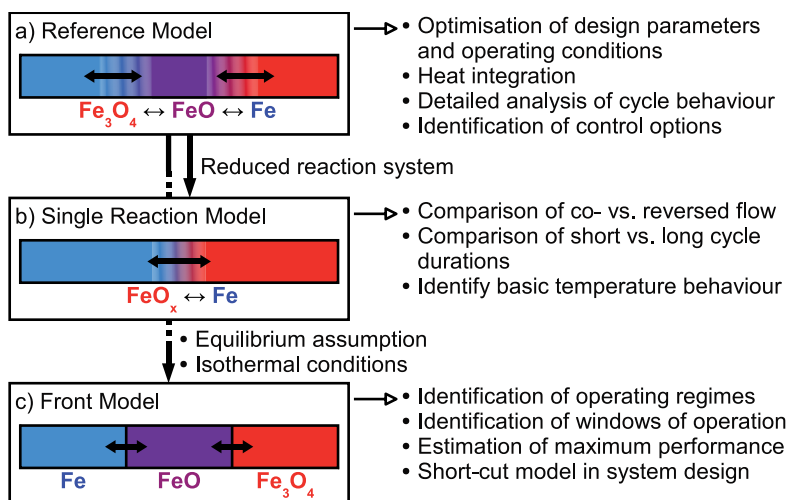


Figure 5: Model hierarchy for the design of the CWGSR.

8 The chemical looping process applies two fluidised beds, one for the reduction of iron oxide particles, the other for their oxidation. Each of the fluidised beds can be approximated as a well mixed reactor with respect to the solid particles and contains a population of particles of varying oxidation degree. In order to achieve a high conversion of the reducing gas at short gas residence times, the particles must have a relatively high oxygen content. Due to this, also highly oxidised particles are moved to the oxidising bed, where they do not contribute to the production of hydrogen, and are still subject to mechanical stress.

A fixed bed reactor with a low length-to-diameter-ratio can be approximated as a stirred tank reactor. In such a reactor, the conversion of the reducing gas is decreasing with increasing degree of reduction of the fixed bed, which leads to low fuel efficiency. To avoid this, the fixed bed may only be reduced to a small extent, which in turn leads to low reaction rates during the oxidation phase.

2.2 The Reference Model

This model (Figure 5a) is the basis of the CWGSR model hierarchy. It describes the CWGSR as a transient system, with a spatial distribution along the axial coordinate. It considers the equilibria of the reactions in a temperature dependent approach and features reaction rate kinetics depending on the temperature and the composition of the gas and the fixed bed. The gas is assumed to be ideal, and because experimental data have shown that the pressure drop over the reactor is generally low, isobaric conditions are assumed.

Based on these assumptions, a set of partial differential equations has been derived from mass and enthalpy balances. They describe the gas phase composition in the CWGSR in terms of molar fractions, x_i^G , the composition of the solid phase, x_i^S , and the temperatures of the gas and solid phases, T^G and T^S :

$$\varepsilon \cdot c_i^G \frac{\partial x_i^G}{\partial t} = -\varepsilon \cdot g \frac{\partial x_i^G}{\partial z} + c_i^G \cdot D_{ax} \frac{\partial^2 x_i^G}{\partial z^2} + \sigma^S \cdot \sum_{j=1}^4 v_{i,j}^G r_j \quad (1)$$

$$c_i^S \frac{\partial x_i^S}{\partial t} = \sum_{j=1}^4 v_{i,j}^S r_j \quad (2)$$

$$\varepsilon c_i^G \cdot \bar{c}_p^G \frac{\partial T^G}{\partial t} = -\varepsilon \cdot g \cdot \bar{c}_p^G \frac{\partial T^G}{\partial z} + q^W + q^{SG} + q^{M+} \quad (3)$$

$$\sigma^S \cdot c_p^S \frac{\partial T^S}{\partial t} = \lambda \frac{\partial^2 T^S}{\partial z^2} - q^{SG} + q^{M+} + q^R \quad (4)$$

The total mass balance of the gas phase in conjunction with the isobaric condition and the assumption of ideal gas yields an ordinary differential equation for the molar gas flux density, g :

$$0 = \varepsilon \frac{\partial g T^G}{\partial z} + \frac{1}{\bar{c}_p^G} (q^W + q^{SG} + q^{M+}) \quad (5)$$

The porosity of the fixed bed, ε , can be estimated from a simple measurement, for example by a water displacement experiment. The gas phase dispersion coefficient, D_{ax} , and the effective heat conductivity in the solid phase, λ , can be estimated from correlations (e.g. in [20]). c_i^S describes the amount of available iron atoms⁹ and thus

⁹ Available iron atoms are those iron atoms in the fixed bed particles which can be accessed by oxygen, either directly from the gas phase or via interstitial mass transport through the iron atom lattice, so they can be reduced and oxidised during the cyclic process.

reflects the oxygen capacity of the fixed bed. Under the assumption that the fixed bed material can be completely converted, this parameter can be calculated from the apparent density of the fixed bed material. Otherwise, it needs to be estimated from experimental data. The heat flux across the reactor wall into the gas phase, q^w , and the heat flux between the gas phase and the solid phase, q^{sg} , follow linear kinetics. The corresponding heat exchange coefficients can also be estimated from correlations for fixed beds ([20]). q^{M+} and q^{M-} represent the enthalpy fluxes associated to the mass transport between the gas phase and the catalyst surface. q^R is the heat source density due to reaction. The gas phase heat capacity, \bar{c}_p^G , depends on the gas composition, while the solid phase heat capacity, c_p^S , is assumed to be constant.

The density of the catalytic material in the fixed bed, σ^S , is the ratio of the weighed in solid mass and the reactor volume. $v_{i,j}^G$ and $v_{i,j}^S$ represent the stoichiometric coefficients of the chemical gas components and the solid phases (index i) in the reactions (index j). Four reactions are considered in the model: the oxidation and reduction reactions between iron and wuestite (Fe-FeO) and wuestite and magnetite (FeO-Fe₃O₄) under atmospheres of hydrogen / steam and carbon monoxide / carbon dioxide. Thermogravimetric experiments with a specific material ([21]) revealed that the reaction rates, r_j , can be described very well with simple power law kinetics. Although these kinetics are not physically justified in the context of gas-solid reactions, their agreement with the experimental data was superior to a number of other kinetic approaches¹⁰. As an example, the rate expression of the reaction of iron and wuestite under hydrogen / steam ($\text{FeO} + \text{H}_2 \rightleftharpoons \text{Fe} + \text{H}_2\text{O}$) is given:

$$r_1 = \begin{cases} k_{1,+}(T^S) \cdot (x_{\text{FeO}}^S)^{n+} \cdot \left(x_{\text{H}_2} - \frac{x_{\text{H}_2\text{O}}}{K_{\text{eq},1}(T^S)} \right)^{m+} & ; \text{ if } \frac{x_{\text{H}_2\text{O}}}{x_{\text{H}_2}} > K_{\text{eq},1}(T^S) \\ k_{1,-}(T^S) \cdot (x_{\text{Fe}}^S)^{n-} \cdot \left(x_{\text{H}_2} - \frac{x_{\text{H}_2\text{O}}}{K_{\text{eq},1}(T^S)} \right)^{m-} & ; \text{ if } \frac{x_{\text{H}_2\text{O}}}{x_{\text{H}_2}} \leq K_{\text{eq},1}(T^S) \end{cases} \quad (6)$$

The kinetic parameters, such as the reaction rate coefficient, the activation energy and the reaction orders with respect to the gas composition and the state of the solid phase have also been estimated from thermogravimetric experiments.

The Reference Model requires appropriate boundary and initial conditions. Danckwerts boundary conditions ([22]) are used for the component gas phase balances (Equation 1). Dirichlet boundary conditions are used for the enthalpy balance and the

¹⁰ In the kinetic study, power law kinetics were compared with Avrami-Erofeev kinetics, the shrinking core model, the crackling core model and the changing voidage model. The results of this study are not published yet.

total mass balance in the gas phase (Equations 3 and 5). Under periodic reversal of the flow direction, the positions of these boundary conditions change. The solid phase enthalpy balance (Equation 4) requires two boundary conditions, which are given by insulation conditions at both ends of the reactor.

The initial conditions of the model depend on the simulated mode of operation. For a single reduction or oxidation run, the initial conditions describe the compositions and temperatures in the gas phase and solid phase at initial time. Under cyclic steady state, the initial conditions demand that all spatially distributed states at the beginning of the cycle ($t=0$) must be identical to the states at the end of the cycle ($t=t_{end}$):

$$\begin{aligned} x_i^G(z, t=0) &= x_i^G(z, t_{end}) & ; & & x_i^S(z, t=0) &= x_i^S(z, t_{end}) \\ T^G(z, t=0) &= T^G(z, t_{end}) & ; & & T^S(z, t=0) &= T^S(z, t_{end}) \end{aligned} \quad (7)$$

To solve this model, it was discretised along the spatial coordinate according to the finite volume method. The resulting differential-algebraic equation system was implemented in the simulation environment Matlab and integrated along the time coordinate using implicit Runge-Kutta schemes.

A CWGSR mini-plant with a fixed bed of 167 g (length 65 cm, diameter 2 cm) was set up in order to validate the Reference Model. The fixed bed consisted of pellets with an average diameter of 3 mm and a porosity of 0.67. The pellets were produced from hematite particles with an average diameter of 2 μm , which were pelletised by adding 15 mass percent of sodium silicate (water glass). Due to the high porosity of the pellets and the high gas diffusion coefficients at typical operating temperatures in the CWGSR, mass transport in these pellets is not rate determining, so it can be neglected in the model.

To compensate the heat losses across the reactor wall, the fixed bed was located inside an oven which provided approximately constant temperatures along the reactor length.

A series of reduction experiments has been conducted with this mini-plant, each starting from a completely oxidised fixed bed (consisting of Fe_3O_4 ¹¹). A mixture of hydrogen and nitrogen was used as the feed gas. Experiments with different molar fractions of hydrogen and total gas flow rates were carried out. In Figure 6 (solid lines), the hydrogen fraction at the outlet during four selected experiments is shown over time. These profiles indicate that under the given operating conditions, the qualitative behaviour of the CWGSR is dominated by the break-through of reaction waves. Each of

¹¹ Fe_3O_4 is the iron oxide species which can be produced by oxidation with steam under realistic operating conditions and limited time. Theoretically, steam can oxidise the fixed bed to Fe_2O_3 , but that takes longer than the typical phase duration of 1-2 hours, so it is considered irrelevant for the process.

the measured profiles shows the breakthrough of the magnetite / wuestite front after 5-20 minutes. The breakthrough time depends on the applied gas velocity. The molar fraction of hydrogen is approximately constant for some time after that. It corresponds to the equilibrium hydrogen fraction of the FeO-Fe reaction. The breakthrough of the second front (wuestite / iron) is observed after 30 minutes (for high gas velocities) up to 120 minutes (for low gas velocities). After the second breakthrough, the measured molar fraction of hydrogen is equal to the molar fraction at the inlet, so the fixed bed is not reduced any further.

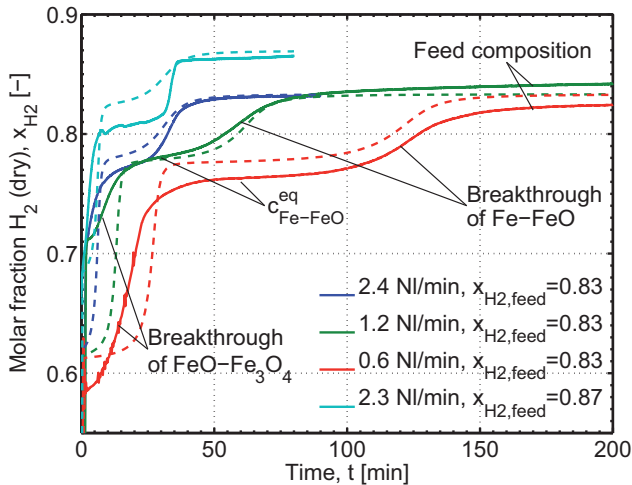


Figure 6: Comparison of simulated (dashed lines) and measured exhaust gas composition (solid lines) during four reduction experiments with hydrogen / nitrogen mixture as feed and different gas flow rates.

Only two parameters need to be adjusted in order to quantitatively reflect this behaviour with the Reference Model. Due to the pelletising process, some of the primary particles in the pellets are completely encapsulated in glass. This effectively prevents the transport of hydrogen to these pellets, so they can not participate in the reaction. This leads to a reduced oxygen capacity of the fixed bed, which is reflected by the model parameter c_i^S , which thus needs to be adjusted. The second parameter that needs to be fitted is the reaction rate constant. During the experiments, the same material was reduced and oxidised repeatedly, which caused a certain degradation after a few cycles. This is described by a decrease of the reaction rate constants. In order to estimate these two parameters, the time constants (meantime and length) of the

breakthroughs from the experiments were compared to the simulated time constants. The minimisation of the residuals between these experimental and simulated time constants yielded that the fixed bed capacity is reduced to 42 % of its stoichiometric value, and that the reaction rate constant is at 30 % of its initial value, as estimated from the previously described kinetic measurements.

With these two adjusted parameters in the Reference Model, the simulation of the breakthrough experiments yields output functions which are shown as dashed lines in Figure 6. The comparison indicates that the model reflects the time constants of the reactor behaviour very well. This is especially the case with regard to the breakthrough of the second reaction wave; the time and the width of these breakthroughs agree very well. The remaining quantitative deviations, especially between the breakthroughs, can not be amended using the two adjustable parameters¹². Thus, the Reference Model is a suitable mathematical representation of the CWGSR.

The Reference Model delivers a large amount of information on the spatio-temporal behaviour of the gas composition, gas velocities and the fixed bed composition. It is most suited to analyse the transient reactor behaviour in many details. As an example, Figure 7 shows the molar fraction of hydrogen at a cyclic steady state during three repeating reduction and oxidation phases with periodic reversal of the gas flow direction. During the reduction phase¹³, a mixture of 90 % hydrogen and 10 % of steam is fed (at $z=0$). During the oxidation phase, pure steam is fed at the opposite end. The concentration fronts indicate the location of the reaction zones, which move forward and backward along the reactor length at different velocities.

This model can be applied for the optimisation of operating parameters such as the duration of each phase. It can also be used to evaluate whether purging phases between the reduction and the oxidation phases are beneficial. Another idea that may be studied using the Reference Model is the application of non-constant gas flow rates during some of the phases. For example, it may be advantageous to reduce the gas velocity towards the end of the oxidation phase in order to achieve high degrees of gas conversion.

In addition to the phase durations, the heat integration of the CWGSR is of high practical relevance. Different concepts are possible: because the CWGSR is a fixed-bed reactor with a slightly exothermic net reaction operated under periodic flow reversal, the temperatures inside the CWGSR can reach much higher values than the gas temperatures at the inlet or outlet, as Matros and Bunimovich have shown ([23]). This

¹² A publication focussing on the experimental works, the model and the model validation is currently under preparation.

¹³ In this example, the first reduction phase is at $t=0-3000$ s; the first oxidation phase is at $t=3000-6000$ s.

finding has been theoretically confirmed for the CWGSR using the Single Reaction Model (Chapter 2.3, [PH 2]), and it can be exploited to design a heat integration concept. Another option is to heat the CWGSR by off-heat from a high temperature fuel cell which is operated on the output gas from the reduction phase, or by heat from an afterburner. The Reference Model is the suitable tool for the validation of these heat integration concepts.

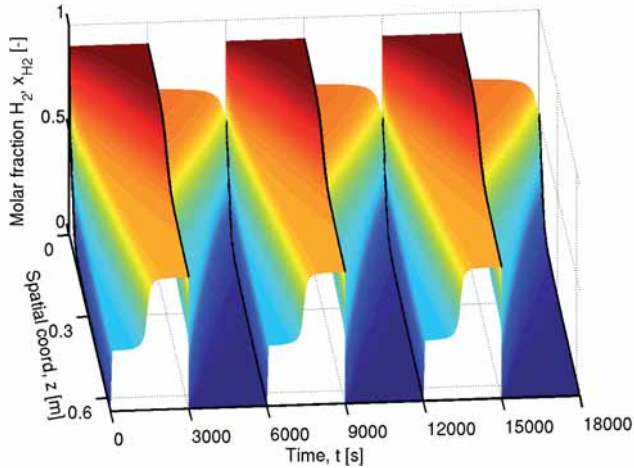


Figure 7: Simulated hydrogen fraction in the gas phase during a cyclic steady state with periodic flow reversal using the Reference Model. Feed gas position at $z = 0$ during $t = 0 \dots 3000\text{s}$, $t = 6000 \dots 9000\text{s}$ and $t = 12000 \dots 15000\text{s}$. Feed gas position at $z = 0,65$ at all other times.

A more qualitative application is the identification of suitable states for process control. Such states should be easily measurable at low cost and they should be sensitive with respect to important states. For example, if the position of a reaction zone can be reliably detected by measuring the gas temperature at the outlet, this state would be a favourable measurement quantity to control the switching time between both cycle phases. The Reference Model can serve as a tool to identify such states.

The application of the Reference Model is limited by two issues. The first one is the relatively high numerical effort that is necessary to solve it, especially if the cyclic steady state needs to be attained from arbitrary initial conditions. The second limitation is due to the large amount of data that is produced by this model, which makes their interpretation in terms of physical and chemical processes rather difficult.

2.3 The Single Reaction Model

In order to gain a better understanding of the process and to make some basic decisions about its design, the Single Reaction Model was derived (Figure 5b, [PH 2]). In contrast to the Reference Model, which considers a two-step reduction / oxidation reaction scheme, this reduced model assumes that the reduction takes place in a single reversible reaction from an oxidised fixed bed species to a reduced species. This alleviates two of the problems of the Reference Model: the Single Reaction Model is faster to solve and the results are easier to interpret from a physical point of view.

The reduction from the Reference Model to the Single Reaction Model is achieved by adding the assumption of a single step reduction to the assumptions of the Reference Model, followed by a derivation of the model equations from the energy and mass balance equations. As a result, the Single Reaction Model has a similar structure as the Reference Model, but a lower dimension. In addition, it contains fewer kinetic parameters, thus parameter studies are less complex. The number of parameters is further reduced by formulating the Single Reaction Model in terms of dimensionless parameters.

With the single reaction model, several important qualitative design decisions were made ([PH 2]). The model showed that a significantly higher fuel efficiency can be obtained under periodic flow reversal and short phase durations¹⁴ (Figure 8). The fuel efficiency is defined as the ratio of the amount of hydrogen obtained from the process and the amount of fuel fed to it, and it is an important performance indicator of the CWGSR¹⁵. However, for very short phase durations, which are in the order of magnitude of the gas residence time, the fuel efficiency decreases rapidly.

The Single Reaction Model also indicates that at periodic flow reversal and short cycle times, the thermal behaviour of the CWGSR resembles the classical Matros reactor ([23]). Because the overall reaction is slightly exothermic, flow reversal leads to an accumulation of sensible energy in the fixed bed, so that sufficiently high temperatures can be obtained at relatively low gas inlet temperatures. This is an important result for the heat integration of the CWGSR.

14 "Short phase durations" refers to phase durations during which only a small part of the fixed bed is converted. However, these phase durations are still multiple gas residence times. In contrary, long cycle times are phase durations during which most or all of the fixed bed is converted.

15 The fuel efficiency is a mass related performance parameter. An energetic assessment can be made with the help of the energetic efficiency, which is defined as the ratio of the heating value of the cleaned product gas and the feed gas.

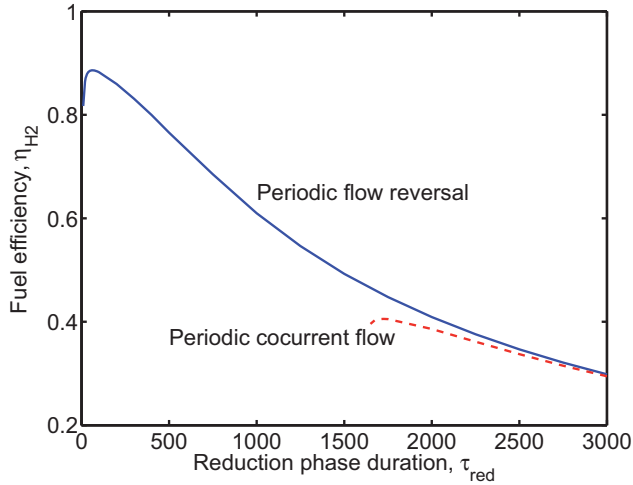


Figure 8: Simulated fuel efficiency according to the Single Reaction Model as function of the reduction phase duration under different operating modes (from [PH 2]).

2.4 The Front Model

In order to identify and describe the qualitative behaviour of the CWGSR, another reduced model was derived (Figure 5c, [PH 4]). Assuming periodic flow reversal (a favourable mode of operation according to the Single Reaction Model), isothermal conditions and chemical equilibria at all locations in the reactor, this model represents the limit case of the Reference Model at infinitely high Damköhler numbers and thermal equilibrium with an isothermal, heated environment. A wave analysis ([24]) of the system shows that the reactions take place at sharp fronts, which move along the axial coordinate during each phase. Because these fronts are the dominating phenomenon that determines the dynamic behaviour of the system under the given assumptions, this reduced model is called the Front Model. The wave analysis quantifies the front velocities during each phase as functions of the fuel gas composition and the temperature. A typical example is the velocity of the iron-wuestite (Fe-FeO) front during the reduction phase for high fixed bed oxygen capacities, which reads (see [PH 4]):

$$w_{Fe-FeO}^{red} = \frac{u \cdot \varepsilon}{\Delta C_{Fe-FeO}} \cdot (c_{CO_2, Fe-FeO}^{eq} - c_{CO_2, feed}) \quad (8)$$

In Equation 6, u represents the true gas phase velocity, ε is the volumetric gas fraction and ΔC_{Fe-FeO} is the amount of oxygen taken up by the solid phase in this front. The concentration difference inside the brackets¹⁶ can be interpreted as the driving force of this front.

The velocities of both fronts during each phase can be calculated individually. They depend on the composition of the feed gases and on the temperature dependent equilibrium compositions. The average velocity of each front over a complete cycle is then formed by a summation of the velocities during each phase weighted with the duration of the phase:

$$\bar{w}_{Fe-FeO} = \frac{\tau_{red} \cdot w_{Fe-FeO}^{red} + \tau_{ox} \cdot w_{Fe-FeO}^{ox}}{\tau_{red} + \tau_{ox}} \quad (9)$$

With the relative duration of the reduction phase,

$$S^I = \frac{\tau_{red}}{\tau_{red} + \tau_{ox}} \quad (10)$$

the average front velocity becomes

$$\bar{w}_{Fe-FeO} = S^I \cdot w_{Fe-FeO}^{red} + (1 - S^I) \cdot w_{Fe-FeO}^{ox} \quad (11)$$

Depending on the sign of these average front velocities, the fronts are located near either end of the reactor at cyclic steady state. With two fronts, this yields four different operating regimes. Because one of these regimes is physically impossible – the sequence of the fronts may not change – it decomposes into two degenerated regimes, so the reactor may be operated in one of five distinct operating regimes. As shown before, the average front velocities depend on the fuel gas composition, the temperature and the ratio of the phase durations. Thus, the operating regime depends on these parameters. Figure 9 shows an example of a regime map for an arbitrarily chosen fuel gas composition of 65 % H₂, 11 % H₂O, 17 % CO, 4 % CO₂, where the area of existence of each regime is shown as a function of the reactor temperature and the relative duration of the reduction phase.

The fuel efficiency and average product concentration can also be described as functions of the same parameters. Figure 10 shows these two quantities for the same example as in Figure 9. These two diagrams not only quantify the maximum attainable fuel efficiency from this fuel gas, but they also indicate that high efficiency and high

¹⁶ The concentration difference in Equation 8 is the concentration of carbon dioxide at the equilibrium between iron and wuestite minus its concentration in the feed.

product concentration can not be obtained simultaneously. Useful compromises between both performance indicators are attainable in the regime where both fronts lie at opposite ends of the reactor. Together with an upper bound for the operating temperature due to material restrictions, this defines the range of preferable operating conditions.

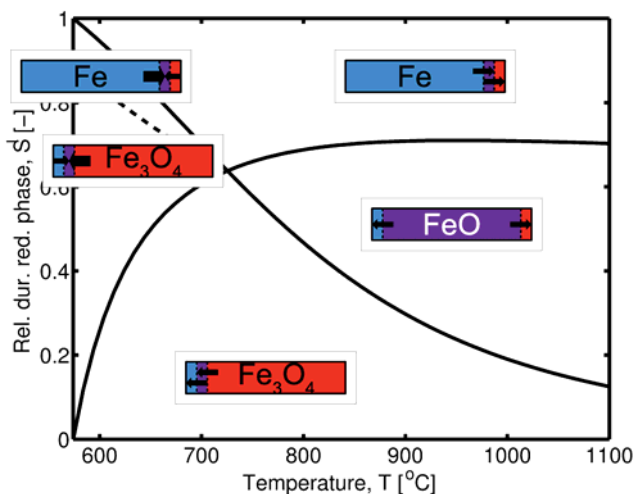


Figure 9: Operating regimes of the CWGSR for a given fuel gas composition as a function of the reactor temperature and the ratio of phase durations (from [PH 4]).

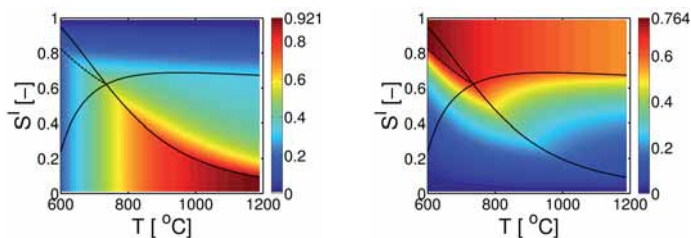


Figure 10: Fuel efficiency (left) and product concentration (right) for a given fuel as functions of operating conditions (from [PH 4]).

Besides these results, the identification of the moving fronts as the dominating process in the CWGSR greatly helps to interpret the results of the detailed model from a physical point of view. Furthermore, the Front Model has been used as a short-cut model in system design ([PH 6]).

2.5 Summary

The proposed model hierarchy for the Cyclic Water Gas Shift Reactor comprises three models. The Reference Model is experimentally validated and yields many details about the transient behaviour of spatially distributed states in the fixed bed reactor. Compared to the Reference Model, the Single Reaction Model uses a reduced reaction system. Based on this model, several important qualitative design decisions have been made. The Front Model describes a limit case of the Reference Model. Its results are very intuitive. In addition to an improved qualitative understanding of the CWGSR behaviour, the Front Model also allows to identify suitable operating conditions and estimate attainable efficiencies.

The Single Reaction Model and the Front Model are derived from the Reference Model. The approaches for the model reduction are physically or chemically motivated, leading to a change in the list of assumptions which ultimately result in different equation systems. While the Reference Model and the Single Reaction Model have very similar mathematical structures, namely PDEs in time and one spatial coordinate, the Front Model consists of only two algebraic equations.

The design of the CWGSR is an ongoing process, and the model hierarchy will be extended according to its needs. One potential extension is a quasi steady state model. It can be derived under the assumption of periodic flow reversal and short phase durations from the Reference Model by time integration over a complete cycle ([25], unpublished results). Such a model approximates the cyclic steady state under these assumptions and can be applied to obtain good initial conditions either for the cyclic steady state of the Reference Model or for the optimisation of operating and design parameters. These problems can be solved much faster with the quasi steady state model, compared to optimisations with the Reference Model. The results can then be validated by use of the fully dynamic Reference Model.

3 Structured reforming reactor

3.1 The Indirect Internal Reforming Reactor (IIR)

Molten Carbonate Fuel Cells (MCFC) are operated at temperatures of about 600 °C and produce approximately equal amounts of heat and electrical power. The electrochemical reactions at the anode are preceded by the endothermic reforming process, which transforms the fuel gas (for example natural gas or bio gas) into a gas mixture containing large fractions of hydrogen and carbon monoxide. This gas is then converted electrochemically in the fuel cell. The high operating temperature of the MCFC and the availability of heat in these systems enable the integration of the electrochemical and the reforming process within a single containment. The option with the most intense integration is the so-called direct internal reforming ([26]), where the reforming process takes place inside the anode channel of the fuel cell. This option is realised in the majority of modern high temperature fuel cells.

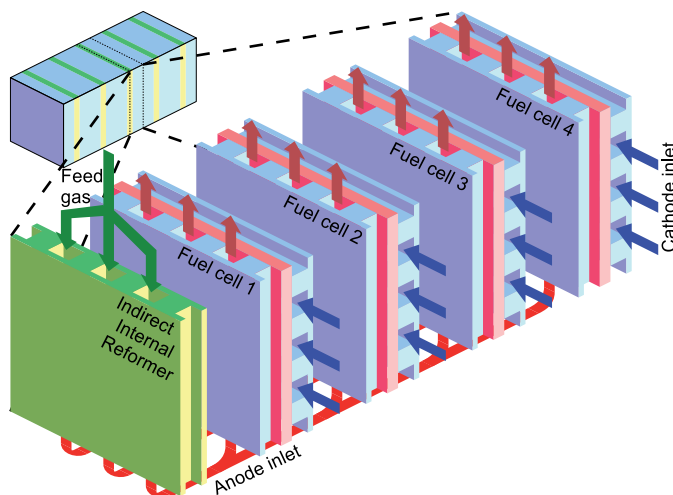


Figure 11: Arrangement of the Indirect Internal Reforming Reactor (IIR) in a Molten Carbonate Fuel Cell stack (MCFC).

Another integration concept is the indirect internal reforming (IIR), which is specific for MCFC. Here, dedicated reforming reactors are inserted into the fuel cell stack (Figure 11). The IIR reactor is thermally coupled with the fuel cells via the separation sheet between them. This provides the necessary heat for the reforming process and

the required cooling for the fuel cell. A purposeful design of the IIR reactor can even be used to manipulate the spatial temperature profiles in the neighbouring fuel cells. Thus, hot and cold spots in the fuel cells can be avoided, which increases their lifetime and efficiency.

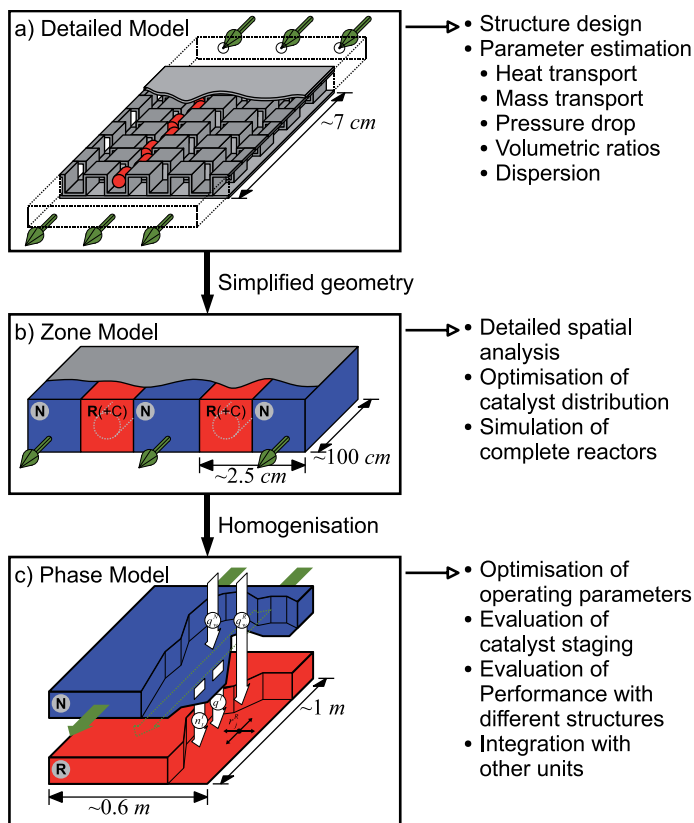


Figure 12: Model hierarchy for the design of the IIR.

In the Hotmodule by MTU Onsite Energy, Ottobrunn ([27], [28]), IIR units are inserted into the fuel cell stack after every eighth fuel cell. The IIR reactors used by the MTU are arranged reactors (see Figure 12a, [29]-[31]), where catalyst pellets (red cylinders in Figure 12a) are arranged in a structure of corrugated metal sheets. Under typical operating conditions, this design leads to transport limited reaction rates. The transport properties in the reactor strongly depend on the structure. This means that the reactor behaviour is dominated by the transport processes on a small scale. The reverse

conclusion is that a purposeful design of the geometrical structure can be used to design the IIR such that the temperature profile in the neighbouring fuel cells takes a preferable shape.

The design of an IIR requires mathematical models that describe the processes of transport and chemical reactions in the structure on a small scale, models for the analysis and optimisation of a complete IIR unit, and models for the design of the coupled system of the IIR and the MCFC. The model hierarchy illustrated in Figure 12 fulfils all these purposes ([PH 9]).

3.2 The Detailed Model

The hierarchy is based on the Detailed Model (Figure 13a, [PH 3]). It reflects an assembly of several repeating geometrical sections of the structure, the so-called elementary cells, plus an inlet and an outlet zone (top and bottom of Figure 13a). The size of the Detailed Model is chosen so that the gas flow in some of the elementary cells is undistorted by the effects at the inlet and the outlet. In this example, the Detailed Model considers one row of catalyst pellets, which are shown as white rectangular shapes in the figure. They are arranged in a slightly zig-zag manner. The characteristic length scales in this model are the size of the catalyst pellets of about 2 mm and the lengths of the corrugated sheets of about 3 mm. The Navier-Stokes equations are used to describe the transport of mass and energy between the gas phase and the pellets as well as the reaction at the surface of the pellets in three spatial dimensions.

As shown in [PH 9], the Detailed Model is suitable for a wide range of purposes. One important qualitative result obtained from it is the identification of two zones in the IIR structure. Figure 13 shows spatial profiles of the molar fraction of methane¹⁷, the temperature and the gas velocity at a certain set of boundary conditions. The methane molar fractions in the vicinity of the catalyst pellets (visible as white boxes) in Figure 13a are close to chemical equilibrium. Further away from the pellets, the gas composition changes only slowly due to mass transport to and from the pellets. This mass transport is hindered by the corrugated sheets. The gas temperature near the pellets is significantly lower than the gas temperature far away from them (Figure 13b). As with the mass transport, the heat transfer from the pellet surfaces to the gas far away from them is slowed down by the sheets. With regard to the gas velocity, the gas is almost stagnant near the pellets (Figure 13c). These results indicate that the gas phase can be divided into two zones: the reactive zone near the pellets (red box in Figure 13a) and the non-reactive zone far away from it (blue box).

¹⁷ Methane is an educt in the reforming process.

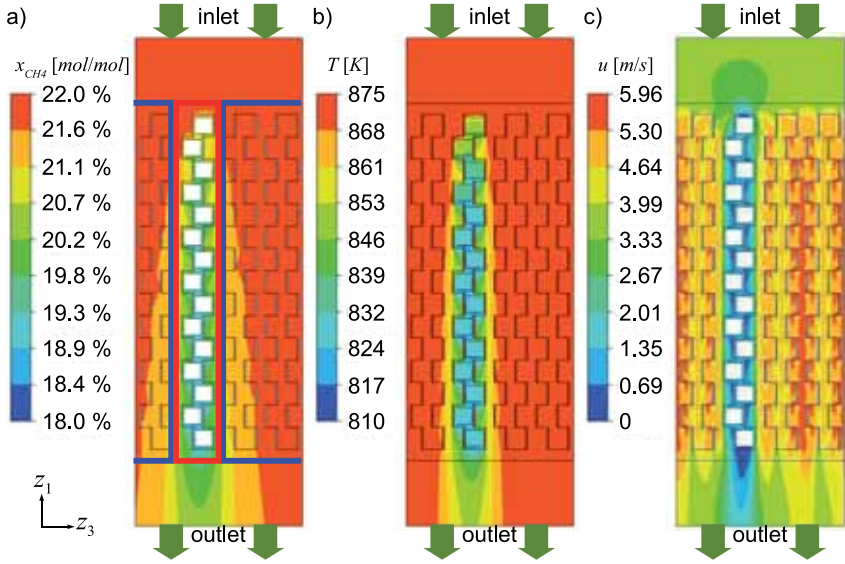


Figure 13: Simulation results from the Detailed Model of the IIR: a) molar fraction of methane, b) gas temperature and c) gas velocity (from [PH 9]).

The reduced models of this hierarchy, namely the Zone Model and the Phase Model, avoid the description of the detailed geometry by using simplified approaches to reflect the transport processes between the two zones. The detailed information about the transport processes as simulated in the Detailed Model is aggregated in the transport parameters of the reduced models. The Detailed Model can be used to estimate these parameters. The estimation of pressure drop coefficients and the heat exchange coefficient between both zones is briefly outlined in the following.

The pressure difference per unit length in a structured reactor is a function of the structure geometry (characteristic length, d , and void fraction, ε), the gas properties (density, ρ , and viscosity, μ) and the superficial gas velocity, u :

$$\frac{\Delta p}{L} = f(d, \varepsilon, \rho, \mu, u) \quad (12)$$

Note that the friction correlation, f , is not further specified. It may be described by the Ergun equation ([32]), Darcy's law ([33]) or any other suitable correlation. Each of these correlations includes one or more parameters. The Detailed Model can be used to conduct numerical experiments under different conditions (velocity, viscosity etc.) to obtain values for $\Delta p/L$, from which the unknown parameters of the friction correlation

can be estimated. This approach has been applied to estimate anisotropic coefficients in the gas phase close to the catalyst pellets and in the gas phase which is free of pellets. It can also be used to investigate the dependencies of the coefficients from the variables listed in Equation 12. A similar method has been applied by Mahr and Mewes to estimate pressure drop coefficients in a structured Katapak bed ([34]).

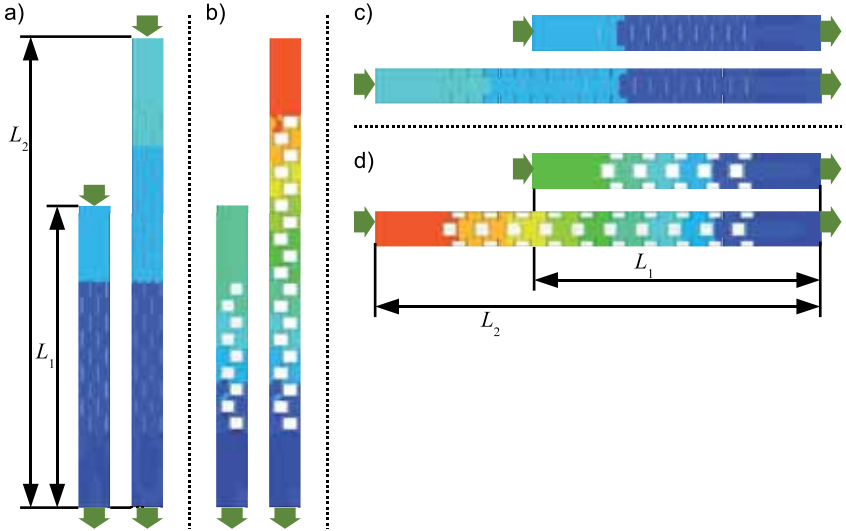


Figure 14: Detailed Models used to estimate anisotropic permeabilities in the reactive and the non-reactive zone (from [PH 9]).

In the given structure, the pressure gradient is not constant over the whole geometry of a Detailed Model. Especially near the inlet and outlet, the gradients are expected to deviate from their value at fully developed flow. In order to obtain a more representative estimate of the pressure drop, two simulations of the Detailed Model under identical boundary conditions, but with different lengths have been performed (Figure 14). Assuming that the pressure losses in the inlet and outlet regions are identical in both models, the difference of both pressure drops can be used together with the difference in length to calculate a value for the friction correlation at given conditions¹⁸:

$$\frac{\Delta p_1 - \Delta p_2}{L_1 - L_2} = f(d, \varepsilon, \rho, \mu, u) \quad (13)$$

¹⁸ A derivation of this equation is given in Heidebrecht et al. ([PH 9]).

This approach has been applied to estimate anisotropic permeabilities in the IIR structure. It requires numerical experiments with the Detailed Model with and without catalyst pellets and with different gas flow directions (see Figure 14).

In the Phase Model (see Chapter 3.4 and [PH 9]), the heat flux density between both zones is described by linear kinetics:

$$q^I = k^I \cdot (T^N - T^R) \quad (14)$$

Here, T^N and T^R are representative temperatures of the non-reactive and the reactive gas, q^I is the heat flux density between both zones and k^I is the heat exchange coefficient that needs to be estimated. In order to obtain values that represent the average of a whole elementary cell, this equation is integrated over the interfacial area of such a cell:

$$Q^I = k^I A^I \cdot (T^N - T^R) \quad (15)$$

where Q^I is the total heat flux between both zones in an elementary cell, and A^I is the interfacial area between the two zones in this cell. Using an adiabatic version of the Detailed Model¹⁹, the heat flux between the reactor walls and the reactive zone is zero. Because the gas velocity in the reactive zone is low, this convective heat transport is negligible compared to the heat flux across the interface between the reactive and the non-reactive zone. Thus, under steady state conditions the heat flux across the interface is approximately equal to the heat of reaction produced in the elementary cell. The heat of reaction equals the integral of the reaction rates times the reaction enthalpies over the whole catalyst surface:

$$Q^I \approx Q_{cat} = \int_{A_{cat}} \sum_j \Delta_R h_j^0(T) \cdot r_j dA \quad (16)$$

The representative temperatures of the two zones are obtained by averaging over the volume of the non-reactive gas and the surface of the catalyst pellets:

$$T^N = \frac{1}{V^N} \int_{V^N} T dV \quad (17)$$

$$T^R = \frac{1}{A_{cat}} \int_{A_{cat}} T dA \quad (18)$$

¹⁹ In this version of the Detailed Model, the heat fluxes through the top and bottom metal sheets are zero.

The quantities in Equations 16-18 can be evaluated from simulation results of the Detailed Model. After insertion into Equation 15, the heat exchange parameter can be estimated.

Further parameters such as the volume fraction of each zone and mass exchange parameters have been estimated from the Detailed Model with similar approaches ([PH 9]). The Detailed Model can also be applied to estimate representative axial dispersion coefficients, for example as shown by Freund et al. ([35]).

3.3 The Zone Model

The numerical effort to solve the Detailed Model is too high to describe a complete reactor at this level of detail. For the analysis of existing or the design of new flow fields on a reactor's scale, the Zone Model was derived (Figure 12b, [PH 3], [PH 9]). This model is based on the identification of the two zones from the detailed model.

The reduction from the Detailed Model to the Zone Model is achieved in two steps:

- A cuboidal volume around the catalyst pellets is defined as the reactive zone (see Figure 12b). The size of this volume can be defined with the help of the results from the Detailed Model. The reactions are modelled as quasi-homogeneous reactions in this zone.
- The geometrical structure of the reactor is neglected. To represent the flow resistance of the original structure, a Darcy term with anisotropic permeabilities is added to the momentum balance. The permeabilities can be estimated from versions of the Detailed Model as shown in the previous subsection.

Apart from the addition of the Darcy term in the momentum balance and the homogeneous reaction terms in the mass and energy balances of the reactive volumes, the Zone Model uses the same set of partial differential equations as the Detailed Model. However, the reduction of the geometry from detailed structures of the corrugated sheets to cuboidal gas zones is sufficient to allow the simulation of a complete IIR reactor with the Zone Model.

Figure 15 shows two exemplary results from the Zone Model of a complete IIR reactor. The cut out drawing in Figure 15a indicates the locations of the reactive and the non-reactive zones in these figures. The IIR reactor is subdivided into four sections (Figure 15a). Section 1 contains neither corrugated sheets nor catalyst pellets, so the gas passes without reaction in an upward direction. Section 2 comprises structures as shown in the previous chapter, but with the channels and pellet rows in a horizontal

arrangement (as shown in Figure 13, but rotated by 90°). Upon entering this section, the gas is redirected to a horizontal flow direction, and the reforming reaction takes place in the reactive zones. This can be clearly seen by the funnel-like shapes around these zones in Figure 15a. Section 3 comprises of essentially the same structures as Section 2, but this time with a downward main flow direction. At the end of this section, the reaction rate decreases because the reactant concentration in the non-reactive phase decreases. In order to enforce the reaction rate in the last section of the IIR reactor, Section 4 applies the same structure of corrugated sheets as in the previous sections, but with a higher density of catalyst pellets. This staged design helps to sustain a relatively constant reaction rate over the whole reactor, which can also be seen by the smooth transition from high to low methane concentrations in Figure 15a. The Zone Model can also be applied to evaluate the performance of other staged arrangements of structures.

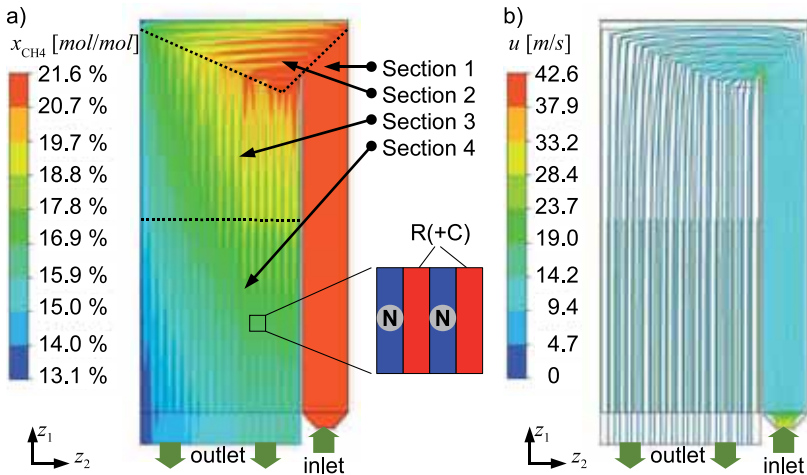


Figure 15: Methane molar fraction (a) and streamlines (b) in an indirect internal reforming reactor simulated with the Zone Model (from [PH 9]).

Besides this, the Zone Model is suitable to analyse reactor-wide flow fields. In the flow field used in this version of the Zone Model, one might intuitively presume two deficits: A dead zone with insufficient supply of reactants may occur in the upper left corner of the reactor, and a bypass of gas may happen around the separating wall between Sections 1, 2 and 3. Figure 15b shows streamlines in the IIR according to the Zone Model. They start at the inlet at equidistant positions. At the reactor outlet, the streamlines leave the

reactor in an almost equidistant pattern, so the gas is relatively homogeneously distributed. Some streamlines also touch the upper left corner of the reactor, so obviously this corner is also supplied with reactants. At the joint between Sections 1, 2 and 3, the streamlines are denser, but a bypass can not be observed at this position. Thus, this reactor design has no deficits with respect to gas distribution.

3.4 The Phase Model

The IIR reactor is thermally coupled with a high temperature Molten Carbonate Fuel Cell (MCFC). Due to this coupling, the endothermic reforming process withdraws a spatially distributed heat flux from the neighbouring fuel cells, thus influencing the cells' spatial temperature profiles. Because the temperature distribution is a very important state within the MCFC, the catalyst and structure placement in the IIR reactor should be designed such that a preferable temperature profile is obtained in the fuel cells. A combination of the Zone Model with a spatially distributed fuel cell model is too complex to be solved efficiently in the framework of an optimisation. Thus, an even more reduced model of the IIR is necessary.

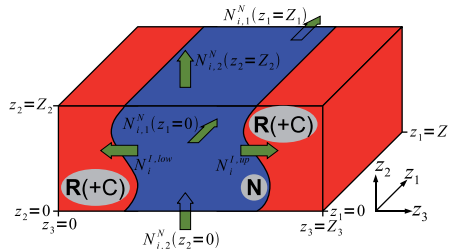


Figure 16: Repeating section of the IIR Zone Model, comprising non-reactive (N) and reactive (R) volumes (from [PH 9]).

The so-called Phase Model is derived by mathematical means and by additional physical assumptions from the Zone Model. The first physical assumption is that no mass transport occurs through the alternating non-reactive and reactive zones (in z_3 -direction, Figure 16). Furthermore, it is assumed that mass transport along z_1 and z_2 in the reactive zone is negligible. In the following, the derivation of the partial molar balance in the non-reactive gas is shown as an example. It considers a repeating cut out section of the Zone Model as shown in Figure 16 (see also [PH 9]). The general formulation of the transient component balance in three cartesian coordinates, as used in the Zone Model, reads:

$$\frac{\partial c_i}{\partial t} = -\frac{\partial n_{i,k}}{\partial z_k} + \sigma_i \quad (19)$$

This equation is formulated in Tensor notation ([36]). $n_{i,k}$ refers to the one-dimensional tensor of molar flux densities of species i , including convective and diffusive contributions. Two integrations are applied to this equation to obtain a reduced formulation. The first integration is over the complete volume of the non-reactive zone. After some manipulation, the following equation is obtained:

$$\begin{aligned} \int_{V^N} \frac{\partial c_i}{\partial t} dV &= N_{i,1}^N(z_1=0) - N_{i,1}^N(z_1=Z_1) \\ &+ N_{i,2}^N(z_2=0) - N_{i,2}^N(z_2=Z_2) - N_i^{I,up} - N_i^{I,low} + \int_{V^N} \sigma_i dV \end{aligned} \quad (20)$$

where the $N_{i,k}^N$ are the total molar fluxes of species i in direction k across the boundaries of the cut out section (see Figure 16). $N_i^{I,up/low}$ are the molar fluxes across the interface between both zones. According to the first mentioned physical assumption, the mass fluxes between the non-reactive and the reactive zones through opposing interfaces must be equal: $N_i^{I,up} = N_i^{I,low} := N_i^I$. Furthermore, constant profile assumptions are used to evaluate the two remaining integral expressions:

$$c_i(z \in V^N, t) = c_i^N(t) \quad ; \quad \sigma_i(z \in V^N, t) = \sigma_i^N(t) \quad (21)$$

With the following definition of superficial molar flux densities and the average molar flux density across the zone interface

$$n_{i,1}^N = N_{i,1}^N / (Z_2 Z_3) \quad ; \quad n_{i,2}^N = N_{i,2}^N / (Z_1 Z_3) \quad (22)$$

$$n_i^I = N_i^I / A^I \quad (23)$$

we obtain

$$\begin{aligned} V^N \frac{\partial c_i^N}{\partial t} &= -\left(n_{i,1}^N(z_1=Z_1) - n_{i,1}^N(z_1=0)\right) \cdot Z_2 Z_3 \\ &- \left(n_{i,2}^N(z_2=Z_2) - n_{i,2}^N(z_2=0)\right) \cdot Z_1 Z_3 - 2A^I \cdot n_i^I + V^N \cdot \sigma_i^N \end{aligned} \quad (24)$$

Dividing by $V = Z_1 Z_2 Z_3$ and letting Z_1 and Z_2 approach zero, finishes the first part of the reduction procedure:

$$\varepsilon^N \frac{\partial c_i^N}{\partial t} = -\frac{\partial n_{i,1}^N}{\partial z_1} - \frac{\partial n_{i,2}^N}{\partial z_2} - a^I \cdot n_i^I + \varepsilon^N \cdot \sigma_i^N \quad (25)$$

Here, $\varepsilon^N = V^N/V$ and $a' = 2 A'/V$. In the non-reactive zone, the last term of Equation 25 is zero.

The second integration is performed over the height of the reactor. This is motivated by the fact that variations in the concentration along z_2 are small compared to those along z_1 . Because the flux densities at the boundaries of the integration are zero²⁰, this essentially eliminates the derivative term with respect to this coordinate, so the final reduced equation for the non-reactive gas reads:

$$\varepsilon^N \frac{\partial c_i^N}{\partial t} = - \frac{\partial n_{i,1}^N}{\partial z_1} - a' \cdot n_i^I \quad (26)$$

A similar procedure for the partial molar balance in the reactive gas yields, under the assumption of stagnant gas in this volume:

$$\varepsilon^R \frac{\partial c_i^R}{\partial t} = a' \cdot n_i^I + \varepsilon^R \cdot \sigma_i^R \quad (27)$$

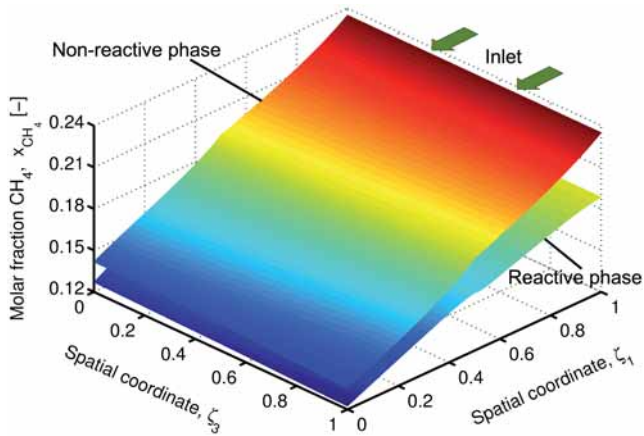


Figure 17: Methane molar fractions from the Phase Model of the IIR reactor. The two planes represent states from the reactive and the non-reactive phase (from [PH 9]).

The derivation of the reduced model is completed by reduction of the remaining balance equations in a similar way. A comprehensive list of the equations is given by Pfafferoth et al. ([PH 5]). Equations 26 and 27 indicate the structure of the reduced model. The

20 I.e. $n_{i,2}^N|_{z_2=0} = n_{i,2}^N|_{z_2=1} = 0$.

zones are no longer described at discrete locations in space, but instead they are homogenised with respect to space. This model can be interpreted as two gas phases that are both present at every location in the reactor, and which exchange mass via an interfacial area. This is the reason why this model is called the Phase Model. This is illustrated in Figure 17, where the molar fractions of methane in both phases in an IIR according to the Phase Model are displayed. Each of the two planes in Figure 17 shows molar fractions that are typical for the corresponding zone at the respective location.

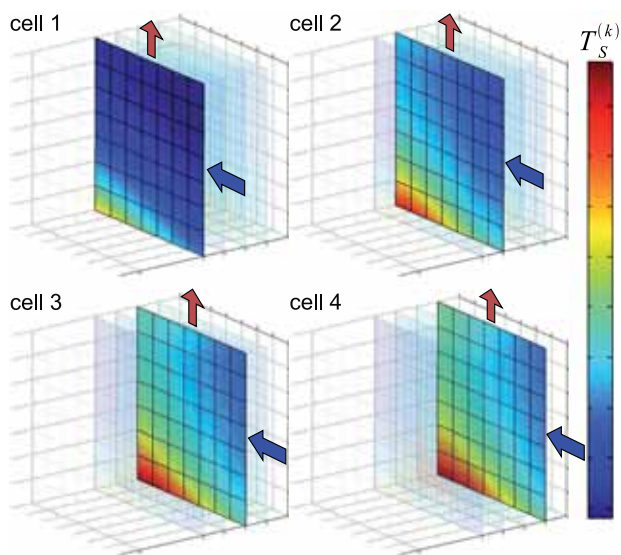


Figure 18: Temperature distributions in the fuel cells according to the stack model of an MCFC (from [PH 5]). In order to protect intellectual property of MTU Onsite Energy, the absolute temperature values are not given.

The dimension and complexity of the Phase Model corresponds very well to those of the spatially distributed MCFC model ([26], [37]), so both can be combined in the stack model ([PH 5]). A typical result of the stack model is shown in Figure 18, where the impact of the IIR on the temperature of the fuel cells becomes visible. Fuel cell 1, which is directly attached to the IIR (c.f. Figure 11), has significantly lower temperatures than the other cells, which are farther away from the cold reforming reactor. In the current fuel cell design, a temperature peak is observed near the anode inlet / cathode outlet corner. The stack model can be used to identify design changes to the IIR and the fuel cells that reduce this hot spot, for example by a modified arrangement of the catalyst

staging in both types of units. Also, the stack model allows to take operating parameters such as the inlet conditions of the fuel gas or the amount of air²¹ into account. Also, by comparison of stack models with different numbers of fuel cells per IIR, the impact of this design parameter on the temperature distribution and stack performance can be evaluated.

3.5 Summary

The Indirect Internal Reforming reactor is an arranged, structured reactor. It applies a regular structure on the millimetre scale in order to control the reaction rate by means of mass transport limitation. Because the geometrical design on a small scale determines the overall reactor behaviour, the proposed model hierarchy consists of three models, each describing the reactor on a different scale. The Detailed Model focusses on an assembly of only a few elementary cells and serves to estimate its properties regarding the transport of mass, energy and momentum. It also shows that the gas in the reactor can be subdivided into a reactive zone around the catalyst pellets and a non-reactive zone. Based on this finding, the Zone Model neglects the detailed geometrical structure and uses a reduced representation of both types of zones instead. Due to this reduction, the zone model can be used to design the flow field of a complete reactor. The Phase Model is the most reduced description of the IIR in this hierarchy. It describes representative states for both zones in a homogenised approach, and it can be combined with models of other reactors in order to optimise their integration with the IIR.

The reduction from the Detailed Model to the Zone Model is achieved primarily by simplification of the geometrical structure. Both models apply the Navier-Stokes equations. The Zone Model uses an additional friction term in the momentum balance to reflect the friction forces that are exerted by the structure internals upon the flowing gas; it also includes a reactive source term in the component mass balances, because the reactions are modelled as homogeneous reactions in this model. The reduction to the Phase Model leads to an increase of the number of partial differential equations; because both phases are described all over the reactor volume, their number effectively doubles. However, the number of spatial coordinates is reduced from three to two, and many spatial derivatives in the PDEs are eliminated in the Phase Model. Moreover, the solution of the Zone Model is numerically expensive because the reaction rate

21 In an MCFC, air is added to the afterburner which is located at the anode outlet. The off-gas from the burner is fed into the cathode channel, which is a unique feature of the MCFC. Due to this, the air number has a strong impact on the cell temperature, the cathode gas composition and the energetic performance of the MCFC and is thus an important operating parameter.

coefficients and the permeabilities change discontinuously over the spatial coordinate, whereas in the Phase Model, these parameters are constant. This leads to a significant decrease in the numerical solution effort, despite the increased number of PDEs.

Although this model hierarchy was developed for a specific structured reactor, its principles may well be transferred to other types of reactors with an arranged structure, provided that the reactions therein are transport-limited. One example is the class of Katapak structures ([38], [39]), where the catalyst particles are placed inside cages of wired gauze and the reactant flows past them through zig-zag channels. Although the model hierarchy shown in this chapter is not directly applicable to a Katapak structure, many principles and applications of this hierarchy can be transferred to it. However, it would be desirable to develop a general methodological foundation for the model reduction of arranged reactors. Such a method could be based on the works on the volume averaging method in porous media by Whitaker and Ochoa-Tapia ([40]-[42]). That technique has originally been developed for non-regular structures with a low ratio of characteristic structure length to reactor size. How this can be applied or adapted to systems with relatively large structures (compared to the reactor size²²), is one of the open questions that need to be solved on the way towards a general model reduction methodology for structured reactors.

²² For example, in some Katapak columns, only a few repeating units are placed over the diameter of the reactor.

4 Optimal design of TPR experiments

4.1 The Temperature Programmed Reduction (TPR) method

The experimental method of TPR is widely applied to estimate kinetic parameters of reduction reactions of metal oxides ([43], [44]). Its working principle is illustrated inside the box in Figure 19. A reducing gas, e.g. hydrogen, continuously flows through a small sample of the metal oxide powder. Due to the reducing atmosphere, the metal oxide is reduced and steam is produced from the hydrogen. A sensor is placed behind the sample which measures the steam concentration in the gas. This concentration is proportional to the actual overall reduction rate in the sample. At the beginning of the experiment, the sample temperature starts at low values and is increased at a constant rate, so it follows a linear profile. Thus, reaction rate at initial time is virtually zero and it increases with temperature. Once the sample is reduced, the reaction rate approaches zero again, and the TPR experiment ends²³. The resulting time dependent measurement signal (red profile in Figure 19) is then used to estimate unknown kinetic parameters such as reaction rate coefficients, activation energies, orders of reaction and oxygen capacities. In addition, the co-variance matrix of the estimates can be obtained from that data. Also, TPR data can be used to discriminate between rivaling kinetic models.

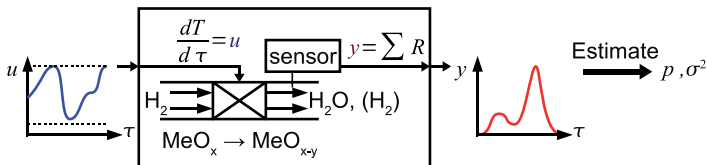


Figure 19: Physical principle of the TPR (shown inside the box), input quantities (blue) and output signal (red).

In traditional TPR experiments, the only control parameter that can be changed from one TPR run to another is the temperature gradient. Usually, a series of several TPR experiments with different temperature gradients is conducted and the parameters are estimated from the whole ensemble of measurement curves. However, in a system with three reactions²⁴, twelve parameters need to be estimated. With twelve unknowns and only one control parameter, the control options of the TPR method are very limited. This

²³ Typical temperature gradients are several Kelvin per minute. A single TPR run takes between 15 and 90 minutes, depending on the reaction rates and the temperature gradients. A typical sampling rate of the sensor is one measurement per second.

²⁴ E.g. the reduction of haematite (Fe_2O_3) via magnetite (Fe_3O_4) and wuestite (FeO) to iron.

is also shown by Pineau et al. ([45]), who present a list of TPR studies on the reduction kinetics of iron oxide in hydrogen atmosphere by different authors. They show that estimates vary significantly. Although some of these deviations can be explained by morphological differences in the metal oxides in the studies, this indicates that the estimates have a large variance. Also with regard to model discrimination, the TPR method is not well suited ([PH 1]). Very different kinetic models fitted the data from a series of TPR experiments equally well.

In order to improve the TPR method, its control options need to be increased. This can be done by lifting the restriction of a constant temperature gradient and applying a time dependent gradient instead. This leads to non-linear temperature profiles, which is the reason why this method is referred to as Non-linear Temperature Programmed Reduction (N-TPR). The control function, namely the time dependent temperature gradient (blue profile in Figure 19), can be designed so that the precision of the parameter estimates is maximised.

The resulting optimal control problem is not easily solved by numerical means. With respect to practical applicability, a reduced problem is formulated. Thus, the model hierarchy of this experimental design problem comprises two elements (Figure 20).

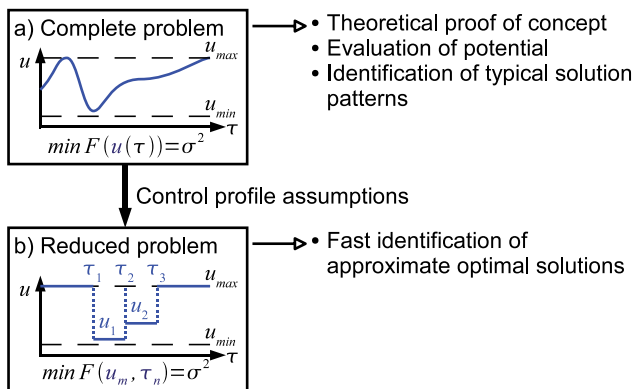


Figure 20: Model hierarchy for the design of optimal non-linear TPR experiments.

4.2 The Complete Problem

Designing an N-TPR experiment is an attempt to identify a control profile that yields a measurement signal which minimises the variances of the parameter estimate. Several

optimality criteria have been proposed which associate an objective function value to a given co-variance matrix ([46], [47]). From these, the D-optimality criterion has been chosen, because in addition to the individual variances of the parameters, it also considers the co-variances of the parameters estimates ([48]). After two reasonable simplifications (see [PH 7]), the objective function reads:

$$\max_{u(\tau)} \left\{ \det \int_{\tau=0}^{\tau_c} \left(\frac{\partial y}{\partial p} \right) \cdot \left(\frac{\partial y}{\partial p} \right)^T d\tau \right\} \quad (28)$$

The partial derivatives inside the integral are the time-dependent sensitivity functions of the measurement output, y , with respect to the model parameters, p . The argument in the integral is the combined sensitivity matrix of the measurement, and it is integrated over the whole duration of the TPR experiment. The determinant of this matrix is the objective that has to be maximised. In other words, the optimisation identifies a control function, $u(\tau)$, at which the measurement function, $y(\tau)$, is most sensitive with respect to the estimated parameters, p .

This optimisation problem is constrained by the transient model equations of the TPR system, which include ordinary differential equations for the temperature and the sample composition²⁵. In addition, a larger number of differential equations is used to describe the Jacobian functions, which are needed to evaluate the sensitivity expressions in the integral of the objective function. Furthermore, several algebraic constraint equations are required. Due to physical constraints, the temperature and its gradient are bounded below and above, so the complete problem also contains some inequality constraints. Overall, for a system with three reactions, the problem comprises 40 ODE constraints, 13 algebraic constraints and 5 inequality constraints. A detailed discussion and a comprehensive list of the complete problem is given by Heidebrecht et al. ([PH 7]). The whole problem is formulated in terms of dimensionless parameters.

The complete problem was discretised in time according to the method of orthogonal collocation on finite elements ([49]), with three collocation points per finite element and a typical number of 100 to 300 finite elements. Typically, a discretised problem comprises about ten thousand unknowns and a few hundred degrees of freedom. The discretised problem was implemented in AMPL ([50]) and solved using the algorithms CONOPT and IPOPT ([51]).

²⁵ Often, the number of reduction reactions considered in the system is identical to the number of ordinary differential equations needed to describe the sample composition. For example, a TPR model for a three-step reduction of haematite comprises three ODEs for the sample composition plus one for the temperature.

Different versions of the complete problem with one and two reactions were solved, and system parameters were varied systematically. A typical result for a system with two reactions is shown in Figure 21. It comprises four diagrams: In the lower left diagram, the control profile is shown. The upper left diagram shows the corresponding temperature profile and in the upper right diagram, the sample composition is depicted. The lower right diagram shows the expected measurement signal from the TPR experiment. In each diagram, dotted lines represent the profiles from the best possible linear TPR experiment, which applies the maximum allowable gradient²⁶. The solid lines show the profile according to the optimal non-linear experiment.

In the optimal control profile, the temperature gradient is at the upper bound except during a certain period of time in the middle of the experiment²⁷. This period begins at the time when the peak of the first reaction has just passed. First, the control function switches to its lower bound, so the temperature is decreased. Then, the temperature gradient is kept close to zero, so an almost isothermal period is applied. During this period, the first reaction continues to proceed at a low rate, while the second reaction produces no measurable contribution to the output signal. At the end of the isothermal phase, the first reaction has reached virtually full conversion. Then, the temperature gradient is set back to maximum, and the second reaction peak is observed.

The effect of the non-linear control becomes evident in the lower right diagram. In the linear experiment, both peaks of the two reactions are close together, which leads to high co-variances of the estimates of the corresponding parameters. Due to the decrease of temperature and the isothermal period in the non-linear experiment, the occurrence of the second reaction peak is delayed towards later times, so the co-variances of the parameter estimates are decreased. This period is referred to as the delay phase. The complete optimisation problem has been solved for many other cases with two reactions. In the majority of these cases, the optimal control profile shows a similar delay phase. With respect to the objective function, non-linear TPR experiments yield 10-40% higher values compared to the best possible linear TPR runs.

²⁶ Note that in this example, $0.25 \geq u(\tau) \geq -0.25$ were applied as upper and lower bounds of the (dimensionless) control function.

²⁷ This was expected from an analytical solution of the complete problem for a system with a single reaction, neglecting the sensitivities with respect to the activation energy (see [PH 7]).

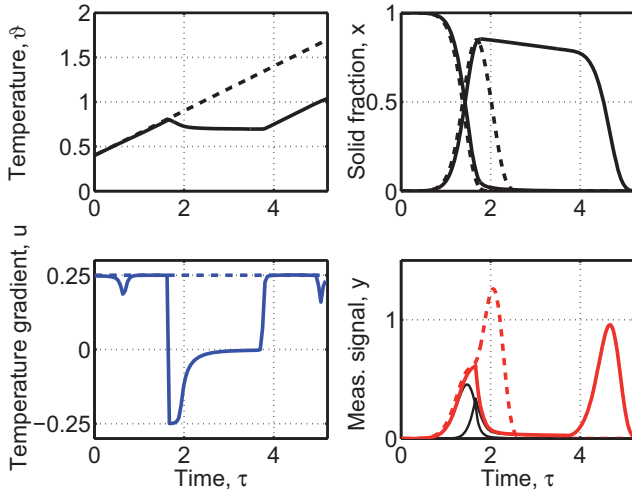


Figure 21: Exemplary results of the complete problem for a system with two reactions (from [PH 7]).

Similar optimisation problems have been set up and solved with regard to improving the model discrimination properties of the TPR method. The objective function used for this purpose describes the difference between the expected output signal of two competing models:

$$\max_{u(\tau)} \int_{\tau=0}^{\tau_f} (y^{(1)}(\tau) - y^{(2)}(\tau))^2 d\tau \quad (29)$$

where $y^{(1)}$ and $y^{(2)}$ are the output signals of the two models. This objective function requires no sensitivity information, so compared to the previous problem, it has fewer constraints.

A typical solution of the complete problem for model discrimination is shown in Figure 22. Both models consider a single reaction, but they use different kinetic approaches. In the upper right diagram, the solid black and the dotted green profile indicate that both models were chosen so that they are indistinguishable from a linear TPR experiment with maximum temperature gradient. Reducing the temperature gradient in a linear experiment, the two signals shown as the red and the black dotted lines are obtained. Although the difference between both model outputs can be dramatically increased already with a linear experiment, the two curves are qualitatively very similar, and a clear discrimination requires precise measurements. Application of

the optimal control profile (solid blue line in Figure 22, lower left diagram) leads to the measurement signals shown in the lower right diagram. The non-linear experiment not only increases the quantitative difference between both outputs, but they also become qualitatively different, and can therefore be discriminated with higher certainty.

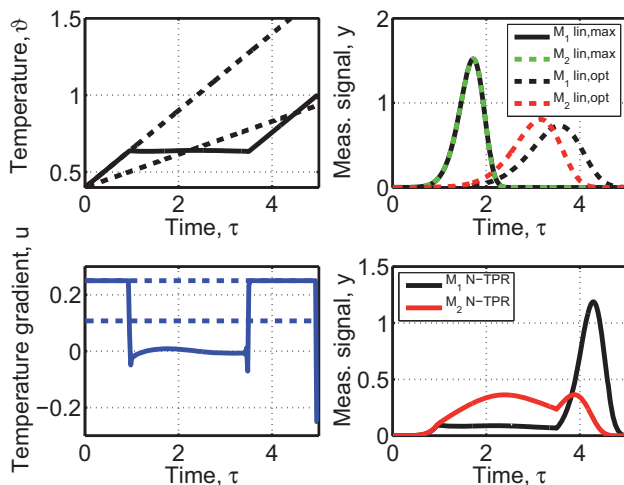


Figure 22: Exemplary results of the complete problem for model discrimination (from [PH 7]). Upper right diagram: Model outputs from different linear experiments; lower right diagram: Model outputs from optimal non-linear TPR experiment.

4.3 The Reduced Problem

The numerical determination of optimal control profiles from the complete problems can be difficult. Convergence to an optimum is not achieved from arbitrary initial points, and so the solution usually requires a multi-step procedure, which varies for different problems. This is basically because this optimal control problem is singular. With respect to practical application in a laboratory environment, these optimal control profiles need to be computed in an automated way. For this purpose, reduced problems have been proposed.

It was observed from the solutions of the complete problems that the optimal control profiles for certain classes of problems²⁸, especially the shape of the delay phases, are

²⁸ "Classes of problems" denotes groups of complete problems with a similar structure, for example problems with a single reaction, or with two consecutive reactions.

qualitatively similar. This leads to the idea to capture these control profiles by piecewise constant functions. A reduced control profile for a system with two reactions is illustrated in Figure 23. According to this scheme, the application of the reduced control profile reduces the degrees of freedom to five, represented by the switching times $\tau_{1,2,3}$ and the temperature gradients $u_{1,2}$.

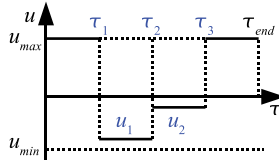


Figure 23: Schematic reduced control profile for systems with two reactions (from [PH 7]).

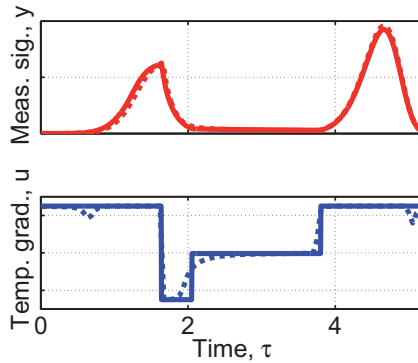


Figure 24: Example of a solution of the reduced problem. The solution of the complete problem is shown in dotted lines (from [PH 7]).

Figure 24 shows the solution of the reduced problem (solid lines) which corresponds to the profiles of the complete problem in Figure 21 (dotted lines). Obviously, the control profiles and the output signals of both solutions are very similar. The reduced problem can be solved very reliably in an automated way within less than a minute using the simulation environment Matlab on a standard PC. Thus, the reduced problem can be implemented in the control software of a TPR device, where it identifies and proposes non-linear TPR experiments in an automated way, only based on the user's input of the type of system and *a priori* estimates of the system parameters.

As discussed by Heidebrecht et al. ([PH 7]), cases have been observed where the reduced problem has at least two local minima. One of them approximates the solution of the complete problem very well, but the other optimum strongly differs from that. It depends on the system parameters which of the two solutions of the reduced model is the global optimum. A first analysis of this effect indicated that these optima also deviate with respect to their robustness. In a real N-TPR experiment, the temperature profile can only be an approximation of the theoretical optimum, so it is important to have a low sensitivity of the objective function value with respect to changes in the control function. How this can be included in the optimal design is left as a subject for further studies.

4.4 Summary

The design of non-linear TPR experiments leads to an optimal control problem, which has been set up and solved numerically for many different variations of the problem. The solutions showed that the N-TPR method yields better parameter estimates compared to the linear TPR method and that the model discrimination properties can be improved. With respect to applicability, a reduced formulation was proposed which can be solved in a fully automated way and approximates the solutions of the corresponding complete problems very well.

The reduction of the complete problem to the reduced problem is solely based on profile assumptions regarding the control function. This empirical approach is motivated by the observation that classes of similar problems yield qualitatively similar optimal profiles. The reduction is justified by the very good agreement between the solutions of both types of problems. However, the agreement is not always satisfactory, as some of the reduced problems showed multiple optima which could not be seen in the solutions of the complete problems. This point has not been solved yet.

The idea of optimal experimental design can be combined with other transient analysis techniques such as cyclic voltammetry or temperature programmed desorption. Similar ideas in the field of chromatography have led to the widely applied methods of temperature programmed gas chromatography ([52], [53]) and gradient elution liquid chromatography ([54], [55]). In these methods, control profiles are used to separate the peaks at the outlet of the chromatographic column and to reduce the duration of the experiments. However, these input profiles are not based on the results of an unconstrained optimisation (a complete problem as in Section 4.2), but use simplified approaches such as linear temperature profiles *a priori*. In relation to the approach presented in this chapter, this means that only reduced problems are solved based on an intuitive selection of control profiles.

5 Mass integration of high temperature fuel cell systems

5.1 Introduction

High temperature fuel cells such as the SOFC and the MCFC²⁹ can be operated with a wide variety of fuels such as natural gas, alcohols, coal and biomass. A reduced scheme of a typical stationary high temperature fuel cell power plant is shown in Figure 25; it consists of a fuel processing unit (gasifier and reforming reactor are discussed here) which converts the raw fuel into a gas mixture rich of hydrogen and carbon monoxide, the fuel cell and a catalytic afterburner (not shown). In this scheme, gas cleaning units such as sulphur adsorption beds or dust removal units are not explicitly shown. One of the strongest advantages of high temperature over low temperature fuel cells is their resistance with respect to carbon monoxide, which significantly reduces the gas cleaning effort. Moreover, due to their high operating temperatures, their off-heat can be utilised in the fuel processing unit, which usually operates under endothermal conditions.

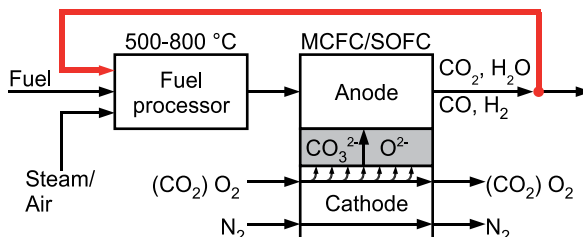


Figure 25: Principle of the mass integration of a fuel converter with a high temperature fuel cell.

The fuel processor requires oxygen, which is typically provided by a feed of steam or air. Both options come with certain drawbacks. The feeding of air also introduces a large amount of nitrogen, which dilutes the product gas. The application of steam requires a high amount of energy to heat up and vaporise the water, and it increases the heat demand in the fuel processing unit. The off-gas from the fuel cell anode is oxidised to a high extent, and it is available at fuel cell temperature, which is close to the fuel processor temperature. Thus, this exhaust gas can be used to substitute a part or all of the external oxygen supply to the fuel processor. This leads to a partial recycle of the anode exhaust gas to the fuel processor as illustrated by the red line in Figure 25. In a fully integrated system, the oxygen supply to the fuel processor is accomplished by

²⁹ SOFC: Solid Oxide Fuel Cell ; MCFC: Molten Carbonate Fuel Cell

ion transport across the fuel cell electrolyte layer, whereby undesired species like nitrogen are automatically separated from air oxygen.

This idea leads to the questions whether the external oxygen feed can be completely replaced by the recycle gas and at which recycle ratios this can be accomplished. These questions are answered using two different sets of models which are indicated in Figure 26. Each set comprises a model for the fuel processors, the fuel cells and the afterburner ([PH 8]).

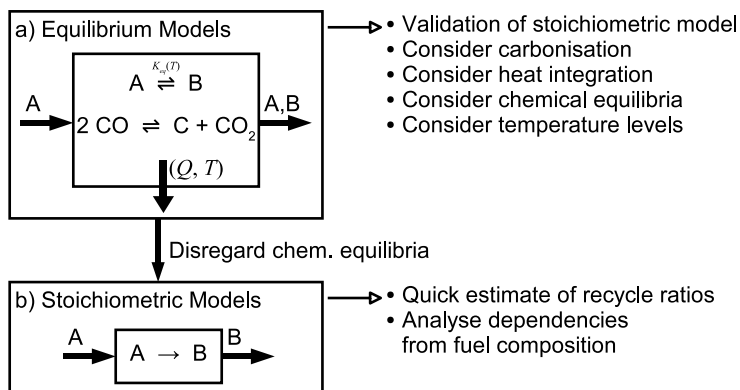


Figure 26: Model hierarchy for the evaluation of the mass integration principle.

5.2 Equilibrium Models

In this set of spatially lumped models, the gas is assumed to be in equilibrium with respect to the methane steam reforming reaction and the water gas shift reaction in the fuel processor. In the fuel cells, only the equilibrium with respect to the water gas shift reaction is considered.

Each unit is assumed to operate isothermally at a given, individual temperature. Ingoing or outgoing heat fluxes are calculated from the enthalpy balance of each unit. These heat fluxes are used in a pinch analysis ([1]) to evaluate whether the complete system can be heat integrated. Because carbon deposition can be a serious issue in such systems, a thermodynamical criterion is evaluated in each fuel processor and fuel cell model which indicates whether carbon is deposited under the conditions that prevail in the unit. These models have also been applied as short cut models in a system design study, where a more detailed discussion of the models and the carbonisation check is given ([PH 6]).

The system has three operating parameters. The first one is the fuel utilisation, η_{fuel} , which determines the electrochemical conversion at the outlet of the fuel cell anode. The second operating parameter is the amount of steam fed into the fuel processing unit, which is described by the steam to carbon ratio, S/C ³⁰. This allows to consider partial replacement of the external oxygen feed. The third operating variable is the recycle ratio of the anode exhaust gas, RR , which is defined as the molar flow rate of the recycle stream per molar flow rate of the anode exhaust gas. At a given combination of fuel utilisation and steam feed rate, the lowest possible recycle ratio is desired which fulfils the inequality constraints of carbonisation and heat integration. This optimisation is repeatedly carried out over a range of η_{fuel} and S/C values.

An exemplary result for an SOFC system fed with methane and with given unit temperatures is shown in Figure 27. The coloured plane shows the minimal recycle ratio required to suppress carbonisation as a function of the other two operating parameters, the fuel utilisation and the steam to carbon ratio. Two characteristic operating points at a typical fuel utilisation of $\eta_{fuel} = 80\%$ are marked: The conventional point without gas recycle ($RR = 0$, $S/C = 1.05$) and the fully integrated point without steam feed ($RR = 0.34$, $S/C = 0$). The recycle ratio that is necessary to achieve complete mass integration is moderate. It causes an increase of the volumetric gas flow rate through the anode by about 50 %.

At lower fuel utilisation, the oxygen content in the anode off-gas decreases, so the recycle ratio needs to be increased in order to satisfy the oxygen demand of the fuel processor. At a fuel utilisation of about $\eta_{fuel} = 25\%$, the necessary recycle ratio for complete integration reaches its upper limit; at fuel utilisations less than that, a complete mass integration is not possible. Towards higher degrees of fuel utilisation, at around $\eta_{fuel} = 85\%$, the heat production by the SOFC and the burner becomes insufficient to satisfy the heat demand of the reformer, so the heat integration constraint is violated. This boundary is indicated by the transparent plane near $\eta_{fuel} = 90\%$ in Figure 27.

³⁰ Only steam is considered as a gasification / reforming agent in this study.

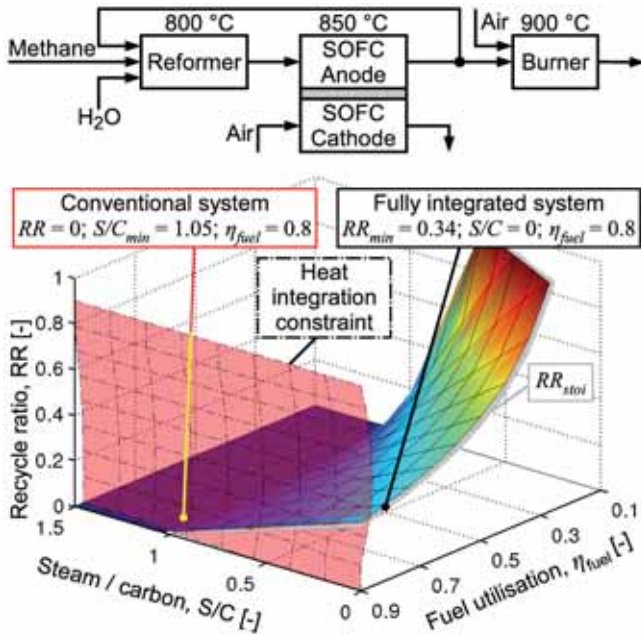


Figure 27: Minimal recycle ratio for an SOFC system with methane according to the Equilibrium Models (coloured plane) and according to the Stoichiometric Model (grey plane) (from [PH 8]).

5.3 Stoichiometric Model

The repeated solution of the Equilibrium Models for different fuel utilisations and steam feed rates as shown in Figure 27 requires several hours time on a typical PC. For the purpose of quick estimation of the minimal recycle rate for a wide variety of fuels, a reduced model is required. The Stoichiometric Model neglects the chemical equilibria of the reforming reactions, and it disregards the enthalpy balances and the carbonisation constraints. A basic assumption of the Stoichiometric Model is that the fuel processing unit works under stoichiometric conditions. Thus, the molar fluxes of methane, carbon dioxide and steam at the outlet of the fuel processor are zero. These three conditions determine the atomic feed rate of oxygen and the extent of both reforming reactions in the fuel processor.

Applying these assumptions to the mass balance equations of a system with an SOFC or an MCFC yields a simple algebraic equation describing the stoichiometric recycle

ratio for a given fuel composition, fuel utilisation and steam feed rate. For the SOFC using a fuel with the elementary composition CH_YO_Z , this equation reads (for the detailed derivation, see [PH 8]):

$$RR_{stoi}^{SOFC} = \frac{1 - Z - S/C}{\eta_{fuel} \cdot (2 + Y/2 - Z)} \quad (30)$$

The stoichiometric recycle ratio for the MCFC is exactly half as much. This is due to the carbonate ions that migrate through the MCFC electrolyte, which transport more oxygen atoms per amount of electrical current than the O^{2-} -ions in the SOFC.

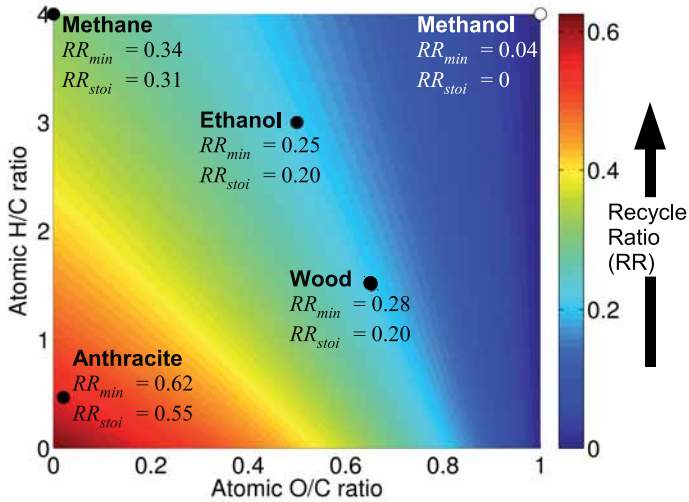


Figure 28: Minimal recycle ratios for the mass integration of SOFC plants ($\eta_{fuel} = 80\%$, $S/C = 0$). The colour indicates the results from the Stoichiometric Model; the results from the Equilibrium Model with five different fuels are given (from [PH 8]).

In the case of SOFC systems, the recycle ratio obtained from the stoichiometric calculation (grey plane in Figure 27) approximates the results from the Equilibrium Model very closely. This is due to several reasons. Under equilibrium conditions and at the high operating temperatures in an SOFC, the equilibrium of the methane steam reforming reaction is far on the product side and the equilibrium of the water gas shift reaction is far on the reactant side. Thus, the concentrations of methane and carbon dioxide are both low. This is in good agreement with the assumptions of the

Stoichiometric Model. Furthermore, due to the high temperatures in the reformer and the SOFC, carbonisation only occurs in atmospheres with a high ratio of carbon monoxide to carbon dioxide; it can easily be avoided by a small increase of the recycle ratio.

To evaluate the agreement between both models for SOFC systems, the fuel composition was varied systematically; the two axes in Figure 28 represent the hydrogen and the oxygen content of the fuel. The results obtained from the Stoichiometric Model are indicated by the background colour. The recycle ratios according to both models are given for five different fuels. The deviations indicate that the Stoichiometric Model yields a good approximation for the minimal recycle ratio in SOFC systems.

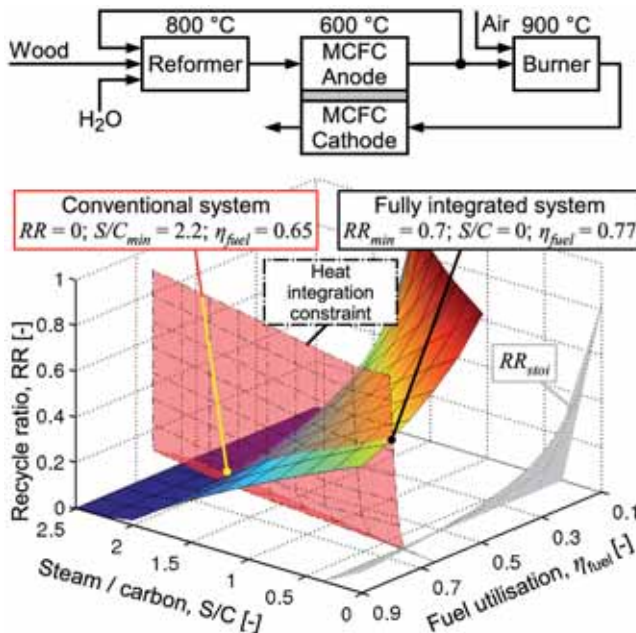


Figure 29: Minimal recycle ratio for an MCFC system with wood according to the Equilibrium Models (coloured plane) and according to the Stoichiometric Model (grey plane) (from [PH 8]).

The results for the MCFC system show a very different picture, as illustrated by a wood-fueled system in Figure 29. Due to the lower temperatures and the increased content of

carbon in the anode gas due to the flow of carbonate ions through the electrolyte, the system operates deep inside the carbon deposition regime unless high recycle ratios are applied. The range of infeasible conditions (no complete integration possible due to low fuel utilisation) is enlarged. Heat integration limits the possible fuel utilisation to values significantly below 80 %. This makes the mass integration in MCFC systems unattractive.

Furthermore, because the assumptions from the Stoichiometric Model are not even approximately fulfilled in an MCFC, the recycle ratios predicted by both models strongly deviate. Thus, the Stoichiometric Model is only applicable in the context of SOFC systems.

5.4 Summary

The feasibility of mass integration of high temperature fuel cells with their preceding fuel processors by anode exhaust gas recycle is investigated with two different sets of models. The set of Equilibrium Models considers the temperature levels of the system's units, and it accounts for carbonisation and system wide heat integration. The Stoichiometric Model is based on the assumption of stoichiometric fuel conversion. Both sets of models are applied to estimate the minimal recycle ratio depending on the fuel composition, fuel utilisation in the fuel cell and the feed rate of steam to the fuel processor. They show that the integration is possible at moderate recycle ratios for a wide range of fuels in the SOFC, but it is not attractive in MCFC systems. The results obtained from both models for SOFC systems agree very well.

The reduction of the Equilibrium Models to the Stoichiometric Models is mainly based on physical assumptions concerning the product gas of the fuel processor. These assumptions are equivalent to assumptions regarding the extents of reaction in this unit and the oxygen feed rate.

Both models focus on the feasibility of the integration concept, but not on an evaluation of its benefit in terms of efficiency or economic profit. Besides the advantage of a simpler system due to the integration, the recycle stream also increases the gas flow rate through the fuel processor and the anode channels, leading to a higher pressure drop and thereby increased internal energy consumption. How this affects the efficiency or profitability of a system, strongly depends on its design parameters.

6 Concluding remarks

In this work, four examples have been shown how model hierarchies can be used in process design. The first two examples focus on reactor design, the third on experimental design and the fourth example treats the integration of a system consisting of several process units. The models in each hierarchy are different with respect to their complexity, detail level, degree of abstraction and their numerical effort.

Model reduction is an essential element of the development of model hierarchies. In the examples shown here, the derivation of reduced models has different motivations. In the case of the structured IIR reactor (Chapter 3), model reductions are conducted in order to extend a model or its solution domain. The Detailed Model was reduced in order to extend the solution domain from a cut-out section to the complete reactor. The further reduction of the Zone Model enabled the combination of the resulting Phase Model with fuel cell models to a representation of a fuel cell stack.

Complex models yield a lot of data, but simple models can convey more insight and understanding of a process, which is another motivation for model reduction. Both reduced models of the hierarchy for the CWGSR (Chapter 2) follow this idea. Also, the reduction of the Equilibrium Model for the mass integration of high temperature fuel cells in Chapter 5 is conducted partially due to this reason.

Because computational power is limited and some applications demand quick solutions, the decrease of computational effort is the third reason for model reduction in this work. The reduction of the Complete Problems to the Reduced Problems in the design of N-TPR experiments (Chapter 4) is a good example for this. This is also partially the reason for the derivation of the Equilibrium Model in Chapter 5.

According to the categories of model hierarchies proposed by Hangos and Cameron ([8]), the hierarchy of the structured reactor (Chapter 3) is driven by characteristic sizes. Each model describes the structured reactor on a different size: the geometrical structure on the millimetre scale, the complete reactor and the reactor integrated with fuel cells. According to this scheme, the other model hierarchies would be classified as driven by the level of detail; their models describe the same process on different levels of abstraction.

The technical approach to reduce a model can be entirely mathematical. A simple example for this is the transformation of mass balances to equations in terms of extents of reaction, as shown by Heidebrecht et al. ([56]). In this reduction, the dimension of a model is reduced from five molar fractions to two extents of reaction. Another example

is the reduction by proper orthogonal decomposition (POD), as applied by Mangold et al. ([57]) to a transient, spatially distributed model of a high temperature fuel cell.

In other cases, model reduction is obtained by modification of the set of assumptions. This may call for a completely new derivation of the model equations based on the altered assumptions, as with the Front Model (Chapter 2.4) or the Stoichiometric Model (Chapter 5.3). In other cases, the equations of the more complex model can be changed according to the modified assumptions to obtain the reduced model. This is the case with the derivation of the Phase Model (Chapter 3.4), which is derived from the three-dimensional balance equations of the Zone Model. The same applies to the Single Reaction Model of the IIR reactor (Chapter 2.3), where the partial differential equations of the Reference Model can be used as an initial point to derive the reduced model. Also, the derivation of the Reduced Problem for the design of N-TPR experiments (Chapter 4.3) is a good example where the original equations are preserved and only slightly modified.

In general, model reduction leads to a reduction of the numerical effort³¹. However, this usually leads to a loss of precision due to neglected physical phenomena or approximations. This can be seen in the Phase Model of the IIR reactor (Chapter 3.4), where the exact locations of the catalyst pellets are no longer reflected in the model and only representative states are calculated; or in the Front Model of the CWGSR (Chapter 2.4), which yields no information about the dispersive character of the reaction front or the temperature distribution.

Moreover, the applicability of reduced models is generally more restricted than their parent model's. For example, the permeabilities used in the Zone Model of the IIR (Chapter 3.3) depend on the gas velocity³². However, they are estimated from the Detailed Model (Chapter 3.2) for a certain range of gas flow rates. Applying gas velocities to the Zone Model which are outside this range leads to wrong estimates of the pressure drop. Another example are the Stoichiometric Models (Chapter 5.3) whose application is limited to SOFC systems, because the deviation to the Equilibrium Models in MCFC systems is far too large.

Thus, qualitative and especially quantitative results from reduced models have to be validated or rendered more precisely, either by using their parent models or by experiments. An illustrative example for this is a result from the Front Model (Chapter 2.4). In Figures 9 and 10, the optimal operating regime is identified and the

³¹ This should be true if the reduced model describes the same system as the original model.

³² That means that the pressure drop in the IIR is actually not proportional to the gas velocity, as postulated in Darcy's law.

optimal phase duration can be determined. However, this result is only an initial guess for an optimisation using the more detailed Reference Model.

Process modelling is motivated by the desire to answer process related questions. This work shows how model hierarchies provide tools for a wide variety of applications. These range from conceptual process analysis (see the CWGSR Front Model, Chapter 2.4) to the detailed simulation of a complex reactor (see the IIR zone model, Chapter 3.3). The models are specifically tailored for their respective applications, which makes their usage efficient in terms of numerical effort and interpretability. The second advantage of model hierarchies is the reduced model development effort, which shows in almost all of the examples in this work. Usually, not all models have to be derived “from scratch”, because they are based on similar assumptions or have similar equation structures. This accelerates the modelling process. The third strong advantage of developing models in the framework of a hierarchy is that they are compatible; a good example is the estimation of pressure loss coefficients and heat transport parameters from the Detailed Model of the IIR reactor, which are then used in the reduced models of this hierarchy (Chapter 3.2). These advantages make model hierarchies a powerful tool for the design of complex processes.

References

- [1] L.T. Biegler, I.E. Grossmann, A.W. Westerberg, *Systematic methods of chemical process design*, Prentice Hall PTR, Upper Saddle River, 1997, ISBN 9780134924229.
- [2] W.D. Seider, J.D. Seader, D.R. Lewin, *Process design principles: synthesis, analysis, and evaluation*, Wiley, New York, 1999, ISBN 0471395749.
- [3] F. Keil, *Scientific computing in chemical engineering II*, Springer, Berlin, 1999, ISBN 9783540658511.
- [4] R. Smith, *Chemical process design and integration*, Wiley, Chichester, 2005, ISBN 9780471486817.
- [5] G.D. Ingram, I.T. Cameron, K.M. Hantos, Classification and analysis of integrating frameworks in multiscale modelling, *Chemical Engineering Science* 59 (2004), 2171-2187.
- [6] A. de Saint-Exupéry, *Terre des hommes*, Gallimard, Paris, 1972, ISBN 9782070360215.
- [7] Ockham's razor, *The new Encyclopædia Britannica*, 15th ed., Encyclopædia Britannica, 2007.
- [8] K.M. Hantos, I.T. Cameron, *Process modelling and model analysis*, Academic Press, San Diego, 2001, ISBN 0121569314.
- [9] M. Baerns, H. Hofmann, A. Renken, *Chemische Reaktionstechnik*, 2nd ed., Thieme, Stuttgart, 1992, ISBN 3136875028.
- [10] W.L. McCabe, J.C. Smith, P. Harriott, *Unit operations of chemical engineering*, McGraw-Hill, Boston, 1976, ISBN 0071247106.
- [11] A. Messerschmitt, *Verfahren zur Erzeugung von Wasserstoff durch abwechselnde Oxidation und Reduktion von Eisen in von aussen beheizten, in den Heizräumen angeordneten Zersetzern*, German Patent DE 266863, 1911.
- [12] V. Hacker, R. Fankhauser, G. Faleschini, H. Fuchs, K. Friedrich, M. Muhr, K. Kordes, Hydrogen production by steam-iron process, *Journal of Power Sources* 86 (2000), 531-535.
- [13] K. Svoboda, G. Slowinski, J. Rogut, D. Baxter, Thermodynamic possibilities and constraints for pure hydrogen production by iron based chemical looping process at lower temperatures, *Energy Conversion and Management* 48 (2007), 3063-3073.
- [14] K. Otsuka, C. Yamada, T. Kaburagi, S. Takenaka, Hydrogen storage and production by redox of iron oxide for polymer electrolyte fuel cell vehicles, *International Journal of Hydrogen Energy* 28 (2003), 335-342.
- [15] K. Urasaki, N. Tanimoto, T. Hayashi, Y. Sekine, E. Kikuchi, M. Matsukata, Hydrogen production via steam-iron reaction using iron oxide modified with very small amounts of palladium and zirconia, *Applied Catalysis A: General* 288 (2005), 143-148.
- [16] E.J. Anthony, Solid looping cycles: A new technology for coal conversion, *Industrial & Engineering Chemistry Research* 47 (2008), 1747-1754.

- [17] K.S. Go, S.R. Son, S.D. Kim, K.S. Kang, C.S. Park, Hydrogen production from two-step steam methane reforming in a fluidized bed reactor, *International Journal of Hydrogen Energy* 34 (2009), 1301-1309.
- [18] P. Chiesa, G. Lozza, A. Malandrino, M. Romano, V. Piccolo, Three-reactors chemical looping process for hydrogen production, *International Journal of Hydrogen Energy* 33 (2008), 2233-2245.
- [19] J.P.E. Cleeton, C.D. Bohn, C.R. Müller, J.S. Dennis, S.A. Scott, Clean hydrogen production and electricity from coal via chemical looping: Identifying a suitable operating regime, *International Journal of Hydrogen Energy* 34 (2009), 1-12.
- [20] S. Kabelac, *VDI-Wärmeatlas*, 10th ed., Springer, Berlin, 2006, ISBN .
- [21] V. Galvita, T. Hempel, H. Lorenz, L.K. Rihko-Struckmann, K. Sundmacher, Deactivation of modified iron oxide materials in the cyclic water gas shift process for CO-free hydrogen production, *Industrial & Engineering Chemistry Research* 47 (2008), 303-310.
- [22] P.V. Danckwerts, Continuous flow systems – Distribution of residence times, *Chemical Engineering Science* 2 (), 1-13.
- [23] Y.S. Matros, G.A. Bunimovich, Reverse-flow operation in fixed bed catalytic reactors, *Catalysis Reviews* 38 (1996), 1-68.
- [24] F.G. Helfferich, The Theory of Precipitation / Dissolution Waves, *AIChE Journal* 32 (1989), 75-87.
- [25] A. Gorbach, G. Eigenberger, G. Kolios, General approach for the reduction of detailed models for fast cycling processes, *Industrial & Engineering Chemistry Research* 44 (8) (2005), 2369-2381.
- [26] P. Heidebrecht, K. Sundmacher, Dynamic model of a cross-flow molten carbonate fuel cell with direct internal reforming, *Journal of the Electrochemical Society* 152 (2005), A2217-A2228.
- [27] M. Bischoff, G. Huppmann, Operating experience with a 250 kWel molten carbonate fuel cell (MCFC) power plant, *Journal of Power Sources* 105 (2002), 216-221.
- [28] M. Bischoff, Molten carbonate fuel cells: A high temperature fuel cell on the edge of commercialization, *Journal of Power Sources* 160 (2006), 842-845.
- [29] K. Pangarkar, T.J. Schildhauer, J.R. van Ommen, J. Nijenhuis, F. Kapteijn, J.A. Moulijn, Structured packings for multiphase catalytic reactors, *Industrial & Engineering Chemistry Research* 47 (2008), 3720-3751.
- [30] M.T. Kreutzer, F. Kapteijn, J.A. Moulijn, Shouldn't catalysts shape up? Structured reactors in general and gas-liquid monolith reactors in particular, *Catalysis Today* 111 (2006), 111-118.
- [31] A. Cybulski, J.A. Moulijn (Eds.), *Structured catalysts and reactors*, 2nd ed., Taylor & Francis, Boca Raton, 2006, ISBN 0824723430.
- [32] S. Ergun, Fluid flow through packed columns, *Chemical Engineering Progress* 48 (1952), 89-94.
- [33] R.B. Bird, W.E. Stewart, E.N. Lightfoot, *Transport phenomena*, 2nd ed., Wiley, New York, 2007, ISBN 0470115394.

- [34] B. Mahr, D. Mewes, CFD modelling and calculation of dynamic two-phase flow in columns equipped with structured packings, *Chemical Engineering Research and Design* 85 (A8) (2007), 1112-1122.
- [35] H. Freund, J. Bauer, T. Zeiser, G. Emig, Detailed simulation of transport processes in fixed-beds, *Industrial & Engineering Chemistry Research* 44 (2005), 6423-6434.
- [36] M.F. Jischa, *Konvektiver Impuls-, Wärme- und Stoffaustausch*, Vieweg, Braunschweig, 1982, ISBN 3528081449.
- [37] M. Gundermann, P. Heidebrecht, K. Sundmacher, Validation of a mathematical model using an industrial MCFC plant, *Journal of Fuel Cell Science and Technology* 3 (2006), 303-307.
- [38] C. von Scala, M. Wehrli, G. Gaiser, Heat transfer measurements and simulation of Katapak-M catalyst supports, *Chemical Engineering Science* 54 (1999), 1375-1381.
- [39] M. Piironen, H. Haario, I. Turunen, Modelling of Katapak reactor for hydrogenation of anthraquinones, *Chemical Engineering Science* 56 (2001), 859-864.
- [40] S. Whitaker, Flow in Prous Media I: A Theoretical Derivation of Darcy's Law, *Transport in Porous Media* 1 (1986), 3-25.
- [41] J.A. Ochoa-Tapia, S. Whitaker, Momentum Transfer at the boundary between a porous medium and a homogeneous fluid - I. Theoretical development, *International Journal of Heat and Mass Transfer* 38 (1995), 2635-2646.
- [42] S. Whitaker, The Forchheimer Equation: A Theoretical Development, *Transport in Porous Media* 25 (1996), 27-61.
- [43] H.E. Kissinger, Reaction kinetics in differential thermal analysis, *Analytical Chemistry* 29 (1957), 1702-1706.
- [44] N.W. Hurst, S.J. Gentry, A. Jones, Temperature programmed reduction, *Catalysis Reviews – Science and Engineering* 24 (1982), 233-309.
- [45] A. Pineau, N. Kanari, I. Gaballah, Kinetics of reduction of iron oxides by H₂ – part I: Low temperature reduction of hematite, *Thermochimica Acta* 447 (2006), 89-100.
- [46] F. Pukelsheim, *Optimal Design of Experiments*, Wiley, New York, 1993, ISBN 0898716047 .
- [47] A.C. Atkinson, A.N. Donev, R.D. Tobias, *Optimum experimental design*, Oxford University Press, Oxford, 2007, ISBN 9780199296590.
- [48] Y. Bard, *Nonlinear parameter estimation*, Academic Press, New York, 1974, ISBN 9780120782505.
- [49] L.T. Biegler, *Nonlinear programming: Concepts, algorithms and applications to chemical processes*, SIAM, Philadelphia, 2010, ISBN 9780898717020.
- [50] R. Fourer, D.M. Gay, B.W. Kernigham, *AMPL: a modeling language for mathematical programming*, 2nd ed., Brooks/Cole - Thomson, Pacific Grove, 2003, ISBN 0534388094.
- [51] A. Wächter, L.T. Biegler, On the implementation of a primal-dual interior point filter line search algorithm for large-scale nonlinear programming, *Mathematical Programming* 106 (2006), 25-57.

- [52] P.J.F. Sandra, Gas chromatography, *Ullmann's Encyclopedia of Industrial Chemistry*, 7th ed., Wiley-VCH, 2010.
- [53] D.E. Bautz, J.W. Dolan, W.D. Raddatz, L.R. Snyder, Computer Simulation (Based on a Linear-Elution-Strength Approximation) as an Aid for Optimizing Separations by Programmed-Temperature Gas Chromatography, *Analytical Chemistry* 62 (1990), 1560-1567.
- [54] L.R. Snyder, Linear elution adsorption chromatography VII. Gradient elution theory, *Journal of Chromatography* 13 (1964), 415-434.
- [55] L.R. Snyder, J.W. Dolan, J.R. Gant, Gradient elution in high-performance liquid chromatography I. Theoretical basis for reversed-phase systems, *Journal of Chromatography* 165 (1979), 3-30.
- [56] P. Heidebrecht, K. Sundmacher, Conceptual design of the integration of the reforming process in high temperature fuel cells, *Journal of Power Sources* 145 (2005), 40-49.
- [57] M. Mangold, M. Sheng, Nonlinear model reduction of a two-dimensional MCFC model with internal reforming, *Fuel Cells* 4 (2004), 68-77.

Selected publications from the author

- [PH 1] P. Heidebrecht, V. Galvita, K. Sundmacher, An alternative method for parameter identification from Temperature Programmed Reduction (TPR) data, *Chemical Engineering Science* 63 (2008), 4776-4788.
- [PH 2] P. Heidebrecht, C. Hertel, K. Sundmacher, Conceptual Analysis of a Cyclic Water Gas Shift Reactor, *Int. Journal of Chemical Reaction Engineering* 6 (2008), A19.
- [PH 3] M. Pfafferodt, P. Heidebrecht, K. Sundmacher, U. Würtenberger, M. Bednarz, Multi-scale Simulation of the Indirect Internal Reforming unit (IIR) in a Molten Carbonate Fuel Cell (MCFC), *Industrial & Engineering Chemistry Research* 47 (2008), 4332-4341.
- [PH 4] P. Heidebrecht, K. Sundmacher, Thermodynamic analysis of a cyclic water gas-shift reactor (CWGSR) for hydrogen production, *Chemical Engineering Science* 64 (2009), 5057-5065.
- [PH 5] M. Pfafferodt, P. Heidebrecht, K. Sundmacher, Stack modeling of a Molten Carbonate Fuel Cell (MCFC), *Fuel Cells* 10, 4 (2010), 619-635.
- [PH 6] P. Heidebrecht, B. Hartono, C. Hertel, K. Sundmacher, Biomass-Based Fuel Cell Power Plants: Evaluation of Novel Reactors and Process Designs, *Industrial & Engineering Chemistry Research* 49, 21 (2010), 10859-10875.
- [PH 7] P. Heidebrecht, L.T. Biegler, K. Sundmacher, Optimal Design of Nonlinear Temperature Programmed Reduction (N-TPR) Experiments, *AIChE Journal* 57 (2011), 2888-2901.
- [PH 8] B. Hartono, P. Heidebrecht, K. Sundmacher, Mass Integration of High Temperature Fuel Cell Plants, *International Journal of Hydrogen Energy* 36 (2011), 7240-7250.
- [PH 9] P. Heidebrecht, M. Pfafferodt, K. Sundmacher, Hierarchical Modeling Strategy for Structured Reactors, *Chemical Engineering Science* 66 (2011), 4389-4402.

[PH 1]

P. Heidebrecht, V. Galvita, K. Sundmacher

An alternative method for parameter identification from
Temperature Programmed Reduction (TPR) data

Chemical Engineering Science 63 (2008), 4776-4788

An alternative method for parameter identification from temperature programmed reduction (TPR) data

Peter Heidebrecht^{a,*}, Vladimir Galvita^a, Kai Sundmacher^{a,b}

^aMax-Planck-Institute Dynamics of Complex Technical Systems, Sandtorstraße 1, 39106 Magdeburg, Germany

^bProcess Systems Engineering, Otto-von-Guericke-University, Universitätsplatz 2, 39106 Magdeburg, Germany

Received 28 February 2007; received in revised form 5 September 2007; accepted 7 October 2007

Available online 22 October 2007

Abstract

The experimental method of temperature programmed reduction (TPR) for the investigation of gas–solid reactions is well established and widely used since the 1970s. With regard to the temporal and financial effort for TPR measurements, the quantitative model-based analysis of the data is not adequately developed. The TPR data analysis is comprised of two aspects: a discrete model identification and a continuous parameter optimisation. In this contribution, a general model for TPR experiments is introduced and a strategy for the model identification is proposed. This results in a large number of continuous optimisation problems which can be solved very efficiently by a proposed optimisation algorithm that is especially tailored for the problem at hand. The applicability of the method is demonstrated using TPR measurements of iron oxide in hydrogen gas.

© 2007 Elsevier Ltd. All rights reserved.

Keywords: Temperature programmed reduction (TPR); Model discrimination; Parameter identification; Multi-phase reactions

1. Introduction

Reduction reactions of metal oxides play an important role, especially in processes in the steel industry, but also in catalyst preparation (Hu et al., 2000; Lambrou and Efstathiou, 2006; van den Berg et al., 2003; Kanervo and Krause, 2001; Tiernan et al., 2001). Historically, the oxidation of iron oxide with steam was a method for the production of clean hydrogen (Messerschmitt, 1911), an idea that has drawn some attention in the last few years regarding clean-up processes for hydrogen for use in fuel cells (Hacker, 2003; Galvita and Sundmacher, 2007). Purposeful design of such catalysts and processes requires detailed knowledge about the relevant reactions.

Temperature programmed reduction (TPR) and temperature programmed oxidation (TPO) are established methods for kinetic analysis of these processes (Kissinger, 1957; Doyle, 1961; Hurst et al., 1982). The principle is simple: gas containing the reaction educts continuously flows through a small probe of porous solid material (Fig. 1). At the beginning, temperature

is low, so all reaction rates are virtually zero. Temperature is then increased at a constant rate, so the reaction rates increase depending on the activity and the actual degree of reduction of the solid material, until the material is completely reduced. The concentration of the gaseous reaction products (or the consumption of the reaction educts) is measured at the outlet with a high sampling rate. This experiment is repeated with different heating rates or with varying feed gas compositions. TPR experiments are performed under high technical standards using fully automated laboratory devices.

Although the method is well established and widely used, the results can vary strongly. Pineau et al. (2006) list activation energies of iron oxide reduction using hydrogen measured by different authors using the TPR method. The results for the apparent activation energy range from 18 to 246 kJ/mol. In part this can be explained by different compositions and particle sizes of the solid material due to preparation method, gas impurities and different temperature ranges in the TPR procedure. But in part these deviations are also due to inaccurate data analysis.

Usually the analysis of the experimental data has several objectives: To identify the reaction scheme and to determine

* Corresponding author. Tel.: +49 391 6110 285.

E-mail address: heidebrecht@mpi-magdeburg.mpg.de (P. Heidebrecht).

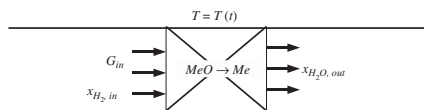


Fig. 1. Scheme of a TPR reactor.

Table 1

Classical ensemble of kinetic models for reduction reactions (from Vyazovkin and Wight, 1997)

	$f(z)$
Power law/contracting cylinder	$(1 - z)^{1/2}$
Power law/contracting sphere	$(1 - z)^{2/3}$
Power law	$(1 - z)^{3/4}$
First order	$(1 - z)$
Second order	$(1 - z)^2$
Avrami–Erofeev	$2 \cdot (1 - z) \cdot [-\log(1 - z)]^{1/2}$
Avrami–Erofeev	$3 \cdot (1 - z) \cdot [-\log(1 - z)]^{2/3}$
Avrami–Erofeev	$4 \cdot (1 - z) \cdot [-\log(1 - z)]^{3/4}$
1D diffusion	$(1 - z)^0 \cdot (1 - (1 - z)^4)^{-1}$
2D diffusion	$(1 - z)^{1/2} \cdot (1 - (1 - z)^{1/2})^{-1}$
3D diffusion	$(1 - z)^{2/3} \cdot (1 - (1 - z)^{1/3})^{-1}$

the parameters (reaction rate constant and activation energy) of each reaction. Usually, data analysis is based on an ordinary differential equation describing the progress of the reduction:

$$\frac{dz}{dt} = k_0 \cdot \exp\left(-\frac{E_A}{RT}\right) \cdot f(z), \quad (1)$$

where z is the degree of reduction and the temperature T is a linear function of time:

$$T = T_0 + b \cdot (t - t_0). \quad (2)$$

While the second factor on the right-hand side in Eq. (1) considers the temperature dependence by an Arrhenius term, the last factor describes the relation between reaction rate and the degree of reduction, following one of the kinetics in Table 1, which are commonly used in gas–solid reactions (Vyazovkin and Wight, 1997). Several authors propose analytical approximate solutions (Wimmers et al., 1986; Doyle, 1961; Šesták et al., 1973). These approximate solutions allow to quickly calculate the TPR profile for any reaction and compare it with the measured TPR data.

However, the approximate solution is only strictly valid under the assumption that each reaction happens independently from all other reactions. This is true for the following cases or combinations of them:

- The solid material is reduced in only one single reaction step.
- The solid material is composed of oxides of different metals, each being reduced independently from all the others in a single reduction step.

- A metal oxide is reduced in several steps, but in the TPR experiment, the next step occurs only after the previous one is completed.

This restricts the method either to very simple cases (single reaction) or to very unlikely ones (reduction step is completed before the next reduction step starts). For all other cases with multi-step reductions or mixtures of different metal oxide species, this method can at best deliver rough estimates, but in no way can it be applied for a reliable parameter estimation. Nevertheless, it is common practice that the approximate solutions for several consecutive reactions are simply superimposed to calculate the TPR curve, which is then used to fit the unknown parameters by means of least square optimisation. Although this method is quite fast, it is not physically correct and usually leads to considerable deviations between measurement and simulation.

In addition, many studies presume a certain reaction mechanism based on *a priori* knowledge, on additional measurements, on experience, or sometimes simply by assumption. This means that the number of species and reactions as well as their exact stoichiometry is fixed. This is valid if the mechanism is known for sure, but for a realistic powdery material with particles of different sizes, possible segregation of metal species at the surface, different behaviour of the particle bulks, one often cannot tell *a priori* which reactions are relevant in each part of this solid material. Thus often times neither the number of reactions is known nor their mechanism.

In this contribution we propose a new modelling approach for TPR/TPO systems and an efficient algorithm for parameter estimation. The model is still simple, but it allows to consider more complex material behaviour involving parallel and multi-step reductions. The amount of *a priori* knowledge required for this model is minimal. The estimation algorithm is a combination of standard minimisation algorithms, but it is especially tailored for this type of problem. The time required for this optimisation is several hours, which is in the same order of magnitude as for the TPR experiments. Regarding the effort spent to obtain the experimental data (in terms of time and money spent), it is justified to spend a similar amount of (computing) time to extract a maximum of information from the data. The result of this parameter identification method is not one single reaction scheme and its optimal kinetic parameters, but a whole range of models which fit the experimental data well. At this point, physical and chemical interpretation is required to help choose one or two plausible models which can then be assumed to adequately describe the reduction process.

In the following sections the modelling approach is introduced first and some requirements concerning the experimental data are mentioned. After that, the optimisation algorithm is introduced. The whole method is then demonstrated for the reduction of iron oxide. In the conclusion, possibilities and limitations of the method are discussed, and some indications for further development are given. Throughout this contribution, only TPR is discussed, but all methods apply to TPO experiments as well.

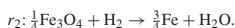
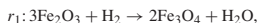
2. Modelling

2.1. Modelling based on “a priori” reaction scheme

TPR experiments are usually conducted using a small probe of fixed bed material, through which gas flows continuously (see Fig. 1). The model is set up under the following assumptions:

- Using a small amount of solid material and applying high gas velocities, the conversion of the gas is low. This leads not only to the assumption of homogeneous conditions throughout the reactor (CSTR assumption), but the gas composition in the reactor can be approximated by the inlet gas composition with regard to the reaction kinetics (differential reactor).
- The gas residence time is small compared to the characteristic time of the reduction process of the fixed bed. Thus the molar fractions of the gas can be considered to be in quasi-steady state.
- The product concentration in the gas is negligible, so that no backward reaction (oxidation in case of a TPR) occurs.
- Due to the high gas flow rate and the low heat capacity of the reactor, the temperature follows the given profile of the TPR device without lag or deviation.

Usually, a multi-step reduction process is modelled under the assumption of a specific reaction scheme. For the sake of clarity, we chose a simple example: the reduction of iron oxide with hydrogen in a presumed two-step reduction process (i.e., without considering the intermediate FeO species):



The stoichiometry of the reaction scheme is normalised so that exactly one oxygen atom is taken from the fixed bed material in each reaction step. This has the advantage of comparable reaction rates. The balances of the fixed bed species in the reactor read:

$$\begin{aligned} \frac{dn_{\text{Fe}_2\text{O}_3}}{dt} &= 0 - 3 \cdot r_1, \\ \frac{dn_{\text{Fe}_3\text{O}_4}}{dt} &= +2 \cdot r_1 - \frac{1}{4} \cdot r_2. \end{aligned} \quad (3)$$

The stoichiometry of the reactions and the composition of the solid species allows to define oxygen capacities of each metal oxide species. It is the amount of oxygen per metal atom that can be released in the next reduction step. In the first reaction of the example, one oxygen atom is taken from 3Fe₂O₃ molecules (hematite), so the oxygen capacity of this species is one-third of the maximum number of hematite molecules available. The maximum amount of hematite is half the total amount of iron in the fixed bed, n_{Fe} . Thus the oxygen capacity of hematite per iron atom is one-sixth. An equivalent procedure is performed

for the Fe₃O₄ species:

$$\begin{aligned} C_{\text{Fe}_2\text{O}_3} &= \frac{1}{3}n_{\text{Fe}_2\text{O}_3, \text{max}}, \\ n_{\text{Fe}_2\text{O}_3, \text{max}} &= \frac{1}{2}n_{\text{Fe}} \Rightarrow C_{\text{Fe}_2\text{O}_3} = \frac{1}{6}n_{\text{Fe}}, \\ C_{\text{Fe}_3\text{O}_4} &= 4n_{\text{Fe}_3\text{O}_4, \text{max}}, \\ n_{\text{Fe}_3\text{O}_4, \text{max}} &= \frac{1}{3}n_{\text{Fe}} \Rightarrow C_{\text{Fe}_3\text{O}_4} = \frac{8}{6}n_{\text{Fe}}. \end{aligned} \quad (4)$$

The total oxygen capacity is the sum of all capacities:

$$C_t = \sum_i C_i = \frac{9}{6}n_{\text{Fe}}. \quad (5)$$

Furthermore we introduce the characteristic time constant as the time required to reduce the whole fixed bed at a standard reaction rate:

$$t^\theta = \frac{C_t}{r^\theta}. \quad (6)$$

By introducing the following dimensionless numbers:

$$\tau = \frac{t}{t^\theta}, \quad (7)$$

$$\alpha_i = 1 - \frac{n_i}{n_{i, \text{max}}}, \quad (8)$$

$$\Theta_i = \frac{C_i}{C_t}, \quad (9)$$

$$\rho_j = \frac{r_j}{r_j^\theta}, \quad (10)$$

$$Da_j = \frac{r_j^\theta}{r^\theta} \quad (11)$$

into Eq. (3) we obtain the dimensionless balance equations

$$\begin{aligned} \frac{d\alpha_{\text{Fe}_2\text{O}_3}}{d\tau} &= 0 + \frac{Da_1\rho_1}{\Theta_{\text{Fe}_2\text{O}_3}}, \\ \frac{d\alpha_{\text{Fe}_3\text{O}_4}}{d\tau} &= -\frac{Da_1\rho_1}{\Theta_{\text{Fe}_2\text{O}_3}} + \frac{Da_2\rho_2}{\Theta_{\text{Fe}_3\text{O}_4}}. \end{aligned} \quad (12)$$

In this dimensionless notation, the stoichiometric coefficients of the reaction scheme (Eq. (3)) disappear, as they are incorporated in the oxygen capacities, $\Theta_{\text{Fe}_2\text{O}_3}$ and $\Theta_{\text{Fe}_3\text{O}_4}$. Assuming that the reaction scheme is not known for sure *a priori*, the stoichiometry is also to be considered as unknown. Thus, the oxygen capacities are to be considered as unknown parameters that have to be identified together with the Damköhler numbers, Da_j , and the Arrhenius numbers, Arr_j , describing the reaction activation energies.

2.2. Modelling based on the oxygen storage scheme

2.2.1. Mass balances

The dimensionless model formulation, which is given in Eq. (12) for a simple example, can be extended to a general

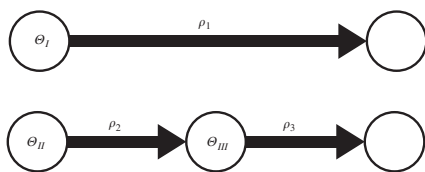


Fig. 2. Example for an oxygen storage scheme. The reduction process is interpreted as mass being transferred from one oxygen storage into another by reduction reactions, ending at terminal storages.

modelling concept for reduction processes. The cornerstones of this concept are listed in the following:

- Each reducible species in the solid material represents an oxygen storage. Knowledge about the exact chemical composition of this species is not required. The corresponding degree of reduction, α , describes how far this storage has been emptied ($\alpha = 0$ is a full storage, $\alpha = 1$ is an empty storage).
- Reduction reactions transform molecules of one species into molecules of another species. This means that metal atoms are transferred from one oxygen storage to another one, or one storage is emptied while the other one is filled. Thus reactions are fluxes from a source storage to a destination storage.
- Each oxygen storage possesses its own oxygen capacity. It describes the amount of oxygen that is released when the whole storage is emptied into the next storage. All capacities are related to the total oxygen capacity.
- A terminal storage is a storage of mass which cannot be reduced further. Any series of storages connected by reaction fluxes ends in a terminal storage. The oxygen capacity of a terminal storage is zero.

In Fig. 2, this is depicted using an example. Assume a system consisting of two different reducible species. Species I is reduced in a single-step process (by reaction 1), while species II is reduced in a two-step process via intermediate species III (reactions 2 and 3). For example, this could be a storage network for a mixture of iron oxide and ceria oxide, where iron is reduced in two steps and ceria is reduced in a single step. Note that the final form of ceria, Ce_2O_3 , contains oxygen, but cannot be further reduced, so it is a terminal storage. Note that two parallel storages do not necessarily imply the existence of two different species. Topochemical effects can be the reason why the same species reacts differently at different locations in the solid material. This needs to be described as two parallel storages.

Once a storage scheme including its reactions has been chosen, the balance equations for the degrees of reduction are clearly defined. For each reaction originating from the respective storage, a reaction term with a positive sign occurs, divided by the capacity of the source storage. For each reaction

ending in the considered storage, a reaction term with a negative sign appears, which is divided by the capacity of the reaction source (see the first term on the right-hand side in Eq. (12b)). The general balance equation then reads

$$\frac{d\alpha_i}{d\tau} = \sum_j v_{i,j}^S \frac{Da_j \rho_j}{\tilde{\theta}_j}, \quad (13)$$

where $\tilde{\theta}_j$ is the capacity of the source storage of reaction j . In the example in Fig. 2,

$$\begin{pmatrix} \tilde{\theta}_1 \\ \tilde{\theta}_2 \\ \tilde{\theta}_3 \end{pmatrix} = \begin{pmatrix} \theta_I \\ \theta_{II} \\ \theta_{III} \end{pmatrix} \quad (14)$$

and

$$v^S = \begin{pmatrix} +1 & 0 & 0 \\ 0 & +1 & 0 \\ 0 & -1 & +1 \end{pmatrix}. \quad (15)$$

As initial conditions for a completely oxidised material, the degrees of reduction for all source storages usually are zero, except for the intermediate storages, which equal unity. In our example:

$$\alpha_I(\tau = 0) = \alpha_{II}(\tau = 0) = 0, \quad \alpha_{III}(\tau = 0) = 1. \quad (16)$$

2.2.2. Output concentration

The steady state component mass balances at the reactor (see Fig. 1) for any component k read

$$0 = G_{in} \cdot (x_{k,in} - x_k) + A \cdot \sum_j (v_{k,j} - x_k \cdot \bar{v}_j) \cdot r_j, \quad (17)$$

where

$$\bar{v}_j = \sum_k v_{k,j}. \quad (18)$$

Rearranging and solving for the molar fraction at the outlet, one obtains

$$x_k = \frac{G_{in} x_{k,in} + A \sum_j v_{k,j} r_j}{G_{in} + A \sum_j \bar{v}_j r_j}. \quad (19)$$

This is the gas composition at the reactor outlet which is measured during the TPR experiment. Assuming that

- the conversion is low compared to the convective flow rate ($G_{in} \gg A \sum_j \bar{v}_j r_j$, compare for assumptions in Section 2.1),
- only the product species is of interest, i.e., $x_{k,in} = 0$ and $v_{k,j} = +1$,

one obtains the molar fraction of the reaction product at the outlet:

$$x_{out} = \frac{A}{G_{in}} \sum_j r_j. \quad (20)$$

Using Eqs. (10) and (11), the dimensionless formulation reads

$$x_{\text{out}} = \frac{1}{G_{\text{in}}} \sum_j Da_{j,j} \rho_j, \quad (21)$$

where

$$\tilde{G}_{\text{in}} = \frac{G_{\text{in}} \cdot t^{\theta}}{AC_t}. \quad (22)$$

It can be shown that for a normalised TPR curve (area below the curve equals unity), this parameter must also be unity (see Appendix). Thus, the output molar fraction of the gaseous product is

$$x_{\text{out}} = \sum_j Da_{j,j} \rho_j. \quad (23)$$

2.2.3. Temperature

In most TPR experiments, temperature is simply a linear function of time. In dimensionless formulation, this reads

$$\vartheta(\tau) = \vartheta_0 + \beta \cdot \tau, \quad (24)$$

where

$$\vartheta = \frac{T}{T^{\theta}} \quad (25)$$

and β stands for the dimensionless “heating rate”, i.e., temperature gradient:

$$\beta = \frac{b \cdot t^{\theta}}{T^{\theta}}. \quad (26)$$

2.2.4. Reaction kinetics

In the literature on TPR, one usually finds a set of commonly used kinetic expressions for gas–solid reactions, defining the relation between the degree of reduction and the reaction rate for different reaction mechanisms (see Table 1). In addition, each reaction rate also obeys to Arrhenius’ law:

$$r_j = k_{0,j} \cdot \exp\left(-\frac{E_{A,j}}{RT}\right) \cdot f_j(x). \quad (27)$$

The standard reaction rate (see the definition of the Damköhler number, Eq. (12)), should be a typical rate for this reaction. Therefore, it is defined as the reaction rate constant at a typical reference temperature, where the reaction rate is significant in a TPR experiment:

$$r_j^{\theta} = k_{0,j} \cdot \exp\left(-\frac{E_{A,j}}{RT^{\theta}}\right). \quad (28)$$

Thus, with the Arrhenius number

$$Arr_j = \frac{E_{A,j}}{RT^{\theta}}, \quad (29)$$

The dimensionless reaction rate is

$$\rho_j = \exp\left(Arr_j \left(\frac{1}{\vartheta_j^{\text{ref}}} - \frac{1}{\vartheta}\right)\right) \cdot f_j(x). \quad (30)$$

This formulation of the standard reaction rate leads to the following definition of the Damköhler number:

$$Da_j = \frac{k_{0,j} \cdot t^{\theta}}{C_t} \cdot \exp\left(-\frac{E_{A,j}}{RT_j^{\text{ref}}}\right). \quad (31)$$

Due to this definition, all Damköhler numbers are in the order of magnitude of unity, which has strong numerical advantages for the parameter identification algorithm.

2.2.5. Discussion of the model

The proposed dimensionless model consists of Eqs. (13), (23) and (24), together with the reaction rates (Eq. (30) and Table 1) and appropriate initial conditions.

The strong advantage of this modelling concept is that no knowledge is required about the chemical processes and the occurring metal oxide species in the solid material. While the starting point for a conventional model (Section 2.1) is a reaction scheme, the starting point for this model is a storage scheme (Fig. 2). The number of reactions and storages in the scheme can be chosen according to the experimental data without the necessity to interpret the data with respect to possible chemical species and their presumed reduction reactions. Thus, one can avoid a fixation on favourite reaction schemes. However, that does not imply ignoring knowledge about the reaction system. The models generated by this method should still be interpretable from a physical point of view. For example, knowledge about the possible number of reduction steps of certain species may be used to eliminate physically impossible schemes. In any case, one should take care only to exclude really impossible storage schemes and not to eliminate schemes that one feels are unlikely, but which are still possible. In the case of a single storage with only one reaction, this model can be solved by an analytical approximation (Wimmers et al., 1986). For more than one reaction, no generally applicable analytical solution is available, so numerical ODE-solvers are required. The numerical treatment of the model is simple, because it is explicit with respect to the state variables, can be formulated in vectorised form and therefore it can be solved very efficiently with standard algorithms (any ODE-solver in Matlab, for example).

Beyond the features shown in the example in Fig. 2, the storage concept can also incorporate parallel reactions with identical source and destination; for example, there could be two reactions between storages II and III. Note that in the example, the number of storages equals the number of reactions, but this is not necessarily the case.

3. Experimental data

TPR data are recorded by automated TPR devices. Usually, the sampling rate is in the order of 1 s, whereas one single TPR curve takes several hours to measure, depending on the heating rate applied. Due to the non-linear character of the model, it is advisable to cover a wide range of experimental conditions, that means a wide range of heating rates. Within this range, the heating rate of the experiments should be about equally

distributed in order to avoid overweighting of experiments with low or high heating rates.

To obtain a measure for the typical variance of the measurement, i.e., the measurement error, repeated measurements are required. Assuming that the measurement error is nearly identical for all heating rates, it is sufficient to perform repeated measurements at one single arbitrarily chosen heating rate. Note that these additional measurements are used solely to estimate the typical measurement variance. They should not be included in the parameter estimation in order to avoid an overweighting of the results at this heating rate.

4. Parameter estimation algorithm

Analysis of TPR data is an inverse problem that can be split into two parts. The first part is to identify a suitable model, consisting of a storage scheme (i.e., reaction network) and appropriate reaction mechanisms, the second part is to identify the kinetic parameters of the reactions. While the first part is a discrete model identification, the second part is a continuous parameter optimisation problem. The two aspects are discussed separately.

4.1. Model identification

TPR experiments do not deliver separate data on each reaction occurring in the system, but only the sum of all reaction rates, which is a lumped information. From the raw TPR data, one cannot say with certainty how many relevant reactions occur. Also, the data give no information whether the reactions are parallel or consecutive reactions. In fact, two peaks in a TPR curve could be a two-step reduction process of one metal oxide, but it could also be a one-step reduction of the same metal oxide at different topologies in the solid material.

However, the data give a good hint concerning the number of reactions which should at least be considered. This is the starting point for the model identification. A certain number of reactions can be arranged in a storage scheme in different ways. While there are two options in the case of two reactions (consecutive or parallel), the number of possible schemes quickly increases for three or more reactions (see Fig. 3 for possible storage schemes with three storages and three reactions). According to Table 1, each reaction can follow any of nine kinetic laws, which means that for each scheme with n reactions, we have 9^n possible models. A model is defined by a storage scheme and kinetic laws for each reaction. The parameters of every single model must be fitted to the experimental data.

To reduce the number of models considerably, the kinetic laws from Table 1 are grouped and rearranged in Table 2. One can see that kinetics 1...5 from Table 1 have the same structure, but they have a different order of reaction. The same holds true for the three reaction kinetic expressions according to Avrami–Erofeev, which only deviate by one single parameter. The diffusion limited kinetics can also be described by one single equation. Thus, it is possible to reduce the number of models by reducing the number of kinetic laws. As a result, each reaction is not only described by a Damköhler and an Arrhenius number, but also by an additional parameter denoting the order of reaction. Although this increases the number of unknown parameters slightly, it significantly decreases the number of possible models.

Our approach to the model identification problem is to optimise the parameters of each possible model. In order to keep computation times at a reasonable level, an efficient optimisation is required, for which an algorithm is proposed in Section 4.3. The measure for the quality of a model fit is the sum of the squares of the errors. After optimising all models with the minimum number of reactions, a certain number of these usually shows nearly equally good fits.

In the next step, the number of reactions considered is increased by one, all possible storage schemes are set up and all possible kinetic laws are assigned to each reaction, and the parameters of each new model are optimised. Note that with each additional reaction, not only the number of possible storage schemes and combinations of reaction kinetics, but also the number of parameters increases.

This procedure is repeated until the deviation of the best models from the experimental data is in the same order of magnitude as the variance of repeated measurements. The result is a large number of fitted models, some of which approximate the measured data quite well. Afterwards, physical and chemical knowledge come into play. They are required to exclude models that fit well, but are physically implausible, and to identify one or two models that not only fit well to the experimental data, but also allow a good physical interpretation.

4.2. Discussion of the approach

This frontal approach to the combinatorial problem is sometimes called a “brute force” approach, and most authors try to avoid it. One alternative approach is to select only a few models using *a priori* knowledge about the chemical processes in the system. This strategy excludes possible models that might actually be better than the selected ones. Another strategy would

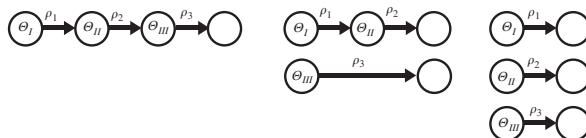


Fig. 3. Possible storage schemes for three reactions and three storages.

Table 2
Reduction kinetics with variable reaction order

	$f(x)$	m
Power law (PL)	$(1 - \alpha)^m$	$\frac{1}{2} \leq m \leq 2$
Avrami–Erofeev (AE)	$\frac{1 - \alpha}{1 - m} \cdot [-\log(1 - \alpha)]^m$	$\frac{1}{2} \leq m \leq \frac{3}{4}$
Diffusion (Diff.)	$\frac{(1 - \alpha)^{1-1/m}}{1 - (1 - \alpha)^{1/m}}$	$1 \leq m \leq 3$

be to start with a selected model and then use statistical tests for parameter significance, lack of fit, as well as forward model selection (for example see Li et al., 2006, and also Joshi et al., 2006; Maria, 2004). There are two problems in applying this method to TPR data. First, there is no systematic way to decide how to extend an existing model by one reaction. In the general case, the reactions in TPR are coupled and non-linear, so adding a new reaction is not just like adding an additional term to the simulated data. The second point is that any model selection strategy requires statistical tests of parameter significance and of model lack of fit. Usually, these require the degrees of freedom of the problem, which is the number of linearly independent measurements minus the number of model parameters. In TPR curves, the measurement points are not linearly independent, so the degrees of freedom are unknown and the existing statistical tests for parameter significance and model discrimination are not applicable here. This seems to be a general problem with transient experiments and requires the development of new statistical tools, which is not the focus of this contribution.

The advantage of the frontal approach is that it is not limited by the knowledge of the experimentalist. It also considers storage schemes and combinations of reactions which have not been considered of before. The method usually produces a number of well fitting models instead of one single model. At this point, knowledge about the chemistry and physical processes are of great value, for many models that are not physically interpretable can be eliminated after the optimisation. Some groups of models can be eliminated prior to the optimisation process, if they are physically impossible (for example, models with three diffusion limited consecutive reactions). But many models which seem to be interpretable at first may become unlikely once their parameters are determined. The necessity of post-optimisation interpretation and elimination of impossible models may seem laborious, but it possibly is preferable to the search for proper models prior to the optimisation, which also can be time-consuming. Even models that cannot be interpreted by physical means can be applied as black box models, although their applicability is certainly limited to processes similar to TPR experiments.

Despite its advantages, this method also has some drawbacks. Consideration of reaction schemes with four or more reactions quickly leads to long computational times of several days. Furthermore, the number of resulting models also increases significantly, yielding a large number of models to be interpreted after optimisation.

4.3. Parameter optimisation

With the frontal approach to the model identification problem, the number of possible models is high and an efficient algorithm is required to optimise their parameter sets within reasonable time.

Given a model (a storage scheme and kinetic laws for each reaction), the parameter optimisation has to identify a set of model parameters which best fits the model to the measurement data. The quality of the fit is described by the sum of residuals squared, $F(p)$. The residual is the difference between the simulated output, $x_{\text{out},\text{sim}}(p)$, depending on the model parameters, p , and the measured TPR data, $x_{\text{out},\text{meas}}$. In this optimisation, several TPR curves at different heating rates are considered simultaneously. The parameter vector, p , comprises one Damköhler number, one Arrhenius number and the order of reaction for each reaction as well as the oxygen capacities for each storage in the model. Each parameter value is confined by upper and lower bounds given by the non-negativity condition of all parameters, the range of realistic values for the Arrhenius number, and the limits of the order of reaction (Table 2). Let $x_{\text{out},\text{meas}}$ be the vector of all measured points and $x_{\text{out},\text{sim}}(p)$ be the vector of the corresponding simulated values, then the minimisation problem reads

$$\min_p F(p) = X(p)^T \cdot X(p) \quad (32)$$

subject to the dynamic model equations and

$$p_{\min} \leq p \leq p_{\max}, \quad (33)$$

where¹

$$X(p) = x_{\text{out},\text{sim}}(p) - x_{\text{out},\text{meas}}. \quad (34)$$

In principle, this parameter optimisation problem can be solved by virtually all existing algorithms capable of handling inequality constraints, for example any SQP-based algorithm. However, these do not take advantage of the special structure of the problem at hand and cannot easily be manipulated to do so. Thus an optimisation algorithm is developed which is especially tailored for this problem. The objective function is a quadratic function, so the iterative Gauss–Newton algorithm is well suited for this type of optimisation problem. The Marquardt correction (Marquardt number, λ) improves the performance of this algorithm for non-linear problems like the one here (Edgar and Himmelblau, 2001; Fletcher, 2000). In a Gauss–Newton–Marquardt step, the parameters are repeatedly changed according to

$$\Delta p = [J^T J + \lambda]^{-1} \cdot J^T \cdot X. \quad (35)$$

This algorithm requires the gradient of the vector X with respect to the model parameters, which is the Jacobian of the model, J .

¹ Assuming an identical sampling rate for all measured TPR curves, experiments with a high heating rate include fewer data points than those curves generated at a low heating rate. This must be compensated using a weighting factor for the errors in that curve in such way that the sum of residuals squared of each curve has the same weight. For simplicity, this shall be omitted in the following.

Usually, this gradient is approximated numerically by repeated evaluation of X at slightly varied parameter sets. Each evaluation of X requires to simulate all TPR curves at the given parameter set. For n parameters, the approximation of J requires $n + 1$ function evaluations, which is quite time-consuming. To avoid this, an ODE system for the Jacobian matrix is derived and integrated simultaneously with the model ODEs (see Appendix as well as Caracotsios and Stewart, 1985). This leads to a slight increase in integration time for each evaluation of X , but it strongly reduces the number of required function evaluations. The code is further improved if the model ODEs can optionally be solved alone or be solved together with the ODEs of the Jacobian. To consider the inequality constraints (Eq. (33)), an active set strategy in combination with a reduced gradient is applied.

The algorithm of a single optimisation step is depicted in Fig. 4. At first, the errors, the Jacobian and the sum of residuals squared is calculated. Eq. (35) delivers the parameter change according to the Gauss–Newton–Marquardt correction. The next step is to check which parameters are already at their bounds and would violate it if they followed the proposed parameter change; these form the active set. The entries in the Jacobian corresponding to the active parameters are eliminated and the Gauss–Newton instruction is repeated for a reduced set of parameters (principle of the reduced gradient). The active parameters are not changed.

The proposed parameter change is then checked for violations of the inequality constraints. If one or more modified parameters would violate any constraint, the parameter change is reduced in such a way that the first inequality constraint is just active. According to the Marquardt modification, the algorithm now evaluates the sum of residuals squared at the modified parameters to check whether this proposed correction leads to a decrease of the objective function. If not, the step size is decreased by increasing the Marquardt number by a given factor and the procedure is repeated. If the parameter change is favourable, it is accepted and the Marquardt number is decreased by a certain factor. The optimisation step is aborted if the Marquardt number becomes too high, which means that the step size becomes very small.

So far, only conventional optimisation elements are combined in this algorithm. However, the optimisation problem has a special structure which can be utilised to refine the optimisation algorithm. Each reaction basically contributes a peak shape to the simulated TPR curve, although these can vary strongly in height and shape. In some cases it is favourable not to try to adjust all reaction parameters simultaneously, but to adjust the parameters of each reaction separately. Thus, the algorithm should be able to conduct “full steps”, where all parameters are manipulated simultaneously, and “partial steps”, where only a part of the parameter vector is optimised which belongs to a single reaction. While in a full step, a single Gauss–Newton iteration is conducted, the partial step can be different: At first, two or three Gauss–Newton iterations are performed exclusively for the parameters of reaction 1, then for the next reaction and so on.

Fig. 5 shows the strategy using full and partial steps for the parameter optimisation. While full steps are usually faster and

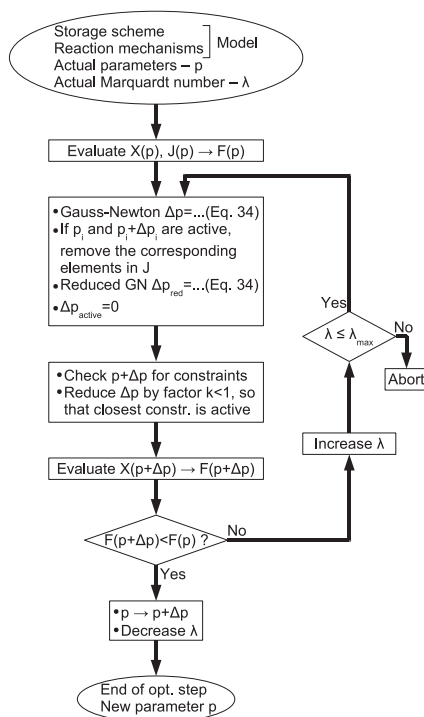


Fig. 4. Algorithm of a single parameter optimisation step. The algorithm is based on a Gauss–Newton–Marquardt correction and uses active set and reduced gradients strategies.

more efficient than a series of partial steps, these can greatly enhance the convergence of the optimisation. They are useful at the beginning of an optimisation, when the guessed parameters are far away from the optimum and the simulated curve is very different from the measured curve. After beginning with a few partial steps, the algorithm attempts to continue with full steps to achieve a faster convergence. As long as the objective function is sufficiently decreased by each full step, they are repeatedly used. If the progress of the optimisation by full steps is too slow, a partial step is used again. This can happen due to two reasons: Either the parameters are already close to their optimum or the objective function is strongly non-linear with respect to the parameters of one single reaction. In the first case, the partial step cannot decrease the objective function very much further, so the descent in the objective function will remain small, leading to a successful termination of the

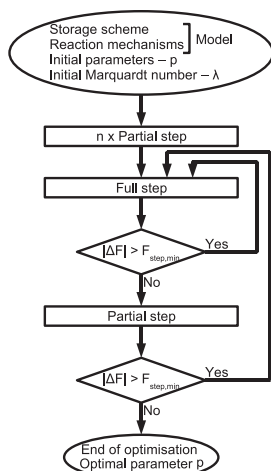


Fig. 5. Utilisation of partial and full steps in the parameter optimisation. Both kinds of optimisation steps are conducted according to Fig. 4. Full steps optimise all parameters simultaneously, while partial steps consider the parameters of each reaction separately.

algorithm. In the second case, the partial step improves the parameters of each reaction separately, bringing the parameters closer to an optimum, from where a full step can be applied with better results.

One more aspect can be utilised to greatly decrease the computation time. In this optimisation, it is not necessary to obtain the optimum with a high precision. It is perfectly sufficient to see whether a model converges to a good fit or not. Thus, the maximum number of optimisation steps can be limited to a number depending on the complexity of the model. If required, the parameters of the best models can be refined afterwards, but this is not necessary for models with a mediocre or bad fit.

5. Exemplary application to iron oxide reduction

The functionality of the proposed method is demonstrated using an example: the reduction of iron oxide with hydrogen. TPR experiments have been conducted with four different heating rates (3, 5, 10 and 20 K/min) and seven repeated measurements at one single heating rate (10 K/min). Each curve has been normalised so that the area below the curve equals unity.

The repeated measurements at 10 K/min are shown in Fig. 6. Computing an average curve and calculating the sum of residuals squared (F_i) of each TPR curve at 10 K/min relative to the average, one obtains the values listed in Table 3, from

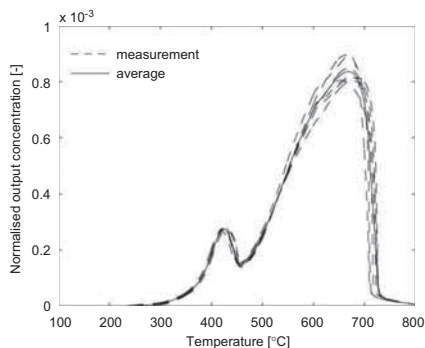


Fig. 6. Repeated TPR measurements of iron oxide in hydrogen at a heating rate of 10 K/min (dashed lines) together with the average TPR curve (solid line). The deviation between the measurements and their average indicates the precision of the measurement and serves as criterion for model extension.

which a variance, s^2 , is estimated according to

$$s^2 = \frac{1}{n-1} \cdot \sum F_i. \quad (36)$$

Note that the value given in Table 3 is valid for a single TPR curve. In this example, four TPR curves are considered for parameter fitting, so the threshold value for adequate models should be four times higher at about $F = 33$. A model with a residual squared of about this value can be assumed to be adequate. Note that this is not a statistically sound approach, but it basically compares the model error to the measurement error to judge the quality of a model fit.

The four TPR curves at different heating rates which are used for the parameter identification are shown in Fig. 7. The curves at lower heating rate suggest a minimum of two reactions. Thus, the optimisation is started with models containing two reactions, although the curve at 20 K/min shows three peaks, indicating three reactions. The two reactions can be arranged in series or in parallel, thus two different schemes are treated. Each reaction can follow any of the three reaction mechanism groups (see Table 2), thus each scheme contains nine different models with eight parameters each (Damköhler, Arrhenius, order of reaction for each reaction plus capacity for each storage). The sum of residuals squared of the best fitting model is about 71, so the deviation of these models from the measurement is higher than the variance of the repeated measurements.

In the next step, all models consisting of three reactions are considered. Fig. 3 illustrates the three possible storage schemes for three reactions. With three possible mechanisms for each reaction, this results in 27 models per scheme, thus 81 models with 12 parameters each are to be optimised.

The best fitting models are listed in Table 4. The sum of residuals squared of several models approach the variance of

Table 3

Deviations between the repeated TPR curves and estimated variance of the measurement error

No. of TPR curve, i	1	2	3	4	5	6	7	Variance s^2
Sum of errors squared rel. to average, F_i	2.6	9.7	10.7	17.6	1.7	2.2	4.5	8.2

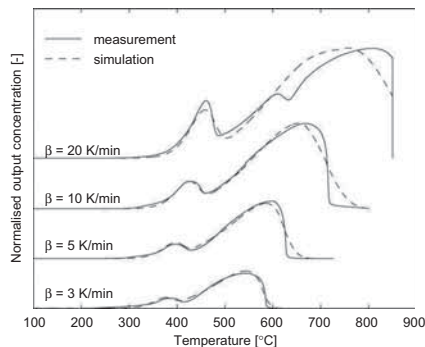


Fig. 7. TPR curves of iron oxide in hydrogen at heating rates of 3, 5, 10 and 20 K/min, which are used for the parameter identification (solid lines) together with the simulated TPR curves from model 1 in Table 4 (dashed lines).

the measurement ($F = 33$), although no model actually reaches or surpasses this threshold value. Judging solely by the sum of residuals squared, the first eight models can be considered to be of about equal fit. The optimum parameter sets can be reproduced by repeating the optimisation with different initial parameter values, so we expect that the optima shown here are global ones. However, this is just an indication of the solution being the global optimum. A sound proof of global optimality is beyond the scope of this contribution. To converge reliably and quickly, the optimisation algorithm requires appropriate initial parameter values. This requires the user to specify reference temperatures for each reaction and to roughly guess the corresponding oxygen capacities. Both can be estimated roughly from the TPR data diagrams. For the Damköhler and Arrhenius numbers as well as for the orders of reaction, average parameter values can be used.

In Fig. 7, the simulated curves of model no. 1 are plotted along with the measurement curves. The curves correspond fairly nicely, but the third peak which can be seen in the TPR curve at 20 K/min is not reflected by the model. The reason for this could be that this peak is small compared to the two other peaks and only occurs in one of the four TPR curves. The error caused by this qualitative inaccuracy of the model is small compared to others, so the first eight models do not show this third peak at all. The third peak appears in models no. 9 and 10 (not shown here), which in turn have a worse quantitative fit than other models.

The next issue that needs to be considered in the discussion of the models are the storage schemes. Some of the models in Table 4 (1, 2, 6, 7, 9, 10) simply show a three-step reduction, which can be interpreted as the classical three steps of iron oxide reduction. The other models have a different storage scheme which assumes that part of the iron oxide, possibly the finest particles, is reduced in a single step at low temperature. The bulk of the iron oxide, which is located on the surface and inside large particles, is reduced in two sequential reduction steps at higher temperatures.

Going more into the details of the reaction mechanism, models no. 9 and 10 assume that three reduction steps happen according to Avrami–Erofeev (or power law, respectively) followed by a diffusion-limited process and then again an Avrami–Erofeev step. It is not plausible why the third reaction should not be diffusion limited if the previous is dominated by mass transport inside the particles.

Concerning the parameter values, the activation energies are within a reasonable range. The third reaction shows a relatively low value, while the diffusion limited reactions in models 9 and 10 have a very high activation energy, which is typical for diffusion of atoms in metals. Most of the reaction order parameters are located at their minimum or maximum value. The oxygen capacities are similar for each model. The ratio between the first and the third oxygen capacity differs from what one would expect from the three possible iron oxide species (Fe_2O_3 , Fe_3O_4 , and FeO), which have a stoichiometric oxygen capacity ratio of 1:2:6. This indicates that the first peak is not merely the fast reduction of hematite (Fe_2O_3) to magnetite (Fe_3O_4), but some other fast reduction process, probably occurring at the finest particles of the fixed bed. The Damköhler numbers are not given here. Due to their definition (Eq. (31)), their values are at around 1, so discussion of this parameter yields no additional insights. Although some conclusions can be drawn from these results, it does not seem possible to clearly identify the actual reaction mechanism. Note that this is not necessarily a flaw of the modelling and optimisation procedure, but possibly in the TPR data. For example, if more TPR curves with high heating rate would be used instead of those with low temperature gradients, models showing a third peak would have been preferred. A better design of experiments could improve this situation, but probably the question for the reaction mechanism cannot be answered from TPR experiments alone.

A combination with other experimental techniques like TGA (thermogravimetric analysis) could help to discriminate between different reduction models. The modelling approach and the optimisation strategy proposed in this contribution can also be applied to TGA experiments.

Table 4
Ten best fitting models with three reactions

No	Scheme	Mechanism			Resid. squar.	Activ. energy (kJ/mol)			Reaction order			Oxygen cap.		
		R_1	R_2	R_3		$E_{A,1}$	$E_{A,2}$	$E_{A,3}$	m_1	m_2	m_3	Θ_1	Θ_2	Θ_3
1	•→•→•→○	AE	PL	AE	40.3	77	72	18	0.5	0.5	0.75	0.09	0.03	0.89
2	•→•→•→○	PL	PL	AE	40.6	92	72	18	0.5	0.5	0.75	0.10	0.03	0.90
3	•→○	AE	PL	AE	41.0	82	73	18	0.5	0.5	0.75	0.07	0.03	0.91
4	•→○	PL	PL	AE	42.0	94	76	20	0.5	0.54	0.75	0.09	0.03	0.91
5	•→○	AE	PL	PL	43.7	82	69	10	0.56	0.5	0.5	0.05	0.03	0.93
6	•→•→•→○	PL	PL	PL	44.0	91	68	11	0.5	0.5	0.5	0.08	0.03	0.91
7	•→•→•→○	AE	PL	PL	44.4	78	67	13	0.5	0.5	0.5	0.07	0.03	0.90
8	•→○	PL	PL	PL	44.6	96	69	11	0.5	0.5	0.5	0.07	0.03	0.93
9	•→•→•→○	AE	Diff.	AE	52.2	79	125	33	0.5	2.0	0.75	0.10	0.03	0.90
10	•→•→•→○	PL	Diff.	AE	52.6	96	125	33	0.5	2.0	0.75	0.11	0.03	0.90

The storage scheme, the reaction mechanisms, the sum of residuals squared and most parameter values are listed.

6. Conclusions

The example shows that the modelling approach for reduction processes via the oxygen storage concept allows to quickly and methodically establish a large number of models without *a priori* knowledge about reaction mechanisms and the topochemical behaviour of the specific metal oxide. It not only simplifies the modelling, but it also allows to survey a broad and exhaustive range of models, including non-intuitive models, which can show a good fit to experimental data and can be interpreted by physical and chemical means.

The parameters of the numerous models are fitted to experimental data by a specially tailored optimisation algorithm. It takes advantage of the special structure of the problem by allowing to optimise the parameters of single reactions alone or to simultaneously treat the parameters of all reactions. In the demonstrated example, the cumulative computation time was about 10h, which is significantly lower than the time required for the TPR measurements.

No statistical analysis of the optimisation results is presented here. This is because the standard methods like test of parameter significance or model discrimination are not suited for this type of problem. Nevertheless, repeated measurements provide an estimate of typical measurement errors and this serves as an orientation for the quality of a model fit.

The result of the method is not a single mechanism together with a set of parameters, but a whole list of well fitting models. The number of these strongly depends on the experimental data, whether it allows to discriminate different models or not. Some of the good models can be rejected due to unlikely parameter combinations, lack of interpretation or impossible combinations of reaction mechanisms. However, usually a certain number of well fitting and interpretable models will remain, which can be used further on.

A clear and unambiguous identification of reaction mechanisms can probably not be based on TPR alone. Here, additional

measurement techniques must be included like chemical analysis or other dynamic experiments. The proposed modelling approach and optimisation algorithm is not restricted to TPR measurements, but can also be applied to other dynamic measurement techniques like the isothermal thermogravimetric analysis (TGA). An extension of this method to a combined analysis of TPR and TGA data could help to further discriminate between different models and to increase the precision of the estimated parameters.

Notation

A	surface area in the reactor, m ²
Arr_j	Arrhenius number; Dim-less activation energy, dimensionless
B	heating rate of the TPR experiment, K/s
C_i	surface related oxygen capacity of component i , mol/m ²
C_t	surface related total oxygen capacity, mol/m ²
Da_j	Damköhler number; Dim-less reaction rate constant, dimensionless
$E_{A,j}$	activation energy, J/mol
$f_j(x)$	concentrations dependence of reaction rate, dimensionless
$F(p)$	sum of squares of errors, dimensionless
$g(x, p)$	right-hand side of model ODEs, dimensionless
\bar{G}	molar flow, mol/s
\bar{G}	dim-less molar flow rate, dimensionless
$h(x, p)$	right-hand side of output equation, dimensionless
J	Jacobian of the output concentration, dimensionless
J_x	Jacobian of the model ODEs, dimensionless
$k_{0,j}$	reaction rate constant, mol/m ² s
m_j	reaction order, dimensionless
n_i	surface related amount of component i , mol/m ²

$n_{i,\max}$	maximum amount possible of component i , mol/m ²
p_{\min}, p_{\max}	minimum/maximum parameter value, dimensionless
Δp	dim-less parameter change in optimisation algorithm, dimensionless
P	vector of model parameters, dimensionless
r_j	reaction rate, mol/m ² s
R	gas constant, J/mol K
t	time, s
T	temperature, K
x_i	molar fraction, dimensionless
x_{out}	measured output concentration, dimensionless
$x_{\text{out, meas}}$	
$x_{\text{out, sim}}$	simulated output concentration, dimensionless
$X(p)$	deviation between simulation and measurement, dimensionless

Greek letters

α_i	degree of reduction, dimensionless
β	dim-less heating rate, dimensionless
Θ_j	dim-less oxygen capacity, dimensionless
$\tilde{\Theta}_j$	dim-less ox. cap. related to reaction j , dimensionless
λ	Marquardt number, dimensionless
$v_{i,j}^S$	stoichiometric coefficients of solid component, dimensionless
$v_{k,j}$	stoichiometric coefficients of gas components, dimensionless
\bar{v}_j	change in gas mole numbers due to reaction, dimensionless
ρ_j	dim-less reaction rate, dimensionless
τ	dim-less time, dimensionless
ϑ	dim-less temperature, dimensionless
ϑ_j^{ref}	dim-less reference temperature of reaction j , dimensionless

Subscripts

i	solid component/storage
j	reaction
K	gas component
t	total
0	start of TPR measurement

Superscript

θ	standard values
----------	-----------------

Acknowledgements

The authors would like to thank Dipl.-Ing. Matthias Pfaffrodt for many hours of enlightening discussion on statistical and numerical methods.

Appendix A

A.1. Normalisation of the output concentration profile

The following can be proven for a general case, but for sake of clarity it is demonstrated for the example in Section 2.2

(Fig. 2). The integral of the output concentration over the whole experiment time should be normalised to unity:

$$\int_0^\infty x_{\text{out}} d\tau = 1. \quad (37)$$

For the chosen example, Eq. (13) reads ($\dot{z} = dz/d\tau$)

$$\begin{aligned} \dot{\alpha}_I &= \frac{Da_1 \rho_1}{\Theta_I}, \\ \dot{\alpha}_{II} &= \frac{Da_2 \rho_2}{\Theta_{II}}, \\ \dot{\alpha}_{III} &= \frac{Da_3 \rho_3}{\Theta_{III}} - \frac{Da_2 \rho_2}{\Theta_{II}} = \frac{Da_3 \rho_3}{\Theta_{III}} - \dot{\alpha}_{II} \end{aligned} \quad (38)$$

with the initial conditions from Eq. (16). At the end of the TPR,

$$\alpha_I(\tau = \infty) = \alpha_{II}(\tau = \infty) = \alpha_{III}(\tau = \infty) = 1. \quad (39)$$

Inserting Eq. (23) into Eq. (37), and rearranging the integral expression using the balance equations (Eq. (38)), this yields

$$\begin{aligned} \int_0^\infty x_{\text{out}} d\tau &= \frac{1}{G} \int_0^\infty Da_1 \rho_1 + Da_2 \rho_2 + Da_3 \rho_3 d\tau \\ &= \frac{1}{G} \int_0^\infty \Theta_I \dot{\alpha}_I + \Theta_{II} \dot{\alpha}_{II} + \Theta_{III} (\dot{\alpha}_{III} + \dot{\alpha}_{II}) d\tau \\ &= \frac{1}{G} [\Theta_I \cdot (1 - 0) + \Theta_{II} \cdot (1 - 0) \\ &\quad + \Theta_{III} \cdot (1 - 1 + 1 - 0)] \\ &= \frac{1}{G} [\Theta_I + \Theta_{II} + \Theta_{III}]. \end{aligned} \quad (40)$$

With Eqs. (5) and (9),

$$\sum_i \Theta_i = 1 \quad (41)$$

and thus

$$\tilde{G} = 1.$$

A.2. Jacobian matrix of the TPR model

The model ODE (Eq. (13)) and the equation for the output concentration (Eq. (23)) can be noted as ($\dot{z} = dz/d\tau$):

$$\begin{pmatrix} \dot{z} - g(z, p) \\ x_{\text{out}} - h(z, p) \end{pmatrix} = \begin{pmatrix} 0 \\ 0 \end{pmatrix}. \quad (42)$$

The required Jacobian is the derivative of the deviation between simulation and measurement, $X(p)$, (Eq. (34)) with respect to the model parameters:

$$J = \frac{\partial X}{\partial p} = \frac{\partial x_{\text{out}}}{\partial p} - \frac{\partial x_{\text{meas}}}{\partial p} = \frac{\partial x_{\text{out}}}{\partial p}. \quad (43)$$

It can be derived in the following way. Set up the total derivative of Eq. (42) with respect to the parameters:

$$\begin{aligned} \frac{\partial}{\partial x} \left(\frac{\dot{x} - g}{x_{\text{out}} - h} \right) \cdot \frac{\partial \dot{x}}{\partial p} + \frac{\partial}{\partial x} \left(\frac{\dot{x} - g}{x_{\text{out}} - h} \right) \cdot \frac{\partial x}{\partial p} \\ + \frac{\partial}{\partial p} \left(\frac{\dot{x} - g}{x_{\text{out}} - h} \right) \cdot \frac{\partial p}{\partial p} + \frac{\partial}{\partial x_{\text{out}}} \left(\frac{\dot{x} - g}{x_{\text{out}} - h} \right) \cdot \frac{\partial x_{\text{out}}}{\partial p} \\ = \begin{pmatrix} 0 \\ 0 \end{pmatrix}. \end{aligned} \quad (44)$$

Introducing the Jacobian of the ODE system

$$J_{\text{ODE}} = \frac{\partial \dot{x}}{\partial p}, \quad \dot{J}_{\text{ODE}} = \frac{\partial \dot{\dot{x}}}{\partial p} \quad (45)$$

and evaluating the derivations leads to

$$\begin{aligned} \begin{pmatrix} 1 \\ 0 \end{pmatrix} \cdot \dot{J}_{\text{ODE}} + \begin{pmatrix} -g_x \\ -h_x \end{pmatrix} \cdot J_{\text{ODE}} + \begin{pmatrix} -g_p \\ -h_p \end{pmatrix} + \begin{pmatrix} 0 \\ 1 \end{pmatrix} \cdot J \\ = \begin{pmatrix} 0 \\ 0 \end{pmatrix}. \end{aligned} \quad (46)$$

After short manipulation the result is

$$\begin{aligned} \dot{J}_{\text{ODE}} &= g_x \cdot J_{\text{ODE}} + g_p, \\ J &= h_x \cdot J_{\text{ODE}} + h_p \end{aligned} \quad (47)$$

with the initial condition

$$J_{\text{ODE}}(\tau = 0) = 0. \quad (48)$$

The ODE system in Eq. (47) can be solved together with the model equations by numerical integration. The required Jacobian can then be calculated from the results. The partial derivatives of the model ODEs with respect to the states and the parameters, g_x and g_p , respectively, and the derivatives of the output concentration, h_x and h_p , can be derived analytically. For sake of brevity, they are not given here in detail.

References

- Caracotsios, M., Stewart, W.E., 1985. Sensitivity analysis of initial value problems with mixed ODEs and algebraic equations. *Computers & Chemical Engineering* 9, 359–365.
- Doyle, C.D., 1961. Kinetic analysis of thermogravimetric data. *Journal of Applied Polymer Science* 5 (15), 285–292.

- Edgar, T.F., Himmelblau, D.M., 2001. *Optimization of Chemical Processes*, second ed. McGraw-Hill, New York.
- Fletcher, R., 2000. *Practical Methods of Optimization*, second ed. Wiley, New York.
- Galvita, V., Sundmacher, K., 2007. Redox behaviour and reduction mechanism of $\text{Fe}_2\text{O}_3\text{-CeZrO}_2$ as oxygen storage material. *Journal of Materials Science* 42 (22), 9300–9307.
- Hacker, V., 2003. A novel process for stationary hydrogen production: the reformer sponge iron cycle (RESC). *Journal of Power Sources* 118 (1–2), 311–314.
- Hu, Y., Jin, H., Liu, J., Hao, D., 2000. Reactive behaviors of iron-based shift catalyst promoted by ceria. *Chemical Engineering Journal* 78, 147–152.
- Hurst, N.W., Gentry, S.J., Jones, A., 1982. Temperature programmed reduction. *Catalysis Reviews* 24 (2), 233–309.
- Joshi, M., Kreming, A., Seidel-Morgenstern, A., 2006. Model based statistical analysis of adsorption equilibrium data. *Chemical Engineering Science* 61, 7805–7818.
- Kanervo, J.M., Krause, A.O.I., 2001. Kinetic analysis of temperature-programmed reduction: behavior of a $\text{CrO}_x/\text{Al}_2\text{O}_3$ catalyst. *Journal of Physical Chemistry* 105, 9778–9784.
- Kissinger, H.E., 1957. Reaction kinetics in differential thermal analysis. *Analytical Chemistry* 29 (11), 1702–1706.
- Lambrou, P.S., Efstathiou, A.M., 2006. The effects of Fe on the oxygen storage and release properties of model Pd-Rh/CeO₂-Al₂O₃ three-way catalyst. *Journal of Catalysis* 240, 182–193.
- Li, K., Peng, J.-X., Bai, E.W., 2006. A two-stage algorithm for identification of nonlinear dynamic systems. *Automatica* 42, 1189–1197.
- Maria, G., 2004. A review of algorithms and trends in kinetic model identification for chemical and biochemical systems. *Chemical & Biochemical Engineering Quarterly* 18 (3), 195–222.
- Messerschmitt, A., 1911. Verfahren zur Erzeugung von Wasserstoff durch abwechselnde Oxidation und Reduktion von Eisen in von außen beheizten, in den Hitzeraumen angeordneten Zersettern. German Patent DE 266863.
- Pineau, A., Kanari, N., Gaballah, I., 2006. Kinetics of reduction of iron oxides by H_2 . Part I: low temperature reduction of hematite. *Thermochimica Acta* 447, 89–100.
- Šesták, J., Šastava, V., Wendland, W.W., 1973. The study of heterogeneous processes by thermal analysis. *Thermochimica Acta* 7, 333–556.
- Tieman, M.J., Barnes, P.A., Parkes, G.M.B., 2001. Reduction of iron oxide catalysts: the investigation of kinetic parameters using rate perturbation and linear heating thermoanalytic techniques. *Journal of Physical Chemistry* 105, 220–228.
- van den Berg, F.R., Crajé, M.W.J., van der Kraan, A.M., Geus, J.W., 2003. Reduction behaviour of Fe/ZrO_2 and Fe/K/ZrO_2 Fischer-Tropsch catalysts. *Applied Catalysis A: General* 242, 403–416.
- Vyzovkin, S., Wight, C.A., 1997. Kinetics in solids. *Annual Reviews of Physical Chemistry* 48, 125–149.
- Wimmers, O.J., Arnoldy, P., Mouljin, J.A., 1986. Determination of the reduction mechanism by temperature-programmed reduction: application to small Fe_2O_3 Particles. *Journal of Physical Chemistry* 90 (7), 1331–1337.

[PH 2]

P. Heidebrecht, C. Hertel, K. Sundmacher

Conceptual Analysis of a Cyclic Water Gas Shift Reactor

Int. Journal of Chemical Reaction Engineering 6 (2008),
A19

INTERNATIONAL JOURNAL OF CHEMICAL REACTOR ENGINEERING

Volume 6

2008

Article A19

Conceptual Analysis of a Cyclic Water Gas Shift Reactor

Peter Heidebrecht*

Christoph Hertel[†]

Kai Sundmacher[‡]

*Max-Planck-Institute for Dynamics of Complex Technical Systems, heidebrecht@mpi-magdeburg.mpg.de

[†]Max-Planck-Institute for Dynamics of Complex Technical Systems, hertel@mpi-magdeburg.mpg.de

[‡]Max-Planck-Institute for Dynamics of Complex Technical Systems & Otto-von-Guericke University, sundmacher@mpi-magdeburg.mpg.de

ISSN 1542-6580

Copyright ©2008 The Berkeley Electronic Press. All rights reserved.

Conceptual Analysis of a Cyclic Water Gas Shift Reactor

Peter Heidebrecht, Christoph Hertel, and Kai Sundmacher

Abstract

The cyclic water gas shift reactor (CWGSR) is based on the repeated reduction of a fixed bed using a mixture of hydrogen and carbon monoxide and its subsequent oxidation with steam to produce pure hydrogen. The reactor is analyzed on a conceptual level using a spatially distributed, dynamic model. The model assumptions and the resulting model equations are presented, and important parameters are discussed. Simulation results show that the CWGSR reactor has a poor performance for co-flow configuration of the gases during reduction and oxidation phase, but the reverse-flow configuration seems to be a very attractive option. Parameter variation of the duration of the reduction phase indicates that especially short cycling times not only yield high energetic performance, but they also decrease thermal and morphological stress on the fixed bed material. In addition, the counter-flow CWGSR with short cycling times shows an inherent heat integration like in a Matros reactor, which opens attractive options for system integration of this reactor with other process steps. The behavior of the CWGSR is compared to a pressure swing adsorption reactor (PSA), which shows common features, but also significant differences between both types of cyclic fixed bed reactors.

KEYWORDS: cyclic operation, fixed bed reactor, water gas shift reaction, mathematical model

1. Introduction

A number of actual and future applications require carbon monoxide free hydrogen. Carbon monoxide is a strong catalyst poison, especially for noble catalysts, limiting its tolerable concentration in low temperature fuel cells like the PEMFC (Polymer electrolyte membrane fuel cells, using Platinum electrodes) to 10 ppm. The production of hydrogen was and is still mainly based on fossil fuels like gas, oil and coal and – to a small, but steadily increasing part – from biomass. Apart from the energy intensive Kvaerner process (Lynum et al, 1999), which is restricted to gaseous educts, gasification and reformation processes are applied which usually deliver a mixture of hydrogen, carbon monoxide and carbon dioxide. The cleaning of these gas mixtures from carbon monoxide is usually done via the water gas shift reaction:



Depending on the desired purity level, this process usually comprises several steps like high and low temperature shift reactors, pressure swing adsorption or others. This often leads to a considerable effort for the cleaning process with energetic losses and high investment costs. A simplification of the cleaning process in one single reactor could provide a breakthrough for many energetic and chemical applications. The cyclic water gas shift reactor (CWGSR) could be a solution to this problem.

The water gas shift reaction is a redox reaction, where the carbon within the carbon monoxide is oxidized and the hydrogen within the water molecules is reduced. The principle of the CWGSR is the temporal separation of the two parts of this redox reaction. This is achieved with the help of a fixed bed of some metal oxide, preferably iron oxide (Figure 1). At first, a gas mixture containing carbon monoxide – and possibly hydrogen, if the gas originates from a reforming reactor – is fed into the reactor, reducing the iron oxide. During this, carbon dioxide and water are produced:

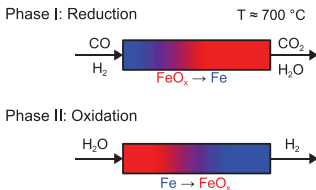
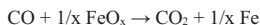


Figure 1. Principle of the cyclic water gas shift reactor (CWGSR).

After a while, when the bed is reduced to a sufficient extent, the feed is switched to steam, which then oxidizes the iron to iron oxide, producing pure hydrogen without contaminants like carbon monoxide at the outlet of the reactor:



The CWGSR, which is sometimes referred to as sponge iron process, can be compared to other cyclic processes such as a conventional fixed bed reactor or a pressure swing adsorption process. In a fixed bed reactor (e.g. Glöckler et al., 2003; Kulkarni and Dudukovic, 1998), the gas flows through porous solid material, which acts as catalyst and as heat storage. Usually, the heat capacity of the fixed bed is much larger than that of the gas inside the reactor, so in addition to the gas composition, which can change very quickly in a fixed bed reactor, the reactor temperature is the important state variable, dominated by a large time constant. In the CWGSR, the fixed bed also serves as an oxygen storage. The degree of reduction, which describes the oxygen content of the fixed bed, determines the reaction rates in the reactor and is thus the second important state variable. As with the heat storage, the oxygen capacity of the fixed bed is significantly higher than the capacity of the gas, so this state variable is also dominated by a large time constant.

Another process similar to the CWGSR is the pressure swing adsorption (PSA, e.g. Malek and Farooq, 1998; Sircar and Golden, 2000). In addition to temperature, which can play an important role in this process, the coverage of the adsorbed species is a second, slow state variable, influencing the adsorption kinetics. Pressure is an important state in PSA, but it is governed by a very low time constant and is not related to the fixed bed. Although the fixed bed in PSA has two state variables (temperature and coverage), it is still different from the CWGSR. In PSA, one or more gas components are adsorbed from the gas stream and the phase is ended before the bed is saturated with these components and they eventually break through. In the desorption phase the focus is to desorb the components again by an auxiliary gas stream. The quality of the output gases during this phase or the phase duration is only of secondary importance. In the CWGSR, the desorption phase corresponds to the reduction phase, where the valuable fuel gas is consumed to reduce the fixed bed. Gas utilization and phase duration are highly important during this phase.

With this in mind, it is evident that although the CWGSR shares some aspects with conventional fixed bed or pressure swing adsorption processes, it has its own unique characteristics which need to be understood for a thorough process design. Although the process idea is not new (Messerschmitt, 1911; Hacker et al., 1998; Hacker et al., 2000), the system has not yet been analyzed on a conceptual level. The aim of this analysis is to give some understanding of the basic behavior of this reactor and to draw some relevant conclusions for the reactor design rather than going into the details of reaction kinetics, mass and heat transfer. Therefore,

a model is set up which neglects a number of aspects like thermodynamic equilibria and complex kinetics in order to capture the very basic behavior of the CWGSR. This model is then used to evaluate suitable operating modes and conditions.

2. Dimensionless model

For a conceptual analysis of the CWGSR a transient, spatially one-dimensional model is sufficient. Simplifying assumptions are set up (see section 2.1) to describe representative gas phase concentrations, flow rates and temperatures (section 2.2). All model equations are then expressed in terms of dimensionless parameters, so a very general description is obtained which can be applied to a CWGSR of any size (section 2.3). The values of the most important model parameters are given at the end of this chapter (section 2.4).

2.1 Model assumptions

The model is derived under the following assumptions:

- The reactor has a constant cross sectional area. Its length is much higher than its width. The two phases (gas phase and solid fixed bed material) occupy constant volume fractions within the reactor. Heat exchange with the environment across the reactor walls is considered by a linear approach.
- The gas is assumed to be ideal. Friction forces and gravity are neglected. Isobaric conditions are applied. Due to the fixed bed, plug flow is assumed. Due to high gas velocities, axial diffusion and heat conduction in the gas phase are neglected.
- The fixed bed material consists of two components: reduced and oxidized species. The relative amount of these is described by the degree of reduction. Changes of the properties of the fixed bed material due to reduction or oxidation are neglected. A constant axial heat conductivity is assumed.
- The reduction and oxidation reactions are of 1st order with respect to the gas concentrations and the degree of reduction of the fixed bed. Mass transport is not explicitly considered.
- The kinetics of heat exchange between solid and gas are very fast, so a pseudo homogeneous enthalpy balance for both phases is used.

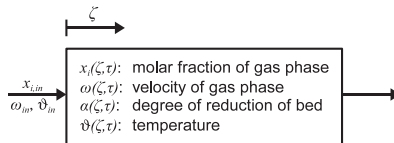


Figure 2. Scheme of the model of the CWGSR. States at the gas inlet and inside the reactor are indicated.

2.2 Dimensional equations

Given the assumptions listed above, one can derive a spatially one-dimensional model. In the gas phase, two states are of interest: the gas velocity and the gas compositions, described here in terms of molar fractions. The gas compositions are given by the following transient partial differential equation:

$$c_i \varepsilon \cdot \frac{\partial x_i}{\partial t} = -c_i \varepsilon \cdot v \cdot \frac{\partial x_i}{\partial z} + (1 - \varepsilon) \cdot a \cdot \sum_j (v_{i,j} - x_i \bar{v}_j) \cdot r_j \quad (1)$$

With the accumulation term on the left hand side of the equation, the first term on the right hand side can be identified as the convective term along the reactor axis. The last term considers the change in concentrations due to reaction and due to non-equimolar reactions (which do not occur in this specific example). The total gas concentration is computed according to the ideal gas law. This equation requires an initial condition for the molar fractions and a boundary condition, which is given by the gas composition at the gas inlet of the reactor (Figure 2).

The total mass balance in combination with the ideal gas law and the isobaric assumption yields the following equation which can be used to calculate the gas velocity:

$$0 = -\frac{\partial v}{\partial z} + \frac{1 - \varepsilon}{\varepsilon} \cdot \frac{a}{c_i} \cdot \sum_j \bar{v}_j \cdot r_j + \frac{1}{T} \cdot \frac{\partial T}{\partial t} + \frac{v}{T} \cdot \frac{\partial T}{\partial z} \quad (2)$$

The second term considers the effect of non-equimolar reactions on the gas velocity, while the last two terms account for temperature effects, for example gas expansion due to increasing temperature. The only boundary condition required to solve this equation is given by the gas velocity at the reactor inlet.

In addition to the gas phase equations, the fixed bed needs to be described. The following ordinary differential equation is a molar mass balance of the reduced metal species and takes into account the reduction and oxidation reactions:

$$\frac{\partial c_{Fe}^a}{\partial t} = \sum_j v_{Fe,j} r_j \quad (3)$$

Only an initial condition for the concentration of the reduced species is required.

The pseudo-homogeneous enthalpy balance assumes that the temperatures of both gas and solid are identical:

$$(1-\varepsilon)c_p^s \frac{\partial T}{\partial t} = -\varepsilon v c_p^g \frac{\partial T}{\partial z} + (1-\varepsilon)\lambda \frac{\partial^2 T}{\partial z^2} + (1-\varepsilon)a \sum_j (-\Delta_r h_j^0) r_j + \frac{2}{R_r} k^h \cdot (T_e - T) \quad (4)$$

The accumulation term contains the heat capacity of the fixed bed material, whereas the capacity of the gas phase is neglected. The convection term only considers heat transport in the gas phase, while the second derivative describes the heat conduction in the fixed bed material according to Fourier's law. The third term accounts for the heats of reaction and the last term stands for the heat exchange with the environment across the reactor walls. This equation requires the reactor temperature profile as initial condition. The two required boundary conditions are given by the gas temperature at the reactor inlet and a zero temperature gradient at the opposite end of the reactor.

2.3 Dimensionless equations

With the dimensional equations listed above and the definitions of the dimensionless parameters (see notation table), the following set of equations forms the dimensionless model equations:

$$\frac{\partial x_i}{\partial \tau} = -\omega \frac{\partial x_i}{\partial \zeta} + \vartheta \cdot \sum_j (v_{i,j} - x_i \bar{v}_j) \cdot Da_j \cdot R_j \quad (5)$$

$$0 = -\frac{\partial \omega}{\partial \zeta} + \vartheta \cdot \sum_j \bar{v}_j \cdot Da_j \cdot R_j + \frac{1}{\vartheta} \cdot \frac{\partial \vartheta}{\partial \tau} + \frac{\omega}{\vartheta} \cdot \frac{\partial \vartheta}{\partial \zeta} \quad (6)$$

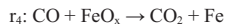
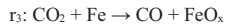
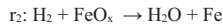
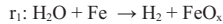
$$\Theta \cdot \frac{\partial \alpha}{\partial \tau} = \sum_j v_{Fe,j} Da_j R_j \quad (7)$$

$$\Psi \cdot \frac{\partial \vartheta}{\partial \tau} = -\omega \cdot \frac{\partial \vartheta}{\partial \zeta} + \frac{1}{Pe} \cdot \frac{\partial^2 \vartheta}{\partial \zeta^2} + \Psi \cdot \sum_j \Delta \vartheta_{ad,j} \cdot Da_j R_j - St \cdot (\vartheta - \vartheta_e) \quad (8)$$

Note that the dimensionless temperature occurs as a factor in Eqs. 5 and 6, where it replaces the reciprocal total gas concentration, c_t . The temperature, ϑ , is the dimensional temperature divided by a typical CWGSR temperature. The gas velocity, ω , is the dimensional velocity related to a typical gas velocity at the reactor inlet. With this definition, both variables are in the order of magnitude of 1.

Reaction rates are required for the reactions of carbon monoxide to carbon dioxide and of hydrogen to water. They include an Arrhenius term to account for

the temperature dependence of the reaction rates. The kinetics usually are assumed to be of first order with respect to each gas concentration, but this reaction order can be varied. The following reactions are considered:



$$R_1 = \exp \left(\gamma_1 \cdot \left(1 - \frac{1}{9} \right) \right) \cdot x_{\text{H}_2\text{O}}^{n_1} \cdot \alpha \quad (9)$$

$$R_2 = \exp \left(\gamma_2 \cdot \left(1 - \frac{1}{9} \right) \right) \cdot x_{\text{H}_2}^{n_2} \cdot (1 - \alpha) \quad (10)$$

$$R_3 = \exp \left(\gamma_3 \cdot \left(1 - \frac{1}{9} \right) \right) \cdot x_{\text{CO}_2}^{n_3} \cdot \alpha \quad (11)$$

$$R_4 = \exp \left(\gamma_4 \cdot \left(1 - \frac{1}{9} \right) \right) \cdot x_{\text{CO}}^{n_4} \cdot (1 - \alpha) \quad (12)$$

The ratios Da_1/Da_2 and Da_3/Da_4 can be interpreted as some kind of equilibrium constants, although this is not strictly applicable in gas-solid reactions.

2.4 Model parameters

Among the most important parameters in this model are the reaction specific Damköhler numbers, Da . Their magnitude is a measure for the reactor size relative to the inlet gas flow. The ratio between two Damköhler numbers is the relative activity of the fixed bed material with respect to the two reactions. As the size of the reactor is not yet fixed, the Damköhler numbers can be chosen arbitrarily for each simulation. However, preliminary experiments conducted with a differential reactor with a fixed bed material based on $\text{Fe}_2\text{O}_3\text{-CeO}_2$ (Figures 3a and 3b, from Galvita and Sundmacher, 2007) indicate that the reduction with H_2 (reaction 2, Figure 3a) is about 3 to 5 times slower than the oxidation using H_2O (reaction 1, Figure 3b). This fact should be reflected by the ratio of the Damköhler numbers Da_1 and Da_2 .

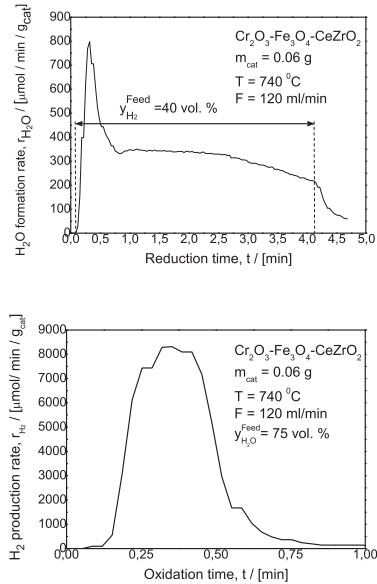


Figure 3. Experimental data from a reduction (top) and oxidation (bottom) of a small sample of $\text{Fe}_2\text{O}_3\text{-CeO}_2$ with H_2 and H_2O , respectively. The reduction is about 3 times slower than the oxidation. From Galvita and Sundmacher, 2007.

Concerning the values of the Damköhler numbers, the breakthrough behavior of the reactor is essential. Ideally, a breakthrough of contaminated hydrogen during the reduction phase should only occur after the complete fixed bed has been fully reduced. At that time, the feed streams would be switched and the oxidation phase would begin. Only for Damköhler numbers approaching infinity the CWGSR would show such behavior. For very low Damköhler numbers, only a small portion of the contaminated hydrogen would be utilized to reduce the fixed bed, the rest of the gas would be lost for the process. Thus, high Damköhler numbers are preferred. In the simulations in this work, we generally apply $Da_1=50$ and $Da_2=15$, which takes into account the ratio between both reaction rates and which is a compromise between ideal reactor behavior and limited reactor size.

Besides the Damköhler numbers, four important parameters can be identified, two of them are capacities. The substantial fixed bed capacity, Θ , is the ratio between the oxygen capacity of the fixed bed and the gas hold up of the reactor. Due to the low density of gas under ambient pressure and at high temperature, and due to the high oxygen capacity of the fixed bed material, this ratio is at about 10^3 . The thermal capacity, Ψ , relates the heat capacity of the fixed bed to the heat capacity of the gas phase, and is at about 10^4 . This means that Equations (7) and (8) are governed by large time constants and change fairly slowly compared to the gas composition, which has a time constant of 1.

Further parameters are the dimensionless heats of reaction, $\Delta \vartheta_{ad,j}$, which are the negative reaction enthalpy divided by the heat capacity of the gas phase and the standard temperature. For the oxidation of H_2 (reaction 2), this is $-6 \cdot 10^{-5}$, while for the oxidation of CO (reaction 4) its value is $4 \cdot 10^{-5}$. The heats of reaction 1 and 3 have the same absolute values, but different signs ($+6 \cdot 10^{-5}$ and $-4 \cdot 10^{-5}$). Although these values seem negligible, note that they are always multiplied with the dimensionless heat capacity, Ψ , which is rather large. To consider the temperature effect on the reaction rate, Arrhenius numbers, γ_j , are introduced. They are defined as activation energies divided by the gas constant and the standard temperature. With a standard temperature of 1000 K and an estimated activation energy of 70 kJ/mol, the Arrhenius numbers are at about 8.4. The Arrhenius numbers are assumed to be identical for all reactions, as kinetic experiments are currently being conducted and no reliable values are available in the literature for the considered reactions.

3. Isothermal simulations

In the simulations of this chapter, Equation (8) is not used, but isothermal conditions ($\vartheta = \text{const.}$) are applied. In addition, carbon monoxide is not explicitly considered here during the reduction phase. The only effect of considering carbon monoxide would be that the whole reaction would be exothermic, which is irrelevant in case of an isothermal model. Nevertheless, the hydrogen which is fed into the reactor during the oxidation phase is considered contaminated. The inlet velocities are always $\omega_{in} = \pm 1$, depending on the flow direction.

The duration of the reduction phase can be fixed arbitrarily. In the simulations shown, this duration was chosen long enough to reduce a major part of the fixed bed, which was the case with $\tau_{\text{reduction}} = 2000$. The duration of the oxidation phase was determined using a quality specification of the hydrogen product. As soon as the hydrogen concentration in the product stream dropped below 90 mol-%, the oxidation phase was stopped and the reduction phase was initiated.

The simulation results show the cyclic steady state, i.e. the repeating cycle which the system attains after a sufficient number of cycles. Starting with arbitrarily chosen initial conditions (no reactants inside the channel, fully oxidized fixed

bed), only three to five cycles were necessary to bring the isothermal simulations with long cycle durations into a cyclic steady state.

3.1 Co-flow operation

At the beginning of the oxidation phase, the fixed bed is virtually completely reduced and steam is fed into the reactor on the left hand side. Most of the steam is converted to hydrogen. Due to the high Damköhler number of the dominant reaction, Da_1 , the reaction proceeds in a front-like shape along the reactor (Figure 4). With time, this front moves along the reactor and eventually reaches its right end. When this happens, the hydrogen concentration in the output stream decreases below the given limit and the reduction phase is initiated.

At the end of the oxidation phase, most of the fixed bed is completely oxidized, but a considerable amount near the right hand side of the reactor is still in a reduced state (see the red curves in Figure 4, right). With this fixed bed, the reduction phase is initiated by feeding contaminated hydrogen into the left end (Figure 5, left). This hydrogen is converted to steam, whereby the reduction degree of the fixed bed is rising near the inlet. Towards the reactor's end, the produced steam meets the reduced fixed bed, so oxidation occurs near the reactor outlet (see both Figures 5). Due to this, the reactor produces contaminated hydrogen, which must be considered as lost fuel gas for the process.

To avoid the losses at the reactor's rear end, the fixed bed there must be oxidized. This can be realized by extending the oxidation phase duration. In that case, the hydrogen concentration at the output would decrease quickly and approach zero. The changing hydrogen concentration may pose a problem for the following processes, but even if not, extending the oxidation phase brings losses in steam and costs time, reducing the efficiency of the process and its production capacity per time.

If not during an extended oxidation phase, the fixed bed near the reactor outlet is reduced after sufficient time during the reduction phase. However, the oxidation occurring during the reduction phase is a clear sign of inefficiency. This can also be seen figuratively in the profiles of the reduction degree at the beginning of each phase. While $\alpha(\zeta)$ increases along the reactor coordinate at the end of the oxidation phase (Figure 4, right), it has a falling slope at the end of the reduction phase (Figure 5, right). The necessary inversion of this profile during each phase can be interpreted as the reason for losses in the feed gas.

Furthermore, notice that the reduction does not proceed in a sharp front, but the concentration profiles show a distinct slope. This is due to the lower Damköhler number of the prevailing reaction, Da_2 . Thus a considerable amount of contaminated feed gas is lost in order to obtain a high degree of reduction throughout the reactor.

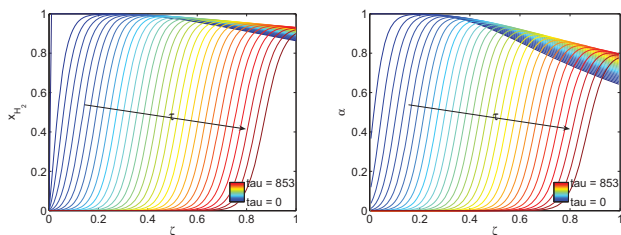


Figure 4. Molar fraction of hydrogen (reaction product, left) and degree of reduction (right) in a co-flow CWGSR during the oxidation phase. Hydrogen is produced in a moving front and the fixed bed material is oxidized from left to right.

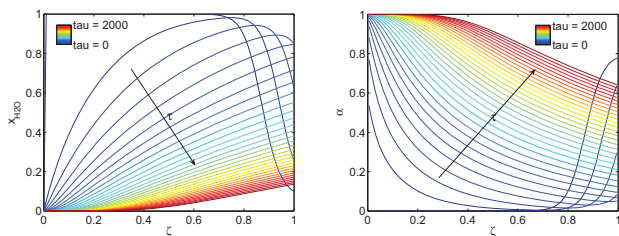


Figure 5. Molar fraction of water (reaction product, left) and degree of reduction (right) in a co-flow CWGSR during reduction phase. In the beginning ($\tau=0$) in the rear end ($\zeta=1$), water is consumed and the bed is oxidized. The hydrogen produced therein can not be used and is lost.

Gas losses are also known from pressure swing adsorption reactors (PSA). However, there are certain differences between the CWGSR and PSA. Considering a PSA for the removal of CO from a reformat gas, the adsorption phase in the PSA is comparable to the oxidation phase in the CWGSR, and the free adsorption surface is the analogue of the degree of reduction. The duration of the adsorption and oxidation phase are both determined by the exhaustion of the fixed bed. In the PSA desorption phase, a sweep gas is used to clean the fixed bed under reduced pressure. Inefficiencies due to co-flow configuration cost additional time and sweep gas, which is an auxiliary component. In the case of CWGSR, this causes losses in valuable fuel gas. This difference has its impact on the operation of a CWGSR.

3.2 Reverse-flow operation

The drawbacks of the co-flow CWGSR are amended under reverse-flow operation, that is if the gas flow direction is reversed during the oxidation phase. Figure 6 shows the profiles of the steam concentration and the degree of reduction during the reduction phase, which are monotonous throughout the whole phase. The advantage of reverse-flow operation is also emphasized in Figure 7, where the outlet concentrations are shown for both modes of operation. The red dashed line shows again that after the reduction phase has begun, a considerable amount of hydrogen leaves the reactor due to the non-oxidized end of the fixed bed. In opposite to that, the profile for reverse-flow not only shows a favorably high hydrogen concentration during the oxidation phase, but it also has a fast transition at the switching time from oxidation to reduction phase. These two aspects make the reverse-flow operation superior to co-flow operation mode.

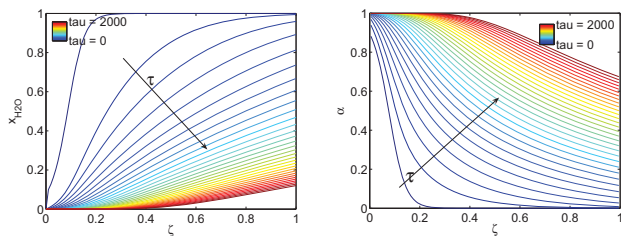


Figure 6. Molar fraction of water (reaction product, left) and degree of reduction (right) in a reverse-flow CWGSR during the reduction phase.

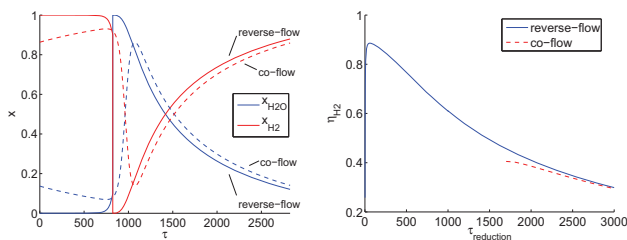


Figure 7. Output concentrations in co-flow (dashed lines) and reverse-flow (full lines) operation modes. The reverse-flow configuration produces higher concentration of hydrogen and shows less losses of combustible gases.

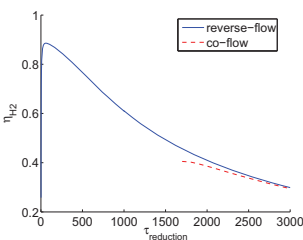


Figure 8. Energetic efficiencies for co- and reverse-flow operation as a function of the duration of the reduction phase.

These qualitative findings are not depending on the chosen reaction kinetics. Although the actual curves look different, other orders of reactions with respect to the gas phase and to the degree of reduction show the same basic behavior for co-flow and reverse-flow. Thus the reverse-flow is preferable over co-flow independent of the real kinetics in the CWGSR.

3.3 Efficiency and cycling duration

The CWGSR is meant to be used in electric power plants based on fuel cells. Therefore, one of the most important issues is the efficiency of the CWGSR. Defining the efficiency as the total amount of clean hydrogen obtained during the oxidation phase divided by the amount of contaminated hydrogen fed into the reactor during the reduction phase yields the following expression:

$$\eta_{H_2} = \frac{\int_{\text{oxidation}} (\omega/\vartheta \cdot x_{H_2})_{\text{out}} d\tau}{\int_{\text{reduction}} (\omega/\vartheta \cdot x_{H_2})_{\text{in}} d\tau} \quad (5)$$

For a given set of parameters, the reduction phase duration can be varied in order to increase the efficiency of the CWGSR. As before, the oxidation phase is stopped as soon as the molar fraction of hydrogen in the output gas drops below 0.9. The result of this parameter study is shown in Figure 8. In the case of co-flow configuration, the reduction phase has to last at least 1700 dimensionless time units, otherwise a hydrogen output concentration of 90 % can not be obtained. In reverse-flow operation, cycling times can be decreased considerably, with the resulting efficiency increasing steadily up to 90%. However, the maximum is not obtained at infinitely short cycle duration, but at about $\tau_{\text{reduction}}=70$. This is because after the switching of gas streams, the first portion of outlet gases must be considered contaminated and can not be used as product gas, which is accounted for in the calculation. Thus, the reverse-flow operation mode with short cycle durations seems to be favorable and promises high energetic efficiencies.

The short cycle duration has an additional advantage over long cycle times. As seen in Figures 4 to 6, long cycle times lead to repeated large changes in the degree of reduction over time. This leads to strong morphological changes of the fixed bed material. The consequence is fast sintering and thereby the deactivation of the metal oxide. Applying short cycle durations means that the reduction degree of the fixed bed does not change much anywhere in the reactor, as can be seen in Figure 9 ($\tau_{\text{reduction}}=70$). This reduces the stress of the material and significantly delays its deactivation.

The fact that short cycle durations are preferred is what discriminates the CWGSR from a pressure swing adsorption reactor. In a PSA, the adsorption phase lasts until short before a breakthrough. After depressurization, these species are

desorbed again until the bed is nearly completely free. Although this is a simplified description of real PSA processes, the point is that the adsorption bed is nearly completely filled and emptied again, which corresponds to long cycle durations. Applying short cycle times to the CWGSR means that a partially loaded fixed bed is loaded with a small additional amount of oxygen and then unloaded again by the same amount. Deep reduction or oxidation are thus avoided in the CWGSR.

4. Non-isothermal simulations

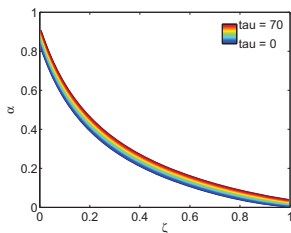


Figure 9. Degree of reduction during reverse-flow operation with short phase duration. The small changes help reduce material deactivation.

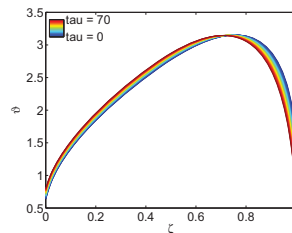


Figure 8. Temperature during reverse-flow operation with short phase duration and similar phase durations for oxidation and reduction. The CWGSR works as a Matros reactor.

After a suitable operating regime for the CWGSR is identified, the thermal behavior is simulated. This is done using the full model (Equations (5) to (8)) including the enthalpy balance. Starting from arbitrary initial conditions, the slow fixed bed states do not change much during each short cycle, so it usually takes several thousand cycles to obtain a cyclic steady state. In this simulation, a mixture of hydrogen and carbon monoxide is fed into the reactor during the reduction phase, so the net reaction is exothermic. Due to the short cycling times, the temperature profile does not change much during each cycle, which is also favorable with respect to thermally controlled deactivation mechanisms. Applying nearly similar durations for the reduction and for the oxidation phase as well as a low inlet temperature of $\vartheta_m=0.5$ leads to an interesting thermal behavior. The net heat released by the water gas shift reaction inside the reactor is convectively transported by the gas flows. In reverse-flow operation, the direction of this transportation mechanism changes frequently, so that for short cycle times, the heat is captured inside the reactor (see Figure 8). This behavior is known from so-called Matros reactors (Matros et al., 1989; Matros et al, 1993) and can be utilized to integrate the

CWGSR into a system without extensive heat exchangers at the inlet and outlet. Relatively cool gas can be supplied into the reactor, which can sustain a high temperature level and emit relatively cold product gases.

5. Conclusions and outlook

The cyclic water gas shift reactor is a fixed bed reactor for the production of carbon monoxide free hydrogen. Although it has some common aspects with a cyclically operated catalytic fixed bed reactor or a pressure swing adsorption reactor, it has some unique features that are analyzed and discussed on a conceptual level in this contribution.

The simulation of the cyclic behavior shows that the co-flow mode of operation has certain drawbacks that curtail its efficiency and lead to high deactivation rates of the fixed bed material. Instead, we suggest to apply a reverse-flow operation mode. Although reverse-flow is more difficult to realize practically, it has significant advantages. Fuel losses occurring in co-flow mode are avoided here and the slope of the reduction profile does not change its sign during each cycle phase. Applying short cycle times can further improve the performance of the reverse-flow mode. Efficiency can reach up to 90% and the almost constant reduction degree of the fixed bed slows down deactivation processes. In addition, a reverse-flow reactor with short cycle duration can work in a heat-integrated manner like a Matros reactor, which offers attractive options for system integration with other process steps like a steam reformer or a low temperature fuel cell.

Further works on the CWGSR include a more detailed modeling of the reactor, taking into account multiple reaction steps, non-linear reaction kinetics (Avrami-Erofeev or diffusion limited kinetics) and radial distributions in the gas flow and temperature. Simultaneously, kinetic experiments are being conducted that will help to understand and incorporate the microscopic behavior of the fixed bed material, and a lab scale CWGSR is being constructed to validate the simulation results from the advanced models.

Notation

In case of dimensional parameters, their unit is given. For dimensionless parameters their definition in terms of dimensional parameters is given.

Latin symbols

a	$[m^2 \cdot m^{-3}]$	Fixed bed surface area per reactor volume
c_{Fe}^a	$[mol \cdot m^{-2}]$	Surface related iron concentration
c_p	$[J \cdot m^{-3} \cdot K^{-1}]$	Volume related heat capacity
c_t	$[mol \cdot m^{-3}]$	Total molar concentration gas phase

$Da_j = \frac{(1-\varepsilon)a L r_j^0}{\varepsilon v^0 c_i^0}$	[-]	Damköhler number (reaction rate constant) of reaction j
$E_{a,j}$	[J·mol ⁻¹]	Activation energy reaction j
k^h	[W·m ⁻² ·K ⁻¹]	Heat transfer coefficient across reactor walls
L	[m]	Reactor length
n_j	[-]	Order of reaction j
$Pe = \frac{\varepsilon v^0 c_{p,g}}{(1-\varepsilon)\lambda/L}$	[-]	Peclet number (inverse heat conductivity) of the fixed bed
R	[J·mol ⁻¹ ·K ⁻¹]	Gas constant
$R_j = \frac{r_j}{r_j^0}$	[-]	Reaction rate of reaction j
R_r	[m]	Reactor radius
r_j	[mol·m ⁻² ·s ⁻¹]	Surface related reaction rate of reaction j
$St = \frac{2L/v^0 k^h}{R_r \varepsilon c_{p,g}}$	[-]	Stanton number (heat exchange coef.) with the environment
T	[K]	Temperature
t	[s]	Time
v	[m·s ⁻¹]	True gas velocity
x_i	[-]	Molar fraction of component i
z	[m]	Spatial coordinate

Greek symbols

$\alpha = \frac{c_{Fe}^a}{c_{Fe,max}^a}$	[-]	Degree of reduction of the fixed bed
$\gamma_j = \frac{E_{a,j}}{RT^0}$	[-]	Arrhenius number (activation energy) of reaction j
$\Delta \vartheta_{ad,j} = \frac{-\Delta_R h_j^0 \varepsilon c_i^0}{(1-\varepsilon)c_{p,s} T^0}$	[-]	Adiabatic temperature increase due to reaction j
$\Delta_r h_j^0$	[J·mol ⁻¹]	Reaction enthalpy of reaction j
ε	[-]	Fixed bed porosity, gas volume fraction
$\zeta = \frac{z}{L}$	[-]	Axial reactor coordinate
η	[-]	Energetic efficiency
$\Theta = \frac{(1-\varepsilon)a c_{Fe,max}^a}{\varepsilon c_i^0}$	[-]	Substantial (oxygen) capacity of the fixed bed

$\vartheta = \frac{T}{T^0}$	[-]	Reactor temperature
λ	$[W \cdot m^{-1} \cdot K^{-1}]$	Heat conductivity fixed bed material
$\nu_{i,j}$	[-]	Stoichiometric coefficient of gas component i in reaction j
$\bar{\nu}_j$	[-]	Net stoichiometric coefficient of reaction j
$\tau = \frac{t}{L/v^0}$	[-]	Time
$\omega = \frac{v}{v^0}$	[-]	True gas velocity
$\Psi = \frac{(1-\varepsilon)c_{p,s}}{\varepsilon c_{p,g}}$	[-]	Heat capacity of the fixed bed

Lower indices

e	Outside the reactor
Fe	Iron species
i	Gas component
j	Reaction

Upper indices

G	Gas phase
S	Solid phase, fixed bed
θ	Standard value

References

- Galvita, V., Sundmacher, K., "Cyclic water gas shift reactor (CWGS) for carbon monoxide removal from hydrogen feed gas for PEM fuel cells", *Chem. Eng. J.*, 134, 168-174 (2007).
- Glöckler, B., Kolios, G., Eigenberger, G., "Analysis of a novel reverse-flow reactor concept for autothermal methane steam reforming", *Chem. Eng. Sci.*, 58, 593-601 (2003).
- Hacker, V., Faleschini, G., Fuchsa, H., Fankhauser, R., Simader, G., Ghaemi, M. Spreitz, B., Friedrich, K., "Usage of biomass gas for fuel cells by the SIR process", *J. Power Sources*, 71, 226-230 (1998).
- Hacker, V., Fankhauser, R., Faleschini, G., Fuchs, H., Friedrich, K., Muhr, M., Kordes, K., "Hydrogen production by steam-iron process", *J. Power Sources*, 86, 531-535 (2000).

Kulkarni, M.S., Dudukovic, M.P., "Periodic operation of asymmetric bidirectional fixed-bed reactors with temperature limitations", *Ind. Eng. Chem. Res.*, 37(3), 770-781 (1998).

Lynum, S., Hox, K., Hugdahl, J., "Method and device for the pyrolytic decomposition of hydrocarbons", Patent US 5997837 (1999).

Malek, A., Farooq, S., "Hydrogen purification from refinery fuel gas by pressure swing adsorption", *AIChE Journal* 44, 9, 1985-1992 (1998).

Matros, Y.S., Bunimovich, G.A., Noskov, A.S., "The decontamination of gases by unsteady-state catalytic method. Theory and Practice", *Catalysis Today*, 17, 261-274 (1993).

Matros, Y.S., Delmon, B., Yates, J.T. (Eds.), "Catalytic Processes under Unsteady-State Conditions", in: "Studies in Surface Science and Catalysis", 43, Elsevier, (1989).

Messerschmitt, "Verfahren zur Erzeugung von Wasserstoff durch abwechselnde Oxidation und Reduktion von Eisen in von außen beheizten, in den Heizräumen angeordneten Zersetzern", German Patent DE 266863 (1911).

Sircar, S., Golden, T.C., "Purification of hydrogen by pressure swing adsorption", *Sep. Sci. & Tech.* 35, 5, 667-687 (2000).

[PH 3]

M. Pfafferodt, P. Heidebrecht, K. Sundmacher,
U. Würtenberger, M. Bednarz

Multi-scale Simulation of the Indirect Internal Reforming unit
(IIR) in a Molten Carbonate Fuel Cell (MCFC)

Industrial & Engineering Chemistry Research 47 (2008),
4332-4341

Multiscale Simulation of the Indirect Internal Reforming Unit (IIR) in a Molten Carbonate Fuel Cell (MCFC)

Matthias Pfafferoth,[†] Peter Heidebrecht,[‡] Kai Sundmacher,^{*,†,‡} Uwe Würtenberger,[§] and Marc Bednarz[§]

Process Systems Engineering, Otto-von-Guericke-University Magdeburg, Universitätsplatz 2, 39106 Magdeburg, Germany, Max Planck Institute for Dynamics of Complex Technical Systems, Sandtorstrasse 1, 39106 Magdeburg, Germany, and CFC Solutions GmbH, Christa-Mc-Auliffe-Strasse 1, 85521 Ottobrunn, Germany

This paper studies the coupled mass and heat transport as well as the reactions in an indirect internal reforming (IIR) unit of a molten carbonate fuel cell (MCFC). The aims of the work are first to identify the dominating transport processes for a specific design. Because the temperature field is one major issue in MCFCs, the second aim is to predict the spatially distributed temperature field within the unit. In a first step, several variants of a microscale model, describing only a small detail of the IIR unit, are created. The governing equations and the boundary conditions of this model are given. The results of these simulations, especially the temperature and concentration distributions, are discussed. They show that the gas phase is divided into a reactive and a nonreactive zone in the actual design of the IIR and the reforming process is dominated by mass transfer between these zones. In a second step, a macroscale model of the entire IIR unit is presented. It considers a simplified geometry, but it incorporates the two gas zones identified by the microscale model.

1. Introduction

The molten carbonate fuel cell (MCFC) is suitable for stationary coproduction of electricity and high-graded heat. A stationary fuel cell power plant based on an MCFC was developed by the CFC Solutions GmbH, the so-called HotModule.¹ A variety of fuel gases can be used: natural gas, gas from biomass fermentation, gasified coal, or waste gas. The fuel gas has to be reformed before it can be used for electrochemical conversion. The reforming can be done either in an external reformer (ER), in a special unit attached to the fuel cells in the stack called the indirect internal reformer (IIR), or in direct neighborhood to the anode of the fuel cell (direct internal reforming, DIR).

In today's MCFCs, which are fuelled with natural gas, the external reformer is used to crack the hydrocarbon chains. The heat for the reaction is provided by the exhaust gas of the fuel cell. Therefore, the ER and the fuel cell are thermally coupled by a heat exchanger. Such reforming reactors are widely used in the chemical industries and are discussed in detail in the literature.^{2,3}

The IIR units are special flat reactors located within the fuel cell stack between two fuel cells (Figure 1). In this integrated reactor concept, heat exchange between the endothermic reforming reactions and the heat-releasing electrochemical reactions in the neighboring fuel cells is realized. Thus, the IIR influences the temperature profile of the fuel cell stack. Because the rate of the (electro-)chemical reactions as well as the rate of the undesired degradation processes strongly depend on the temperature distribution, an understanding of the gas flow and the reactions within the IIR is needed. This can be used to develop new IIR designs, leading to higher cell efficiency and increased lifetime. In previous studies, the IIR is included as part of a lumped-parameter MCFC model⁴ or is implemented as an additional layer in 2D simulations of an MCFC.⁵

A mathematical model for a MCFC is presented in the literature.⁶ Within this paper, the chemical and electrochemical processes within the fuel cell are discussed in detail. This MCFC model was validated using data obtained from an industrial MCFC system.⁷ In addition to the electrochemical reactions and the direct internal reforming, the IIR is taken into account for the validation process.

However, these models do not have the level of detail needed for a further optimization of the MCFC stack. In the above-mentioned models, a flat 2D representation of the different components of a MCFC is considered. While this is a valid approach for a first spatially distributed simulation, a detailed simulation of each part is needed to further improve the model accuracy. In this contribution, the IIR unit is simulated. The complex 3D geometry of the reforming reactor as well as the spatial distribution of the catalyst pellets for the reforming reaction are taken into account. Models at two scales are created for a detailed analysis of the structure. This helps to understand the behavior of the IIR unit as a cooling device for the neighboring fuel cells. Together with similar multiscale simulations for the anode and cathode compartments as well as models of the electrodes and the electrolyte, these simulations lead to a revised model of the MCFC stack and to a model-based design of the next generation of MCFC stacks.

The simulation results presented in this contribution were obtained within an industrial cooperation project. To protect the intellectual property, no exact quantitative data can be given. However, the model equations and boundary conditions for the IIR models are given in detail, and the transition from the microscale to the macroscale and their relevance for the MCFC are discussed qualitatively.

In the following, the multiscale approach is described. The microscale model is introduced, and its results are shown. Further on, some important conclusions are drawn. On the basis of these, the macroscale model is presented together with simulation results obtained from it.

* Corresponding author. Tel.: +49 391 6110 351. Fax: +49 391 6110 523. E-mail: sundmacher@mpi-magdeburg.mpg.de.

[†] Otto-von-Guericke-University Magdeburg.

[‡] Max Planck Institute for Dynamics of Complex Technical Systems.

[§] CFC Solutions GmbH.

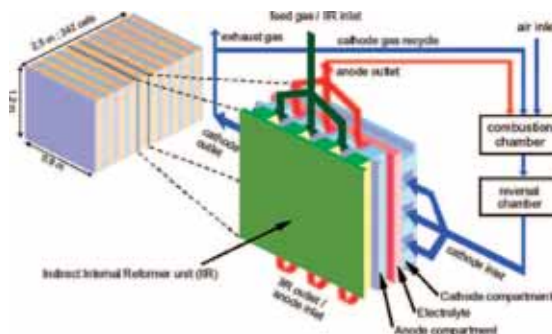


Figure 1. Structure of an MCFC stack. The schematic view shows the IIR unit and one cell consisting of the anode compartment, the electrolyte, and the cathode compartment. The gas flow within the stack is indicated by the arrows. Heat exchange between the endothermic reactions in the IIR unit and the heat-releasing electrochemical reactions in the fuel cell is possible.

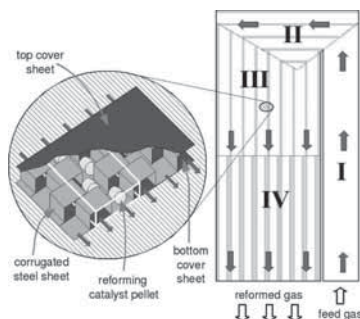


Figure 2. Schemes of the entire IIR unit⁸ with gas flow directions (sectors I–IV) and a cutout detail of the structure. In the zoom view, the structure of the staggered corrugated sheet including the flow direction is shown. One row of cages filled with catalyst pellets is indicated by the white frame.

2. Multiscale Modeling

The structure of the IIR unit as well as a cutout detail are shown in Figure 2. The flow direction within the reactor is enforced by corrugated steel sheets. The repeating pattern of the sheets creates rows of cages in which the cylindrical reforming catalyst pellets can be placed (see cutout detail in Figure 2).

The IIR unit is divided into four sections with different flow directions and different spatial reforming catalyst distributions. On the lower right-hand side, the gas enters the IIR unit (section I). There are no catalyst pellets installed within this section. Following the orientation of the corrugated sheets, the gas changes its main flow direction, entering section II. The last two sections follow after a second redirection of the gas (sections III and IV). In sections II, III, and IV, catalyst pellets are inserted into the structure formed by the corrugated sheet. The reforming reactions take place at the surface of these catalyst pellets. Different allocations of the catalyst pellets are used within these three sections.

A detailed simulation of the entire IIR unit would exceed the memory capacity and the computational power of a high-

end computer. Therefore, different models on multiple scales were simulated. This multiscale modeling approach is often used to solve large physical problems that have important features at multiple scales, particularly spatial scales.^{9–13} Models for the different scales are created to analyze the physical effects at each scale. In our approach, the results of the smaller-scale simulations are used to develop the larger-scale models.

The multiscale approach in this contribution includes two different scales. In the first step, microscale models of a small detail of the entire IIR unit are implemented, taking into account the exact 3D geometry (Section 3). The models are solved for different catalyst allocations. The simulation results provide a good understanding of the spatially distributed velocity, temperature, and gas composition (Section 4). On the basis of these results, a macroscale model of the entire reforming unit is created using a simplified geometry (Section 5). All simulations were performed using the commercial CFD tool CFX (version 10.0).

3. Definition of the Microscale Model

In the microscale model, a repeating detail of the structure of the IIR unit is simulated. It comprises the corrugated sheets as well as the top and bottom sheets. The staggered corrugated sheets form small cages into which cylindrical catalyst pellets can be placed. As indicated by the white wire frame in Figure 2, these cages are arranged in rows. The width of the microscale model is chosen to be 4 such rows, which is the smallest repeating width within the actual design. The length is chosen to be 15 pellet cages. Note that not all cage rows necessarily have to be filled with pellets. Actually, different allocations of catalyst pellets are used in the four sections of the IIR unit. A gas inlet section and a gas outlet section are added according to the experimental setup (see Figure 3).

3.1. Assumptions. The following assumptions are used in the models:

- The gas mixture is considered as ideal, containing the species CH_4 , H_2O , CO , CO_2 , and H_2 . Its inlet composition corresponds to a prereformed gas, i.e., the product gas of an external reformer.

- Molecular diffusion within the gas is taken into account. The diffusion coefficients of the gas mixture are estimated using the correlation of Chapman–Enskog for the binary diffusion

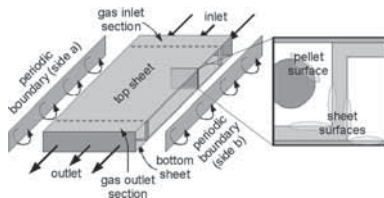


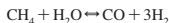
Figure 3. Structure of the microscale model with boundary conditions. External boundaries: gas inlet and gas outlet; top and bottom sheet; periodic boundary between the left-hand side (side a) and the right-hand side (side b) of the model. Internal boundaries: heat and mass flow due to the reforming reactions at the pellet surface; heat transfer at the sheet surfaces (corrugated sheet and the inner side of the top and bottom sheet).

coefficients¹⁴ and the extended approach of Wilke¹⁵ for the diffusion coefficients within the gas mixture. For the estimation of the diffusion coefficients, a fixed temperature and the equilibrium composition of the gas mixture are assumed. The diffusion coefficients used in the models are listed in Table 3; see Section 3.4.

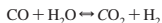
- Using the global length of $l = 0.018$ m estimated by CFX for the geometry and the average velocity within the microscale model ($u = 1.6$ m s⁻¹) as well as the density ($\rho = 0.24$ kg m⁻³) and the dynamic viscosity ($\mu = 1 \times 10^{-5}$ kg m⁻¹ s⁻¹) calculated for an average temperature and composition of the gas mixture, a Reynolds number of $Re = 691$ is calculated, indicating laminar flow. Because of the fact that, within the complex geometry, the laminar flow is frequently interrupted by the corrugated sheet and the catalyst pellets, a k - ϵ -turbulence model is used in the simulations.

- Neither in the microscopic nor in the macroscopic model are the neighboring fuel cells considered. A constant temperature is assumed for the top and bottom sheets. Therefore, the heat flux through the top and bottom sheets is a result of the difference between the temperature set at these boundaries and the calculated gas temperature near the wall.

- The reforming reactions take place at the surface of the catalyst pellets. In the literature, different expressions for the kinetics of the methane reforming reaction



and the water gas shift reaction



can be found.^{16–19} The kinetics depend on the exact chemical composition of the catalyst. Furthermore, the catalyst pellets are porous, so the conversion of the gas includes mass transport and chemical reactions inside the pores. In this work, the catalyst pellets are assumed to be highly active, so that the concentration at the catalyst surface is close to the chemical equilibrium. Thus, the mass transport inside the pellets is not considered explicitly, but they are assumed to be solid particles with a highly active catalytic surface. Simple power laws are used as reaction rate expressions that provide a good approximation of the reactions rates near chemical equilibrium conditions:

$$r_{\text{ref}} = k_{0,\text{ref}}^A \left[\left(\frac{p}{p^0} \right)^2 x_{\text{CH}_4} x_{\text{H}_2\text{O}} - \frac{1}{K_{\text{ref}}(T)} \left(\frac{p}{p^0} \right)^4 x_{\text{CO}} x_{\text{H}_2}^3 \right] \quad (1)$$

$$r_{\text{wgsr}} = k_{0,\text{wgsr}}^A \left(\frac{p}{p^0} \right)^2 \left[x_{\text{CO}} x_{\text{H}_2\text{O}} - \frac{1}{K_{\text{wgsr}}(T)} x_{\text{CO}_2} x_{\text{H}_2} \right] \quad (2)$$

Table 1. Governing Equations Used in the Microscale Model

continuity balance	$\nabla(\rho \mathbf{u}) = 0$	(3)
momentum balance	$\nabla(\rho \mathbf{u} \mathbf{u}) = -\nabla p + \nabla \tau$	(4)
with the stress tensor	$\tau = \mu_{\text{eff}}(\nabla \mathbf{u} + (\nabla \mathbf{u})^T)$	
energy balance—gas phase	$\nabla(\rho \mathbf{u} h) = \nabla(\lambda_{\text{gas}} \nabla T_{\text{gas}}) + \nabla(\mathbf{u} \tau)$	(5)
energy balance—solid phase	$0 = \nabla(\lambda_{\text{solid}} \nabla T_{\text{solid}})$	(6)
component mass balance	$\nabla(\rho \mathbf{u} w_i) = \nabla((\rho D_i + \mu_j S_{Cj}) \nabla w_i)$	(7)

The reaction rate constants, $k_{0,\text{ref}}^A$ and $k_{0,\text{wgsr}}^A$, are assigned sufficiently high values so that the gas at the pellet surface is always close to equilibrium. The equilibrium constants, $K_{\text{ref}}(T)$ and $K_{\text{wgsr}}(T)$, are calculated from thermodynamic equations via the Gibb's enthalpies of these reactions. Because of the fact that the pellets are only in contact with the gas phase, the enthalpies of the reactions are taken from or transferred to the gas phase. The temperature within the pellets is assumed to be equal to the gas temperature around the pellets, and therefore, it is not simulated.

3.2. Equations. The well-known steady-state balance equations for the gas flow within a chemical reactor are used (Table 1). Here, only the partial differential equations, solved by the software tool CFX, are listed. A detailed discussion of these equations can be found in the literature.^{15,20,21} Note that, for the microscale model, the reactions at the catalyst surface are accounted for in the boundary conditions and not in the differential equations.

3.3. Boundary Conditions. All boundary conditions used in the microscale model are shown in Figure 3 and listed in Table 2. On the one hand, there are the external boundaries of the simulation domain at the gas inlet and the gas outlet, the outer surface of the top and bottom metal sheets, and the periodic boundary between the left and right sides of the model. On the other hand, internal boundaries have to be taken into account: the surface of the catalyst pellets and the inner surfaces of the metal sheets.

The external boundary conditions are given in eqs 8–16. The overall mass flow at the gas inlet is used to calculate the gas velocity, taking into account the gas density, which in turn depends on the gas temperature and the gas composition (eq 8). At the gas outlet, the pressure is constrained such that the average value is equal to the given relative pressure (eq 11). The left side and the right side of the simulation domain are connected by a periodic domain interface. Here, conservative interface fluxes are considered for the temperature of the solid as well as for the temperature, the momentum, and the mass fractions of the gas (eqs 13–16).

Within the simulation domain, the internal boundaries between the gas and the catalyst pellets and those between the gas and the metal sheets have to be considered (eqs 17–22). At the surface of the metal sheets, the no-slip condition for the velocity is applied (eq 17). Additionally, a conservative heat flux between the solid phase and the gas phase is taken into account (eq 18). Further on, the sheet surface is impermeable for all gas components (eq 19).

At the surface of the catalyst pellets, the reforming reactions are taken into account. Because of the fact that a mass-averaged velocity is used, the overall gas velocity at the surface of the catalyst pellets is equal to zero (no-slip boundary condition; eq 20). A mass transfer exists between the gas and the pellet surface (eq 22). These component mass fluxes correspond to the rates of both reactions defined in eqs 1 and 2. The heat of reaction at the catalyst surface is implicitly accounted for in the enthalpy balance, so it does not explicitly occur in the boundary conditions. It can be obtained by combining eqs 21 and 22

Table 2. List of All Internal and External Boundary Conditions Used in the Microscale Models

external boundaries		
gas inlet		
velocity	$u_{inlet} = \dot{m}_{in} / [A_{inlet} \rho(T, w_i)]$	(8)
temperature	$T_{gas,inlet} = T_{gas,in}$	(9)
mass fraction	$w_{i,inlet} = w_{i,in}$	(10)
gas outlet		
pressure	$\bar{p}_{outlet} = 1/A \int p_{outlet} dA = p_{out}$	(11)
top and bottom wall		
temperature	$T_{solid,top} = T_{solid,bottom} = T_{solid, outside}$	(12)
periodic boundary between the left and right sides		
velocity	$u_{left} = u_{right}, [\rho u]_{left} = [\rho u]_{right}$	(13)
temperature (gas phase)	$T_{gas,left} = T_{gas,right}, [\rho_{gas} u]_{gas} - \lambda_{gas} \nabla T_{gas,left} = [\rho_{gas} u]_{gas} - \lambda_{gas} \nabla T_{gas,right}$	(14)
temperature (solid phase)	$T_{solid,left} = T_{solid,right}, [-\lambda_{solid} \nabla T_{solid}]_{left} = [-\lambda_{solid} \nabla T_{solid}]_{right}$	(15)
mass fraction	$w_{i,left} = w_{i,right}, [\rho u w_i - (\rho D_i + \mu_j S_{C_i}) \nabla w_i]_{left} = [\rho u w_i - (\rho D_i + \mu_j S_{C_i}) \nabla w_i]_{right}$	(16)
internal boundaries		
sheet surface		
velocity	$u_{surface} = 0$	(17)
temperature	$T_{solid,surface} = T_{gas,surface}, [-\lambda_{solid} \nabla T_{solid}]_{surface} = [-\lambda_{gas} \nabla T_{gas}]_{surface}$	(18)
mass fraction	$[-(\rho D_i + \mu_j S_{C_i}) \nabla w_i]_{surface} = 0$	(19)
pellet surface		
velocity	$u_{pellet} = 0$	(20)
temperature	$[\rho_{gas} u]_{gas} - \lambda_{gas} \nabla T_{gas,pellet} = 0$	(21)
mass fraction	$[-((\rho D_i + \mu_j S_{C_i}) \nabla w_i)]_{pellet} = (v_{i,ref} \mu_{ref}^A + v_{i,wgsr} \mu_{wgsr}^A) M_i$	(22)

Table 3. Model Parameters

property	symbol	value
metal sheet		
density	ρ	7854 kg m ⁻³
specific heat capacity	c_p	434 J kg ⁻¹ K ⁻¹
thermal conductivity	λ	60.5 W m ⁻¹ K ⁻¹
diffusion coefficient		
methane	D_{CH_4}	2×10^{-4} m ² s ⁻¹
water	D_{H_2O}	3×10^{-4} m ² s ⁻¹
hydrogen	D_{H_2}	5×10^{-4} m ² s ⁻¹
carbon dioxide	D_{CO_2}	2×10^{-4} m ² s ⁻¹
carbon monoxide	D_{CO}	2×10^{-4} m ² s ⁻¹
reaction rate coefficients		
methane reforming reaction	$k_{0,ref}^A$	0.3 mol m ⁻² s ⁻¹
water gas shift reaction	$k_{0,wgsr}^A$	1.0 mol m ⁻² s ⁻¹

together with the expression for the enthalpy of the mixture. Because the pellets are not modeled, there is not heat flux in the solid phase at these boundaries.

3.4. Parameters. The parameters used in the model are listed in Table 3. For the metal sheets, the properties of steel are applied, whereas the values for the diffusion coefficients within the mixture are calculated by taking into account a representative temperature and composition of the gas mixture (see Section 3.1). The thermodynamic properties of the gas, the heat capacity, the enthalpy, and the entropy, are provided by the material library of the simulation tool CFX using the NASA format.^{22,23} Constant values are used for the reaction rate coefficients. With the values given here, the gas at the pellet surface is very close to equilibrium. Because the exact values of the rate constants are not relevant, they are considered constant with regard to the temperature.

4. Simulation Results of the Microscale Model

Three different variants of the microscale model are considered. Of the four rows of cages, 1, 2, or 3 rows are filled with catalyst pellets. In the first part of this section, the results of a configuration with one row filled with catalyst pellets are discussed in detail. After that, the results of the three different configurations are compared. The boundary conditions at the gas inlet as well as for the top and bottom sheets are listed in Table 4. These values are used for all simulations.

Table 4. Operating Conditions for the Microscale Models

	symbol	value
inlet gas temperature	T_{inlet}	883.15 K
inlet mass flux	\dot{m}_{inlet}	0.298×10^{-6} kg s ⁻¹
inlet mass fraction of CH ₄	w_{i,CH_4}	0.267
inlet mass fraction of H ₂ O	w_{i,H_2O}	0.621
inlet mass fraction of H ₂	w_{i,H_2}	0.014
inlet mass fraction of CO	$w_{i,CO}$	0.000
inlet mass fraction of CO ₂	w_{i,CO_2}	0.098
temperature at top and bottom sheet	$T_{solid,outside}$	893.15 K

Using the previously discussed model equations and boundary conditions, one simulation takes about 2 h calculation time on an Intel Xeon processor with 3.2 GHz CPU speed. Up to 0.7 GB of RAM are needed during the simulation procedure.

4.1. Results for a Catalyst Allocation of 1–4 Rows. Figure 4 shows the simulated velocity profile from the microscale model. The gas enters the simulation domain at the inlet boundary located at the top of the simulation domain with the velocity calculated from the given mass flow rate. Within the inlet section, the transition from the constant velocity at the inlet boundary to an inhomogeneous velocity profile at the beginning of the corrugated sheets takes place. Figure 4a shows the velocity profile in the middle XY-plane. Because of the reduced cross-sectional area near the catalyst pellets and the no-slip boundary condition, the gas velocity is decreased around the pellets, whereas the velocity is increased in the areas without catalyst pellets. In the cross-section profiles (parts b–d of Figure 4), one can see that the velocity profile is repeated in a constant pattern after the first few catalyst pellets. In the vicinity of the catalyst pellets, the gas is meandering slowly around the pellets and it is almost stagnant compared to the gas in the other parts of the geometry. The ratio of the velocity close to the pellets to the velocity in the rest of the IIR unit is about 1:10. In the whole geometry, the gas flow is repeatedly split by the corrugated sheet. This results in additional turbulence and mixing effects due to flow separation.

The temperature profile is displayed in Figure 5. The cross-section plots show that, after the sixth catalyst pellet, a steady repeating pattern is reached. They also indicate that the heat sink at the pellet surface due to the endothermic reforming process is balanced by heat fluxes from the remaining gas phase (mainly in the x-direction) and from the top and bottom sheets

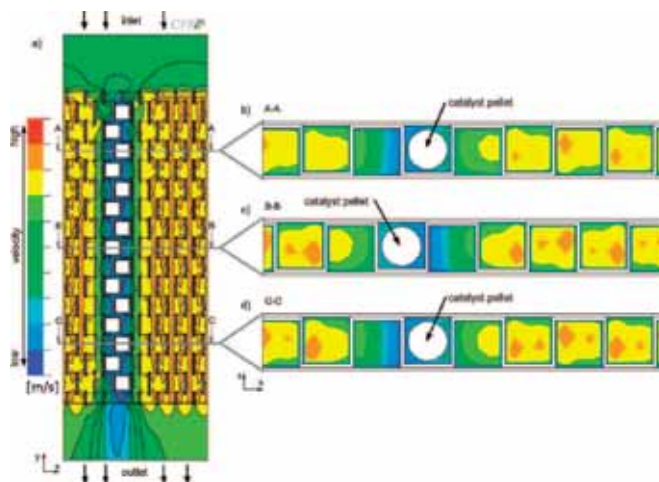


Figure 4. Simulated velocities for the microscale model with 1 of 4 rows filled with catalyst pellets: (a) velocity profile in the XY-plane and (b)–(d) velocity profiles in the XZ-plane at the 3rd, 8th, and 13th pellet, respectively. A steady repeating velocity pattern develops after the first few pellets.

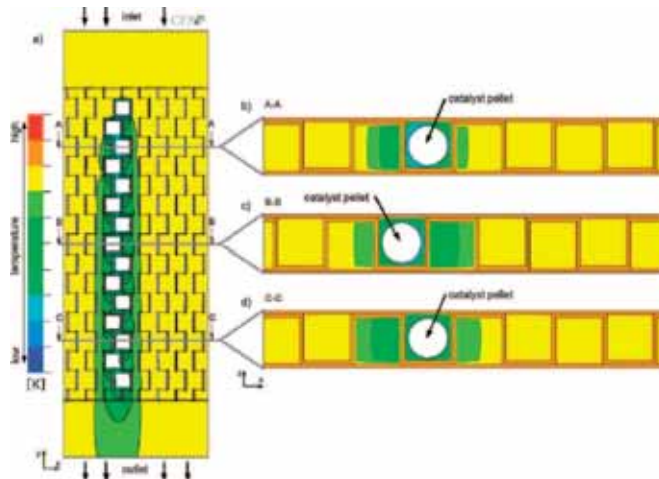


Figure 5. Simulated temperature profile for the microscale model with 1 of 4 rows filled with catalyst pellets: (a) temperature distribution in the XY-plane and (b)–(d) temperature distribution in the XZ-plane at the 3rd, 8th, and 13th pellet, respectively. The cross-section plot indicates a steady repeating temperature profile after the 7th pellet.

via the gas phase (mainly in the z -direction). Compared to the temperature differences in the solid parts, the temperature differences in the gas phase are larger by 1 order of magnitude, which is due to the different heat conductivities and the characteristic lengths of the heat transport. A quantitative comparison shows that the heat flux from the top or bottom

sheet is much higher than the heat flux from the warm gas phase toward the cold pellets (Figure 5 parts b and c).

In MCFC, a temperature change of 10 K is considered significant with respect to degradation rates and electrochemical performance. The IIR unit is intensively thermally coupled to the fuel cells in the stack, so that a temperature difference of

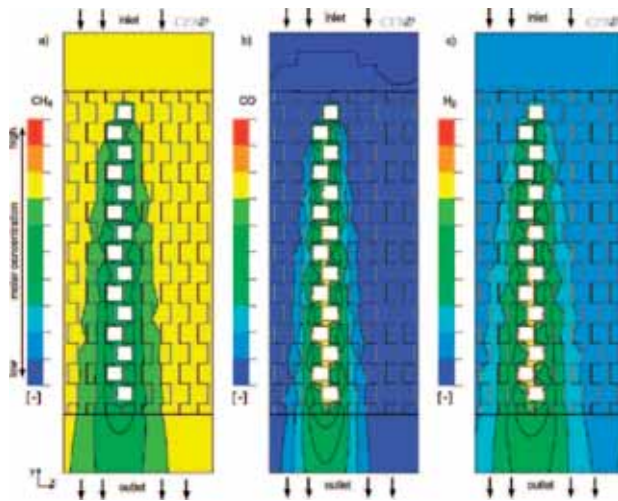


Figure 6. Simulated gas compositions for the microscale model with 1 of 4 rows filled with catalyst pellets. The plots show the profiles in the XY -plane for the molar fraction of the following species: (a) methane, (b) carbon monoxide, and (c) hydrogen. A reactive zone near the catalyst pellets and a nonreactive zone are clearly distinguishable.

10 K within the IIR unit may also be considered significant. In the simulation results, the temperature difference between the gas around the pellets and the remaining gas is several times higher than this threshold value. Thus, the temperature profile shows a distinct separation of the gas phase into a cold fraction near the catalyst pellets and a warm fraction in the zone without pellets.

The concentration profiles for methane, carbon monoxide, and hydrogen are shown in Figure 6. Methane is consumed by the reforming reaction at the surface of the catalyst pellets (Figure 6a). This results in a gradient in the molar fraction between the gas near the pellet surface and the gas far from the catalyst. The difference is in the order of several mole percent. Similar gradients can be observed for the products of the reforming reactions, namely, carbon monoxide (Figure 6b) and hydrogen (Figure 6c). The highest concentrations of the reaction products can be found near the catalyst pellets, whereas the lowest concentrations are in the free-flowing gas. The mass transport of the educts to the catalyst pellets as well as the mass transport of the products from the catalyst pellets results in funnel-shaped concentration profiles.

After a few catalyst pellets, the gas composition in the proximity of the pellets reaches the chemical equilibrium. In this part, the reactions are limited by the catalyst activity. Once the gas around the pellets has reached its equilibrium composition, the reforming process is dominated by the mass transport of the reacting species toward and away from the pellet surface. Thus, the rate of the reforming process is independent from the catalyst activity, at least as long as it is sufficiently high. This is an important feature of this reactor, because it provides a constant thermal profile even in the case of catalyst degradation, which is inevitable in real systems.

The concentration profiles as well as the temperature profile and the velocity profile indicate that the reactor is divided into

two zones. The first zone is a reactive zone near the catalyst pellets. Because the flow is hindered by the pellets, the velocity is reduced in this zone. Additionally, the endothermic reforming reactions taking place at the surface of the catalyst pellets result in a significant temperature drop in this zone. The second is a nonreactive zone, which contains the gas in the free rows that have no contact to the catalyst surface. The exchange of mass and heat between the two zones due to diffusion and heat conduction, which are enforced by turbulence, determine the reaction rate in the overall system.

4.2. Comparison of Different Catalyst Distributions. In addition to the model with an allocation of one row filled with catalyst pellets, simulations have also been carried out for models with 2 or 3 rows of cages filled with pellets. The additional catalyst pellets extend the reactive zone within the simulation domain and reduce the nonreactive zone. For all these simulations, the inlet conditions listed in Table 4 are used.

Figure 7 compares the temperature profiles for the three model variants. In each of them, a similar pattern for the temperature is visible. The scale of the figures is identical and also corresponds to the scale used in Figure 5. A balance between the heat flux through the top and bottom sheets into the gas and the energy needed for the endothermic reaction is reached near the seventh catalyst pellet. After that, a constant pattern is visible in the temperature profiles. The simulations show nearly identical temperatures at the surface of the catalyst pellets in all three model variants. The more pellets are used, the more gas is converted, causing an increasing heat consumption in the reactive zone. However, the heat exchange area between the reactive and nonreactive zones is identical in each variant, while the heat exchange area between the top and bottom sheets and the reactive zone also grows with the number of catalyst

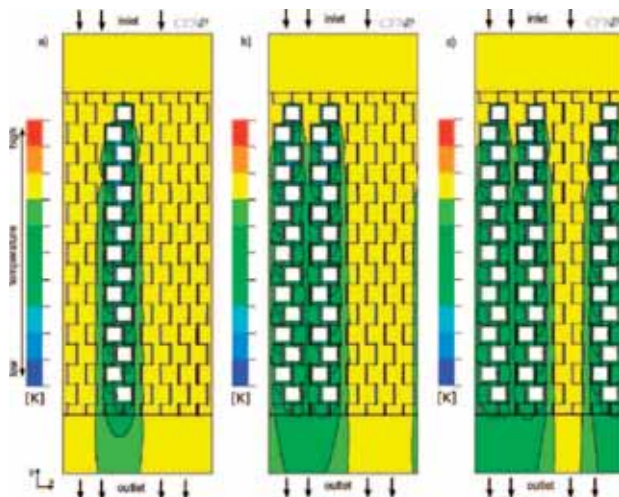


Figure 7. Temperature distributions for different catalyst allocations in the XY -plane for models with 1, 2, and 3 catalyst pellet rows. The same temperature scale is used for all three plots. In each of the plots, a repeating pattern in the temperature profile is visible.

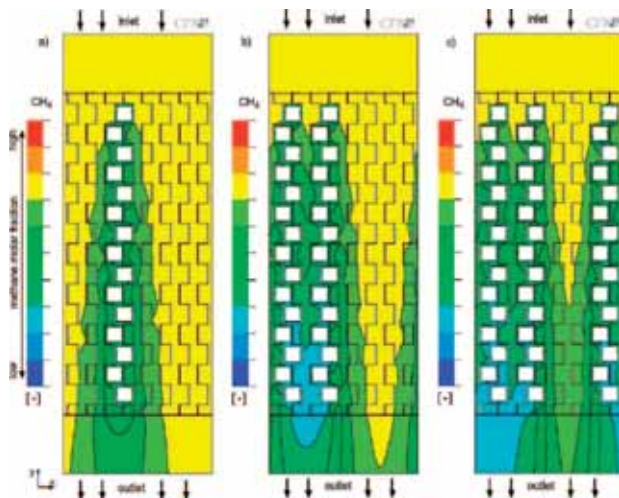


Figure 8. Methane molar fraction for different catalyst allocations in the XY -plane for models with 1, 2, and 3 catalyst pellet rows. The methane concentration range is equal for all three plots. Because of the increased flow through the reactive zone, the lowest methane molar fraction can be observed if 3 of 4 rows are allocated with catalyst pellets.

pellets. This confirms the findings discussed in Section 4.1, that the mean heat supply to the reforming process happens directly through the outer metal sheets.

The different concentration profiles for methane are shown in Figure 8. The scale of each figure is identical and also

corresponds to the scale used in Figure 6. For each model variant, the reactive zone and the nonreactive zone as well as the funnel-shaped profiles are clearly visible. Mass transfer is only possible at the interfaces between the two zones. The lowest methane concentrations are found in the center of the reactive

Table 5. Governing Equations Used in the Macroscale Models

continuity balance	$\nabla(\rho \mathbf{u}) = 0$	(24)
momentum balance	$\nabla(\rho \mathbf{u} \mathbf{u}) = -\nabla p + \nabla \tau - (\mu/K) \mathbf{u}$	(25)
energy balance (gas phase)	$\nabla(\rho \mathbf{u} h) = \nabla(\lambda_{\text{gas}} \nabla T_{\text{gas}}) + \nabla(\mathbf{u} \tau)$	(26)
component mass balance	$\nabla(\rho \mathbf{u} w_i) = \nabla((\rho D_i + \mu_d / Sc_i) \nabla w_i) + (v_{\text{ref},i}^V \nabla_{\text{ref}} + v_{\text{wgst},i}^V \nabla_{\text{wgst}}) M_i$	(27)

zone, where the gas is in chemical equilibrium. Fresh, unreacted gas cannot reach this area.

On the one hand, the yield of the reforming reactions is increasing with the number of catalyst pellets used, but on the other hand, the pressure drop rises as well. Further on, the temperature difference between the metal sheets and the gas and, therefore, the heat flux through the top and bottom sheets depends also on the amount of catalyst surface available for the reactions. Therefore, one can manipulate the temperature profile of the neighboring fuel cells by changing the amount and the distribution of the catalyst pellets within the IIR unit. Thus, the cooling effect of the reforming unit can be adapted to the spatial distribution of the heat released by the electrochemical reactions in the neighboring fuel cell.

In conclusion, the analysis of the microscale models has shown two important features of this reactor. First, the reaction rate is governed by mass transfer between a reactive and a nonreactive zone. Catalyst degradation does not influence the reaction progress, so a constant temperature profile can be expected in the IIR unit even after long operation time. The second point is that the main heat transport route toward the cold reaction zone is through the top and bottom sheets and then directly into the reactive zone.

5. Macroscopic Model of the Entire IIR Unit

The model for the entire IIR is based on the results obtained from the microscale model. The IIR model is derived in several steps. First, the reactive and nonreactive zones are represented by cuboid volumes. The width of the reactive zone corresponds to the width of the zone of low gas velocities (Figure 4), which is identical to the width of the zone with low temperature (Figure 5). The exact geometry of the catalyst pellets is neglected, and the surface reaction is replaced by a homogeneous gas-phase reaction filling the whole reactive cuboid. The new, volumetric reaction rate constants are calculated from the surface-area-related rate constants as follows:

$$k_{0,j}^V = k_{0,j}^A \frac{A_t}{V_t} \quad (23)$$

In a second step, the exact geometry of the corrugated sheet is neglected. To include the flow resistance of the sheets and the catalyst pellets in the model, an additional pressure drop term based on Darcy's law with anisotropic permeabilities is included in the equations. These permeabilities take into account the orientation of the corrugated sheet and the pellets. They are estimated by comparison of simulated and measured pressure drops on a full-scale IIR unit. In addition to being an obstacle to convective mass transport, the sheets are also an obstacle to diffusive mass transport and they have a certain heat conductivity. However, parameter studies using the microscale model demonstrate that turbulent convection is the dominant mechanism for the transfer of mass and heat in the gas phase. The effect of neglecting the sheets with respect to the gas velocities is already accounted for with the anisotropic Darcy's law in the momentum balance. The heat conductivity of the corrugated sheets is negligible compared to the convective transport in the gas phase.

The third step is to expand this simplified geometry to the size of the whole IIR unit. In this step, the orientation of the

corrugated sheets and the catalyst pellet allocation in the four sections of the IIR unit are taken into account (see Figure 2).

For the complete model, similar equations as for the microscale models are used (Table 5). As mentioned above, an additional term is added to the momentum balance (eq 25, last term). Furthermore, a source term is added to the component mass balances to incorporate the reforming reactions as volume reactions (eq 27, last term). As for the microscale model, a constant temperature for the top and bottom boundaries is applied. At the gas inlet on the bottom right (see Figure 2), the gas temperature, the mass flow, and the gas composition are set, whereas at the gas outlet, the relative pressure is given. For all other walls, the no-slip boundary condition is set and the same temperature as for the top and bottom walls is applied.

6. Simulation Results for the Entire IIR Unit

Because of the reactions taking place in the IIR, a start-up strategy is needed to solve the model of the entire IIR unit. First, all equations are solved without the chemical reactions. After that, the reactions are activated and the solution process is restarted. Using the same computational hardware as for the microscale models, simulation results are available after around four days of computation time. Up to 1.0 GB RAM is needed during the solution process.

In Figure 9, the temperature distribution within the entire IIR unit is shown. Because a constant temperature for the top and bottom walls is assumed in the simulation, the heat flux through these walls is proportional to this temperature. The gas enters the simulation domain on the bottom right.

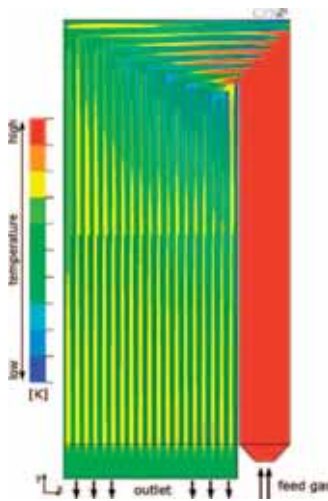


Figure 9. Temperature distribution within the model of the entire IIR unit in the *XY*-plane. The structure of the IIR (four sections with different flow directions and different catalyst allocations) is visible.

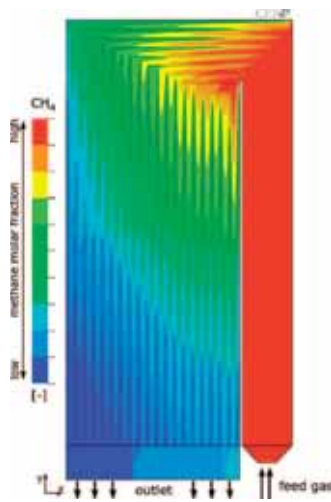


Figure 10. Methane molar fraction within the model of the entire IIR unit in the XY-plane. The molar fraction of methane is continuously reduced. One can clearly distinguish the reactive and nonreactive zones within the IIR unit.

Because of the fact that the feed gas temperature is equal to the temperature of the top and bottom walls in this part of the IIR unit, the heat flux is zero and the gas temperature does not change within section I (see the structure of the IIR unit in Figure 2). At the transition to section II, the gas hits the first catalyst pellets. As a result of the high concentration of methane and the high temperature, a high reaction rate of the methane reforming reaction occurs. The gas mixture is quickly cooled down within the reactive zones. The temperature drop within the reactive zone is in the range of several 10 K. The heat losses are partially compensated by the heat flux through the top and bottom walls. The structure of the IIR unit with separate reactive and nonreactive zones is clearly visible in the temperature profile of the last two sections. As a result of the heat flux through the top and bottom sheets, the temperature rises again along the flow direction. This structure also results in a nearly homogeneous distribution of the heat sink within most parts of the IIR unit due to the endothermic methane reforming reaction.

The methane molar fraction is displayed in Figure 10. Similar to the temperature profile, the methane molar fraction starts to change at the first catalyst pellets. The funnel-shaped concentration profiles observed in the microscale models can also be found in the simulation of the entire reforming unit. Especially in sections III and IV, the molar fraction of methane decreases almost linearly. This corresponds to a nearly homogeneous heat sink in the largest part of the IIR unit. Following the gas flow, the chemical equilibrium is reached at the gas outlet, taking into account the average gas temperature at this point.

As shown in the discussion of the simulation results for the microscale models, the reaction rates are limited by the mass transfer to and from the surface of the catalyst pellets and not by the catalyst activity. Only at the first few pellets is the

kinetically limited behavior visible (Figures 9 and 10). A deactivation of the first catalyst pellets will only result in a small shift of the profiles toward the following catalyst pellets, but it will not significantly alter the temperature profile along the rest of the reactor, thus providing a stable temperature profile for the neighboring fuel cells.

7. Conclusions

Simulations of the IIR unit at two different scales were performed. First, different variants of a microscale 3D model, consisting of small cutouts of the IIR unit, were created. For these simulations, the exact geometry with the corrugated sheets and the individual catalyst pellets was taken into account. Afterward, a macroscale 3D model of the entire IIR unit was solved. In this model, the results from the microscale model were used for a simplification of the geometry.

In the microscale models, different distributions of catalyst pellets were analyzed. It was shown that a stable repeating pattern can be found for the temperature and velocity profiles. For the concentration profiles, a funnel-shaped profile was found. Using these profiles, the simulation domains can be divided into reactive and nonreactive zones. This indicates a mass transport limitation of the reactions and nearly no influence of the catalyst activity on the overall reaction rate within the reforming reactor.

Using the model of the entire IIR unit, concentration and temperature profiles were computed. The reactive and nonreactive zones are accounted for in this model, and they are clearly visible in the simulation results. The results indicate that the rate of the reforming process is nearly homogeneous over wide parts of the IIR unit. This means that the heat sink is almost constant in these parts.

The modeling and simulation of the micro- and macroscale of the IIR unit gave new insight into the thermal behavior of this mass-transport-limited reactor. This clears the path for an analysis of the interaction between the IIR and the fuel cells to which it is connected. Current works include the development and implementation of similar models for the anode and cathode gas compartments. On the basis of these simulations, a fuel cell stack model will be created. This stack model will then be used to design new IIR units in order to obtain more homogeneous temperature profiles in the fuel cells. This will be a significant contribution to a further improvement in efficiency, lifetime, and, ultimately, economic advantage of MCFC systems.

Notation

Latin Letters

- A = area (m^2)
- D = kinematic diffusivity ($\text{m}^2 \text{s}^{-1}$)
- h = enthalpy (J kg^{-1})
- k_0 = reaction rate coefficient ($\text{kg m}^{-2} \text{s}^{-1}$)
- K = equilibrium constant
- m = mass flow density ($\text{kg m}^{-2} \text{s}^{-1}$)
- M = molar mass (mol kg^{-1})
- p = pressure (Pa)
- p^0 = standard pressure (Pa)
- r_0^Δ = surface reaction rate ($\text{kg m}^{-2} \text{s}^{-1}$)
- r_0^\vee = volume reaction rate ($\text{kg m}^{-3} \text{s}^{-1}$)
- Sc_t = turbulence Schmidt number
- T = temperature (K)
- u = velocity (m s^{-1})
- w = mass fraction
- x = molar fraction

Greek Letters

 λ = thermal conductivity ($\text{W m}^{-1} \text{K}^{-1}$) μ = dynamic viscosity ($\text{kg m}^{-1} \text{s}^{-1}$) μ_t = turbulence dynamic viscosity ($\text{kg m}^{-1} \text{s}^{-1}$) ρ = density (kg m^{-3}) τ = stress tensor ($\text{kg m}^{-1} \text{s}^{-2}$) ν = stoichiometric coefficient

Subscripts

eff = effective

 i = component of the gas mixture

ref = methane reforming reaction

wgsr = water gas shift reaction

Literature Cited

- (1) Bode, M. MTU's HotModule enters dual-fuel operation. *Fuel Cells Bull.* **2005**, 12–14.
- (2) Bottino, A.; Comite, A.; Capannelli, G.; Di Felice, R.; Pinacci, P. Steam reforming of methane in equilibrium membrane reactors for integration in power cycles. *Catal. Today* **2006**, *118*, 214–222A.
- (3) Seo, Y.-S.; Seo, D.-J.; Seo, Y.-T.; Yoon, W.-L. Investigation of the characteristics of a compact steam reformer integrate with a water-gas shift reactor. *J. Power Sources* **2006**, *161*, 1208–1216.
- (4) Lukas, M. D.; Leea, K. Y.; Ghezal-Ayagbh, H. Modeling and cycling control of carbonate fuel cell power plants. *Control Eng. Pract.* **2002**, *10*, 197–206.
- (5) Park, H.-K.; Lee, Y.-R.; Kim, M.-H.; Chung, G.-Y.; Nam, S.-W.; Hong, S.-A.; Limb, T.-H.; Lim, H.-C. Studies of the effects of the reformer in an internal-reforming molten carbonate fuel cell by mathematical modeling. *J. Power Sources* **2002**, *104*, 140–147.
- (6) Heidebrecht, P.; Sundmacher, K. Dynamic model of a cross-flow molten carbonate fuel cell with direct internal reforming (DIR-MCFC). *J. Electrochem. Soc.* **2005**, *152* (11), A2217–A2228.
- (7) Gundermann, M.; Heidebrecht, P.; Sundmacher, K. Validation of a mathematical model using an industrial MCFC plant. *J. Fuel Cell Sci. Technol.* **2006**, *3* (3), 303–307.
- (8) Allen, J. P.; Farooque, M.; Novacco, L. J. U.S. Patent 6,200,696, 2001.
- (9) Bauer, M.; Eigenberger, G. Multiscale modeling of hydrodynamics, mass transfer and reaction in bubble column reactors. *Chem. Eng. Sci.* **2001**, *56*, 1067–1074.
- (10) Li, J.; Kwauk, M. Exploring complex systems in chemical engineering—The multi-scale methodology. *Chem. Eng. Sci.* **2003**, *58*, 521–535.
- (11) Braatz, R. D.; Alkire, R. C.; Rusli, E.; Drews, T. O. Multiscale systems engineering with applications to chemical reaction processes. *Chem. Eng. Sci.* **2004**, *59*, 5623–5628.
- (12) Deen, N. G.; van Sint Annaland, M.; Kuipers, J. A. M. Multiscale modeling of dispersed gas–liquid two-phase flow. *Chem. Eng. Sci.* **2004**, *59*, 1853–1861.
- (13) Vlachos, D. G.; Mhadeshwar, A. B.; Kaisare, N. S. Hierarchical multiscale model-based design of experiments, catalysts, and reactors for fuel processing. *Comput. Chem. Eng.* **2006**, *30*, 1712–1724.
- (14) Reid, R. C. *The properties of gases and liquids*; McGraw-Hill, Inc.: New York, 1987; p 581f.
- (15) Slattery, J. C. *Advanced transport phenomena*; Cambridge University Press: New York, 1999; p 462f.
- (16) Hou, K.; Huges, R. The kinetics of methane steam reforming over a Ni/tt-Al₂O catalyst. *Chem. Eng. J.* **2001**, *82*, 311–328.
- (17) Jarosch, K.; Solth, T. El.; de Lasa, H. I. Modelling the catalytic steam reforming of methane: Discrimination between kinetic expressions using sequentially designed experiments. *Chem. Eng. Sci.* **2002**, *57*, 3439–3451.
- (18) Choi, Y.; Stenger, H. G. Water gas shift reaction kinetics and reactor modeling for fuel cell grade hydrogen. *J. Power Sources* **2003**, *124*, 432–439.
- (19) Abashar, E. E. Coupling of steam and dry reforming of methane in catalytic fluidized bed membrane reactors. *Int. J. Hydrogen Energy* **2004**, *29*, 799–808.
- (20) Versteeg, H. K.; Malalasekera, W. *An introduction to computational fluid dynamics: The finite volume method*; Longman Scientific & Technical: Essex, U.K., 1995.
- (21) Bird, R. B.; Stewart, W. E.; Lightfoot, E. N. *Transport phenomena*, 2nd ed.; John Wiley & Sons, Inc.: New York, 2002.
- (22) Gordon, S.; McBride, B. J. *Computer Program for Calculation of Complex Chemical Equilibrium Compositions and Applications: I. Analysis*; NASA Reference Publication 1311; NASA: Washington, DC, 1994.
- (23) McBride, B. J.; Gordon, S. *Computer Program for Calculation of Complex Chemical Equilibrium Compositions and Applications: II. Users Manual and Program Description*; NASA Reference Publication 1311; NASA: Washington, DC, 1996.

Received for review February 19, 2008

Revised manuscript received April 3, 2008

Accepted April 4, 2008

IE800290H

[PH 4]

P. Heidebrecht, K. Sundmacher

Thermodynamic analysis of a cyclic water gas-shift reactor
(CWGSR) for hydrogen production

Chemical Engineering Science 64 (2009), 5057-5065



Contents lists available at ScienceDirect

Chemical Engineering Science

journal homepage: www.elsevier.com/locate/ces

Thermodynamic analysis of a cyclic water gas-shift reactor (CWGSR) for hydrogen production

P. Heidebrecht^a, K. Sundmacher^{a,b,*}^aMax-Planck-Institute for Dynamics of Complex Technical Systems, Sandtorstrasse 1, 39106 Magdeburg, Germany^bOtto-von-Guericke University, Universitätsplatz 2, 39106 Magdeburg, Germany

ARTICLE INFO

Article history:

Received 12 February 2009

Received in revised form 27 July 2009

Accepted 9 August 2009

Available online 14 August 2009

Keywords:

Fixed bed reactor

Wave theory

Steam-iron process

Water gas-shift reaction

ABSTRACT

The cyclic water gas-shift reactor (CWGSR) is a cyclically operated fixed bed reactor for the removal of carbon monoxide from reformat gases. It is based on the repeated reduction of iron oxide by reformat gases and its subsequent oxidation by steam. To evaluate the thermodynamic limits of this reactor, we develop a model under the assumption of chemical equilibrium. For this purpose, we conduct a wave analysis which shows that the reactor behaviour is dominated by the movement of sharp reaction fronts. Depending on the positions of these fronts at cyclic steady state, five different operating regimes of the CWGSR can be identified. Besides the qualitative analysis of the regimes, the equilibrium model also offers a first quantitative analysis regarding the two performance parameters, i.e. fuel utilisation and product concentration. At 750 °C, a fuel utilisation of 55% can be achieved, and the molar hydrogen fraction in the product stream is up to 70%. The equilibrium model can be used for a first estimate of favourable design and operating parameters of the CWGSR.

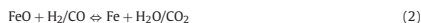
© 2009 Elsevier Ltd. All rights reserved.

1. Introduction

Hydrogen plays an important role in today's chemical industry. Also, in many scenarios of future energy supply systems, hydrogen is considered as a main energy carrier. The main path for hydrogen generation is the steam reforming process, based on fossil fuels or on renewable biomass. Applications like fuel cells, but also some chemical processes, require very pure hydrogen, especially with respect to carbon monoxide. In the classical scheme, a series of two water gas-shift reactors together with a deep-removal reactor (preferential oxidation, palladium membranes, pressure swing adsorption or methanisation) is used to decrease the concentration of carbon monoxide in the reformat gas to sufficiently low levels. While the reforming process operates at temperatures above 700 °C, this cleaning sequence requires the temperature to be lowered to less than 100 °C. Thus, two drawbacks of this process become obvious: the sequence of three reactors with intermediate heat exchangers and the energy loss due to the necessary cooling of the gas.

The cyclic water gas-shift reactor (CWGSR, Fig. 1) (Messerschmitt, 1911) is an alternative to the classical water gas-shift process. It works at temperatures similar to those used in steam reforming

(650–850 °C). Each process cycle is divided into two phases: during the first phase, reformat gas (hydrogen contaminated with carbon monoxide) is fed into a fixed bed of metal oxide. The metal oxide, usually iron oxide, is reduced and the gases are oxidised (Eqs. (1) and (2), forward reaction). After sufficient time, feeds are switched and steam is fed into the reactor. During this second phase, the metal is oxidised again (Eqs. (1) and (2), backward direction), producing a mixture of hydrogen and water which is free of carbon monoxide.



This process has been intensively examined during the last 10 years by a team around Hacker (Fraser et al., 2006; Hacker, 2003; Hacker et al., 1998, 2000). They used commercial iron oxide catalyst pellets and demonstrated the feasibility of the process, evaluated reaction kinetic parameters and proposed a combined process consisting of a reforming reactor and a cyclic water gas-shift reactor. Fraser et al. (2006) presented some theoretical work on the performance of this combined process under equilibrium assumptions. In that study, the CWGSR is considered as a spatially concentrated (CSTR type) reactor. Svoboda et al. (2007) conducted thermodynamic calculations concerning the formation of solid carbon and other undesired solid components.

The analysis in this contribution is based on the wave theory in fixed bed columns such as chromatography (e.g. Rhee et al., 1970;

* Corresponding author.

E-mail addresses: heidebrecht@mpi-magdeburg.mpg.de (P. Heidebrecht), sundmacher@mpi-magdeburg.mpg.de (K. Sundmacher).

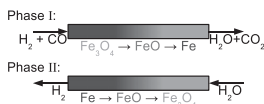


Fig. 1. Principle of the CWGSR.

Helferich and Carr, 1993) and on processes involving precipitation and dissolution of solid species from solutions (Helferich, 1989). The concepts presented in those earlier works are applied here to the class of columns with a reactive fixed bed. This serves for two purposes: to identify the essential difference between a reactor like the CWGSR and other fixed bed processes, and to obtain a conceptual mathematical description of a CWGSR. In opposite to the earlier model based works, this contribution treats the CWGSR as a plug flow reactor and examines the effect of the gas–solid equilibria on the behaviour and performance of the reactor.

Another important aspect in the development of the CWGSR is the development of a suitable fixed bed material. Otsuka et al. (2003) and Takenaka et al. (2004) examine the effect of adding small portions of alumina, molybdenum and cerium to the iron oxide. Galvita and Sundmacher (2007a, 2007b) showed that a mixture of iron oxide with ceria–zirconia combines high activity with good oxygen capacity and low degradation rates. Although these material related issues are essential for a future application of the CWGSR, they are not relevant for the basic behaviour of the reactor and are thus not considered in this contribution.

From the point of view of reactor design, the CWGSR is a complex system: It is spatially distributed and inherently dynamic, it is non-isothermal, it has several gas–solid reactions with discrete equilibria and convective transport phenomena which are superimposed by diffusion processes. Therefore, reactor design should be based on a mathematical model. In a previous publication (Heidebrecht et al., 2008), we used a spatially distributed CWGSR model with finite reaction kinetics to compare co-current and reverse-current operation and to derive some statements about the optimal duration of the phases. Although that model did not consider the multi-step reaction scheme of the iron/iron oxide system, it delivered some basic insight into the process: application of flow reversal, that is gases flowing in opposite direction during oxidation and reduction phase, is advantageous.

In the following, we analyse the basic behaviour of a CWGSR under idealising assumptions such as isothermal conditions, chemical equilibrium and the absence of diffusion. This equilibrium model is easy to solve, it shows the thermodynamic limits of the CWGSR and it can be conveniently used to identify good operating conditions. The purpose of the model is not to precisely predict the reactor performance, but to give a good understanding of the basic reactor behaviour.

2. CWGSR modelling under equilibrium condition

2.1. Model assumptions

The considerations and equations in this section are all derived under the following assumptions:

- Isothermal conditions, $T > 574^\circ\text{C}$.
- Isobaric conditions.
- Ideal plug flow reactor: no radial gradients or axial dispersion.
- Ideal gas.
- Chemical equilibrium between gas and solid phases.

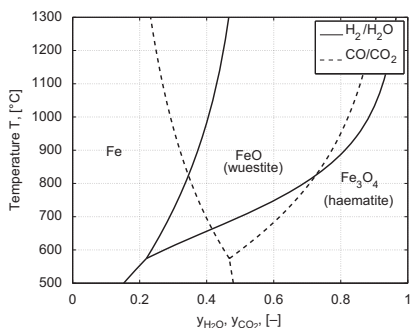


Fig. 2. Equilibrium lines of the systems $\text{H}_2/\text{H}_2\text{O}$ and CO/CO_2 over iron/iron oxide.

- Occurrence of magnetite (Fe_2O_3) is negligible under normal operating conditions.
- The possibility of carbonisation is not considered.
- Reversed flow is applied (see Fig. 1).
- The duration of each phase is significantly longer than the gas residence time, so gas phase balances are considered to be in quasi steady state.
- The duration of each phase is significantly shorter than the time needed for complete conversion of the fixed bed.
- The feed gas during the first phase is in equilibrium with iron, and the feed gas during the second phase is in equilibrium with haematite (Fe_3O_4).
- Constant feed flow rates during each phase.

Regarding the assumption of chemical equilibrium, Fig. 2 shows the equilibrium lines for the two relevant reacting systems: iron/iron oxide under atmospheres of steam/hydrogen and under carbon dioxide/carbon monoxide. Note that at most points in this diagram (each point defined by a gas composition and temperature), the gas phase is in equilibrium with a pure solid phase of iron, wuestite or haematite. Only for combinations of gas compositions and temperatures that fall exactly on one of the equilibrium lines, any mixture of the neighbouring solid species may exist.

Note that the equilibrium lines are independent from the total gas pressure, because the reactions are equimolar with respect to the reactants in the gas phase.

2.2. Wave analysis

In this chapter, we apply the wave theory to reacting fixed bed reactors such as the CWGSR. With this, we not only motivate and derive the model equations used in Chapter 2.3, but we also identify the essential difference between reacting fixed bed processes and other fixed bed reactors. Any reader more interested in the results rather than in the derivation of this model may skip this chapter and continue reading with Chapter 2.3.

Wave theory has been applied to fixed bed reactors before, as has been stated in the introduction section. In the following derivation, we frequently refer to the work by Helferich (1989), who applied this theory to fixed bed reactors with precipitation and dissolution.

Consider the CWGSR as a fixed bed reactor, in which oxygen can be transferred from the gas phase to the solid phase and vice versa.

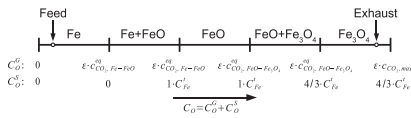


Fig. 3. Phase diagram of a CWGSR under CO/CO₂ atmosphere.

In this sense, the CWGSR is similar to a precipitation/dissolution reactor. Consider further operating the reactor during a reduction phase with a gas mixture of carbon monoxide and carbon dioxide. To characterize the composition in the gas and in the solid phase at any point in the reactor, define the total oxygen content:

$$C_O = \varepsilon \cdot c_{CO_2} + 1 \cdot C_{FeO} + 4 \cdot C_{Fe_3O_4} = C_O^g + C_O^s \quad (3)$$

where ε is the gas volume fraction, and c_{CO_2} is the molar concentration of carbon dioxide in the gas phase. C_{FeO} and $C_{Fe_3O_4}$ are the molar amounts of the iron oxide species, related to the total reactor volume (that is gas phase volume plus solid phase volume). Note that only those oxygen atoms are accounted for which may participate in the reaction: only one oxygen atom may be transferred to the solid phase from carbon dioxide. The oxygen atom in carbon monoxide cannot be transferred, so it is not counted here. The total oxygen content can be split into the oxygen content of the gas phase, C_O^g , and that of the solid phase, C_O^s .

The solid concentrations obey one equality constraint:

$$C_{Fe} + C_{FeO} + 3 \cdot C_{Fe_3O_4} = C_{Fe}^f \quad (4)$$

Eq. (4) states that iron atoms occur in the form of iron, wuestite or haematite, but the total amount of iron atoms per reactor volume is fixed. Pure iron is described by $C_{Fe} = C_{Fe}^f$ and $C_{FeO} = C_{Fe_3O_4} = 0$, while pure haematite corresponds to $3 \cdot C_{Fe_3O_4} = C_{Fe}^f$ and $C_{Fe} + C_{FeO} = 0$.

For isothermal conditions, under chemical equilibrium conditions and in the absence of dissipation (see assumptions, Chapter 2.1) and with the help of the corresponding equilibrium diagram (Fig. 2), a phase diagram as shown in Fig. 3 can be constructed. At zero and very low total oxygen content, the gas phase is in equilibrium with pure iron, and the carbon dioxide fraction increases with increasing oxygen content ($0 < c_{CO_2} < c_{CO_2, Fe-FeO}^{eq}$). As soon as the gas composition reaches the first equilibrium line, a further increase of oxygen content leads to an increase of the wuestite fraction, while the gas composition stays constant ($c_{CO_2} = c_{CO_2, Fe-FeO}^{eq}$). For sufficiently high oxygen content, all iron appears in the form of wuestite, and the carbon dioxide fraction is increased further ($c_{CO_2, Fe-FeO}^{eq} < c_{CO_2} < c_{CO_2, FeO-Fe_3O_4}^{eq}$). This region is then followed by a mixture of wuestite and haematite with constant gas composition ($c_{CO_2} = c_{CO_2, FeO-Fe_3O_4}^{eq}$), and finally a region with pure haematite and increasing carbon dioxide fraction, until the gas phase contains no more carbon monoxide ($c_{CO_2, FeO-Fe_3O_4}^{eq} < c_{CO_2} < c_{max}$).

Assuming that the feed gas during the reduction phase contains mainly carbon monoxide, the feed point in the phase diagram is located in the Fe-region. Assuming further that there is some pure haematite left at the end of the reactor, the end point is situated in the Fe₃O₄-region. These two points define the initial profile in the reactor, which stretches over all five regions. For illustration, this may correspond to an initial condition where the whole fixed bed is completely oxidised and where the gas has very high carbon dioxide concentration, except for the feed position, where the fraction of carbon dioxide is small.

In the following, we apply the wave theory developed by Helfferich (1989) to each of these regions. In regions with

continuously differentiable composition profiles, the wave velocity is calculated from

$$w = u \cdot \frac{\partial C_O^g}{\partial C_O} \quad (5)$$

For the first, the third and the fifth region, (those with pure iron, wuestite or haematite), solid composition may not change under equilibrium condition, so $dC_O = dC_O^g + dC_O^s = dC_O^g$ with arbitrary dC_O^g . Inserting this into Eq. (5) yields that in these regions, waves travel with the convective velocity of the gas:

$$w_{Fe} = w_{FeO} = w_{Fe_3O_4} = u \quad (6)$$

In the mixed solid regions (second and fourth region), the gas composition may not change, so $dC_O = dC_O^g + dC_O^s = dC_O^s$ and $dC_O^g = 0$. So at first glance, these regions have standing waves. However, these standing waves are preceded by fast waves upstream, which is why they form shocks after sufficient time. As soon as these two regions have attained their shock profile, and as soon as a whole gas residence time has passed, there are only three regions with finite length in the reactor: first, the region with pure iron, next with pure wuestite and finally the region with pure haematite. At the boundaries between these regions, the shocks form step-like transitions in solid and gas phase compositions. In the Fe-region, the gas composition equals the feed composition. In the wuestite region, the gas composition is equal to the equilibrium composition between iron and wuestite. In the haematite region, it is equal to the equilibrium line between wuestite and haematite.

With these gas compositions at the upstream and downstream ends of the shocks, the shock velocities can be calculated. According to Helfferich (1989), an integral form of Eq. (5) has to be applied:

$$w = u \cdot \frac{\Delta C_O^g}{\Delta C_O} = u \cdot \frac{\Delta C_O^g}{\Delta C_O^g + \Delta C_O^s} = u \cdot \frac{\varepsilon \cdot \Delta c_{CO_2}}{\varepsilon \cdot \Delta c_{CO_2} + \Delta C_O^s} \quad (7)$$

For the case of the CWGSR, typical differences of oxygen content in both phases at a front can be estimated. This reveals that the solid oxygen capacity, ΔC_O^s , is usually about four orders of magnitude higher than the change in gas phase oxygen content, ΔC_O^g (see Appendix A). This gives rise to the following slightly simpler equation for the shock velocities:

$$w \approx u \cdot \frac{\Delta C_O^g}{\Delta C_O^s} \quad (8)$$

Thus, the shock velocities are

$$w_{Fe-FeO} = u \cdot \frac{\varepsilon \cdot (c_{CO_2, Fe-FeO}^{eq} - c_{CO_2, feed})}{1 \cdot C_{Fe}^f - 0 \cdot C_{Fe}^f} = \frac{u \cdot \varepsilon}{\Delta C_{Fe-FeO}} \cdot (c_{CO_2, Fe-FeO}^{eq} - c_{CO_2, feed}) \quad (9)$$

$$w_{FeO-Fe_3O_4} = u \cdot \frac{\varepsilon \cdot (c_{CO_2, FeO-Fe_3O_4}^{eq} - c_{CO_2, Fe-FeO}^{eq})}{\frac{4}{3} \cdot C_{Fe}^f - 1 \cdot C_{Fe}^f} = \frac{u \cdot \varepsilon}{\Delta C_{FeO-Fe_3O_4}} \cdot (c_{CO_2, FeO-Fe_3O_4}^{eq} - c_{CO_2, Fe-FeO}^{eq}) \quad (10)$$

These shocks are also maintained during the oxidation phase with reversal of the flow direction. After a time span corresponding to the gas residence time in the reactor, the fronts are then moving in the opposite direction at different velocities. Due to the fact that the durations of the reduction and the oxidation phase are assumed to be much longer than the gas residence time, this shock movement happens with constant velocity during most of the time of each phase.

The results of this wave analysis illuminate the differences between reacting fixed beds like the CWGSR and other fixed bed

reactors. In adsorption columns such as chromatographic columns, compositions in the gas phase and in the solid (adsorbed) phase are uniquely related to each other under equilibrium conditions. This relationship is continuously differentiable. In reacting fixed beds, the gas phase composition determines the solid phase composition (except in those regions travelling as shocks), but the solid composition does not uniquely determine the gas phase composition. This relationship is discrete. In adsorption beds, the occurrence of shock depends on the nonlinearity of adsorption isotherms (see Glöckler et al., 2003), while transitions in reacting fixed beds always occur as shocks. Thus, adsorption reactors are quite different from reacting fixed beds.

The precipitation/dissolution reactor discussed by Helfferich (1989) has more in common with the reacting fixed bed. In precipitation, the liquid phase composition determines whether precipitation occurs or whether dissolution is possible, which is called metasomatic behaviour. This is essentially the same in reacting fixed beds: the gas composition determines whether reduction or oxidation of the solid is possible. However, there is one difference between a precipitation reactor and a reacting fixed bed: the latter has a defined capacity. That means that if an oxidising gas enters the reactor over a fully oxidised solid phase, the gas is going to pass unchanged, because the solid phase capacity is exploited. At the end of the fully oxidised region, when the gas encounters a less oxidised solid phase, a shock occurs and the fully oxidised region grows in downstream direction. In a precipitation reactor, feeding a supersaturated solution over a precipitate bank causes precipitation at the feed position, whereas the amount of precipitate grows towards infinity at the inlet. The occurrence of shocks at both ends of a region of the solid phase is the difference between these two reactors. This also has an impact on the overall reactor behaviour.

2.3. The CWGSR front model

As shown in the previous section, three regions evolve in the CWGSR. These consist of solid phases of pure iron, wuestite or haematite, respectively. The regions are separated by reaction fronts (called shocks in wave theory) which move in downstream direction of the gas flow at a considerably slower velocity compared to the convective gas velocity. In extension to the derivation in the previous chapter, in a typical CWGSR, a mixture of carbon monoxide/carbon dioxide and hydrogen/steam is fed during cycle phase 1 (reduction), and pure steam is fed during phase 2 (oxidation). This situation together with the movement direction of the fronts is illustrated in Fig. 4. The presence of both carbon monoxide and hydrogen during the reduction phase leads to a superposition of the front velocities caused by both reacting systems, shown here for the first front (Fe–FeO):

$$w_{\text{Fe-FeO}}^I = \frac{\varepsilon \cdot u^I}{\Delta C_{\text{Fe-FeO}}} \cdot (c_{\text{H}_2\text{O,Fe-FeO}}^{\text{eq}} - c_{\text{H}_2\text{O,feed}}^I + c_{\text{CO}_2,\text{Fe-FeO}}^{\text{eq}} - c_{\text{CO}_2,\text{feed}}^I) \quad (11)$$

Because the reactions are equimolar with respect to the gas phase (one mole of hydrogen forms one mole of water, one mole of carbon monoxide forms one mole of carbon dioxide), and due to the assumptions of constant temperature, pressure and feed flow rate, the gas velocity is constant during each cycle phase and identical to its value at feed position.

The equilibrium lines are represented depending on relative molar fractions, so we first replace the product of velocity and molar concentration by the product of molar flow density and

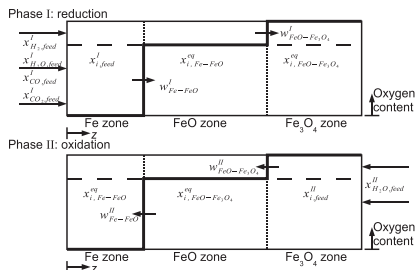


Fig. 4. Moving fronts in the equilibrium model.

molar fraction:

$$w_{\text{Fe-FeO}} = \frac{\varepsilon \cdot g_{\text{feed}}^I}{\Delta C_{\text{Fe-FeO}}} \cdot (x_{\text{H}_2\text{O,Fe-FeO}}^{\text{eq}} - x_{\text{H}_2\text{O,feed}}^I + x_{\text{CO}_2,\text{Fe-FeO}}^{\text{eq}} - x_{\text{CO}_2,\text{feed}}^I) \quad (12)$$

The relative molar fractions are defined as:

$$y_{\text{H}_2\text{O}} = \frac{x_{\text{H}_2\text{O}}}{x_{\text{H}_2} + x_{\text{H}_2\text{O}}}; \quad y_{\text{CO}_2} = \frac{x_{\text{CO}_2}}{x_{\text{CO}} + x_{\text{CO}_2}} \quad (13)$$

Because of the equimolar reactions and the assumptions of quasi steady-state gas phase, the denominators in Eq. (13) are constant in space and time. They are identical to their values at feed conditions. These denominators describe the fraction of hydrogen species ($\text{H}_2 + \text{H}_2\text{O}$) and carbon species ($\text{CO} + \text{CO}_2$) in the gas. For convenience, they are denoted Y :

$$Y_{\text{H}}^{\text{II}} = x_{\text{H}_2}^{\text{II}}(z, t) + x_{\text{H}_2\text{O}}^{\text{II}}(z, t) = x_{\text{H}_2,\text{feed}}^{\text{II}} + x_{\text{H}_2\text{O},\text{feed}}^{\text{II}} \quad (14)$$

$$Y_{\text{C}}^{\text{II}} = x_{\text{CO}}^{\text{II}}(z, t) + x_{\text{CO}_2}^{\text{II}}(z, t) = x_{\text{CO,feed}}^{\text{II}} + x_{\text{CO}_2,\text{feed}}^{\text{II}} \quad (15)$$

Substituting the molar fractions in Eq. (12) by relative molar fractions, the velocity reads:

$$w_{\text{Fe-FeO}}^I = \frac{\varepsilon \cdot g_{\text{feed}}^I}{\Delta C_{\text{Fe-FeO}}} \cdot (Y_{\text{H}}^I \cdot (y_{\text{H}_2\text{O,Fe-FeO}}^{\text{eq}} - y_{\text{H}_2\text{O,feed}}^I) + Y_{\text{C}}^I \cdot (y_{\text{CO}_2,\text{Fe-FeO}}^{\text{eq}} - y_{\text{CO}_2,\text{feed}}^I)) \quad (16)$$

The equilibrium values in this equation can be obtained directly from the equilibrium diagram (Fig. 2). Analogously, the velocity for the second front during phase I and the velocities of both fronts during phase II is obtained as:

$$w_{\text{FeO-Fe}_3\text{O}_4}^I = \frac{\varepsilon \cdot g_{\text{feed}}^I}{\Delta C_{\text{FeO-Fe}_3\text{O}_4}} \cdot (Y_{\text{H}}^I \cdot (y_{\text{H}_2\text{O,FeO-Fe}_3\text{O}_4}^{\text{eq}} - y_{\text{H}_2\text{O,Fe-FeO}}^{\text{eq}}) + Y_{\text{C}}^I \cdot (y_{\text{CO}_2,\text{FeO-Fe}_3\text{O}_4}^{\text{eq}} - y_{\text{CO}_2,\text{Fe-FeO}}^{\text{eq}})) \quad (17)$$

$$w_{\text{FeO-Fe}_3\text{O}_4}^{\text{II}} = \frac{\varepsilon \cdot g_{\text{feed}}^{\text{II}}}{\Delta C_{\text{FeO-Fe}_3\text{O}_4}} \cdot Y_{\text{H}}^{\text{II}} \cdot (y_{\text{H}_2\text{O,feed}}^{\text{II}} - y_{\text{H}_2\text{O,FeO-Fe}_3\text{O}_4}^{\text{eq}}) \quad (18)$$

$$w_{\text{Fe-FeO}}^{\text{II}} = \frac{\varepsilon \cdot g_{\text{feed}}^{\text{II}}}{\Delta C_{\text{Fe-FeO}}} \cdot Y_{\text{H}}^{\text{II}} \cdot (y_{\text{H}_2\text{O,FeO-Fe}_3\text{O}_4}^{\text{eq}} - y_{\text{H}_2\text{O,Fe-FeO}}^{\text{eq}}) \quad (19)$$

In these equations, the gas volume fraction is constant, the solid oxygen capacities are material constants and the equilibrium molar fractions are fixed once the temperature is chosen. Usually, the feed compositions and the molar flow rates are given by the product specifications of the preceding processes, so they can be considered

as given parameters. With that, the velocities of the two fronts during both cycle phases can be calculated.

To describe the average front velocities during each cycle, the phase durations have to be considered as well. With the relative duration of the reduction phase

$$S^I = \frac{t^I}{t^I + t^{II}} \quad (20)$$

we get for the average front velocities

$$\bar{w}_{\text{Fe-FeO}} = S^I \cdot w_{\text{Fe-FeO}}^I + (1 - S^I) \cdot w_{\text{Fe-FeO}}^{II} \quad (21)$$

$$\bar{w}_{\text{FeO-Fe}_3\text{O}_4} = S^I \cdot w_{\text{FeO-Fe}_3\text{O}_4}^I + (1 - S^I) \cdot w_{\text{FeO-Fe}_3\text{O}_4}^{II} \quad (22)$$

These velocities describe the movement of the reaction fronts averaged over one cycle. They are valid only if the fronts can move freely, that is as long as they are moving somewhere inside the reactor. If, after a finite number of cycles, one front reaches one end of the reactor, its movement is hindered during one of the two phases. The front then still moves forward and backward, but it hits the end of the reactor during each cycle. Thereby its average velocity becomes zero. Although Eqs. (21) and (22) are no longer applicable in this case, they indicate at which end of the reactor each front is going to stay after a finite number of cycles.

3. Results of the equilibrium model

3.1. Qualitative results: operating regimes

The CWGSR is supposed to be operated at a cyclic steady state. This includes that the operating conditions like flow rates and phase durations are the same during each cycle. After a complete cycle is performed, the fronts have moved forward and backward and ended at their initial positions. For each front, there are three possibilities: the average velocity may be negative, positive or equal to zero. If it is positive, the front is moving towards the right hand side of the reactor, if it is negative, it moves to its left hand side. Although the front still moves forward and backward during each cycle, at cyclic steady state it will always stay close to one end of the reactor, depending on the sign of its average velocity. The case where the average velocity is exactly zero is just between these two cases. The front moves forward and backward again at any position within the reactor. Realising an average velocity of precisely zero is very difficult in practise, so we do not discuss this case explicitly here. This case automatically appears at the boundary between the two other cases.

In a system with two reaction fronts, and with two possible positions for each front at cyclic steady state, there are four different operating regimes for the reactor. These are depicted in Fig. 5. In regime 1, the duration of the first phase is relatively long (S^I close to 1), so both average velocities are positive and both reaction fronts move forth and back in the vicinity of the right hand side of the reactor. During phase I, the fixed bed is completely reduced and it is expected that considerable amounts of combustible gas pass the reactor unused. However, during the short oxidation phase, the product gas is in equilibrium with pure iron, so maximum hydrogen concentration is obtained.

Regime 3 is the direct opposite to this case. Here, the first phase is quite short, so both average front velocities are negative, causing the fronts to stay close to the left hand side. During the short reduction phase, the exhaust gas is in equilibrium with haematite, so it is oxidised as far as thermodynamically possible. But, only during the first part of the oxidation phase, the gas is in equilibrium with iron, so during most of the second phase, only low concentrations of hydrogen are produced.

Regime 2 is between these two regimes. The iron–wuestite front is moving left, while the wuestite–haematite front shows a positive

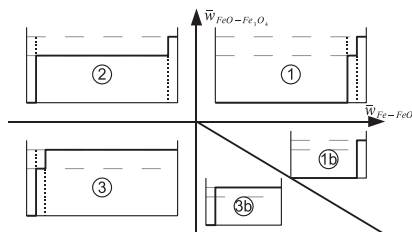


Fig. 5. Operating regimes according to the equilibrium model.

Table 1
Assumed feed gas compositions during oxidation and reduction phase.

Phase	x_{H_2}	$x_{\text{H}_2\text{O}}$	x_{CO}	x_{CO_2}	(CH_4)	Y_{H}	Y_{C}	$y_{\text{H}_2\text{O,red}}$	$y_{\text{CO,red}}$
I	0.65	0.11	0.17	0.04	(0.03)	0.76	0.21	0.14	0.19
II	0	1	0	0	(0)	1	0	1	

velocity. Most of the fixed bed is filled with wuestite. During a part of the reduction phase, haematite is present at the gas exit, providing a high fuel gas utilisation. Also, iron is present during a part of the oxidation phase, resulting in a high concentration of hydrogen during the oxidation phase.

In principle, the fourth combination would be that the iron–wuestite front is at the right end and the wuestite–haematite front is at the left end of the reactor. This is an irregular combination, because the sequence of the fronts cannot be reversed in this reactor: the wuestite zone has to be located to the right of the iron–wuestite front and to the left of the wuestite–haematite front. Thus, the two fronts are moving together as one front and there is no wuestite zone between them. The velocity of this common front is an average of the two individual front velocities:

$$\bar{w}_{\text{Fe-Fe}_3\text{O}_4} = \frac{\bar{w}_{\text{Fe-FeO}} \cdot \Delta C_{\text{Fe-FeO}} + \bar{w}_{\text{FeO-Fe}_3\text{O}_4} \cdot \Delta C_{\text{FeO-Fe}_3\text{O}_4}}{\Delta C_{\text{Fe-FeO}} + \Delta C_{\text{FeO-Fe}_3\text{O}_4}} \quad (16)$$

This velocity may have a positive or a negative sign, too. Thus this case is subdivided into two cases: one with a common front at the left side and one where the common front is at the right end of the reactor. The behaviour of these two sub-cases corresponds to regimes 1 and 3, respectively.

For given feed gas compositions and molar feed flow rates, the operation regime depends only on two parameters: the reactor temperature and the relative phase duration. To give an example, certain feed gas compositions are assumed (Table 1). The feed gas during phase I corresponds to the equilibrium product of methane steam reforming with a steam-to-carbon ratio of 1.5. In Fig. 6, the different regimes are shown for these parameter values in dependence of the two parameters, temperature and relative phase duration.

At temperatures above 735 °C, regimes 1–3 (right/right, left/right and left/left) occur. There, starting from high relative phase durations (large S^I), both fronts are on the right (regime 1), because they move to the right for a long time, and then back again only for a considerably shorter time. When the relative phase duration is decreased, the Fe–FeO front velocity changes its sign and it moves to the left end (regime 2). Finally, for sufficiently low values of S^I , both fronts are at the left hand side and the reactor falls into regime 3.

At a temperature of about 735 °C, regime 2 ceases to exist and the areas of regime 1 and 3 touch in a single point. Below this temperature, regimes 1b and 3b appear between regimes 1 and 3. With

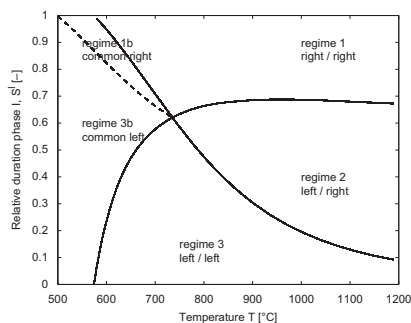


Fig. 6. Regime diagram for feed gas compositions from Table 1.

both fronts at the right hand side, regime 1b is very similar to regime 1, and with both fronts at the left hand side, regimes 3b and 3 are alike. There is no regime with separate fronts between regime 3/3b and 1/1b, which is the main difference to the reactor behaviour at temperatures above 735 °C.

The separating lines between the regimes, which are plotted in Fig. 6, are the positions where one of the front velocities becomes zero. At the line between regimes 1 and 2, $\dot{w}_{FeO-FeO} = 0$, and between regimes 2 and 3, $\dot{w}_{FeO-FeO} = 0$. The separation line between regime 1b and 3b is marked by $\dot{w}_{Fe-FeO} = 0$.

The range of existence of each regime changes with temperature, because the positions of the equilibria are temperature dependent. At about 735 °C, the two separation lines cross, and regime 2 ceases to exist below that temperature. Whether this occurs in a regime diagram and at what temperature depends on the set of feed conditions. There are feed conditions where the three regimes exist across the whole temperature range. However, in the case here, regimes 1b and 3b occur below this temperature.

At 574 °C, the equilibrium lines iron-wüstite and wüstite-haematite intersect and wüstite ceases to exist as a thermodynamically stable phase. This is a thermodynamic fact and independent from the feed conditions. Below this temperature, the system has only one reaction front. In the regime diagram, regimes 1 and 3 exist only above this temperature. In the case plotted here, regimes 1b and 3b occur at these low temperatures. These regimes only have one single front, which very well corresponds to the thermodynamic facts. At about 500 °C, regime 1b also ends. This is because with lower temperatures, higher hydrogen contents are needed in the gas to reduce haematite to iron. Below the temperature where the equilibrium line reaches the fuel gas composition, reduction becomes impossible and the front can only be at the left end of the reactor.

These qualitative results show that a CWGSR has a complex behaviour. The equilibrium model reveals that depending on the relative phase duration and the reactor temperature, the CWGSR operates in quite different regimes. This is valuable knowledge for the design of the reactor. Experimental results and simulation data obtained from more detailed models can be interpreted better with these results in mind.

3.2. Quantitative results

To quantify the performance of the CWGSR under specified operating conditions, we consider two measures. The first measure is the

Table 2

Average molar fraction of hydrogen in the exhaust gas during oxidation phase.

Regime	Average molar fraction of hydrogen in product stream
1	$\bar{x}_{H_2, out}^{ox} = x_{H_2, Fe-FeO}^{eq}$
2	$\bar{g}_{H_2, out}^{ox} = (1 - S') \cdot \bar{x}_{H_2, FeO-FeO}^{eq} + S' \cdot \bar{w}_{Fe-FeO} \cdot \Delta C_{Fe-FeO}$
3	$\bar{g}_{H_2, out}^{ox} = (1 - S') \cdot \bar{x}_{H_2, FeO-FeO}^{eq} + S' \cdot \bar{w}_{FeO-FeO} \cdot \Delta C_{FeO-FeO} + S' \cdot \bar{w}_{Fe-FeO} \cdot \Delta C_{Fe-FeO}$
3b	$\bar{g}_{H_2, out}^{ox} = (1 - S') \cdot \bar{x}_{H_2, FeO-FeO}^{eq} + S' \cdot \bar{w}_{FeO-FeO} \cdot \Delta C_{FeO-FeO} + S' \cdot \bar{w}_{Fe-FeO} \cdot \Delta C_{Fe-FeO}$
1b	$\bar{x}_{H_2, out}^{ox} = x_{H_2, Fe-FeO}^{eq}$

average concentration of hydrogen in the reactor outlet during the oxidation phase. Usually, this product is a mixture of steam and hydrogen, and one prefers high hydrogen contents. Table 2 lists equations for the average molar fraction of hydrogen at the outlet during the oxidation phase for each regime. The second measure is the fuel gas utilisation. This is the ratio between the amount of fuel gas that is consumed in the reduction of the fixed bed and the total amount of fuel gas fed into the reactor during the reduction phase. If the cyclic steady state is considered, the amount of consumed fuel gas and the amount of hydrogen produced during each cycle are identical. Thus the average molar fraction of hydrogen can be used to calculate the fuel utilisation:

$$\eta_{fuel} = \frac{g_{red}^{H_2} \cdot (1 - S') \cdot \bar{x}_{H_2, out}^{ox}}{g_{feed}^{H_2} \cdot S' \cdot (x_{H_2, feed} + x_{CO, feed})} \quad (17)$$

Fig. 7 shows that fuel utilisation is maximal for short reduction phase duration (low S') and at high temperatures, in regime 3. In this region, the exhaust gas during phase I is in equilibrium with haematite, which guarantees the highest possible conversion of the fuel gas during the whole phase I. In addition, the wüstite-haematite equilibrium lines shift to lower contents of hydrogen and carbon monoxide with increasing temperature, so fuel utilisation increases with temperature.

The maximum hydrogen content is obtained at different operating conditions, as shown in Fig. 8. At high relative phase duration S' , both reaction fronts are located at the right hand side of the reactor (regime 1). During the whole oxidation phase, the exhaust gas is in equilibrium with Fe, which gives the highest possible hydrogen content. The iron-wüstite equilibrium line under a mixture of hydrogen and steam shifts to higher hydrogen contents with decreasing temperature, so low temperatures are preferred here.

The two diagrams indicate that the maximum fuel utilisation obtainable for the given feed gas and iron/iron oxide as a fixed bed material is at about 90% and would be even higher at higher temperatures. Temperature limitations have a considerable impact on the maximum utilisation. At 750 °C, which is the preferred operating temperature of the actual fixed bed material, the maximum fuel utilisation decreases to 55%. In the product gas, hydrogen contents of nearly 80% are possible at low temperatures (the rest of the product gas is steam). At 750 °C, the hydrogen content can be up to 70%.

The obtainable fuel utilisation and hydrogen content depend on the fuel gas used. For a given temperature, the relative molar fractions at the wüstite-haematite equilibrium lines are fixed. The positions of these equilibria for hydrogen/steam and carbon monoxide/carbon dioxide determine the exhaust gas composition during the reduction process (phase I). The farther away the fuel gas composition is from this equilibrium composition, the higher the possible utilisation of the fuel gas becomes. A lean reformate gas with high contents of carbon dioxide and steam yields low fuel utilisations in the CWGSR. To give an example: if the fuel gas originates from a steam reforming process, then low steam to carbon ratio (about 1.5) is preferred because this leads to large fractions of hydrogen and carbon monoxide and therefore to high degrees of fuel utilisation in the CWGSR. In contrast to this, if a classical sequence (high and low temperature shift reactor plus preferential oxidation) is applied, one

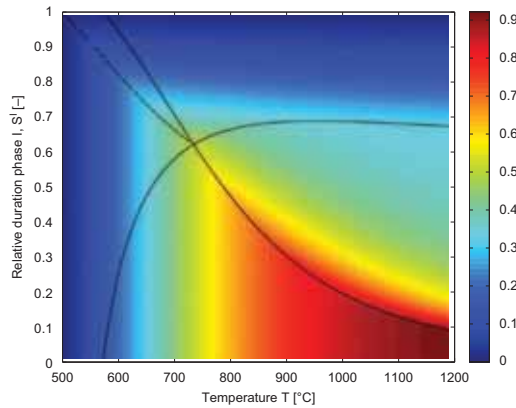


Fig. 7. Fuel utilisation corresponding to the system shown in Fig. 6.

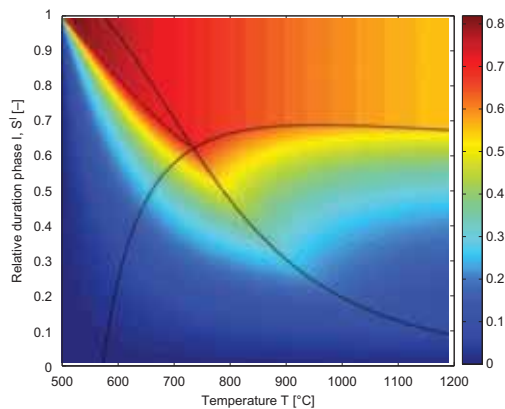


Fig. 8. Average hydrogen concentration corresponding to the system shown in Fig. 6.

usually aims at high methane conversion and low carbon monoxide contents in the reforming process, so a high steam to carbon ratio is favoured.

According to the example presented in Figs. 7 and 8, the maxima of fuel utilisation and hydrogen content do not fall together: while regime 1 favours high hydrogen contents, especially at low temperatures, regime 3 offers good fuel utilisation, especially at high temperatures. Therefore, the optimum point (or area) of operation is not obvious and must be discussed in more detail.

For a given temperature, say 850 °C, the cross sections of the profiles from Figs. 7 and 8 are plotted in Fig. 9. One can observe that

fuel utilisation is constant in regime 3 and the same holds for the hydrogen content in regime 1. So, it seems advisable to operate the CWGSR at the right border of regime 3 or the left border of regime 1, or somewhere in between these two points. Thus, the optimum operating point is somewhere in regime 2, where both fronts are located at opposite ends of the reactor.

A more precise analysis depends on the particular application of the CWGSR. If high water contents in the product hydrogen are acceptable, then one would prefer to operate the CWGSR at the boundary between regimes 3 and 2 in order to obtain the highest fuel utilisation possible. The other boundary is preferred in case if

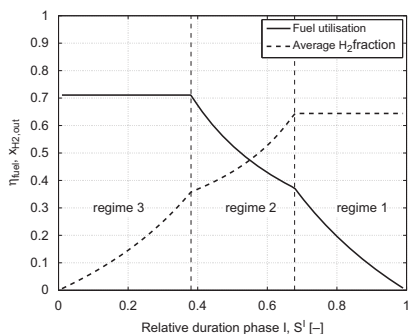


Fig. 9. Fuel utilisation and average hydrogen content at $T = 850^\circ\text{C}$ (cross section through the profiles displayed in Figs. 7 and 8).

steam in the product hydrogen should be minimised and the fuel utilisation is less important.

These quantitative conclusions can be drawn from the equilibrium model for any feed composition. For a more precise evaluation, one needs to weigh and add the two criteria. In addition, one may add another term considering the decreased lifetime of the fixed bed at higher temperatures, or simply impose an upper bound on the temperature in order to limit the degradation rate. The resulting function may be plotted in the same coordinates as Figs. 6–8 and the optimal operating conditions be found graphically.

In a real reactor, some of the model assumptions are invalid. Most importantly, the equilibrium assumption and the plug flow assumption are not applicable in that case. This means that compared to the results shown here, the reaction fronts in a real reactor are not sharp, but they are stretched along the axial coordinate of the reactor. This leads to a decrease in gas phase conversions and thereby a decrease of reactor efficiency. In addition, the boundaries between the different operating regimes are expected to be less sharp. A direct comparison of the theoretical predictions with experimental values is not possible at this time. Although numerous experimental studies have been published (see introduction section), they usually apply spatially concentrated reactors far from chemical equilibrium in order to obtain kinetic data. The behaviour of such reactors is not dominated by the movement of the reaction fronts and is thus not comparable to the theoretical calculations given here.

3.3. Influence of non-isothermal temperature profiles

The assumption of isothermal conditions in the thermodynamic model helped to reduce the number of model variables to the minimum. Introducing the energy balance into the model would also require additional parameters, such as the heat capacity of the fixed bed (which may vary for different designs of the material), the estimated heat exchange parameters across the reactor wall or the effective thermal conductivity of the fixed bed. These additional parameters would have added to the complexity of the model without contributing to the understanding of the basic behaviour of the reactor, which is why the energy balance was left out.

However, with the results discussed in the previous sections and the equilibrium diagram in Fig. 2, one can now qualitatively discuss the impact of non-homogeneous temperature profiles. Assume

a nominal reactor temperature and a deviation of, say, 50K from it at one of the reaction fronts. Such a temperature difference is realistic (see Thaler et al., 2006), and it may be an upper limit that can be tolerated with respect to degradation issues. As a consequence, the position of the equilibrium of this front changes by several percent in relative molar fractions, $y_{\text{H}_2\text{O}}$ and y_{CO_2} . This has a certain impact on the front velocities and thereby on the borders of some of the operating regimes in Fig. 6. However, this is only a quantitative change. The qualitative conclusions about the different operating regimes and the analysis of suitable operating conditions are still valid under non-isothermal conditions.

4. Conclusions and outlook

The CWGSR is a cyclic fixed bed reactor in which the fixed bed material not only acts as a promoter for the reactions, but it is a reactant itself. This fact together with the discrete character of gas–solid reaction equilibria creates reaction fronts in the CWGSR when operated at or close to equilibrium conditions. This discriminates it from many classical fixed bed reactors.

As a step towards the proper design and operation of this reactor and other similar gas–solid reactors, the equilibrium model is a suitable tool for its thermodynamic evaluation and to estimate preferable design parameters and operating conditions. Due to the assumption of heterogeneous chemical equilibrium between the gas phase and the fixed bed, no spatially distributed model is required, but only the description of reaction front velocities. With the averaging of the state variables over one cycle, the model consists of a few explicit algebraic equations. They describe the average velocities of the reaction fronts and thereby their position at cyclic steady state.

For a given fuel gas composition, these positions vary depending on the relative duration of the cycle phases and on the assumed reactor temperature. These positions determine the reactor behaviour. In a qualitative analysis, up to five different regimes have been identified under identical feed gas conditions. Knowledge of these regimes and their area of occurrence is an important base for system design.

In a quantitative analysis, the model reveals the limits of the CWGSR performance. For a temperature of 750°C , which is preferable for an iron oxide based material, about 50% of the assumed reformat gas can be converted, and a mixture of 70% hydrogen and 30% steam can be obtained. Furthermore, the model has been used to identify suitable windows of operating conditions. Although there is no obvious point of optimal operating conditions for all cases and applications, the model indicates that a favourable operating regime has the iron–wuestite reaction front and the wuestite–haematite front at opposite ends of the reactor (regime 2).

The equilibrium model revealed several basic features of the CWGSR. Future developments include the spatially distributed modelling of the reactor together with a series of kinetic measurements for the estimation of the reaction kinetic parameters. Based on the insights from the equilibrium model and using the detailed information from the spatially distributed model, optimised reactor design, operation and control will be developed. The results will then be validated with experiments using a mini plant.

Notation

C_i	molar amount of solid species i per reactor volume, mol m^{-3}
c_i	molar concentration of gas species i (per gas volume), mol m^{-3}
C_{Fe}^t	total amount of iron atoms per reactor volume, mol m^{-3}
C_{O}	total oxygen content per reactor volume, mol m^{-3}

$C_D^{S/G}$	oxygen content solid/gas phase per reactor volume, mol m ⁻³
g	molar flow density, mol m ⁻² s ⁻¹
S^I	relative duration of phase I, 1
$t^{I/II}$	duration of phase I/II, s
u	convective gas velocity, m s ⁻¹
w	wave, shock, front velocity, m s ⁻¹
x_i	molar fraction of gas species i , 1
y_i	relative molar fraction of gas species i , 1
Y_{H_2O}/C	proportion of H ₂ +H ₂ O or CO+CO ₂ , 1
z	axial reactor coordinate, m

Greek letters

$\Delta C_{Fe-FeO/FeO-Fe_3O_4}$	oxygen capacity solid phase at reaction fronts (Eqs. (1), (2)), mol m ⁻³
ε	volumetric fraction gas phase, 1
η_{fuel}	fuel utilisation, fuel recovery degree, 1

Indices, upper

I/II	cycle phase I or II (reduction/oxidation)
eq	equilibrium
$\bar{w}_{H_2,out}^{all}$	average value over one cycle

Indices, lower

CO, CO ₂ , H ₂ , H ₂ O	gas species
Fe, FeO, Fe ₃ O ₄	solid species
feed	feed gas conditions
Fe-FeO	equilibrium/reaction front of reaction in Eq. (2)
FeO-Fe ₃ O ₄	equilibrium/reaction front of reaction in Eq. (1)
O	oxygen

Acknowledgements

This project is part of the research project “ProBio—integrated process systems for energetic use of bio mass in fuel cells” jointly funded by the Fraunhofer-Gesellschaft and the Max Planck Society in Germany.

Appendix A. Estimates of oxygen contents at reaction fronts

To estimate the oxygen contents in Eq. (7), consider the example of an iron–wuestite front under an atmosphere of pure carbon monoxide. Assume a volumetric fraction of the gas phase of $\varepsilon = 0.5$ and that the wuestite is completely reduced to iron at this front.

With the mass density and the molar mass of wuestite, ρ_{FeO} and M_{FeO} , the difference in solid oxygen content over this front is:

$$\Delta C^S = (1 - \varepsilon) \cdot \frac{\rho_{FeO}}{M_{FeO}} \cdot 1 \cdot \frac{\text{mol O}}{\text{mol FeO}} = 0.5 \cdot \frac{5.75 \text{ g/cm}^3}{71.85 \text{ g/mol}} = 4 \times 10^{-2} \frac{\text{mol}}{\text{cm}^3} \quad (\text{A.1})$$

For the gas phase, assume that half of the carbon monoxide is oxidised at the front. Furthermore, assume a temperature of $T = 900 \text{ K}$ and a pressure of $p = 1 \text{ bar}$:

$$\Delta C^G = \varepsilon \cdot 0.5 \cdot \frac{p}{RT} = 0.5 \cdot 0.5 \cdot \frac{10^{-5} \text{ Pa}}{8.314 \text{ J/K/mol} \cdot 900 \text{ K}} = 3.3 \times 10^{-6} \frac{\text{mol}}{\text{cm}^3} \quad (\text{A.2})$$

Thus, the oxygen capacity of the solid phase is typically about four orders of magnitude higher than oxygen capacities in the gas phase.

References

- Fraser, S.D., Monsberger, M., Hacker, V., 2006. A thermodynamic analysis of the reformer sponge iron cycle. *Journal of Power Sources* 161, 420–431.
- Galvita, V., Sundmacher, K., 2007a. Redox behavior and reduction mechanism of Fe₃O₄–CeZrO₂ as oxygen storage material. *Journal of Materials Science* 42, 9300–9307.
- Galvita, V., Sundmacher, K., 2007b. Cyclic water gas shift reactor (CWGS) for carbon monoxide removal from hydrogen feed gas for PEM fuel cells. *Chemical Engineering Journal* 134, 168–174.
- Glöckler, B., Kolios, G., Eigenberger, G., 2003. Analysis of a novel reverse-flow reactor concept for autothermal methane steam reforming. *Chemical Engineering Science* 58, 593–601.
- Hacker, V., Faleschini, G., Fuchs, H., Fankhauser, R., Simader, G., Ghaemi, M., Spreitz, B., Friedrich, K., 1998. Usage of biomass gas for fuel cells by the SIR process. *Journal of Power Sources* 71, 226–230.
- Hacker, V., Fankhauser, R., Faleschini, G., Fuchs, H., Friedrich, K., Muhr, M., Kordsch, K., 2000. Hydrogen production by steam-iron process. *Journal of Power Sources* 86, 531–535.
- Hacker, V., 2003. A novel process for stationary hydrogen production: the reformer sponge iron cycle (RESC). *Journal of Power Sources* 118, 311–314.
- Heidebrecht, P., Hertel, C., Sundmacher, K., 2008. Conceptual analysis of a cyclic water gas shift reactor. *International Journal of Chemical Reactor Engineering* 6, A19.
- Hefferich, F.G., 1989. The theory of precipitation/dissolution waves. *AIChE Journal* 35 (2), 75–87.
- Hefferich, F.G., Carr, P.W., 1993. Non-linear waves in chromatography—I. Waves, shocks, and shapes. *AIChE Journal* 35 (1), 75–87.
- Messerschmitt, 1911. Verfahren zur Erzeugung von Wasserstoff durch abwechselnde Oxidation und Reduktion von Eisen in von aussen beheizten, in den Heizräumen angeordneten Zersetzern. German Patent DE 266863.
- Otsuka, K., Kaburagi, T., Yamada, C., Takenaka, S., 2003. Chemical storage of hydrogen by modified iron oxides. *Journal of Power Sources* 122, 111–121.
- Rhee, H.-K., Aris, R., Amundson, N.R., 1970. On the theory of multicomponent chromatography. *Philosophical Transactions of the Royal Society of London Series A—Mathematical and Physical Sciences* 267 (1182), 419–455.
- Svoboda, K., Slowinski, G., Rogut, J., Baxter, D., 2007. Thermodynamic possibilities and constraints for pure hydrogen production by iron based chemical looping process at lower temperatures. *Energy Conversion and Management* 48, 3063–3073.
- Takenaka, S., Kaburagi, T., Yamada, C., Nomura, K., Otsuka, K., 2004. Storage and supply of hydrogen by means of the redox of the iron oxides modified with Mo and Rh species. *Journal of Catalysis* 228, 66–74.
- Thaler, M., Hacker, V., Anilkumar, M., Albering, J., Besenhard, J.O., Schröttner, H., Schmied, M., 2006. Investigations of cycle behaviour of the contact mass in the RESC process for hydrogen production. *International Journal of Hydrogen Energy* 31, 2025–2031.

[PH 5]

M. Pfafferodt, P. Heidebrecht, K. Sundmacher

Stack modeling of a Molten Carbonate Fuel Cell (MCFC)

Fuel Cells 10, 4 (2010), 619-635



Stack Modelling of a Molten Carbonate Fuel Cell (MCFC)

M. Pfafferoth¹, P. Heidebrecht², and K. Sundmacher^{1,2*}

¹ Process Systems Engineering, Otto von Guericke University Magdeburg, Universitätsplatz 2, 39106 Magdeburg, Germany

² Max Planck Institute for Dynamics of Complex Technical Systems, Sandtorstrasse 1, 39106 Magdeburg, Germany

Received October 02, 2009; accepted January 22, 2010

Abstract

A model of a molten carbonate fuel cell (MCFC) stack including internal steam reforming is presented. It comprises a symmetric section of the stack, consisting of one half indirect internal reforming unit (IIR) and four fuel cells. The model describes the gas phase compositions, the gas and solid temperatures and the current density distribution within the highly integrated system. The model assumptions, the differential equations and boundary conditions as well as the coupling equations used in the model are shown.

The strategy to solve the system of partial differential equations is outlined. The simulation results show that the fuel cells within the stack operate at different temperatures. This is expected to have an impact on the voltages as well as the degradation rates within the individual fuel cells.

Keywords: FEM, High Temperature, Internal Reforming, Mathematical Modelling, Molten Carbonate Fuel Cell, MCFC, Numerical Simulation

1 Introduction

Fuel cells are an efficient technology for the generation of electric power. The molten carbonate fuel cell (MCFC) – a high temperature fuel cell – is suitable for the co-production of electricity and high-graded heat in stationary applications [1]. A power plant technology based on the MCFC principle, the so-called HotModule, is developed and manufactured by the MTU Onsite Energy in Ottobrunn, Germany [2].

The temperature is an important state variable for the operation of high temperature fuel cells such as the MCFC [3]. Within an MCFC system, the temperature is typically at about 600 °C. This is high enough to allow for internal reforming, the production of hydrogen from different types of fuels such as natural gas, waste gas or gas from bio mass fermentation [4]. Also, no expensive catalysts are required due to the high temperatures; nickel and nickel oxide are sufficiently active to be used as reforming catalyst and electrode catalysts.

The temperature field in the MCFC is determined by several interacting processes. The steam reforming process is endothermic, thus it constitutes a heat sink. In contrast, the electrochemical reactions at both electrodes as well as the ion transport through the electrolyte produce heat. Energy is transported convectively by anode and cathode gases and is conducted in the solid parts of the cell stack. The anodic and

cathodic gas flows constitute directed heat transport mechanisms, while the heat conduction is an omnidirectional heat transport mechanism. Together, these processes generate a spatially distributed temperature profile. For an efficient and economically competitive operation, this temperature profile has to be within a certain temperature window. Too low temperatures decrease the local reaction rates and the ion conductivity, thus decreasing the cell voltage and thereby resulting in low efficiency. Too high temperatures cause fast degradation of the catalyst material, thus reducing the system's life-time.

The direct measurement of the temperature profile within the fuel cell system, especially inside the fuel cell stack, is extremely difficult and unreliable. The high temperature, the aggressive atmosphere within the stack due to the molten carbonate electrolyte and the need for electric isolation of the sensors are the main problems regarding temperature measurements. Therefore, mathematical modelling and numerical simulation have to be applied to estimate the steady state and dynamical temperature profiles.

The HotModule has a cross-flow configuration of the anode and cathode gas channels. Thus, for an adequate description of the temperature profiles within each fuel cell,

[*] Corresponding author, sundmacher@mpi-magdeburg.mpg.de

Fuel Cells

Pfafferodt et al.: Stack Modelling of a Molten Carbonate Fuel Cell (MCFC)

at least a 2D model of the cell plane is needed. Furthermore, if the temperature profile perpendicular to the cell plane should be taken into account, one has to consider the stack length as a third coordinate.

Within the literature, different models exist for MCFCs. The complexity of the models varies from a lumped representation of the fuel cell stack [5,6] over the simulation of a small 3D cutout section of one cell [7] to models of one fuel cell, taking into account the 3D geometry [8] or a simplified 2D representation of the cell plane [9–13]. An agglomerate model where the volume averaged stack is simulated was presented by Brouwer et al. [14]. The models are used to analyse the system states within the fuel cell, especially the temperatures, the (spatially distributed) current density and the cell voltage. Furthermore, these models allow the development of suitable temperature control strategies [5,6,15] or the optimisation of design parameters such as the catalyst distribution within the MCFC stack [16].

The model discussed in this paper is an extension of the single cell model presented first by Heidebrecht and Sundmacher [12]. That model has been validated by Gundermann et al. based on experimental data collected at an industrial scale MCFC plant [13,17]. In contrast to that previous model, the stack model presented here considers all three spatial directions, including one half of an indirect internal reforming unit (IIR) and four fuel cells.

Especially this reforming unit, which is inserted into the stack at certain positions, causes significant temperature gradients in stack direction and discriminates this stack model from previous ones. The 3D structure of the MCFC stack is described using two spatial coordinates for the fuel cell plane and implementing the heat exchange in the third direction along the stack length *via* source terms in the corresponding equations.

2 Working Principle

The working principle of a MCFC is shown in Figure 1. The fuel cell is assembled in a planar structure. The electrodes are porous metallic structures and a eutectic molten carbonate salt is used as an electrolyte. Above the anode and below the cathode, gas channels are located, through which the gaseous reaction educts and products are transported. A reforming catalyst is placed into the anode channels for Direct Internal Reforming (DIR). An additional gas channel is attached to the fuel cell. It contains reforming catalyst for IIR and is referred to as 'reforming unit' [18].

The typical fuel gas of an MCFC system mainly consists of methane and steam. This gas mixture has to be reformed

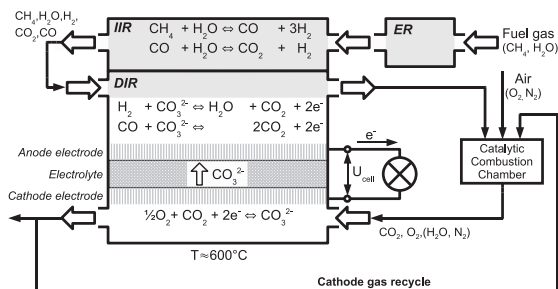


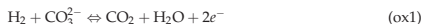
Fig. 1 Working principle of the considered MCFC system.

prior to electrochemical conversion. Both, the methane steam reforming reaction (ref1) and the water gas shift reaction (ref2) are taken into account in the model:



A part of the methane steam reforming is performed outside the fuel cell stack in an external reformer, which is not included in this model. From there, the gas mixture containing methane, water, hydrogen, carbon monoxide and carbon dioxide is transported into the reforming unit. This gas compartment is thermally coupled to the fuel cell. Thereby, the heat needed for the endothermic reforming process is directly provided by the electrochemical reactions within the neighbouring fuel cell [19]. At typical MCFC temperatures, conversion in the reforming unit is limited by the corresponding chemical equilibrium.

The effluent from the reforming unit is redirected into the anode gas channel. Within the anode gas compartment, not only the reforming reactions ((ref1) and (ref2)) have to be taken into account, but also the electrochemical oxidation of hydrogen (ox1) and carbon monoxide (ox2). They react with carbonate ions from the electrolyte to water, carbon dioxide and electrons:



The reforming reactions ((ref1) and (ref2)) within the anode channel are not only thermally coupled to the electrochemical reactions. Due to the continuous removal of hydrogen and carbon monoxide, the equilibrium limited reforming process is pushed to almost complete conversion of methane.

The anode exhaust gas is mixed with air and completely burned in the catalytic combustion chamber. Because air is fed in excess, the exhaust gas of the combustion chamber still contains a significant amount of oxygen. This gas is redirected into the cathode channel, where the electrochemical reduction (red) takes place. New carbonate ions are produced from carbon dioxide, oxygen and two electrons according to the backward directions of the following cathode reaction:



The carbonate ions are transported to the anode through the electrolyte. The electrochemical reactions at the anode act as an electron source while the electrochemical reaction at the cathode acts as an electron sink. Both are connected *via* an electric load and thus the fuel cell serves as an electric energy supply device.

In the HotModule, one part of the cathode exhaust gas is recycled to the catalytic combustion chamber while the rest of the gas leaves the fuel cell system.

3 MCFC Stack Model

Within the HotModule MCFC power plant, 343 fuel cells and 42 IIR units are arranged in a fuel cell stack. A repeating pattern formed by eight fuel cells with an active cell area of approximately 1 m² followed by one reforming unit is used.

Under two assumptions, the stack behaviour can be represented by a symmetric section consisting of four fuel cells and one half IIR unit. The first assumption neglects thermal effects at both ends of the stack. The second assumption says that the sequence of anode and cathode channels along the stack direction has no significant impact on the temperature profile. The structure of this so-called symmetric stack model is shown in Figure 2.

The IIR unit is attached to the first fuel cell. It is arranged in a counter flow configuration compared to the anode gas compartments. In each fuel cell, the anode and the cathode gas channels are oriented to each other in a cross flow configuration. The solid components of each fuel cell, the electrolyte, the electrolyte matrix and the channel walls, are combined in the solid phase. In addition to the above-mentioned components, the model includes the heat exchanger, the catalytic combustion chamber and the reversal chamber. These auxiliary components are common for all cells in the HotModule system.

The gas flow directions within the symmetric stack model are indicated in Figure 2. The feed gas (IN), which is assumed to have passed through the external reformer, is heated up in the heat exchanger (HEA) by the hot gas from the catalytic combustion chamber and flows into the reforming unit (IIR, reforming reactions (ref1) and (ref2)). After that, the gas flow is splitted into four equal parts which are redirected into the anode compartments (A) of the fuel cells (reforming reactions

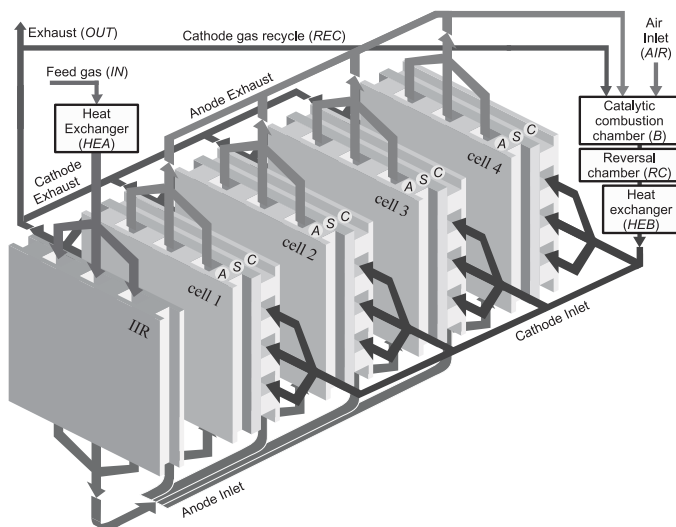


Fig. 2 Structure and gas flows in the symmetric MCFC stack model, consisting of four fuel cells and one half IIR unit.

Fuel Cells

Pfafferodt et al.: Stack Modelling of a Molten Carbonate Fuel Cell (MCFC)

(ref1) and (ref2); oxidation reactions ($\alpha x1$) and ($\alpha x2$)). The exhaust gases of the four anode gas compartments are mixed with the cathode gas recycle (REC) and completely burned with air (AIR) in the catalytic combustion chamber (B). After that, the gas goes into the reversal chamber (RC), where the blower is located. The gas is redirected into the second chamber of the heat exchanger (HEB). Within the heat exchanger, the energy of the gas is used to heat up the feed gas. In the next step, the gas flow is equally splitted to the cathode gas compartments of the four fuel cells (C, reduction reaction (red)). A part of the cathode exhaust gas is used in the cathode gas recycle (REC), which is redirected into the catalytic combustion chamber (B), while the rest leaves the fuel cell system (OUT).

In addition to the coupling of the different compartments by the convective mass flow, they are also thermally coupled in stack direction. Furthermore, the electrochemical reaction rates at both electrodes of each fuel cell are coupled *via* the charge balance.

To achieve a more general description that is also valid for equivalent systems, the complete symmetric stack model is formulated in terms of dimensionless variables. The definition of the most important dimensionless variables is shown in Table 1. A complete list of all dimensionless variables is included in the work of Heidebrecht [11].

3.1 General Assumptions

The presented symmetric stack model is an extension of the model proposed by Heidebrecht et al. [11,12]. It is based on partial and total mass balances as well as enthalpy and charge balances. One purpose of the symmetric stack model is to simulate load change scenarios, thus it is formulated in transient equations.

The main assumptions applied to the modelling of the symmetric MCFC stack are:

- Ideal gas behaviour.
- Isobaric conditions.
- Symmetric boundary conditions at both ends of the symmetric model in stack direction.
- All solid parts of a fuel cell are combined into one single solid phase with an average heat conductivity and a cumulative heat capacity.
- There are no concentration, temperature or velocity gradients perpendicular to the cell plane within the different parts of the symmetric stack model. This assumption corresponds to plug flow conditions within the gas compartments and reduces the geometry of the reforming unit,

the anode and cathode gas compartments as well as the solid phase to two spatial dimensions. The heat and mass transport between the different parts along the stack length are represented as exchange terms in the corresponding balance equations.

- Gas compositions in the channels of the IIR unit and the anode gas compartment are usually close to the chemical equilibrium of the reforming reactions. Therefore, power law kinetics are applied to describe their reaction rates. The kinetics of the electrochemical reactions are described by Butler–Volmer equations [12].
- The heat capacity of the gas mixture depends on the molar fractions, $\chi_{i,r}$, but not on the temperature. The heat capacities, $c_{p,i}$, of the pure components are calculated at a reference temperature of $T^* = 600^\circ\text{C}$, corresponding to a dimensionless temperature of $\theta^* = 2.93$.

$$\bar{c}_p = \sum_i \chi_{i,r} c_{p,i} \text{ with } c_{p,i} = c_{p,i}(\theta^*) = \text{const.} \quad (1)$$

- The electric potentials of each cell are independent from the potentials of the neighbouring fuel cells. This is equivalent to the assumption that in each bipolar plate between two cells, complete equilibration of the electric potential is achieved. This is a proper assumption if the neighbouring cells show similar current density profiles. In that case only small currents occur along the plane of the bipolar plates, resulting in a virtually constant potential in each bipolar plate. The validity of this assumption will be checked carefully using the simulation results (see Section 5.2).

3.2 Governing Equations

In the following, all equations needed to describe the symmetric stack model are presented. The definition a single fuel cell model is based on previous works [11,12,16]. The equations for the anode, the solid and the cathode are adapted and the changes are shown. For a detailed derivation of these model equations, especially the equations for the reaction kinetics and the thermodynamic expressions, we refer to the corresponding publications. Within the symmetric stack model, equations for the heat exchanger and the two-phase model for the reforming unit are added. Furthermore, the heat transport between the different gas compartments along the stack direction is implemented.

The symmetric stack model can be used for an arbitrary number of fuel cells, specified by n_{cells} . The standard configuration includes four fuel cells and one half reforming unit, a combination which is currently used in industrial fuel cell stacks.

3.2.1 Feed Gas

The feed gas (IN) for the MCFC system is assumed to be a partially reformed gas from an external reformer. The composition, $\chi_{i,\text{IN}}$, the temperature, θ_{IN} , and the molar flux, I_{IN} , of

Table 1 Definition of important dimensionless variables.

Variable	Definition	Standard value
Temperature	$\theta = T/T^*$	with $T^* = 298.15\text{ K}$
Current density	$I = \bar{I}/I^*$	with $I^* = 1406.4\text{ A}$
Molar flow	$\Gamma = \bar{\Gamma}/\Gamma^*$	with $\Gamma^* = 6.377 \times 10^{-3}\text{ mol/s}$
Voltage	$U = \bar{U}/U^*$	with $U^* = 0.0257\text{ V}$

Table 2 Input parameters of the symmetric stack model at base conditions.

Description	Variable	Dimensionless value
Feed gas		
Molar flow	Γ_{IN}	3.30 (approx. 60% fuel utilisation)
Temperature	ϑ_{IN}	2.18 ($\approx 366^\circ\text{C}$)
Methane molar fraction	$Z_{\text{CH}_4, \text{IN}}$	0.22
Water molar fraction	$Z_{\text{H}_2\text{O}, \text{IN}}$	0.57
Hydrogen molar fraction	$Z_{\text{H}_2, \text{IN}}$	0.15
Carbon monoxide molar fraction	$Z_{\text{CO}, \text{IN}}$	0.00
Carbon dioxide molar fraction	$Z_{\text{CO}_2, \text{IN}}$	0.05
Air		
Molar flow	Γ_{AIR}	21.96 ($\lambda_{\text{AIR}} = 2.56$)
Temperature	ϑ_{AIR}	1.08 ($= 43^\circ\text{C}$)
Oxygen molar fraction	$Z_{\text{O}_2, \text{IN}}$	0.21
Nitrogen molar fraction	$Z_{\text{N}_2, \text{IN}}$	0.79
Total cell current	I_{cell}	0.45 ($80\text{ mA}/\text{cm}^2$)
Electric power of the blower per cell	P_{blower}	2.775 ($100\text{ W}/\text{cell}$)
Cathode gas recycle ratio	f_{REC}	0.70

the feed gas are input parameters of the symmetric stack model. They are given in Table 2 for the simulated load case.

3.2.2 Heat Exchanger (side A)

The gas is heated up in a heat exchanger (HEA) before it reaches the reforming unit. The exhaust gas from the catalytic combustion chamber passes the hot side of the heat exchanger. This gas chamber of the heat exchanger is modelled as a spatially lumped tank. The component mass fraction, $Z_{i, \text{HEA}}$, the gas temperature, ϑ_{HEA} , and the total molar flow, Γ_{HEA} , are calculated from the following equations:

$$\frac{V_{\text{HEA}}}{\vartheta_{\text{HEA}}} \frac{\partial Z_{i, \text{HEA}}}{\partial \tau} = \Gamma_{\text{IN}} (Z_{i, \text{IN}} - Z_{i, \text{HEA}}) \quad (2)$$

$$\frac{V_{\text{HEA}}}{\vartheta_{\text{HEA}}} \frac{\partial \vartheta_{\text{HEA}}}{\partial \tau} = \Gamma_{\text{IN}} \frac{\bar{c}_{\text{PIN}}}{\bar{c}_{\text{PHEA}}} (\vartheta_{\text{IN}} - \vartheta_{\text{HEA}}) - \frac{Q_{\text{HE}}}{\bar{c}_{\text{PHEA}}} \quad (3)$$

$$\begin{aligned} \Gamma_{\text{HEA}} &= \Gamma_{\text{IN}} \\ &\times \left(1 + \frac{\bar{c}_{\text{PIN}}}{\bar{c}_{\text{PHEA}}} \left(\frac{\vartheta_{\text{IN}}}{\vartheta_{\text{HEA}}} - 1 \right) \right) \\ &- \frac{Q_{\text{HE}}}{\bar{c}_{\text{PHEA}} \vartheta_{\text{HEA}}} \end{aligned} \quad (4)$$

The heat exchanged between the two gas chambers of the heat exchanger, Q_{HE} , depends on the temperature difference between the two gas flows and is given by

$$Q_{\text{HE}} = S_{\text{HE}} (\vartheta_{\text{HEA}} - \vartheta_{\text{HEB}}) \quad (5)$$

3.3.3 Indirect Internal Reforming Unit

A detailed analysis of the actual design of the IIR showed that the reform-

ing reactions are mass transport limited [18]. Based on these findings we derived a reduced model for the IIR unit which is used in this symmetric stack model. The basic structure of the model for the reforming unit is shown in Figure 3. The model describes one non-reactive phase (upper index N) and one reactive phase (upper index R) which exchange mass and heat across the interface between them (upper index I). In the non-reactive phase, the gas is convectively moving in the negative ζ_1 -direction, while the gas in the reactive phase is stagnant and is subject to homogeneous reforming reactions.

The volume of the reforming catalyst pellets (upper index P) is taken into account as a dead volume within the reactive phase. The volume fractions of the non-reactive phase, the reactive phase and the catalyst pellets phase sum up to unity:

$$1 = \epsilon_{\text{IIR}}^N + \epsilon_{\text{IIR}}^R + \epsilon_{\text{IIR}}^P \quad (6)$$

Due to the fact that the catalyst pellets are completely surrounded by the reactive phase, the area fraction for the heat exchange between this gas phase of the reforming unit and the solid phase of the neighbouring fuel cell is given by $(\epsilon_{\text{IIR}}^R + \epsilon_{\text{IIR}}^P)$, while for the non-reactive phase, ϵ_{IIR}^N is used.

The component mass balances (Eq. (7)) and the energy balance (Eq. (8)) describe the molar fraction, $Z_{i, \text{IIR}}$, and the temperature, ϑ_{IIR} , within the non-reactive phase:

$$\epsilon_{\text{IIR}}^N \frac{V_{\text{IIR}}}{\vartheta_{\text{IIR}}} \frac{\partial Z_{i, \text{IIR}}^N}{\partial \tau} = -\epsilon_{\text{IIR}}^N \frac{V_{\text{IIR}}}{\vartheta_{\text{IIR}}} \frac{\partial Z_{i, \text{IIR}}^N}{\partial \zeta_1} - n_{i, \text{IIR}}^I - Z_{i, \text{IIR}}^N n_{i, \text{IIR}}^I \quad (7)$$

$$\begin{aligned} \epsilon_{\text{IIR}}^N \frac{V_{\text{IIR}}}{\vartheta_{\text{IIR}}} \frac{\partial \vartheta_{\text{IIR}}^N}{\partial \tau} &= -\epsilon_{\text{IIR}}^N \frac{V_{\text{IIR}}}{\vartheta_{\text{IIR}}} \frac{\partial \vartheta_{\text{IIR}}^N}{\partial \zeta_1} + \frac{1}{\bar{c}_{\text{PIN}}} \times \\ &\left(\left(\sum_i n_{i, \text{IIR}}^I c_{\text{P}_i} \right) (\vartheta_{\text{IIR}}^N - \vartheta_{\text{IIR}}^R) - q_{\text{IIR}}^I + \epsilon_{\text{IIR}}^N q_{\text{IIR}}^N \right) \end{aligned} \quad (8)$$

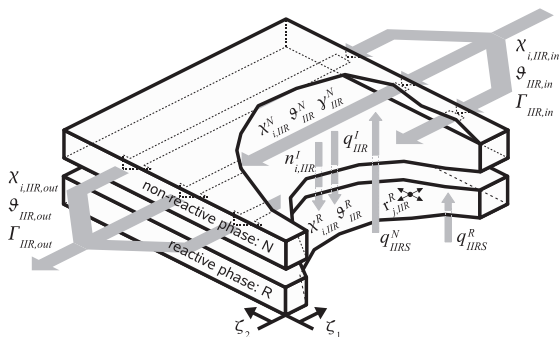


Fig. 3 Structure of the model for the reforming unit consisting of the reactive phase (index N) and the non-reactive phase (index R). All states, fluxes and inlet/outlet conditions are indicated.

Fuel Cells

Pfafferoth et al.: Stack Modelling of a Molten Carbonate Fuel Cell (MCFC)

$n_{i,IIIR}^I$ is the mass flux density across the interface between the reactive and the non-reactive phases and q_{IIIR}^I denotes the interface heat flux density. The heat flux density between the non-reactive gas phase within the reforming unit and the solid of the neighbouring fuel cell is represented by q_{IIIR}^N . It is multiplied by the corresponding area fraction, e_{IIIR}^N , to account for the reduced exchange area. Both equations contain a convective term along the main flow direction (negative ζ_1 -direction).

The molar flow density within the reforming unit, γ_{IIIR}^N , is always negative. It is described by the following equation:

$$0 = -\frac{\partial(e_{IIIR}^N \gamma_{IIIR}^N q_{IIIR}^N)}{\partial \zeta_1} + \frac{1}{c_{PIIR}^N} \times \left(\left(\sum_i n_{i,IIIR}^I c_{Pi} \right) (q_{IIIR}^N - q_{IIIR}^R) - q_{IIIR}^I + e_{IIIR}^N q_{IIIR}^N \right) + q_{IIIR}^N n_{i,IIIR}^I \quad (9)$$

The molar fraction, $\chi_{i,IIIR}^R$, and the temperature, ϑ_{IIIR}^R , within the reactive phase are calculated using Eqs. (10) and (11), respectively:

$$e_{IIIR}^R \frac{V_{IIIR}}{q_{IIIR}^R} \frac{\partial \chi_{i,IIIR}^R}{\partial \tau} = n_{i,IIIR}^I - \chi_{i,IIIR}^R n_{i,IIIR}^I + e_{IIIR}^R \left(\sum_{j=\text{ref}} (v_{ij} - \chi_{i,IIIR}^R \bar{v}_j) D a_{j,IIIR} r_{j,IIIR} \right) \quad (10)$$

$$e_{IIIR}^R \frac{V_{IIIR}}{q_{IIIR}^R} \frac{\partial \vartheta_{IIIR}^R}{\partial \tau} = \frac{1}{c_{PIIR}^R} \times \left(\left(\sum_i n_{i,IIIR}^I c_{Pi} \right) (q_{IIIR}^N - q_{IIIR}^R) + q_{IIIR}^I + e_{IIIR}^R \sum_{j=\text{ref}} (-\Delta_R h_j^\theta (\vartheta_{IIIR}^R)) D a_{j,IIIR} r_{j,IIIR} + (e_{IIIR}^R + e_{IIIR}^P) q_{IIIR}^R \right) \quad (11)$$

The heat flux density between the reactive phase and the solid phase of the neighbouring fuel cell is given by q_{IIIR}^R . The exchange area is taken into account using the corresponding area ratio ($e_{IIIR}^R + e_{IIIR}^P$).

For Eqs. (7)–(9), the necessary boundary conditions correspond to the inlet conditions of the non-reactive phase:

$$\chi_{i,IIIR}^N(\zeta_1 = 1, \zeta_2, \tau) = \chi_{i,IIIR,in}^N = \chi_{i,HEA} \quad (12)$$

$$\vartheta_{IIIR}^N(\zeta_1 = 1, \zeta_2, \tau) = \vartheta_{IIIR,in}^N = \vartheta_{HEA} \quad (13)$$

$$\gamma_{IIIR}^N(\zeta_1 = 1, \zeta_2, \tau) = \gamma_{IIIR,in}^N = -\frac{\Gamma_{HEA}}{c^N} \quad (14)$$

As the convective flow in the reforming unit is in negative ζ_1 -direction, a negative sign for the molar flow density occurs in Eq. (14).

At the outlet of the reforming unit, the average outlet concentrations, $\chi_{i,IIIR,out}$, the average outlet temperature, $\vartheta_{IIIR,out}$ and the total outlet molar flow, $\Gamma_{IIIR,out}$, are calculated:

$$\Gamma_{IIIR,out} \chi_{i,IIIR,out} = \int_0^1 \left[-e_{IIIR}^N \gamma_{IIIR}^N \chi_{i,IIIR}^N \right]_{\zeta_1=0, \zeta_2} d\zeta_2 \quad (15)$$

$$\Gamma_{IIIR,out} \bar{c}_{PIIR,out} (q_{IIIR,out} - q^r) = \int_0^1 \left[-e_{IIIR}^N \gamma_{IIIR}^N \bar{c}_{PIIR} (q_{IIIR}^N - q^r) \right]_{\zeta_1=0, \zeta_2} d\zeta_2 \quad (16)$$

$$\Gamma_{IIIR,out} = \int_0^1 \left[-e_{IIIR}^N \gamma_{IIIR}^N \right]_{\zeta_1=0, \zeta_2} d\zeta_2 \quad (17)$$

The mass flux density across the two-phase interface requires detailed consideration. The component molar flux, $n_{i,IIIR}^I$, is composed of a convective term:

$$n_{i,IIIR}^I = n_{i,IIIR,conv}^I + n_{i,IIIR,diff}^I \quad (18)$$

For the diffusive component molar flux, $n_{i,IIIR,diff}^I$, linear transport kinetics are used

$$n_{i,IIIR,diff}^I = D_{i,IIIR}^I (\chi_{i,IIIR}^N - \chi_{i,IIIR}^R) \quad (19)$$

with $D_{i,IIIR}^I$ being the mass transport coefficient across the interface. These coefficients can also be interpreted as Stanton numbers of mass transport.

The total molar flux across the interface, $n_{i,IIIR}^I$, plus the change in mole numbers due to the reforming reactions have to compensate the expansion effect in the reactive phase due to dynamic temperature changes. At steady state, the right-hand side of Eq. (20) equals zero.

$$n_{i,IIIR}^I + e_{IIIR}^R \sum_{j=\text{ref}} \bar{v}_j D a_{j,IIIR} r_{j,IIIR} = -\frac{1}{q_{IIIR}^R c_{PIIR}^R} \left(\left(\sum_i n_{i,IIIR}^I c_{Pi} \right) (q_{IIIR}^N - q_{IIIR}^R) + q_{IIIR}^I + e_{IIIR}^R \sum_{j=\text{ref}} (-\Delta_R h_j^\theta (\vartheta_{IIIR}^R)) D a_{j,IIIR} r_{j,IIIR} + (e_{IIIR}^R + e_{IIIR}^P) q_{IIIR}^R \right) \quad (20)$$

The difference between the total molar flux, $n_{i,IIIR}^I$, and the sum of the diffusive component molar fluxes, $n_{i,IIIR,diff}^I$, is compensated by the total convective flux at the interface, $n_{i,IIIR,conv}^I$. The sum of the diffusive component fluxes is not equal to zero due to the fact that molar fluxes are used.

$$n_{i,\text{IIR,conv}}^I = n_{i,\text{IIR}}^I - \sum_i n_{i,\text{IIR,diff}}^I \quad (21)$$

The partial convective flux of species i is calculated from the total convective flux taking into account an average molar fraction of species i at the interface.

$$n_{i,\text{IIR,conv}}^I = n_{i,\text{IIR,conv}}^N \frac{Z_{i,\text{IIR}}^N + Z_{i,\text{IIR}}^R}{2} \quad (22)$$

The following expressions are used in the enthalpy equations of the non-reactive and reactive phase (Eqs. (8) and (11)).

$$n_{i,\text{IIR}}^I = \begin{cases} n_{i,\text{IIR}}^I, & \text{if } n_{i,\text{IIR}}^I > 0 \\ 0, & \text{if } n_{i,\text{IIR}}^I \leq 0 \end{cases}; n_{i,\text{IIR}}^I = \begin{cases} 0, & \text{if } n_{i,\text{IIR}}^I > 0 \\ n_{i,\text{IIR}}^I, & \text{if } n_{i,\text{IIR}}^I \leq 0 \end{cases} \quad (23)$$

A linear approach is used for the heat flux between the non-reactive phase and the reactive phase as well as for the heat fluxes between both gas phases and the solid phase of the neighbouring first fuel cell:

$$q_{\text{IIR}}^I = St_{\text{IIR}}^I (g_{\text{IIR}}^N - g_{\text{IIR}}^R) \quad (24)$$

$$q_{\text{IIRS}}^N = St_{\text{IIRS}}^N (g_{\text{S}}^{(1)} - g_{\text{IIR}}^N) \quad (25)$$

$$q_{\text{IIRS}}^R = St_{\text{IIRS}}^R (g_{\text{S}}^{(1)} - g_{\text{IIR}}^R) \quad (26)$$

Within the first fuel cell, the total heat flux density between the reforming unit and the solid phase is needed (Eq. (71) in Section 3.2.10). It is calculated from the heat flux densities in the reactive and the non-reactive phase, accounting for the corresponding area fractions:

$$q_{\text{S,IIR}} = e_{\text{IIR}}^N q_{\text{IIRS}}^N + (e_{\text{IIR}}^R + e_{\text{IIR}}^P) q_{\text{IIRS}}^R \quad (27)$$

3.2.4 Anode Gas Phase

One anode gas phase (A) has to be modelled for each of the four fuel cells. The upper index k is used to identify the number of the actual fuel cell. In the anode channels, both reforming reactions ((ref1) and (ref2)) as well as both electrochemical oxidation reactions ((ox1) and (ox2)) are considered. The component molar fractions, $Z_{i,A}^{(k)}$, the temperature, $g_A^{(k)}$, and the molar flux density, $\gamma_A^{(k)}$, are given by the component mass balance (Eq. (28)), the energy balance (Eq. (29)) and the total mass balance (Eq. (30)).

$$\frac{V_A}{g_A^{(k)}} \frac{\partial g_A^{(k)}}{\partial \tau} = -\gamma_A^{(k)} \frac{dZ_{i,A}^{(k)}}{d\zeta_1} + n_{i,\text{AS}}^{(k)} - Z_{i,A}^{(k)} \sum_i n_{i,\text{AS}}^{(k)} + \sum_{j=\text{ref}} \left(v_{ij} - Z_{i,A}^{(k)} \bar{v}_j \right) Da_{j,A} r_{j,A}^{(k)} \quad (28)$$

$$\frac{V_A}{g_A^{(k)}} \frac{\partial g_A^{(k)}}{\partial \tau} = -\gamma_A^{(k)} \frac{d\zeta_1^{(k)}}{d\zeta_1} + \frac{1}{\zeta_{\text{PA}}^{(k)}} \times \left(\left(\sum_i n_{i,\text{AS}}^{(k)+} c_{p,i} \right) (g_{\text{S}}^{(k)} - g_A^{(k)}) + \sum_{j=\text{ref}} \left(-\Delta_R H_j^\theta (g_A^{(k)}) \right) Da_{j,A} r_{j,A}^{(k)} + q_{\text{AS}}^{(k)} \right) \quad (29)$$

$$0 = -\frac{d(\gamma_A^{(k)} g_A^{(k)})}{d\zeta_1} + \frac{1}{\zeta_{\text{PA}}^{(k)}} \left(\left(\sum_i n_{i,\text{AS}}^{(k)+} c_{p,i} \right) (g_{\text{S}}^{(k)} - g_A^{(k)}) + \sum_{j=\text{ref}} \left(-\Delta_R H_j^\theta (g_A^{(k)}) \right) Da_{j,A} r_{j,A}^{(k)} + q_{\text{AS}}^{(k)} \right) + g_A^{(k)} \sum_i n_{i,\text{AS}}^{(k)} + g_A^{(k)} \sum_{j=\text{ref}} \bar{v}_j Da_{j,A} r_{j,A}^{(k)} \quad (30)$$

Within these equations, $n_{i,\text{AS}}^{(k)}$ denotes the component mass flux density between the anode gas channels and the anode pores. It is defined using linear mass transport kinetics:

$$n_{i,\text{AS}}^{(k)} = D_{i,\text{AS}} \left(\varphi_{i,\text{AC}}^{(k)} - Z_{i,A}^{(k)} \right) \quad (31)$$

$$n_{i,\text{AS}}^{(k)+} = \begin{cases} n_{i,\text{AS}}^{(k)}, & \text{if } n_{i,\text{AS}}^{(k)} > 0 \\ 0, & \text{if } n_{i,\text{AS}}^{(k)} \leq 0 \end{cases} \quad (32)$$

where $\varphi_{i,\text{AC}}^{(k)}$ denotes the gas composition inside the electrode pores in terms of partial pressures. It is described in more detail in Section 3.2.9.

The heat flux density between the anode gas channels and the solid phase, $q_{\text{AS}}^{(k)}$, depends on the temperature difference between these phases:

$$q_{\text{AS}}^{(k)} = St_{\text{AS}} \left(g_{\text{S}}^{(k)} - g_A^{(k)} \right) \quad (33)$$

The gas from the reforming unit is equally distributed to all fuel cells. The boundary conditions for the molar fractions, the temperature and the molar flow density are given by

$$Z_{i,A}^{(k)} (\zeta_1 = 0, \zeta_2, \tau) = Z_{i,A,\text{in}}^{(k)} = Z_{i,\text{IIR,out}}^{(k)} \quad (34)$$

$$g_A^{(k)} (\zeta_1 = 0, \zeta_2, \tau) = g_{A,\text{in}}^{(k)} = g_{\text{IIR,out}}^{(k)} \quad (35)$$

$$\gamma_A^{(k)} (\zeta_1 = 0, \zeta_2, \tau) = \gamma_{A,\text{in}}^{(k)} = \frac{\Gamma_{\text{IIR,out}}}{n_{\text{cells}}} \quad (36)$$

for $k = 1, \dots, n_{\text{cells}}$

At the anode outlets, average values for the molar fractions, $Z_{i,A,\text{out}}^{(k)}$, and the temperature, $g_{A,\text{out}}^{(k)}$, as well as for the

Fuel Cells

Pfafferoth et al.: Stack Modelling of a Molten Carbonate Fuel Cell (MCFC)

total molar flow of the exhaust gas, $\Gamma_{A,out}$, are needed. They are calculated using similar equations as used at the outlet of the reforming unit (Eqs. (15)–(17)), but a summation over all cells is added.

$$\Gamma_{A,out} \chi_{i,A,out} = \sum_{k=1}^{n_{\text{cells}}} \int_0^1 \left[\gamma_A^{(k)} \chi_{i,A}^{(k)} \right]_{\zeta_i=1, \zeta_2} d\zeta_2 \quad (37)$$

$$\begin{aligned} \Gamma_{A,out} \bar{c}_{P,A,out} (\vartheta_{A,out} - \vartheta^r) \\ = \sum_{k=1}^{n_{\text{cells}}} \int_0^1 \left[\gamma_A^{(k)} \bar{c}_{P,A}^{(k)} (\vartheta_A^{(k)} - \vartheta^r) \right]_{\zeta_i=1, \zeta_2} d\zeta_2 \end{aligned} \quad (38)$$

$$\Gamma_{A,out} = \sum_{k=1}^{n_{\text{cells}}} \int_0^1 \left[\gamma_A^{(k)} \right]_{\zeta_i=1, \zeta_2} d\zeta_2 \quad (39)$$

3.2.5 Catalytic Combustion Chamber

Within the catalytic combustion chamber (B), the anode exhaust gas (index A, out) is mixed with air (AIR) and the gas from the cathode gas recycle (REC). Furthermore, all nonoxidised components of the gas are fully oxidised.

$$\Gamma_B \chi_{i,B} = \sum_l \Gamma_l \left(\chi_{i,l} + \sum_{j=\text{comb}} \nu_{i,C} \chi_{j,l} \right) \quad (40)$$

$$\Gamma_B \bar{c}_{P,B} (\vartheta_B - \vartheta^r) = \sum_l \Gamma_l \left(\bar{c}_{P,l} (\vartheta_l - \vartheta^r) + \sum_i \chi_{i,l} (-\Delta_C h_i^\theta(\vartheta^r)) \right) \quad (41)$$

$$\Gamma_B = \sum_l \Gamma_l \left(1 + \sum_{j=\text{comb}} \bar{\nu}_{C,j} \chi_{j,l} \right) \quad (42)$$

for $l = A, \text{out}; \text{REC}; \text{AIR}$

The temperature of the air, ϑ_{AIR} , its composition, $\chi_{i,\text{AIR}}$, as well as the total molar flow of the air, Γ_{AIR} , are input parameters of the model (see Table 2).

3.2.6 Reversal Chamber

The reversal chamber (RC) is a large process volume located between the catalytic combustion chamber and the second chamber of the heat exchanger. For simplicity, it is modelled as a well-mixed tank similar to the modelling of the heat exchangers.

$$\frac{V_{RC}}{\vartheta_{RC}} \frac{\partial \chi_{i,RC}}{\partial \tau} = \Gamma_B (\chi_{i,B} - \chi_{i,RC}) \quad (43)$$

$$\frac{V_{RC}}{\vartheta_{RC}} \frac{\partial \vartheta_{RC}}{\partial \tau} = \Gamma_B \frac{\bar{c}_{P,B}}{\bar{c}_{P,RC}} (\vartheta_B - \vartheta_{RC}) - \frac{Q_{RC}}{\bar{c}_{P,RC}} + \frac{P_{blower}}{\bar{c}_{P,RC}} \quad (44)$$

$$\Gamma_{RC} = \Gamma_B \left(1 + \frac{\bar{c}_{P,B}}{\bar{c}_{P,RC}} (\vartheta_B - \vartheta_{RC}) \right) - \frac{Q_{RC}}{\bar{c}_{P,RC}} + \frac{P_{blower}}{\bar{c}_{P,RC}} \quad (45)$$

Within the reversal chamber, the energy input of the gas blower, P_{blower} , as well as the heat loss to the environment, Q_{RAC} , are taken into account. For the heat loss, Q_{RAC} , a linear approach is used

$$Q_{RC} = St_{RC} (\vartheta_{RC} - \vartheta_{\text{U}}) \quad (46)$$

while the energy input due to the gas blower, P_{blower} , is listed in Table 2 as an input parameter.

3.2.7 Heat Exchanger (side B)

The hot side of the heat exchanger (HEB) is located behind the reversal chamber and before the cathode gas compartments. It is modelled using similar equations as for the cold side of the heat exchanger (Section 3.2.2).

$$\frac{V_{\text{HEB}}}{\vartheta_{\text{HEB}}} \frac{\partial \chi_{i,\text{HEB}}}{\partial \tau} = \Gamma_{RC} (\chi_{i,\text{HEB}} - \chi_{i,\text{HEB}}) \quad (47)$$

$$\frac{V_{\text{HEB}}}{\vartheta_{\text{HEB}}} \frac{\partial \vartheta_{\text{HEB}}}{\partial \tau} = \Gamma_{\text{RAC}} \frac{\bar{c}_{P,RC}}{\bar{c}_{P,\text{HEB}}} (\vartheta_{RC} - \vartheta_{\text{HEB}}) + \frac{Q_{\text{HE}}}{\bar{c}_{P,\text{HEB}}} \quad (48)$$

$$\Gamma_{\text{HEB}} = \Gamma_{RC} \left(1 + \frac{\bar{c}_{P,RC}}{\bar{c}_{P,\text{HEB}}} (\vartheta_{RC} - \vartheta_{\text{HEB}}) \right) + \frac{Q_{\text{HE}}}{\bar{c}_{P,\text{HEB}} \vartheta_{\text{HEB}}} \quad (49)$$

The heat flux between the two chambers of the heat exchanger, Q_{HE} , is described in Eq. (5).

3.2.8 Cathode Gas Phase

The cathode gas phase (C) is modelled in full analogy to the anode gas phase. Because anode and cathode gas flow are arranged in cross flow, the main gas flow direction in the cathode follows the second spatial coordinate, ζ_2 . The electrochemical reduction (red) is the only reaction considered here. Eqs. (50)–(52) describe the molar fractions, $\chi_{i,C}^{(k)}$, the temperature, $\vartheta_C^{(k)}$ and the molar flow, $\gamma_C^{(k)}$, within the cathode channels.

$$\frac{V_C}{\vartheta_C^{(k)}} \frac{\partial \chi_{i,C}^{(k)}}{\partial \tau} = -\gamma_C^{(k)} \frac{d\chi_{i,C}^{(k)}}{d\zeta_2} + n_{i,CS}^{(k)} - \chi_{i,C}^{(k)} \sum_l n_{l,CS}^{(k)} \quad (50)$$

$$\frac{V_C}{\vartheta_C^{(k)}} \frac{\partial \vartheta_C^{(k)}}{\partial \tau} = -\gamma_C^{(k)} \frac{d\vartheta_C^{(k)}}{d\zeta_2} + \frac{1}{\bar{c}_{P,C}} \left(\left(\sum_l n_{l,CS}^{(k)} c_{P,l} \right) (\vartheta_S^{(k)} - \vartheta_C^{(k)}) + q_{CS}^{(k)} \right) \quad (51)$$

$$0 = -\frac{d(\gamma_C^{(k)} \vartheta_C^{(k)})}{d\zeta_2} + \frac{1}{\bar{c}_{PC}^{(k)}} \left(\left(\sum_i n_{i,CS}^{(k)+} c_{Pi} \right) (\vartheta_S^{(k)} - \vartheta_C^{(k)}) + q_C^{(k)} \right) + \vartheta_C^{(k)} \sum_i n_{i,CS}^{(k)} \quad (52)$$

For the mass transport to the electrode pores as well as for the boundary conditions and the calculation of average values at the outlets, similar equations as for the anode (Eqs. (31)–(39)) are used.

The molar flow density from the electrode pores is defined as

$$n_{i,CS}^{(k)} = D_{i,CS} \left(\varphi_{i,CC}^{(k)} - \chi_{i,C}^{(k)} \right) \quad (53)$$

$$n_{i,CS}^{(k)+} = \begin{cases} n_{i,CS}^{(k)}, & \text{if } n_{i,CS}^{(k)} > 0 \\ 0, & \text{if } n_{i,CS}^{(k)} \leq 0 \end{cases} \quad (54)$$

The heat exchange density between the anode and the solid phase is given by

$$q_{CS}^{(k)} = St_{CS} (\vartheta_S^{(k)} - \vartheta_C^{(k)}) \quad (55)$$

For the inlet boundary conditions, the properties of the gas flow from the reversal chamber are used. The gas flow is equally distributed to all cathodes.

$$\chi_{i,C}^{(k)} / (\zeta_1, \zeta_2 = 0, \tau) = \chi_{i,C,in}^{(k)} = \chi_{i,HEB} \quad (56)$$

$$\vartheta_C^{(k)} / (\zeta_1, \zeta_2 = 0, \tau) = \vartheta_{C,in}^{(k)} = \vartheta_{HEB} \quad (57)$$

$$\gamma_C^{(k)} / (\zeta_1, \zeta_2 = 0, \tau) = \gamma_{C,in}^{(k)} = \frac{\Gamma_{HEB}}{n_{cells}} \quad (58)$$

for $k = 1, \dots, n_{cells}$

At the outlets, average values for the composition of the gas, $\chi_{i,C,out}$, and the temperature of the gas, $\vartheta_{C,out}$, as well as for the total molar flow, $\Gamma_{C,out}$, are calculated:

$$\Gamma_{C,out} \chi_{i,C,out} = \sum_{k=1}^{n_{cells}} \int_0^1 \left[\gamma_C^{(k)} \chi_{i,C}^{(k)} \right]_{\zeta_1, \zeta_2=1} d\zeta_1 \quad (59)$$

$$\begin{aligned} \Gamma_{C,out} \bar{c}_{PC,out} (\vartheta_{C,out} - \vartheta^r) \\ = \sum_{k=1}^{n_{cells}} \int_0^1 \left[\gamma_C^{(k)} \bar{c}_{PC}^{(k)} (\vartheta_C^{(k)} - \vartheta^r) \right]_{\zeta_1, \zeta_2=1} d\zeta_1 \end{aligned} \quad (60)$$

$$\Gamma_{C,out} = \sum_{k=1}^{n_{cells}} \int_0^1 \left[\gamma_C^{(k)} \right]_{\zeta_1, \zeta_2=1} d\zeta_1 \quad (61)$$

A part of the cathode exhaust gas is recycled (REC). The cathode gas recycle ratio, f_{REC} , determines the gas fraction of cathode exhaust gas that is redirected towards the catalytic combustion chamber (see Section 3.2.5). The value used for f_{REC} is given in Table 2.

$$\chi_{i,REC} = \chi_{i,C,out} \quad (62)$$

$$\vartheta_{REC} = \vartheta_{C,out} \quad (63)$$

$$\Gamma_{REC} = f_{REC} \Gamma_{C,out} \quad (64)$$

3.2.9 Electrode Pores

Within the electrode pores, the electrochemical reactions take place. The spatial distribution of the gas composition along the pore is neglected and an integral mass balance is used to describe the partial pressure of the components, $\varphi_{i,AC}^{(k)}$ and $\varphi_{i,CC}^{(k)}$, in the pores of the corresponding electrodes:

$$\frac{V_{AC}}{\vartheta_S^{(k)}} \frac{\partial \varphi_{i,AC}^{(k)}}{\partial \tau} = \sum_{j=ox} v_{ij} D a_{j,AC} f_{j,AC}^{(k)} - n_{i,AS}^{(k)} \quad (65)$$

$$\frac{V_{CC}}{\vartheta_S^{(k)}} \frac{\partial \varphi_{i,CC}^{(k)}}{\partial \tau} = \sum_{j=red} v_{ij} D a_{j,CC} f_{j,CC}^{(k)} - n_{i,CS}^{(k)} \quad (66)$$

The component mass flux between the gas channels and the electrode pores, $n_{i,AS}^{(k)}$ and $n_{i,CS}^{(k)}$, are given in Eqs. (31) and (53), respectively. Regarding the enthalpy balance, the electrode pores are considered as part of the solid phase (see Section 3.2.10).

3.2.10 Solid Phase

The enthalpy balance within the solid phase (S) of each fuel cell (Eq. (67)) considers heat conduction along the cell plane, enthalpy exchange due to mass exchange with the gas channels, non-convective heat exchange with the gas phases ($q_{AS}^{(k)}$ and $q_{CS}^{(k)}$), heat source terms due to electrochemical reactions and ion conduction ($q_{S,cell}^{(k)}$) and heat exchange along the stack.

$$\begin{aligned} c_{PS} \frac{\partial \vartheta_S^{(k)}}{\partial \tau} = \frac{l_2}{Pe_S} \frac{\partial^2 \vartheta_S^{(k)}}{\partial \zeta_1^2} + \frac{1}{Pe_{S,l_2}} \frac{\partial^2 \vartheta_S^{(k)}}{\partial \zeta_2^2} \\ + \left(\sum_i (-n_{i,AS}^{(k)}) c_{Pi} \right) (\vartheta_A^{(k)} - \vartheta_S^{(k)}) \\ + \left(\sum_i (-n_{i,CS}^{(k)}) c_{Pi} \right) (\vartheta_C^{(k)} - \vartheta_S^{(k)}) - q_{AS}^{(k)} - q_{CS}^{(k)} + q_{S,cell}^{(k)} + q_{S,stack}^{(k)} \end{aligned} \quad (67)$$

Fuel Cells

Pfafferodt et al.: Stack Modelling of a Molten Carbonate Fuel Cell (MCFC)

The molar flux densities from the anode gas channels to the solid phase are given by

$$n_{i,AS}^{(k)} = \begin{cases} 0, & \text{if } n_{i,AS}^{(k)} > 0 \\ n_{i,AS}^{(k)}, & \text{if } n_{i,AS}^{(k)} \leq 0 \end{cases} \quad (68)$$

and for the cathode gas channels an analogous equation is used

$$n_{i,CS}^{(k)} = \begin{cases} 0, & \text{if } n_{i,CS}^{(k)} > 0 \\ n_{i,CS}^{(k)}, & \text{if } n_{i,CS}^{(k)} \leq 0 \end{cases} \quad (69)$$

The heat source density within the solid phase, $q_{S,cell}$, includes the heat production due to the electrochemical reactions as well as the heat production due to the ion conduction:

$$\begin{aligned} q_{S,cell}^{(k)} = & \sum_{j=ox} \left(-\Delta R h_j^0 (q_S^{(k)}) + n_j \left(\varphi_A^{S(k)} - \varphi_A^{L(k)} \right) \right) D a_{j,AC} r_{j,AC}^{(k)} \\ & + \sum_{j=red} \left(-\Delta R h_j^0 (q_S^{(k)}) + n_j \left(\varphi_C^{S(k)} - \varphi_C^{L(k)} \right) \right) D a_{j,CC} r_{j,CC}^{(k)} \\ & + \left(\varphi_A^{L(k)} - \varphi_C^{L(k)} \right) i_E^{(k)} \frac{1}{F} \end{aligned} \quad (70)$$

The heat exchange in stack direction, $q_{S,stack}^{(k)}$, depends on the location of the fuel cell within the symmetric stack model, i.e.:

$$q_{S,stack}^{(k)} = \begin{cases} q_{S,IR} - q_{S,conn}^{(k),(k+1)}, & \text{if } k = 1 \\ q_{S,conn}^{(k-1),(k)} - q_{S,conn}^{(k),(k+1)}, & \text{if } 1 < k < n_{cells} \\ q_{S,conn}^{(k-1),(k)}, & \text{if } k = n_{cells} \end{cases} \quad (71)$$

Equation (71) shows that each fuel cell is connected to its two neighbouring fuel cells. Taking into account the symmetric boundary conditions on both sides of the symmetric stack model, the reforming unit is directly connected to the first fuel cell, while the last fuel cell is only connected to its predecessor.

The heat exchange between the solid phases of two neighbouring fuel cells, $q_{S,conn}^{(m),(n)}$, depends on the temperature difference between the corresponding solid phases

$$q_{S,conn}^{(m),(n)} = S t_S \left(q_S^{(m)} - q_S^{(n)} \right) \quad (72)$$

The heat flux density between the reforming unit and the first fuel cell, $q_{S,IR}$, is given in Eq. (27).

3.2.11 Electric Potential

The description of the electric potential field is of essential importance for the determination of the current density distribution. For each cell, the dynamic charge balances at both

charged double layers are set up and combined with a discretised form of the Poisson equation.

$$\varphi_A^{S(k)} = 0 \quad (73)$$

$$\frac{\partial \varphi_A^{L(k)}}{\partial \tau} = -\frac{1}{c_A} \left(i^{(k)} - i_A^{(k)} \right) \quad (74)$$

$$\frac{\partial \varphi_C^{L(k)}}{\partial \tau} = -\frac{1}{c_A} \left(i^{(k)} - i_A^{(k)} \right) - \frac{1}{c_E} \left(i^{(k)} - i_E^{(k)} \right) \quad (75)$$

$$\frac{d\varphi_C^{S(k)}}{d\tau} = \frac{I_C^{(k)} - I_A^{(k)}}{c_A} + \frac{I_{cell}^{(k)} - I_E^{(k)}}{c_E} + \frac{I_C^{(k)} - I_C^{(k)}}{c_C} \quad (76)$$

The specific currents and current densities at the anode, within the electrolyte and at the cathode are given by the kinetics of the electrochemical reactions (Eq. (78) and Eq. (80)) and the ion conduction within the electrolyte (Eq. (80)):

$$I_A^{(k)} = \int_A i_A^{(k)} d\zeta \quad (77)$$

$$i_A^{(k)} \left(\varphi_A^{S(k)}, \varphi_A^{L(k)} \right) = \sum_{j=ox} n_j F D a_{j,AC} r_{j,AC}^{(k)} \left(\varphi_A^{S(k)}, \varphi_A^{L(k)} \right) \quad (78)$$

$$I_E^{(k)} = \int_E i_E^{(k)} d\zeta \quad (79)$$

$$i_E^{(k)} \left(\varphi_A^{L(k)}, \varphi_C^{L(k)} \right) = \kappa_E \left(\varphi_A^{L(k)} - \varphi_C^{L(k)} \right) \quad (80)$$

$$I_C^{(k)} = \int_C i_C^{(k)} d\zeta \quad (81)$$

$$i_C^{(k)} \left(\varphi_C^{L(k)}, \varphi_C^{S(k)} \right) = - \sum_{j=red} n_j F D a_{j,CC} r_{j,CC}^{(k)} \left(\varphi_C^{S(k)}, \varphi_C^{L(k)} \right) \quad (82)$$

with $r_{j,AC}^{(k)}$ and $r_{j,CC}^{(k)}$ representing the Butler-Volmer kinetics in the corresponding electrodes (see Section 3.2.12).

Using the specific currents and current densities, the current density distribution of one fuel cell is calculated as

$$i^{(k)} = \left(\frac{1}{c_A + \frac{1}{c_E} + \frac{1}{c_C}} \right) \left(\frac{i_A^{(k)}}{c_A} + \frac{i_E^{(k)}}{c_E} + \frac{i_C^{(k)}}{c_C} - \frac{I_A^{(k)}}{c_A} - \frac{I_E^{(k)}}{c_E} - \frac{I_C^{(k)}}{c_C} \right) + I_{cell}^{(k)} \quad (83)$$

The cell voltage is the electric potential difference between the cathode and anode solid phase, while the voltage of the entire stack model is given as the sum of all cell voltages:

$$U_{\text{cell}}^{(k)} = \varphi_{\text{C}}^{(S(k))} - \varphi_{\text{A}}^{(S(k))} = \varphi_{\text{C}}^{(S(k))} \quad (84)$$

$$U_{\text{stack}} = \sum_k U_{\text{cell}}^{(k)} \quad (85)$$

3.2.12 Reaction Kinetics

In the symmetric stack model, two types of reactions are considered. On the one hand, the methane steam reforming (ref1) and the water gas shift reaction (ref2) within the reactive phase of the reforming unit and within the anode gas compartment are described by a simple power law approach including an Arrhenius term. These reactions are typically close to their chemical equilibrium.

On the other hand, Butler–Volmer kinetics are used for the electrochemical oxidation of hydrogen (ox1) and carbon monoxide (ox2) at the anode

$$r_{\text{ox1}}^{(k)} = \exp \left(\text{Arr}_{\text{ox1}} \left(\frac{1}{g_{\text{ox1}}^{(k)}} - \frac{1}{g_{\text{S}}^{(k)}} \right) \right) \times \left\{ \begin{array}{l} \varphi_{\text{H}_2, \text{AC}}^{(k)} \exp \left(a_{\text{ox1},+} n_{\text{ox1}} \frac{\Delta \varphi_{\text{A,ox1}}^{(k)}}{g_{\text{S}}^{(k)}} \right) \\ - \varphi_{\text{H}_2, \text{O,AC}}^{(k)} \varphi_{\text{CO}_2, \text{AC}}^{(k)} \exp \left(- (1 - a_{\text{ox1},+}) n_{\text{ox1}} \frac{\Delta \varphi_{\text{A,ox1}}^{(k)}}{g_{\text{S}}^{(k)}} \right) \end{array} \right\} \quad (86)$$

$$r_{\text{ox2}}^{(k)} = \exp \left(\text{Arr}_{\text{ox2}} \left(\frac{1}{g_{\text{ox2}}^{(k)}} - \frac{1}{g_{\text{S}}^{(k)}} \right) \right) \times \left\{ \begin{array}{l} \varphi_{\text{O,AC}}^{(k)} \exp \left(a_{\text{ox2},+} n_{\text{ox2}} \frac{\Delta \varphi_{\text{A,ox2}}^{(k)}}{g_{\text{S}}^{(k)}} \right) \\ - \left(\varphi_{\text{CO}_2, \text{AC}}^{(k)} \right)^2 \exp \left(- (1 - a_{\text{ox2},+}) n_{\text{ox2}} \frac{\Delta \varphi_{\text{A,ox2}}^{(k)}}{g_{\text{S}}^{(k)}} \right) \end{array} \right\} \quad (87)$$

and the electrochemical reduction of oxygen (red) at the cathode [12].

$$r_{\text{red}}^{(k)} = \exp \left(\text{Arr}_{\text{red}} \left(\frac{1}{g_{\text{red}}^{(k)}} - \frac{1}{g_{\text{S}}^{(k)}} \right) \right) \times \left\{ \begin{array}{l} \left(\varphi_{\text{CO}_2, \text{CC}}^{(k)} \right)^{-2} \exp \left(2.5 \frac{\Delta \varphi_{\text{C,red}}^{(k)}}{g_{\text{S}}^{(k)}} \right) \\ - \left(\varphi_{\text{O}_2, \text{CC}}^{(k)} \right)^{0.75} \left(\varphi_{\text{CO}_2, \text{CC}}^{(k)} \right)^{-0.5} \exp \left(-0.5 \frac{\Delta \varphi_{\text{C,red}}^{(k)}}{g_{\text{S}}^{(k)}} \right) \end{array} \right\} \quad (88)$$

4 Numerical Solution

The model is solved using COMSOL Multiphysics Version 3.5 [20]. Taking into account all equations, the symmetric stack model consists of 114 PDEs and 26 ODEs as well as a

number of algebraic equations. These equations are highly coupled to each other due to the connection of the gas compartments *via* the gas flow, the thermal interactions between all parts of the fuel cell, especially in stack direction, and the coupling of the electrochemical reaction rates at the anode and cathode of each fuel cell. Using a 6×6 mapped mesh and Lagrange-Quadratic elements, the discretised model has 19,292 degrees of freedom. To reduce the numerical effort, a coarser mesh is used to obtain initial solutions, before the fine mesh is employed to calculate the final solution. The UMFPACK direct solver is used.

The calculation time required to solve the symmetric stack model is about 15 min on a Dual Intel Xeon CPU 3.20GHz. Up to 3.5 GB RAM are needed to calculate a solution.

5 Simulation Results

In this section, selected results from the steady-state simulation of the symmetric stack model with one half reforming unit and four fuel cells are presented in order to demonstrate the functionality and potential of the model. First, a set of input parameters, the so-called base case, is defined (Table 2). The base case conditions correspond to the values of the operating point 4 with an average current density of $i_{\text{avg}} = 80 \text{ mA/cm}^2$ used in the model validation by Gundermann et al. [17, 21]. The feed gas composition corresponds to a mixture of methane and steam with a steam to carbon ratio of about 2.4 which has been reformed in the external reformer to about 20% conversion. In contrast to the work of Gundermann et al., the symmetric stack model considers the stack direction as an additional coordinate, i.e. the impact of a temperature profile along the stack length is shown by the simulation results.

In the following, the simulated results of the gas composition within the reforming unit, the anode channels and the cathode compartments are discussed. Afterwards, the current densities for the four fuel cells are presented. This is followed by a discussion of the temperature distribution within the solid phases and the resulting temperature profile in stack direction. At the end of this section, the results of the symmetric stack model are compared to the results of the validated model by Gundermann et al.

This model has been derived based on a HotModule system build by MTU Onsite Energy, Germany. The simulation results reflect one of its operating points. In order to protect the intellectual property of our industrial partner we omit any absolute values in the following sections. However, we discuss the results qualitatively and draw some conclusions from that.

5.1 Gas Composition

Figures 4–6 show some profiles of the molar fractions in the symmetric stack model. Within the reforming unit and the anode compartments, especially the methane molar frac-

Fuel Cells

Pfafferodt et al.: Stack Modelling of a Molten Carbonate Fuel Cell (MCFC)

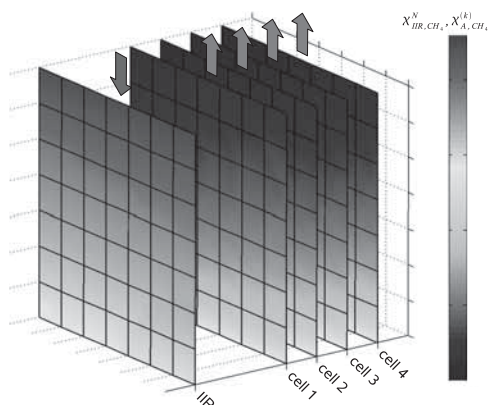


Fig. 4 Methane molar fraction in the non-reactive phase of the reforming unit (IRR) and in the anode gas channels of the four fuel cells. The flow direction within the gas compartments is indicated by the arrows.

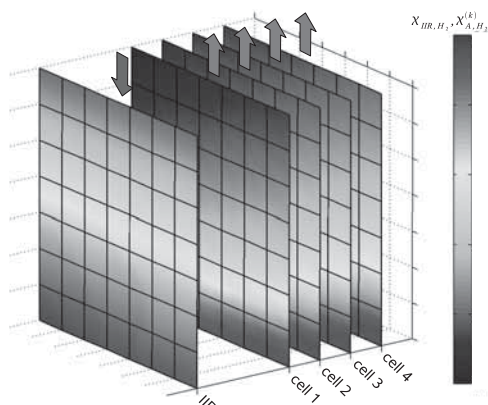


Fig. 5 Hydrogen molar fraction within the reforming unit (IRR) and the anode gas compartments of the four fuel cells. The arrows indicate the flow direction of the gas.

tion (Figure 4) and the hydrogen molar fraction (Figure 5) are of interest, while in the cathode channels, the molar fraction of carbon dioxide (Figure 6) is important.

The molar fraction of methane within the non-reactive phase of the reforming unit and in the anode channels is shown in Figure 4. Within the reforming unit, about 30% of the methane present at the inlet is converted to hydrogen. The chemical equilibrium, taking into account the local gas

temperature, is reached within the reactive phase. Due to the mass transport limitation across the phase interface, equilibrium is not achieved in the non-reactive phase. Within the anode channels, the reforming products are continuously consumed by the electrochemical oxidation, so the methane concentration reaches virtually zero at the anode outlets.

Figure 5 shows the hydrogen molar fraction in the reforming unit and the four fuel cells. Within the reforming unit, methane is converted to hydrogen by the methane reforming reaction. Hence, the hydrogen molar fraction increases to approximately one third at the outlet of the reforming unit. In the anode gas compartments, two processes occur. On the one hand, hydrogen is produced by the reforming process, and on the other hand, hydrogen is consumed by the electrochemical reactions. Thus, the hydrogen molar fraction within the anode slightly increases near the anode gas inlet and after that decreases towards the gas outlet. The high concentration of hydrogen at the anode inlet also results in high electrochemical reactions rates at this point.

The hydrogen molar fraction is especially low at the anode outlet of cell 1 compared to the hydrogen molar fraction at the outlets of the other fuel cells. Considering the methane molar fraction, an inverse characteristic can be observed. This can be attributed to the lower temperatures in cell 1 due to the neighbouring reforming unit. As a result, the rates of the reforming reactions within the anode gas compartment are reduced and the equilibrium of these reactions is moved towards the educts.

Carbon dioxide is an important reactant for the electrochemical reduction reaction in the cathode channels. Its molar fraction is shown in Figure 6. At the cathode inlet, the molar fraction of carbon dioxide is only a few mole percent. Along the channels, carbon dioxide is consumed in the electrochemical reaction. The consumption is higher in the lower cathode channels due to higher electrochemical reactions rates. This almost leads to depletion of carbon dioxide near the bottom left corner, where the anode inlet and the cathode outlet are located. Due to the fact that carbon dioxide is needed as an educt for the electrochemical reduction, its concentration, especially at this point, is critical for higher fuel utilisation.

5.2 Current Density Distribution

Figure 7 presents the current densities for the four fuel cells with an average cell current density of $i_{\text{cell}} = 80 \text{ mA/cm}^2$ as defined for the base case. All profiles are similar to each

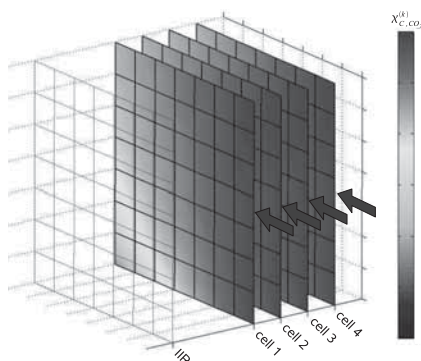


Fig. 6 Molar fraction of carbon dioxide within the cathode gas compartments of the four fuel cells. The gas flow is indicated by the arrows.

other. The maximum difference in local current density between two neighbouring cells is less than $\Delta i = 10 \text{ mA/cm}^2$, although they are calculated independently. This means that the currents flowing through the bipolar plates in perpendicular direction to the stacking direction (ζ_1 and ζ_2) are small. Therefore also the gradients in electric potential in the bipolar plates are small. Thus, the assumption of independent electric potentials for each cell (Section 3.1) is justified.

The rate of the electrochemical reactions, and therefore also the local current density, mainly depends on the concentration profiles of the educts of these reactions. Especially the concentrations of hydrogen in the anode channels and carbon dioxide in the cathode channels govern the current density distribution significantly. Due to the high concentration of hydrogen at the anode inlet, the highest current densities can be found in this region.

According to the superoxide reaction mechanism (Prins-Jansen et al. [22,23]), a negative order of reaction with respect to carbon dioxide is used for the cathodic reduction kinetics. Thus, the current density increases towards the end of the cathode channel, where the carbon dioxide fraction is low. Therefore, the current density peak is located in the vicinity of the anode inlet/cathode outlet, the bottom left corner of each fuel cell.

The main difference in the current density profiles of the four cells is the peak current density. The strong cooling effect in the upper half of cell 1 due to the reforming process in the IIR unit results in lower current densities in this part of the cell. However, because the total cell current is given, this decreased current density in the upper half has to be compensated by high current densities in the peak region. There, the current density reaches values of more than twice the average value.

In contrast, the temperatures in cell 4 are generally higher due to the reduced effect of the cooling by the IIR unit. Thus, the current density distribution is more homogeneous in this cell.

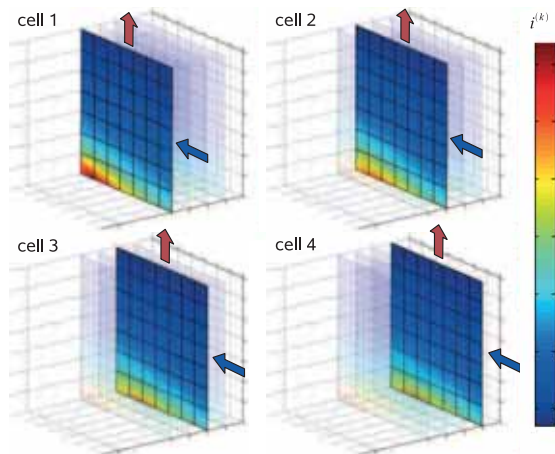


Fig. 7 Current densities within the four fuel cells. The flow directions of the anode and cathode gases are indicated by the arrows.

5.3 Temperature Distribution

The temperature distribution within the solid phases of the four fuel cells is shown in Figure 8. Temperatures are around 600°C , with a maximum temperature difference of approximately 100°C .

In each cell, the highest temperature is located near the same corner where the current density peak is observed. This is mainly because of two reasons. First, the high local current density results in a strong heat source in that area due to losses in the electrochemical reactions and due to the ion conduction. The second reason for the location of the temperature peak is that the cooling effect of the IIR unit is especially strong in the upper half of the symmetric stack model, which effectively lowers the cell temperature there.

The cooling effect of the reforming unit becomes evident when comparing the temperature profiles of the four fuel cells. While the temperatures are generally lowest in cell 1, highest temperatures

Fuel Cells

Pfafferodt et al.: Stack Modelling of a Molten Carbonate Fuel Cell (MCFC)

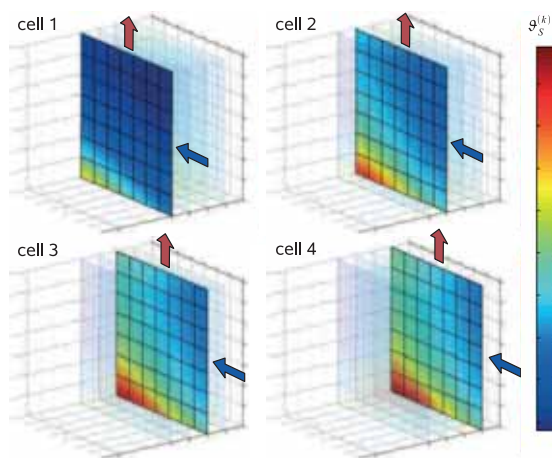


Fig. 8 Temperature profile within the solid phases of the four fuel cells. The reforming unit (IIR), where the endothermic reforming reaction takes place, is located on the left hand side of the first cell. The flow direction within the anode and cathode gas compartments are indicated by the arrows.

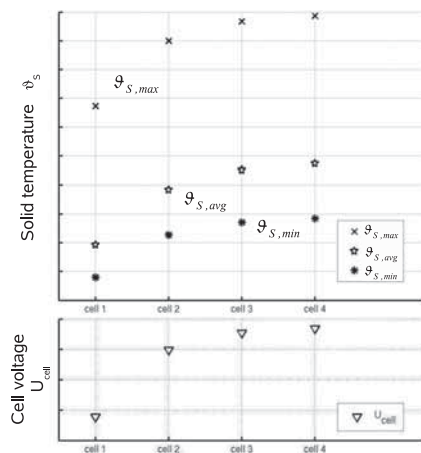


Fig. 9 Minimum, average and maximum temperature within the solid phase of the four fuel cells (top) and the cell voltages (bottom).

are predicted in cell 4, which is farthest away from the IIR unit. This results in an approximately parabolic temperature profile in stack direction.

The temperature levels between the four fuel cells ($T_{S,min}$, $T_{S,avg}$ and $T_{S,max}$) differ by several 10 °C (Figure 9). Compared to the typical temperature difference in each cell, this gradient along the stack direction is significant. However, it seems that the temperature differences over each individual cell are nearly constant. So, although each cell operates at a significantly different temperature level, each cell has nearly the same temperature difference within the cell area.

With respect to cell voltages, an increase by several 10 mV from the first fuel cell to the fourth fuel cell is observed. This is clearly an effect of the cell temperature. A comparison between the cell voltages and the cell temperatures shows a similar slope, indicating a clear dependency between these values.

From these observations, two conclusions can be drawn. First, the individual fuel cells show very similar states with respect to gas composition, voltage and current density. A reduction of the stack model to a model with one single representative cell, as in Gundermann et al. [13] is acceptable, if only these states are of interest. Second, concerning the cell temperature, the four cells show significant differences here. Especially for design and optimisation purposes, where these values are considered important, the temperature profile in stack direction should not be neglected. For these applications, the stack model is a useful tool.

5.4 Comparison to the Validated Model

The load case shown here has previously been used by Gundermann et al. [17]. In their work, it was one of the four load cases for which extensive sets of experimental data were available from a 250 kW_{el} 'HotModule' MCFC power plant manufactured by MTU Onsite Energy, Germany. These data sets were used to identify unknown parameters in a single cell model with an IIR unit. The single cell represented the average behavior of all cells in the stack. As a result, the deviation of the model by Gundermann et al. with respect to the experimental data was less than or equal to the estimated measurement error, thereby validating the model [24]. To demonstrate the validity of our stack model, we compare some important values to those from the simulations of the previously validated model.

A variable which influences nearly all processes within the MCFC stack is the temperature of the solid phases. The temperature profiles show identical characteristics for both models with a maximum at the anode inlet/cathode outlet and a lower temperature in the top half of the fuel cells (see Figure 8). A solid phase temperature between $T_{S,min} = 553^\circ\text{C}$ and $T_{S,max} = 642^\circ\text{C}$ was found in the validated simulations of Gundermann et al., which are well within the temperature range calculated for the symmetric stack model.

The current densities from both models show similar profiles (see Figure 7). For the model of Gundermann et al., a maximum current density of $i_{max} = 164 \text{ mA/cm}^2$ was found. According to the stack model, the maximum current density varies around this value. The cell voltage for both models is around $U_{cell} = 0.80 \text{ V}$, therefore the electric power generated by each cell as well as the efficiency of the MCFC system are nearly identical. Thus, the results of the new symmetric stack model correspond to those from the previously validated model and can be considered to adequately approximate the real stack behaviour.

6 Conclusion

The symmetric stack model presented here allows the simulation of a representative section of a MCFC stack. It consists of one half IIR unit and four fuel cells. The highly non-linear coupling of all parts of the stack, mainly due to the thermal interactions, the mass flow and the corresponding electrochemical reactions at the anode and the cathode of each fuel cell are taken into account.

The functionality of the model has been demonstrated using a steady state simulation based on validated model parameters. The model predicts the gas phase compositions, the temperature profiles and the current density distribution within each of the four fuel cells. The results of the symmetric stack model are similar to the simulation results of an earlier, validated model by Gundermann et al. [25].

The current density distributions for all cells in the stack show similar profiles. But due to the cooling effect of the reforming unit, the cell temperatures deviate by several 10°C . As overheating is one of the reasons for degradation in an MCFC system, one may expect that cells 3 and 4 are degrading fastest in this stack.

Compared to the previous work, the model presented here takes into account the differences of the state variables within the fuel cells along the stack direction. It is shown that the temperature changes along this coordinate are significant with regard to the temperature differences within the cell planes. Therefore it is suitable for applications, where the three-dimensional temperature profile within the stack should be considered.

Due to its generalised formulation, the model can easily be extended to different numbers of fuel cells. Furthermore, inhomogeneous gas feed distributions to the anode or cathode gas compartments of the different fuel cells as well as dif-

ferent gas flows for each fuel cell can be implemented. Additionally, the transient form of the model equations allows the simulation of load changes.

Considering the points listed above, the presented model gives the possibility to optimise design and operating parameters of MCFC systems with regard to homogenised temperature distributions and increased efficiency.

Acknowledgement

This work was financially supported by the MTU Onsite Energy – Fuel Cell Systems GmbH, Ottobrunn, Germany.

Notation

All listed variables are dimensionless quantities. The parameter values given here are valid for the symmetric stack model with one half reforming unit and four fuel cells.

Latin Letters

c	capacity of charged double layers
$c_A = c_E = c_C = 1 \cdot 10^{-5}$	
$c_{P,i}$	molar heat capacity of component i
$\bar{c}_{P,l}$	molar heat capacity of gas mixture in compartment l
$c_{P,S}$	molar heat capacity of solid phase
$Da_{j,l}$	Damköhler number (reaction rate constant) of reaction j in compartment l
$Da_{ref1,IIR}^R$	800
$Da_{ref2,IIR}^R$	800
$Da_{ref1,A}$	200
$Da_{ref1,A}$	200
$Da_{ox1,AC}$	7
$Da_{ox2,AC}$	7
$Da_{red,CC}$	0.15
$D_{i,l}$	mass transport coefficient of component i in gas compartment l
$D_{i,IIR}^J$	16
$D_{i,AC}$	100
$D_{i,CC}$	100
f_{REC}	cathode gas recycle ratio
F	stoichiometric factor
i	electric current density
I	total electric cell current
l_2	geometric length ratio
n_{cells}	number of fuel cells
n_i	mass exchange flux density of component i
n_j	number of exchanged electrons of reaction j
n_t	total mass exchange flux density
P_{blower}	electric power of the blower
Pe_S	Peclet number (heat conduction resistance) of solid phase $Pe_S = 2.5$
q	surface related heat flux density
$q_{S,cell}$	heat source density in solid phase

Fuel Cells

Pfafferodt et al.: Stack Modelling of a Molten Carbonate Fuel Cell (MCFC)

$q_{S, \text{conn}}$	heat flux density between two solid phases
$q_{S, \text{stack}}$	heat flux density in stack direction
θ	heat flux
$r_{j,l}$	reaction rate of reaction j in gas compartment l
St	Stanton number (heat exchange coefficient)
St_{IRS}^N	200
St_{IRS}^R	200
St_{IIR}^H	60
St_{HE}	200
St_{RAC}	2
St_{AS}	40
St_{CS}	140
St_{S}	100
U	voltage
V	volume

Greek Letters

γ	molar flow density (per cross-sectional area) in channels
Γ	molar flow
$\Delta_C h_i^0$	standard enthalpy of combustion of component i
$\Delta_R h_j^0$	standard enthalpy of reaction j
ε	volume fraction ($\varepsilon_{\text{IIR}}^N = 0.75$, $\varepsilon_{\text{IIR}}^R = 0.20$, $\varepsilon_{\text{IIR}}^H = 0.05$)
ζ	spatial coordinate
ϑ	temperature
ϑ^r	reference temperature
κ_E	ion conductivity in electrolyte ($\kappa_E = 1$)
$\nu_{i,j}$	stoichiometric coefficient of component i in reaction j
$\bar{\nu}_j$	sum of stoichiometric coefficients of reaction j
τ	time
φ_i	partial pressure of component i in electrode pores
ϕ	electric potential
χ_i	molar fraction

Subscripts

i	component index
j	reaction index
k	cell index
l	compartment index
t	total
IIR A S C	compartments: reforming unit, anode, solid, cathode
AC CC	compartments: anode pores, cathode pores
B RAC	compartments: combustion chamber, reversal chamber
HEA HEB	compartments: heat exchanger (A: cold side; B: hot side)
AS CS	interface: anode/solid, cathode/solid
IN AIR REC	gas flows: inlet, air, cathode gas recycle

ref1 ref2	reactions: methane steam reforming, water-gas shift reaction
ox1 ox2	reactions: hydrogen oxidation, carbon monoxide oxidation
red	reactions: oxygen reduction
in out	inlet, outlet
cell stack	one cell, entire stack
diff conv	diffusive, convective

Superscripts

$+$ -	forward and backward direction of mass flow
θ	standard conditions
S	solid (electron conducting) phase of electrode
L	liquid (ion conducting) phase of electrode
I	phase interface in reforming unit
N	non-reactive phase in reforming unit
R	reactive phase in reforming unit

References

- [1] P. Tomczyk, *J. Power Sources* **2006**, 160, 858.
- [2] M. Bischoff, *J. Power Sources* **2006**, 160, 842.
- [3] N. Woudstra, T. van der Stelt, K. Hemmes, *J. Fuel Cell Sci.* **2006**, 3, 155.
- [4] T. Watanabe, Y. Izaki, Y. Mugikura, H. Morita, M. Yoshikawa, M. Kawase, F. Yoshida, K. Asano, *J. Power Sources* **2006**, 160, 868.
- [5] F. Yang, X.-J. Zhu, G.-Y. Cao, *J. Power Sources* **2007**, 164, 713.
- [6] F. Yang, X.-J. Zhu, G.-Y. Cao, *J. Power Sources* **2007**, 166, 354.
- [7] L.-j. Yu, G.-p. Ren, X.-m. Jiang, *Energy Conversion Manage.* **2008**, 49, 873.
- [8] P. Iora, S. Campanari, *J. Fuel Cell Sci. Technol.* **2007**, 4, 501.
- [9] M. Baranek, H. Atakuel, *J. Power Sources* **2007**, 172, 831.
- [10] M. Fermeglia, A. Cudicio, G. DeSimone, G. Longo, S. Priol, *Fuel Cells* **2005**, 5, 66.
- [11] P. Heidebrecht, *Ph.D. Theses*, Otto-von-Guericke University, Magdeburg, Germany, **2005**.
- [12] P. Heidebrecht, K. Sundmacher, *J. Electrochem. Soc.* **2005**, 152, A2217.
- [13] M. Gundermann, P. Heidebrecht, K. Sundmacher, *Fuel Cells* **2008**, 8, 96.
- [14] J. Brouwer, F. Jabbari, E. M. Leal, T. Orr, *J. Power Sources* **2006**, 158, 213.
- [15] M. Sheng, M. Mangold, A. Kienle, A strategy for the spatial temperature control of a molten carbonate fuel cell system, *J. Power Sources* **162** (2, Sp. Iss. SI) (**2006**) 1213–1219.
- [16] P. Heidebrecht, K. Sundmacher, *Ind. Eng. Chem. Res.* **2005**, 44, 3522.
- [17] M. Gundermann, P. Heidebrecht, K. Sundmacher, *Ind. Eng. Chem. Res.* **2008**, 47, 2728.

- [18] M. Pfafferodt, P. Heidebrecht, K. Sundmacher, U. Wuerthenberger, M. Bednarz, *Ind. Eng. Chem. Res.* **2008**, *47*, 4332.
- [19] A. Musa, H. J. Steeman, M. De Paepe, *J. Fuel Cell Sci. Technol.* **2007**, *4*, 65.
- [20] COMSOL Multiphysics Reference Manual (Version 3.5), Stockholm, COMSOL 3.5, **2008**.
- [21] M. Gundermann, *Ph.D. Thesis*, Otto-von-Guericke University, Magdeburg, Germany, **2008**.
- [22] J. A. Prins-Jansen, K. Hemmes, J. H. W. de Wit, *Electrochim. Acta* **1997**, *42*, 3585.
- [23] J. A. Prins-Jansen, K. Hemmes, J. H. W. de Wit, *Electrochim. Acta* **1997**, *42*, 3601.
- [24] M. Gundermann, P. Heidebrecht, K. Sundmacher, *J. Fuel Cell Sci. Technol.* **2006**, *3*, 303.

[PH 6]

P. Heidebrecht, B. Hartono, C. Hertel, K. Sundmacher

Biomass-Based Fuel Cell Power Plants:
Evaluation of Novel Reactors and Process Designs

Industrial & Engineering Chemistry Research 49, 21 (2010),
10859-10875

Biomass-Based Fuel Cell Power Plants: Evaluation of Novel Reactors and Process Designs

Peter Heidebrecht,[†] Benny Hartono,[†] Christoph Hertel,[‡] and Kai Sundmacher^{*†,‡}

Max Planck Institute for Dynamics of Complex Technical Systems, Sandtorstrasse 1,
39106 Magdeburg, Germany, and Process Systems Engineering, Otto von Guericke University,
Universitätsplatz 2, 39106 Magdeburg, Germany

This contribution focuses on the model-based system design and the systemwide evaluation of novel reactor concepts for power plants which combine gasification of wood and conversion of its gaseous product in fuel cells. System design was carried out with the help of a model library, which contains models of all reactor units under consideration. Each system was subject to several feasibility checks, and optimization of the most important control parameters was performed. Simulation results show that high temperature gas purification units and high temperature proton exchange membrane fuel cells have strong advantages over their classical counterparts with respect to heat integration and electrical system efficiency. Systems with high and low temperature fuel cells were studied separately, but they show that a combination of both types of fuel cells in a single plant offers the highest efficiency and attractive flexibility with respect to electricity and heat production.

1. Introduction

Biomass is seen as a renewable energy source with a high potential to reduce greenhouse gas emissions and substitute fossil fuels. In 1999, biomass already contributed about two-thirds of the total renewable energy production in the European Union or 4% of the total energy supply. This proportion may rise to about 10% in 2010.¹ Biomass fuels and residues can be converted to a fuel gas via thermal, biological, and mechanical processes. Among these processes, thermal processing attracts the most interest due to its high efficiency, low cost, and versatility in providing gases for a wide product range such as energy, fuel, and chemical products.² Three types of thermal processing are already well-known: combustion, gasification, and pyrolysis. This study concentrates on the conversion of biomass into a combustible gas mixture via gasification.

In order to generate electrical energy from the gasifier product gas, fuel cells are an efficient option. They work based on electrochemical reactions and may be operated on lean gases. Some technical advantages of fuel cells are high efficiency, reduced emissions, and low noise level.

Significant research effort is being put into the coupling of fuel cells with gas produced from biomass gasification. These research activities can be classified according to the applied types of fuel cells: low, intermediate, and high temperature systems. Ersoz et al.³ performed a theoretical study of a low temperature system consisting of a gasifier followed by a reformer, classical water–gas shift process (shift reactors and preferential oxidation reactor), and a proton exchange membrane fuel cell (PEMFC). They considered air as a gasification agent. System heat integration was not considered in their study. According to their simulation results, the electrical efficiency of this system varies between 19% and 30%.

In an earlier study, McIlveen-Wright et al.⁴ investigated the integration of the phosphoric acid fuel cell (PAFC), an intermediate temperature fuel cell, with biomass gasification.

The performance of a PAFC and a molten carbonate fuel cell (MCFC) coupled with biomass gasification were assessed. They found that biomass gasification with a PAFC has much lower electrical efficiency than the system with an MCFC. Thus, we exclude intermediate temperature fuel cells from our investigation.

Possible coupling of high temperature fuel cells, i.e. an MCFC or solid oxide fuel cell (SOFC), with biomass gasification has also been studied intensively. Lobachyov and Richter⁵ compared a biomass gasification system coupled with an MCFC versus a biomass gasification–gas turbine system in terms of efficiency, feasibility, and process requirements. They drew a conclusion that an MCFC power plant has a higher overall efficiency and better economic performance than the system with a gas turbine.

Panopoulos et al.⁶ modeled a biomass steam gasification combined with an SOFC and conducted an exergy analysis of the whole system including its thermal integration. Their calculation results show that the electrical system efficiency is ranging between 30% and 40%. Jin et al.⁷ presented detailed process designs of four system variants: two gasification-based combined cycles designed around different gasifier technologies, a gasification-based SOFC, and a steam-Rankine cycle. Performance and cost analyses of these four systems were compared and ranked. They concluded that the gasification system combined with an SOFC has the highest electrical efficiency among the four systems. Because MCFCs and SOFCs show similar features from a system design perspective, such as high operating temperature, internal reforming, and insensitivity with respect to carbon monoxide, the results for SOFC can be transferred qualitatively to MCFC systems. Therefore, MCFC systems are not explicitly considered in the present contribution.

Integration of high and low temperature fuel cells in a parallel or series system was studied by Yokoo et al.^{8,9} In their studies, methane is fed to a steam reformer. In the parallel system, part of the reformed fuel is fed to an SOFC and the rest is fed to a PEMFC via shift reactors and a CO selective oxidizer. In the series system, all reformed fuel is fed to an SOFC, and then to a CO removal sequence and finally to a PEMFC. They came to a conclusion that the parallel system offers a higher electrical efficiency than a simple SOFC process, but lower than the efficiency provided by the SOFC–PEMFC system in series.

* To whom correspondence should be addressed. Tel.: +49-391-6110-350. E-mail: sundmacher@mpi-magdeburg.mpg.de.

[†] Max Planck Institute for Dynamics of Complex Technical Systems.

[‡] Otto von Guericke University Magdeburg.

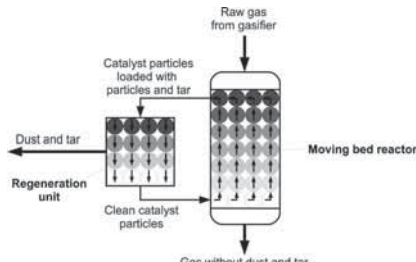


Figure 1. Schematic of the moving bed reactor concept.

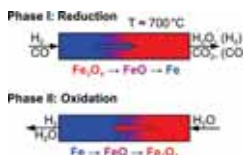


Figure 2. Concept of the cyclic water-gas shift reactor.

Most publications focused on the integration of biomass gasification with only one type of fuel cell. Thermal integration, the possibility of carbon deposition, and the effect of different gasification agents were often not considered. In the present work, we compare different process designs of biomass gasification-fuel cell systems with different types of fuel cells. We also consider aspects such as thermal integration, carbonization, and the most important operating parameters. A second focus is the evaluation of several novel reactors from a systemwide analysis.

2. New Reactor Concepts

The following four reactors are not established units which are currently being developed. They are considered in the design process, and their potential benefits are evaluated in a systemwide context.

2.1. Moving Bed Reactor (MBR). Primary purification of the gasification product requires dust removal and tar reforming. Traditionally, these processes are conducted in two subsequent units or in a scrubber at low temperature. The MBR combines both processes at high temperature (close to the gasifier temperature, 700–850 °C). It consists of a bed of nickel particles with 2–4 mm diameter. The raw gas from the gasifier flows through the bed where the dust is deposited and tar is reformed due to the catalytic activity of the particle bed. The catalyst particles degenerate after a period of time; thus they are continuously removed from the moving bed and fed into a regeneration unit (Figure 1). The MBR was proposed by Herrmann et al.¹⁰

2.2. Cyclic Water-Gas Shift Reactor (CWGSR). The reduction of the CO content in a H₂-rich gas for use in a PEMFC normally involves high and low temperature shift reactors followed by preferential oxidation. As an alternative to this established technology, H₂ purification from CO can be achieved by a novel cyclic water gas shift reactor (CWGSR).^{11,12} It works at a temperature close to the gasifier temperature (650–800 °C). Each process cycle is divided into two phases (Figure 2): during the first phase, the fuel gas is fed into a fixed bed of iron oxide particles. The oxide is reduced and thereby CO and H₂ are oxidized (eqs 1 and 2, forward reaction). After some time, when the bed has been

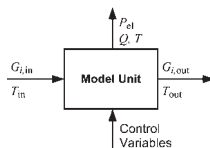
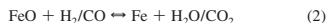


Figure 3. Inlet and outlet streams and input and output variables of a model unit.

sufficiently reduced, feeds are switched and steam is fed into the reactor. During this second phase, the metal is reoxidized (eqs 1 and 2, backward direction), thereby producing H₂ free of CO (Figure 2).¹³



2.3. Electrochemical Preferential Oxidation (ECPPrOx).

Preferential oxidation (PrOx) is a method for CO removal commonly used in series with shift reactors. The success of the PrOx stage depends on complex control of the oxygen partial pressure, the temperature, and the catalyst applied for CO selective oxidation. Electrochemical preferential oxidation (ECPPrOx) is an alternative to the PrOx unit. The design is similar to a conventional PEMFC, but a mixture of Pt/Ru is used at the anode electrode, which is thus able to electrochemically oxidize CO.^{14,15} Under galvanostatic operating conditions (constant current), this reactor shows autonomous oscillations with respect to voltage and CO-coverage at the electrode. These oscillations significantly enhance the average oxidation rate of CO compared to an (unstable) steady state operating point. As its main advantage, ECPPrOx combines CO removal and electricity generation in a single unit.^{16,17}

2.4. High Temperature Proton Exchange Membrane Fuel Cell (HT-PEMFC). One weakness of a PEMFC is its low CO tolerance of only 10 ppm.¹⁸ This limitation is relaxed in a HT-PEMFC, which works at 160–200 °C and, thus, is tolerant to CO concentrations of up to 3%.¹⁹ Because the ion conduction mechanism in the electrolyte of the HT-PEMFC does not require the presence of water, no complex water management is needed. In addition, heat is produced at a higher temperature compared to a conventional low-temperature PEMFC. Thereby, the system's heat integration can be simplified.²⁰

3. Methodology

3.1. Modeling Approach. Our system design is based on mathematical process models, thus we developed a model library which comprises individual models of all process units under consideration. The purpose of these models is to quickly estimate the electrical and thermal performance of different process configurations including the influence of the most important operating parameters. Therefore, spatially lumped steady state models have been set up based on balances of mass and energy, which reflect the most important aspects of each unit.

Although these unit models were derived individually, several general assumptions apply to all of them:

- Isothermal conditions.
- Ideal gas behavior.
- Heat loss to the environment is neglected.
- Eight substances are considered: CO, CO₂, H₂, H₂O, CH₄, N₂, O₂, and C₆H₆O (phenol is selected to represent tar).

- Isentropic compression and expansion for compressors and turbines.
- Minimum temperature difference in heat exchangers, $\Delta T_{\min} = 10\text{ }^{\circ}\text{C}$.
- Ambient conditions are $T = 20\text{ }^{\circ}\text{C}$, $p = 1\text{ bar}$.

- Air components other than O_2 and N_2 are neglected.
 - All units operate at ambient pressure, except pressure swing adsorption (PSA) and palladium membrane (PdM) unit.
- Each unit was modeled as an input–output system, as depicted in Figure 3. It has two groups of input and two groups of output

Table 1. Individual Assumptions and Control Variables of the Modeled Process Units

unit	assumptions	control variable	ref
Gasifier	<ul style="list-style-type: none"> • Operating temperature is $800\text{ }^{\circ}\text{C}$. • The gasifier unit is an atmospheric bubbling fluidized bed reactor. • A fixed mass percentage of biomass is converted to tar (phenol). • Outlet gas composition is in chemical equilibrium with respect to water–gas shift reaction. Methane steam reforming equilibrium is only approximately reached. 	$0 \leq \lambda_{\text{air, gasifier}} \leq 0.8$ $0 \leq \lambda_{\text{steam, gasifier}} \leq 5$	21, 22
Moving Bed Reactor (MBR)	<ul style="list-style-type: none"> • Phenol (tar) is completely reformed to CO and H_2 according to steam reforming and dry reforming reactions. • Outlet gas composition is in chemical equilibrium with respect to steam methane reforming and water–gas shift reaction. • Dust is completely removed from the gas mixture. 	$700\text{ }^{\circ}\text{C} \leq T_{\text{MBR}} \leq 850\text{ }^{\circ}\text{C}$	10
Scrubber	<ul style="list-style-type: none"> • The feed gas is quenched to ambient temperature. • Relative humidity of the outlet gas is 100%. • Phenol and dust are completely removed from the gas mixture. 	N/A	23
High Temperature/Low Temperature Shift Reactor (HTSR/LTSR)	<ul style="list-style-type: none"> • HTSR operating temperature is $300\text{ }^{\circ}\text{C}$. • LTSR operating temperature is $200\text{ }^{\circ}\text{C}$. • Outlet gas composition is in chemical equilibrium with respect to water–gas shift reaction. 	N/A	24, 25
Pressure Swing Adsorption (PSA)	<ul style="list-style-type: none"> • Operating temperature is $30\text{ }^{\circ}\text{C}$. • Upper pressure is 20 bar. • Inlet gas temperature is shifted to PSA operation temperature, thus H_2O is condensed and removed from the inlet gas. • Hydrogen recovery degree is 80%. • The main product stream contains 100% H_2. 	N/A	26, 27
Palladium Membrane (PdM)	<ul style="list-style-type: none"> • Operating temperature is $370\text{ }^{\circ}\text{C}$. • Upper pressure is 6 bar. • Hydrogen recovery degree is 80%. • The main product stream contains 100% H_2. 	N/A	28, 29
Preferential Oxidation (PrOx)	<ul style="list-style-type: none"> • Operating temperature is $90\text{ }^{\circ}\text{C}$. • Carbon monoxide content is decreased to 10 ppm. • Two reactions occur in the reactor, where CO is oxidized to CO_2 and H_2 is oxidized to H_2O. • Selectivity for CO oxidation is 50%. 	N/A	30–32
Electrochemical Preferential Oxidation (ECPrOx)	<ul style="list-style-type: none"> • Operating temperature is $40\text{ }^{\circ}\text{C}$. • Carbon monoxide content is decreased to 10 ppm. 	N/A	14
Cyclic Water–Gas Shift Reactor (CWGSR)	<ul style="list-style-type: none"> • Outlet gas composition is based on equilibria of the system iron/iron oxide under a gas phase of $\text{H}_2/\text{H}_2\text{O}$ or CO/CO_2. 	$650\text{ }^{\circ}\text{C} \leq T_{\text{CWGSR}} \leq 800\text{ }^{\circ}\text{C}$	13
Proton Exchange Membrane Fuel Cell cell (PEMFC)	<ul style="list-style-type: none"> • Operating temperature is $80\text{ }^{\circ}\text{C}$. • Temperature of anode gas is lowered down to ambient temperature; hence, some H_2O is condensed and removed until 100% relative humidity at $30\text{ }^{\circ}\text{C}$ is achieved. • Feasibility constraint: maximum CO content in the anode gas is 10 ppm. 	N/A	33, 34
High Temperature PEMFC (HT-PEMFC)	<ul style="list-style-type: none"> • Operating temperature is $180\text{ }^{\circ}\text{C}$. • Feasibility constraint: maximum CO content in anode gas is 3%. 	N/A	19
Solid Oxide Fuel Cell (SOFC)	<ul style="list-style-type: none"> • Operating temperature is $850\text{ }^{\circ}\text{C}$. • Complete reforming of the feed gas in the anode. • Anode outlet gas composition is in chemical equilibrium with respect to water gas shift reaction. • Minimum cell voltage is 0.7 V. • Minimal steam to carbon ratio is 1.5 (steam is added if necessary). 	Fuel utilization factor: $0 \leq f \leq 1$ (only for sequential process, see section 4.6)	6, 35
Burner	<ul style="list-style-type: none"> • Operating temperature is $900\text{ }^{\circ}\text{C}$. • Air is added according to air number ($\lambda_{\text{air, burner}}$) of 1.2. • CO, H_2, and CH_4 are completely burned. • The exhaust gas is cooled down from operating temperature to the ambient temperature. 	N/A	N/A

Table 2. Properties of Wood Assumed in This Study²⁶

wood composition (dry basis)	
• carbon (wt %)	49.8
• hydrogen (wt %)	6.3
• oxygen (wt %)	43.2
• nitrogen (wt %)	0.1
• tar (wt %)	0.6
higher heating value (MJ/kg)	18.8
moisture content (wt %)	20.0

variables. The first input variables contain information about the molar flow rate of each component in the inlet stream ($G_{i,in}$) and its stream temperature (T_{in}), which are usually determined by the preceding unit. The other input variables, labeled as control variables, represent important operating parameters, which are not fixed a priori, but subject to a system wide optimization. Only the most significant control variables were considered in this study.

The model equations describe specific processes occurring in the unit, such as reactions or heat transfer, and yield several output vectors. The first one gives the data of the outlet gas flow of the unit, which is the molar flow rate of each component in the outlet stream ($G_{i,out}$) and its stream temperature (T_{out}). This output variable is used as an input variable for subsequent units. It should be noted that some of the secondary purification units have two outlet streams and each of them is connected to a subsequent process unit. Those units are the CWGSR, the PdM, and the PSA (see Table 1). Several other units have secondary outlet streams, for example, the cathode outlet gas of the fuel cells. These secondary gas streams do not have any heating value. They are cooled down to ambient temperature and are dismissed from the process. They are not explicitly considered as an output variable.

The second group of the output vectors contains information about the electrical power output or demand (P_{el}), the heat fluxes (\dot{Q}) from or to this unit with their temperature level (T). While the first quantity is used to evaluate the system performance, the latter variables are required for the pinch analysis of the heat integration system.

All process units which were modeled in this study, followed by their most important individual assumptions, are listed in Table 1. In addition, the applied operating parameters as well as their upper and lower bounds are given. To understand how the models were developed, a detailed example of a gasifier model is provided in the Appendix.

3.2. System Configuration. Because none of the unit models assumes a certain reactor size, the models are independent from the actual reactor size; therefore, the biomass feed rate can be chosen arbitrarily. In this study, we assumed a feed rate of 1 kg/s biomass on a dry basis which is equivalent to 1.25 kg/s of “wet” biomass. As feedstock, spruce wood was chosen (Table 2).

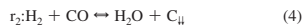
Using the elements of the model library (Table 1), more than 3000 different systems of biomass based fuel cell power plants has been assembled and evaluated systematically. Figure 4 depicts the general sequence of reactors. Biomass is supplied to the gasifier and converted to fuel gas with steam and/or air as the gasification agent. This hot fuel gas passes through a primary purification section to remove particles and tar. The primary purification can either comprise a classical scrubber or

a moving bed reactor. Since it was assumed that both of them remove the particles completely, we did not treat them explicitly in the models. Depending on different applications, the tar free fuel gas must then be further conditioned in a secondary purification section or can be sent directly to a fuel cell. As a final stage, all exhaust gases are combusted in a burner in order to recover useful heat before being released to the environment.

Figure 4 illustrates that the process is a sequence of reactors without recycles. Thus, the unit models were also solved sequentially. At the end, two important indicators of system efficiency can be obtained from the output variables. The first and most important indicator is the electrical power, P_{el} . It is the total electricity produced by the system including all auxiliary power requirements, such as the power demand by the blowers. The second indicator is the amount of high-graded heat that can be provided by the system, $P_{th,600^\circ\text{C}}$. The temperature level of 600 °C was chosen because heat at this temperature may still be used for a wide variety of technical purposes.

3.3. Feasibility Check. Each process scheme at a given set of operating parameters is subject to several feasibility checks. They treat issues such as carbonization, carbon monoxide tolerance, and heat integration.

3.3.1. Carbonization. Carbonization or carbon deposition may occur in high temperature units with a high fraction of carbon monoxide, and it should be avoided. The following two carbonization reactions were considered:



To determine whether carbonization tends to occur or not, we use a thermodynamic criterion: as long as the equilibrium of at least one carbonization reaction favors the educts and not the formation of solid carbon, there exists a mechanism of carbon removal and the process is acceptable. In mathematical form, this can be expressed as

$$\left(\Delta_r g_1^\theta(T) + RT \ln \frac{x_{\text{CO}_2} p^\theta}{x_{\text{CO}}^2 p} > 0 \right) \vee \left(\Delta_r g_2^\theta(T) + RT \ln \frac{x_{\text{H}_2\text{O}} p^\theta}{x_{\text{H}_2} x_{\text{CO}} p} > 0 \right) \quad (5)$$

The carbonization check was conducted only in selected high temperature reactor units. They are the gasifier, the moving bed reactor, the cyclic water–gas shift reactor, and the SOFC. In all other low temperature units, carbonization was assumed to be kinetically limited.

3.3.2. Carbon Monoxide Tolerance. In the work reported here, three different types of fuel cells were considered. Two of them, namely the PEMFC and the HT-PEMFC, are sensitive to CO concentration in the anode feed gas. Hence, if the CO content of the feed gas into these fuel cells is above the tolerance of the corresponding fuel cell (see Table 1), the process is infeasible:

$$x_{\text{CO},\text{in,HT-PEMFC}} \leq x_{\text{CO},\text{lim,HT-PEMFC}} \quad (6)$$

3.3.3. Heat Integration. Every system requires and at the same time releases certain amounts of heat at different temper-

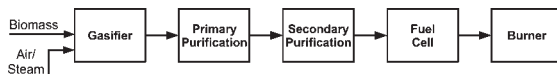


Figure 4. Reference block diagram of biomass-based fuel cell power plant.

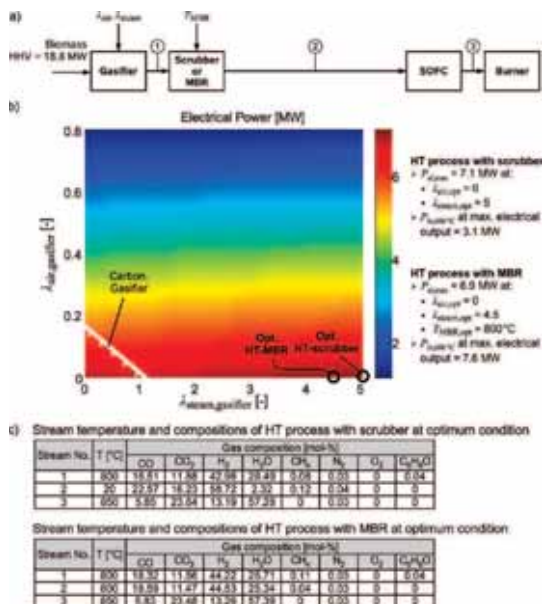


Figure 5. High temperature process. (a) Process structure. (b) Electrical net power (MW) depending on the gasifier air number ($\lambda_{\text{air,gasifier}}$) and steam number ($\lambda_{\text{steam,gasifier}}$). (c) Stream temperature and compositions of high temperature process at optimum conditions.

ature levels. Detailed information about the heat requirement and production are comprised in the output variables of each unit (Q , T). All of these heat fluxes were integrated in composite curves, and a pinch analysis was applied to determine whether the system requires additional heat or it can provide heat as an energetic product.³⁷

We demand that the process is thermally autonomous, meaning that all heat necessities can be satisfied by hot streams within the process. If this requirement is not fulfilled, an amount of fuel (biomass) would have to be combusted only to cover the heat demands, which causes a reduction of efficiency. Thus, the heat integration constraint is satisfied only if the result of the pinch analysis shows that there is no requirement for additional heat, or in a short-term:

$$P_{\text{th,req}} = 0 \quad (7)$$

3.4. Optimization. Each process was optimized in order to maximize the net electrical power output. For this purpose, the system's control variables were manipulated within their given limits (see Table 1). A system may have 2–6 control variables. The feasibility constraints were considered by penalty terms in the optimization.

4. Results and Discussion

4.1. Reference Processes. In the fuel cell literature, two different basic designs of biomass-based fuel cell power plants are well-known. Their key difference lies in the applied fuel cells. In the high temperature process, an SOFC is used. This

simplifies the gas purification and the heat integration. The SOFC is suitable for steady state operation. The second option is a low temperature process based upon a PEMFC. This requires a larger gas purification effort, but a more dynamic operation is possible. In this study, these two designs serve as reference cases and are discussed first.

4.1.1. Conventional High Temperature (HT) Process. The SOFC is a type of fuel cell that can convert CO electrochemically. Thus, CO removal units are not necessary and the fuel gas can be fed directly to the fuel cell after passing through the primary purification. The SOFC also provides heat at high temperature (≈ 850 °C), which brings another advantage and also a drawback. The heat produced can be used to satisfy the heat demand of other units or as a plant product, but it has to be removed from the fuel cell. The usual way to remove the heat is by a large air stream on the cathode side, whereas a considerable pressure drop has to be overcome, so power demand for the air blower is also high.

A widely used primary purification unit is the scrubber. In this unit, the outlet gas from the gasifier is contacted with a spray of water at ambient temperature which is supposed to take up all dust. As the gas is cooled down by the water to about 30 °C, tar components condense and are taken up by the water. From an energetic point of view, this is a quenching process where the originally high-graded heat of the fuel gas is converted to low-graded heat. Thus, its main drawback is the significant loss of exergy, which has severe consequences for the system heat integration. Figure 5a shows the block diagram of a high temperature process with a conventional purification step.

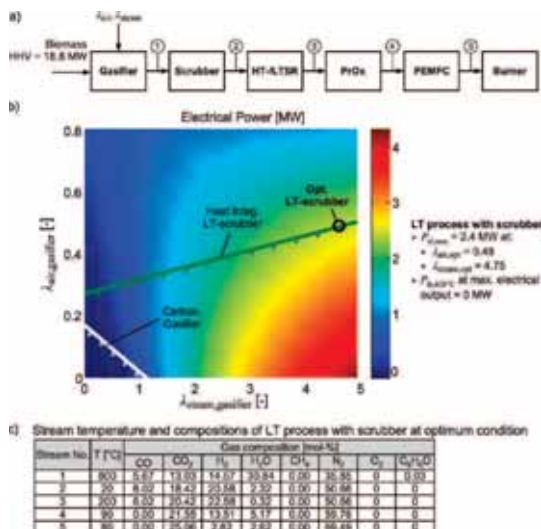


Figure 6. Low temperature process with a scrubber. (a) Process structure. (b) Electrical net power (MW) depending on the gasifier air number ($\lambda_{\text{air,gasifier}}$) and steam number ($\lambda_{\text{steam,gasifier}}$). (c) Stream temperature and compositions of low temperature process at optimum conditions.

This high temperature process has only two control variables (see Table 1): the steam number, $\lambda_{\text{steam,gasifier}}$, and the air number of the gasifier, $\lambda_{\text{air,gasifier}}$. They describe the relative amount of air and steam that is fed to the gasifier per unit biomass. Their definition is given in the Appendix. Their influence on the net power output, P_{el} , is shown in Figure 5b. On the left bottom corner of the diagram, a white line represents a feasibility border. Below this line is an infeasible region in which carbonization can occur in the gasifier. In this region, the product gas of the gasifier contains a large fraction of CO, shifting the equilibria of both carbonization reactions (eqs 3 and 4) to the right-hand side.

In the gasifier, the increase of the steam number shifts the chemical equilibrium of the steam methane reforming (SMR) and water–gas shift reaction (WGSR) to the product side. The concentration of H₂ is, hence, increased while the fractions of CO and CH₄ in the product stream are decreased. This effect, however, only has a minor impact on the electrical power produced if an SOFC is used. All CO and CH₄ in the feed gas of the SOFC are completely reformed to H₂ and CO₂ (see Table 1). Thus, the amount of fuel components available to the SOFC is nearly the same for different steam numbers. On the other hand, the impact of the air number on the performance of the system is notable. The higher the air number, the more biomass is fully oxidized in the gasifier; therefore, less fuel (CO, H₂ and CH₄) is available for the fuel cell and less electricity is produced.

As shown in Figure 5b, the optimal condition of the high temperature process with scrubber is achieved at steam gasification. This process produces electricity of 7.1 MW of electricity which corresponds to an electrical efficiency of about 38% and 3.1 MW of high-graded heat. Gas stream compositions at the optimal condition are listed in the table below the graph. This outcome is found to be in good agreement with the results from Panopoulos et al.⁶

4.1.2. Conventional Low Temperature (LT) Process. CO poisoning of the electrode catalyst is one of the major issues for PEMFC, hence, the CO level of the fuel gas in this system must be lowered down to 10 ppm. For this purpose, high temperature and low temperature shift reactors (HTSR and LTSR) are usually used in combination with a PrOx reactor. In the shift reactors, CO is converted to H₂ according to the water–gas shift reaction. However, the CO level in the outlet gas is still too high for a PEMFC. To further decrease the CO content, a selective oxidation in the PrOx reactor can be employed. A shortcoming of this process is that H₂ is also oxidized together with CO. Figure 6a shows a typical process configuration of a low temperature process.

As discussed before, the main disadvantage of a scrubber is due to the considerable loss of high-graded heat (see section 4.1.1). This drawback becomes obvious in the low temperature process. The main heat consumer is the gasifier and only the burner produces heat at high temperature (900 °C), which is insufficient to cover the system's heat requirements. Thus, the heat demand by the gasifier has to be reduced. This is fulfilled by applying air as a gasification agent, thereby burning a significant portion of the biomass in the gasifier. As a consequence, less fuel is available in the fuel cell and the system's power output is comparably low. In Figure 6b, the white line indicates the area where carbonization occurs in the gasifier. The green line represents the feasibility constraint due to the heat integration.

The maximum electrical power of the conventional low temperature system is produced by a combination of air and steam gasification. Obviously, the system's performance is limited by the heat integration constraint, so no heat is available from the process at this point. A higher electrical power output

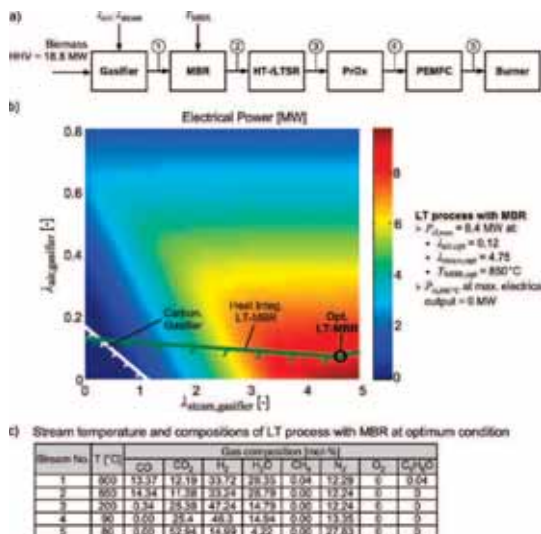


Figure 7. Low temperature process with an MBR. (a) Process structure. (b) Electrical net power (MW) depending on the gasifier air number ($\lambda_{\text{air,gasifier}}$) and steam number ($\lambda_{\text{steam,gasifier}}$). (c) Stream temperature and compositions of low temperature process at optimum condition.

could only be achieved if the process is improved with respect to the heat integration, for example by substituting some of its units.

4.2. Moving Bed Reactor (MBR).

4.2.1. MBR in a Low Temperature Process. An alternative to the scrubber is to use a high temperature primary purification unit such as the MBR (see section 2.1). It works at temperatures close to the gasifier temperature. Its benefit is evident when the MBR replaces the scrubber in the low temperature process. The infeasible region is now shifted toward lower values of the air number (see the green lines in Figures 6 and 7) and operating conditions with attractive power output now become feasible, as illustrated in Figure 7b.

In principle, high H₂ content in the feed gas is preferable for PEMFC. This is achieved by increasing the steam number. With large amounts of steam, chemical equilibria of steam methane reforming and water–gas shift reactions in the gasifier, MBR, and shift reactors are shifted to the product side and more H₂ is produced. Therefore, a higher net power output can be generated compared to cases with a lower steam number. Another approach to influence the chemical equilibria, so that they favor the product side, is by raising the temperature. In this system, only the temperature of the MBR can be manipulated within a certain range (see Table 1), and the optimal operating temperature of the MBR is at its upper bound (850 °C).

The maximum electrical power of this system is about 3.5 times higher than in the LT-system with the scrubber (section 4.1.2, Figure 6). This optimal point also lies on the boundary of the heat integration constraint, thus high-graded thermal power is not delivered by the plant. This version of a low temperature power plant provides electrical efficiency of about 45%. Because the PEMFC is suitable for dynamic operation, this process might be a good option for a peak power plant.

4.2.2. MBR in a High Temperature Process. The effect of using the MBR in the high temperature process is shown in Figure 5. Compared to the high temperature reference process, it has a significant increase in the production of high-graded heat by more than a factor of 2. The difference in electrical power due to tar reforming in the MBR is negligible. Due to this, the power output profile is similar to the profile of the reference case, so both are illustrated in Figure 5b. The new optimal point is now shifted a bit toward a lower steam number.

In contrast to the low temperature process, the effect of the MBR temperature is not perceptible in this system. It is assumed that all fuels are completely reformed at the anode channel of SOFC before being converted electrochemically (see Table 1). Hence, the electrical power output is not influenced by the fuel reforming in the preceding unit. This makes the electrical system efficiency insensitive toward the MBR temperature. We choose 800 °C as the optimal temperature of the MBR simply because the gasifier also operates at this temperature, thus less heat exchanger area is needed.

The high temperature process is suitable for a base load power plant because of the large time constants of the SOFC. Nevertheless, this process fits the requirements of a combined heat and power (CHP) plant since it delivers a considerable amount of electrical and thermal energy.

As a conclusion, the MBR primarily improves the thermal aspects of a process. It increases the production of high-graded heat in the high temperature process and relaxes the limiting constraint of heat integration in the low temperature process. Furthermore, it reduces the number of required heat exchangers and, thereby, simplifies the system design. The influence of the MBR temperature on the system electrical efficiency is noticeable only in systems with low temperature fuel cells.

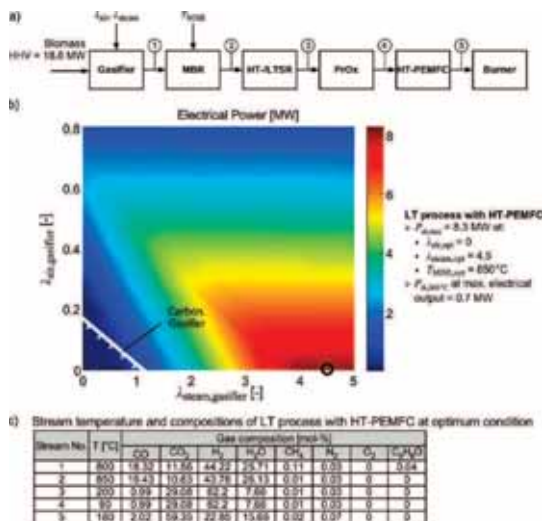


Figure 8. HT-PEMFC in common low temperature process. (a) Process structure. (b) Electrical net power (MW) depending on the gasifier air number ($\lambda_{\text{air,gasifier}}$) and steam number ($\lambda_{\text{steam,gasifier}}$). (c) Stream temperature and compositions of low temperature process with HT-PEMFC at optimum condition.

4.3. High Temperature Proton Exchange Membrane Fuel Cell (HT-PEMFC). The main advantage of the HT-PEMFC is its improved CO tolerance of up to 3%. This fact allows two new process options. The first one is almost similar to the low temperature process, but now the PrOx reactor only needs to decrease the CO content down to 3%. As a consequence, less H₂ is consumed in the PrOx reactor and higher power output is achievable (Figure 8).

The tendency of this process is similar to the reference low temperature process with an MBR (Figure 7), where steam gasification with a high steam number is favorable. The maximum electrical power output of the system with a HT-PEMFC is slightly lower than in the comparable low temperature system with an MBR. This is mainly due to the lower Nernst voltage in the fuel cell at increased temperature. In contrast to the low temperature PEMFC system, this plant also delivers a small amount of heat and no infeasible region due to heat integration exists within the selected range of operating conditions.

The second process option is to eliminate the PrOx reactor from the low temperature process since the shift reactors are able to convert CO down to an acceptable level. This process option is illustrated in Figure 9a. As expected, the tendency is similar to a process employing a normal PEMFC where the highest electrical power is produced in the area of steam gasification. The black line in Figure 9b marks the boundary of the infeasible area due to CO content in the anode feed gas. However, this constraint is not limiting, because the area of maximum electrical power output is still feasible.

Another important benefit of the HT-PEMFC is the improved heat integration due to its operating temperature. This advantage can be clearly seen in the cascaded composite curves in Figure 10 which are used for the pinch analysis (see section 3.3.3). The curves illustrate the situations at optimal conditions. System a is the LT process with the MBR (Figure 7) and system b is

the modified LT process with an HT-PEMFC (Figure 9). The red curve in this figure is the hot composite curve which represents the amount of heat produced by the system at different temperature levels, e.g. the heat produced by the fuel cell. The blue curve is the cold composite curve. It contains the information of heat demands with their temperature levels, such as the amount of heat required to generate the steam.

In both systems, the gasifier needs a quantity of heat which is delivered by the burner. In system a, the heat of the burner must also be used to generate the steam, so that less heat is available for the gasifier. Therefore, to reduce the gasifier's heat necessity, a small amount of air must be fed to the gasifier. In system b, the heat demand for steam generation can be satisfied by the heat produced by the HT-PEMFC. Hence, this system can be operated under pure steam gasification. Additionally, a certain proportion of high-graded heat is still left as a coproduct.

This analysis shows that the application of HT-PEMFC offers two distinct advantages. The first is the simplification of the system due to the CO tolerance of this unit. Second, it extends the area of feasibility with respect to the heat integration, and a low amount of high-graded heat is available as a product.

4.4. Alternative Secondary Purification in the Low Temperature Process.

4.4.1. Pressure Swing Adsorption (PSA) and Palladium Membrane (PdM). PSA is a widely used technology for the purification of H₂. It operates at relatively low temperature (20–50 °C) and separates some gaseous species from a mixture under pressure according to the species' molecular characteristics and affinity for an adsorbent material. In a large scale H₂ production plant, PSA is sequentially used after the shift reactors. It has two outlet streams: one product stream rich of H₂ (99.99%) and one residue stream that contains the other gas

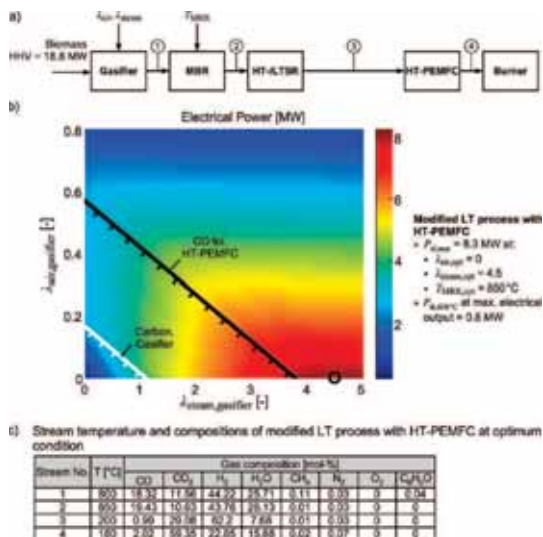


Figure 9. HT-PEMFC in modified low temperature process. (a) Process structure. (b) Electrical net power (MW) depending on the gasifier air number ($\lambda_{air, gasifier}$) and steam number ($\lambda_{steam, gasifier}$). (c) Stream temperature and compositions of modified low temperature process with HT-PEMFC at optimum conditions.

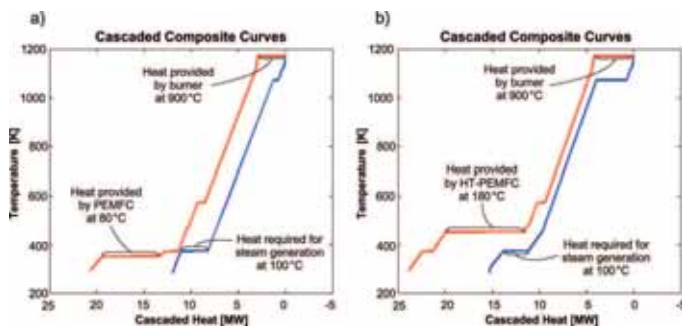


Figure 10. Cascaded composite hot and cold heat flows. (a) For LT process with the MBR (Figure 7). (b) For modified LT process with HT-PEMFC (Figure 9).

components. One drawback of this unit is the relatively high power demand due to the compression of the feed gas.²⁵

Palladium membranes (PdM) are also used to separate H₂ from a gas mixture. They operate at elevated temperature (300–450 °C) and under pressure (2–5 bar). The permeate stream contains 99.9% or better purity of H₂.²⁸ Nevertheless, the high cost of the membranes and the power consumption make this process less attractive.

Since both units, PSA and PdM, are able to produce H₂ with high purity, they can be used to replace the PrOx reactor. The main product stream flows to a PEMFC or a HT-PEMFC, and the residue stream goes directly to the burner. Simulation of

both units gives almost the same results and tendencies, but a process with PSA (Figure 11a) produces slightly higher electricity due to lower power demand, so we focus on this option here. The heat integration is not a limiting factor for either process.

A system with PEMFC always yields more electrical energy with increasing amount of H₂ in the feed stream. Since the purpose of a PSA in the low temperature process is only to separate H₂ from the gas, the key units which determine the quantity of H₂ produced are the gasifier, the MBR and the shift reactors. Thus, a high steam number is favorable for this purpose, as shown in Figure 11b. At high air numbers, a region

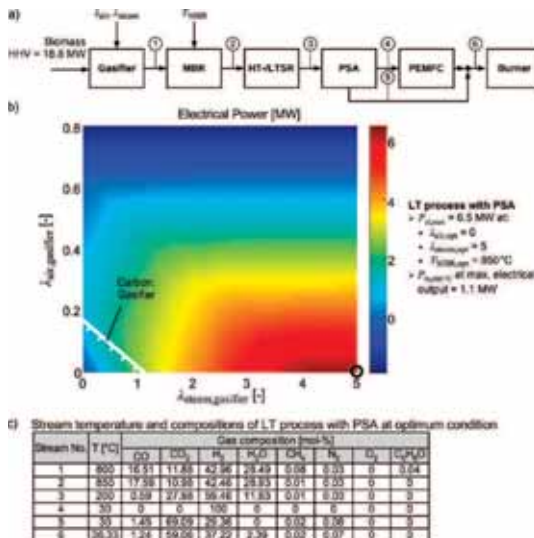


Figure 11. PSA in alternative low temperature process. (a) Process structure. (b) Electrical net power (MW) depending on the gasifier air number ($\lambda_{a,air,gasifier}$) and steam number ($\lambda_{a,steam,gasifier}$). (c) Stream temperature and compositions of low temperature process with PSA at optimum condition.

with negative power output appears. This represents an area where the power consumption of the PSA is higher than the electrical power generated by the fuel cell. At the left bottom corner of the diagram, the carbonization constraint is violated in the gasifier. In terms of electrical efficiency, the low temperature process with PSA yields a lower electrical energy than the low temperature process with PrOx. This is due to the parasitic electrical consumption of the PSA and because only 80% of the H₂ is recovered in the PSA. However, since the side product gas of the PSA is sent directly to the burner, more high-graded heat is now available and, thus, thermal integration is not a limiting factor.

4.4.2. Electrochemical Preferential Oxidation (ECPrOx).

The ECPrOx is another candidate for replacing the classical PrOx. Besides selective oxidation of CO, it also delivers electrical energy as a coproduct (section 2.3). The ECPrOx model that we used is based on the dynamic equations proposed by Zhang and Datta.¹⁴ It describes the time-averaged conditions in a spatially lumped ECPrOx reactor. The result of the system simulation with this model shows a low selectivity of CO oxidation in the ECPrOx unit, which brings the system to an infeasible area. However, recent results indicate that the spatially distributed character of the ECPrOx may not be neglected. So far, no valid and compact model exists that describes the performance of spatially distributed ECPrOx reactor. It is likely that not a single unit of the ECPrOx, but a cascade of electrically coupled reactor stages leads to an attractive selectivity. However, according to the current stage of knowledge about this oscillating reactor, systems with an ECPrOx are not competitive.

4.4.3. Cyclic Water–Gas Shift Reactor (CWGSR).

The CWGSR is an alternative secondary purification reactor that can substitute the shift reactors including the CO deep removal unit (section 2.2). This reactor has two outlet streams: one CO-free

stream that contains H₂ and H₂O and the other is the residue gas with significant amounts of H₂ and CO. The CO-free stream can be used directly by the PEMFC whereas the residue stream is fed to the burner (Figure 12a).

The performance of the CWGSR strongly depends on its operating temperature and the reduction capability of the fuel gas. The thermodynamic equilibria of the reduction reactions are functions of the unit's temperature. Thus, the CWGSR operating temperature is used as an optimization variable. The reduction capability of the fuel gas determines the quantity and quality of H₂ produced. The degree of hydrogen recovery in the CWGSR is increased if the feed gas has high reduction capability, i.e. if the ratios of H₂/H₂O and CO/CO₂ are high. This can be seen in Figure 12b, where higher steam content in the fuel gas leads to worse performance of the CWGSR, thereby producing less clean H₂ and, consequently, less electrical energy.

The CWGSR has a thermodynamic limit where for a lean gas, the reduction of the metal oxide is no longer possible. As a result, no H₂ is produced during the oxidation phase and no electricity is generated by the fuel cell. Such gas compositions occur if the gasifier is operated at a high air number.

Application of the CWGSR in a low temperature fuel cell plant yields a maximum electrical power of 7.2 MW at a relatively low value of the steam number (Figure 12b). It also delivers a small portion of high-graded heat, which is about the same as in the system with the PSA (Figure 11). However, the electrical power is about 14% lower than from the corresponding reference system (LT process with MBR, Figure 7). So, the CWGSR may simplify the plant structure and the heat integration, but it reduces the overall plant efficiency.

4.5. Parallel Plant Concepts.

4.5.1. Parallel System with a PSA. In the low temperature process with PSA, the side stream of the PSA is simply

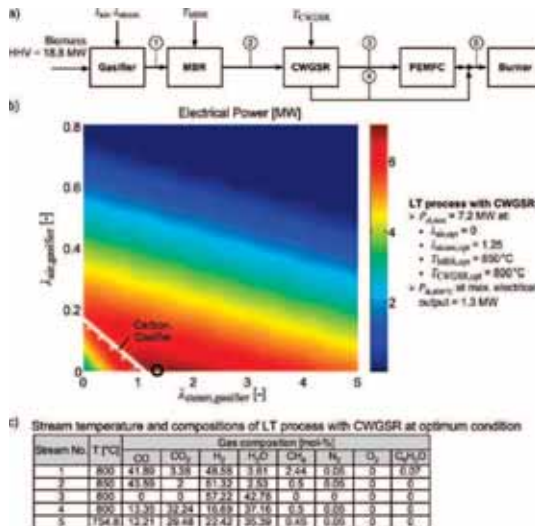


Figure 12. CWGSR in alternative low temperature process. (a) Process structure. (b) Electrical net power (MW) depending on the gasifier air number ($\lambda_{\text{air, gasifier}}$) and steam number ($\lambda_{\text{steam, gasifier}}$). (c) Stream temperature and compositions of low temperature process with CWGSR at optimum conditions.

combusted in the burner. This stream, however, still contains a considerable amount of valuable fuel components (CO, H₂, and CH₄) and is appropriate to be used in the SOFC. This leads to a system with two types of fuel cells: the H₂ rich stream as the main product from the PSA is processed by the PEMFC, while the SOFC converts the residue gas. This process structure, the so-called parallel plant, is illustrated in Figure 13a. In this concept, the PSA is not used as a purification step, but rather as a gas separator.

One problem with this process might be that the temperature of the residue gas (30 °C) has to be raised up to the temperature of the SOFC (850 °C). However, this heat requirement is well covered by the heat produced by the SOFC itself. Figure 13b shows the simulation results of a parallel process with PSA. The addition of an SOFC increases the electrical output by about 23% compared to the normal low temperature process with PSA (Figure 11).

Similar to the low temperature process, higher values of the steam number are preferred in this process. In opposite to the low temperature process with PSA, the heat integration constraint is limiting in the parallel process. The green solid line in Figure 13b denotes the feasibility boundary due to the heat integration. This limit occurs because instead of using the secondary product gas for heat production, it is now used to generate electrical energy and a small amount of heat.

4.5.2. Parallel System with a CWGSR. Just like the PSA, the CWGSR provides one product stream rich of H₂, which is appropriate for a PEMFC, and a second stream which can be utilized in an SOFC. Using the CWGSR to replace the sequence of shift reactors and PSA leads to a simpler parallel plant (Figure 14a).

Much like the PSA in the previous plant, the CWGSR works as a gas separator. With that, the electrical power output is

increased by about 24% compared to the low temperature process with CWGSR (Figure 12). Because the H₂ recovery in the CWGSR is maximal at low values of steam number and because the PEMFC is slightly more efficient than the SOFC due to a more efficient cooling system, the optimal performance is found at a steam number of 1.25. Similar to the parallel system with PSA, the thermal integration constraint also occurs in this process, denoted by the green line. Since the point of optimal performance lies at this boundary, no high-graded heat is available from the process.

4.5.3. Parallel System with a Gas Splitter. The design of the parallel system proposed by Yokoo et al.⁹ looks similar to the low temperature process (Figure 7a). The difference is that the exhaust gas from the primary purification unit (or the steam reformer in Yokoo's system) is split into two streams: one of them passes the secondary purification units before being utilized in the PEMFC, while the other is fed directly to the SOFC. The splitting ratio is defined as the gas fraction which is fed into the PEMFC. In the work of Yokoo et al.,⁹ the splitting ratio is not treated as an optimization variable. In our study, this parameter is subject to optimization and results show that the maximum electrical power is generated at a splitting ratio of about 80%. This means that the PEMFC remains the main electricity producer, and thus, this parallel process shows almost the same electrical power profile as the low temperature process (Figure 7b). The utilization of SOFC relaxes the limiting heat integration constraint (the green line) and, as a result, a higher electrical power output can be produced. This outcome is consistent with the findings from Yokoo et al.,⁹ who computed the electrical efficiency of their system to be at around 50%, whereas our estimation predicts an efficiency of about 48%.

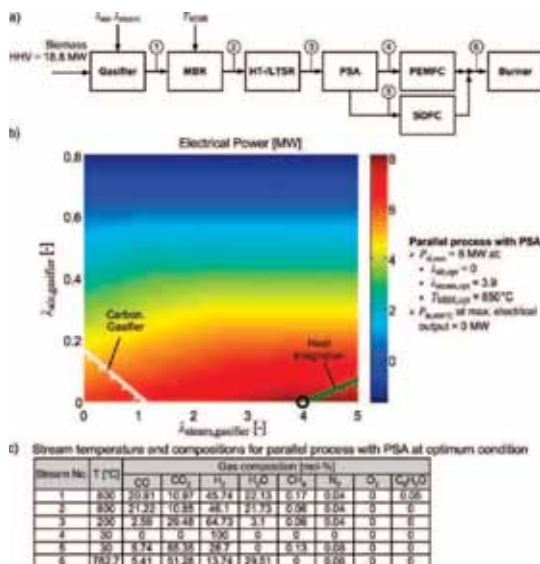


Figure 13. PSA in parallel process. (a) Process structure. (b) Electrical net power (MW) depending on the gasifier air number ($\lambda_{air,gasifier}$) and steam number ($\lambda_{steam,gasifier}$). (c) Stream temperature and compositions of parallel process with PSA at optimum condition.

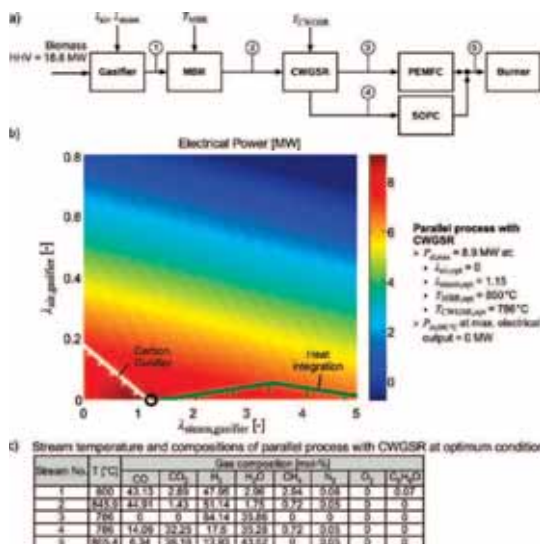


Figure 14. CWGSR in parallel process. (a) Process structure. (b) Electrical net power (MW) depending on the gasifier air number ($\lambda_{air,gasifier}$) and steam number ($\lambda_{steam,gasifier}$). (c) Stream temperature and compositions of parallel process with CWGSR at optimum conditions.

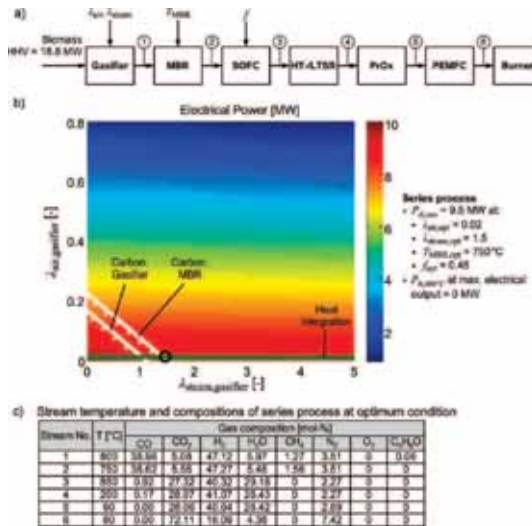


Figure 15. Sequential process. (a) Process structure. (b) Electrical net power (MW) depending on the gasifier air number ($\lambda_{air, gasifier}$) and steam number ($\lambda_{steam, gasifier}$). (c) Stream temperature and compositions of series process at optimum conditions.

The electrical power of the parallel concept is clearly superior to the process with a single fuel cell. But besides high efficiency, these plants offer several additional advantages. By decreasing the splitting performance (in a PSA or CWGSR) or the splitting ratio (in a gas splitter), more fuel gas can be supplied to the SOFC which reduces the electrical efficiency but increases the thermal power output. The parallel processes are, therefore, flexible: they can deliver electrical base-load from the SOFC, electrical peak power by their PEMFC and high-graded heat. The system with PSA produces a slightly lower electrical energy than the system with the CWGSR or a gas splitter because of electrical power consumption in the PSA unit. In addition, the application of the CWGSR also allows a high temperature path of the fuel gas, which leads to less heat losses and requires smaller heat exchanger area in the system.

4.6. Sequential Concept. A further process configuration of biomass based fuel cell power plant is a consecutive combination of high and low temperature fuel cells (Figure 15a). The idea comes from the fact that the SOFC can act as an additional reforming step, besides producing heat and electricity. For that reason, fuel utilization of the SOFC in a sequential process must be less than the maximum possible value of SOFC fuel utilization.

$$\eta_{fuel, SOFC, seq} = f \eta_{fuel, SOFC, max}, 0 \leq f \leq 1 \quad (8)$$

If $f = 1$, the SOFC consumes most of the fuel and only small amount of fuel components is still available in the PEMFC, which may not be able to utilize these gases. In that case, the process equals the high temperature process (Figure 5). On the other hand, if fuel utilization in the SOFC equals to zero, the process turns out to be almost identical to the low temperature process (Figure 7).

The simulation result of the sequential process is shown in Figure 15b. Even though the PEMFC is the main electricity

producer in this process, it is important to realize that the composition of the PEMFC feed gas is strongly influenced by the SOFC. As discussed in section 4.1.1, the change of steam number does not really affect the performance of the SOFC. The quality of the SOFC outlet gas, then, remains almost constant with steam number. Automatically, the fuel gas concentration will also stay nearly the same, as well as the power output of the PEMFC.

Due to the constraint of heat integration, pure steam gasification is not possible in this system, as indicated by the green line. This is because the SOFC consumes only about half of the fuel gas and the burner produces only little high-graded heat. To cover the heat necessity, a small amount of air has to be added to the gasifier.

The sequential system produces the highest electrical power output among all systems under discussion ($P_{el, max} = 9.5$ MW), which is achieved at $f = 0.45$. No thermal energy is provided at this point because it works at the boundary of the heat integration constraint.

The sequential combination of high and low temperature fuel cells is the most efficient system in terms of electrical energy, which is in a good agreement with the result from the work of Yokoo et al.⁹ As with the parallel plant, this system may provide base and peak power as well as heat by control of the fuel utilization in the fuel cells. Compared to the parallel plant with the CWGSR (Figure 14), this system contains more units and requires a larger system of heat exchangers, so both parallel and sequential plants may be seen as equally good systems.

A summary of all processes that have been discussed is given in Table 3. In this table, the maximum electrical efficiency of different processes together with the thermal efficiency is presented.

Table 3. Summary of all Process Variations for the Biomass-Based Fuel Cell Power Plant Presented in This Contribution

name of the process	primary purification	secondary purification	fuel cell	$\eta_{el,max}^a$	η_{th}^b
reference					
• high temperature + scrubber	scrubber	—	SOFC	37.8%	16.5%
• low temperature + scrubber	scrubber	shift reactors + preferential oxidation	PEMFC	12.8%	—
moving bed reactor (MBR)					
• high temperature + MBR	MBR	—	SOFC	36.7%	40.4%
• low temperature + MBR	MBR	shift reactors + preferential oxidation	PEMFC	44.7%	—
high temperature PEMFC (HT-PEMFC)					
• low temperature + HT-PEMFC	MBR	shift reactors + preferential oxidation	HT-PEMFC	44.1%	3.8%
• modified low temperature + HT-PEMFC	MBR	shift reactors	HT-PEMFC	44.1%	3.8%
alternative secondary purification					
• low temperature + palladium membrane	MBR	shift reactors + palladium membrane	PEMFC	23.4%	18.9%
• low temperature + PSA	MBR	shift reactors + PSA	PEMFC	34.6%	5.8%
• low temperature + cyclic water–gas shift reactor	MBR	cyclic water–gas shift reactor	PEMFC	38.3%	6.9%
parallel plant					
• parallel plant with PSA	MBR	shift reactors + PSA	SOFC + PEMFC, parallel	42.5%	—
• parallel plant with cyclic water–gas shift reactor	MBR	cyclic water–gas shift reactor	SOFC + PEMFC, parallel	47.3%	—
• parallel plant with gas splitter	MBR	shift reactors + preferential oxidation	SOFC + PEMFC, parallel	47.8%	—
sequential plant					
• high temperature + low temperature	MBR	SOFC + shift reactors + preferential oxidation	SOFC + PEMFC, sequential	50.5%	—

^a Maximal electrical efficiency: $\eta_{el,max} = P_{el,max}/HHV$ of biomass. ^b Thermal efficiency at maximal electrical efficiency: $\eta_{th} = P_{th,600^\circ C}/HHV$ of biomass. Here, 600 °C is used as a temperature reference of high-graded heat produced.

5. Conclusions and Outlook

Four novel reactor concepts for a biomass gasification–fuel cell system have been evaluated in a systemwide context. It turns out that the high temperature gas purification units and the HT-PEMFC offer significant advantages due to better heat integration compared to their classical counterparts. The application of the MBR (see section 2.1) in high temperature systems leads to an increased production of high-graded heat, whereas in the low temperature process, it allows the system to work at higher efficiencies due to relaxation of the heat integration constraint. The ECPrOx (see section 2.3) does not seem to be attractive, but this result is only preliminary since the optimal reaction control in this unit is not yet known. Besides its function as a secondary gas purification unit, the CWGSR (see section 2.2) is especially interesting as a gas separator, because it allows the design of a novel type of power plants combining high and low temperature fuel cells.

Regarding optimal system design, attractive electrical efficiencies can be obtained by high or low temperature fuel cell systems. Plants with high temperature fuel cells are best suited for combined production of electric base power and high-graded heat plant (CHP). Systems with low temperature fuel cells usually operate at their heat integration limit and provide electrical peak power, but no high-graded heat.

The most efficient plants combine high and low temperature fuel cells in a parallel or sequential arrangement. These plants are made possible by units such as the CWGSR that separate a fraction of high purity hydrogen from the fuel gas for use in the PEMFC. These systems offer electric base and peak load as well as high-graded heat in a flexible, efficient way.

Future works include the continued development of the attractive novel reactors on an experimental and theoretical basis as well as the more detailed analysis and design of the combined fuel cell power plants. No recycles have been

considered in this study in order to keep the number of system options at a reasonable level. However, the anode exhaust gas of the SOFC may be used to substitute partially or completely the gasification agent, thereby providing an attractive option for mass integration. This option will be subjected to further studies.

Acknowledgment

The presented results were obtained within the framework of the research project ProBio (Integrated process systems for energetic use of biomass in fuel cells), jointly funded by the Max Planck Society and the Fraunhofer-Gesellschaft in Germany.

Appendix: Gasifier Model

As an example for the unit models used in the model library, the gasifier model is introduced here. Gasification converts wood to gaseous fuel with the help of steam and/or air as gasification agent. The gasification process is divided into two zones: the preheating and the reaction zone (Figure 16).

Before entering the fluidized bed, all inlet streams are heated up to the gasifier temperature in the preheating zone. The heat demand for the wood moisture is computed together with the H₂O feed, while the heat demands for the dry wood and the air are calculated individually.

The amounts of H₂O and air flow rate are determined by using the definition of the steam and the air numbers. Air number is the ratio of air flow and the amount of air needed to fully combust the biomass:

$$\lambda_{air,gasifier} = \frac{G_{air} x_{O_2,air}}{G_{C,wood} + \frac{1}{4}G_{H,wood} - \frac{1}{2}G_{O,wood}} \quad (A.1)$$

The steam number is defined as the ratio of steam fed into the gasifier to the amount of steam required to completely reform the biomass into fuel substances (CO and H₂):

$$\lambda_{\text{steam,gasifier}} = \frac{G_{\text{H}_2\text{O}}}{G_{\text{C,wood}} - G_{\text{O,wood}}} \quad (\text{A.2})$$

The atomic flow rate from the wood can be computed as follows:

$$G_{i,\text{wood}} = m_{\text{wood,dry}} y_{i,\text{wood,dry}} / M_i; \quad i = \{\text{C, H, O, N}\} \quad (\text{A.3})$$

where $m_{\text{wood,dry}}$ is the mass flow rate of dry wood, $y_{\text{wood,dry}}$ is dry wood composition (see Table 2) and M_i is the molar mass of atom species i .

The amount of H₂O that enters the gasifier is the sum of the H₂O feed and the wood moisture:

$$G_{\text{H}_2\text{O}} = G_{\text{H}_2\text{O,feed}} + m_{\text{wood}} w_{\text{H}_2\text{O}} / M_{\text{H}_2\text{O}} \quad (\text{A.4})$$

where $w_{\text{H}_2\text{O}}$ is the moisture content of wood (wt %) and $M_{\text{H}_2\text{O}}$ is the molar mass of H₂O.

With the wood composition assumed in this study, 20% moisture content corresponds already to a steam number of 0.96. This indicates that pure air gasification is not possible with this type of fuel, and although it is not shown explicitly in the figures, $\lambda_{\text{steam,gasifier}} = 0.96$ is a lower bound for the steam number. Lower steam numbers can only be realized if the wood has less moisture.

The heat demand in the preheating zone is calculated as follows:

$$Q_{\text{wood}} T_0^{\text{gasifier}} = m_{\text{wood,dry}} c_{p,\text{wood}} (T_{\text{gasifier}} - T_0) \quad (\text{A.5})$$

Steam preheating is separated into three sections: water heating, evaporation, and steam heating.

$$Q_{\text{steam}} T_0^{100^\circ\text{C}} = G_{\text{H}_2\text{O}} (\Delta h_{\text{H}_2\text{O},l}^\theta(100^\circ\text{C}) - \Delta h_{\text{H}_2\text{O},l}^\theta(T_0)) \quad (\text{A.6})$$

$$Q_{\text{steam}} T_0^{100^\circ\text{C}} = G_{\text{H}_2\text{O}} (\Delta h_{\text{H}_2\text{O},g}^\theta(100^\circ\text{C}) - \Delta h_{\text{H}_2\text{O},l}^\theta(100^\circ\text{C})) \quad (\text{A.7})$$

$$Q_{\text{steam}} T_0^{\text{gasifier}} = G_{\text{H}_2\text{O}} (\Delta h_{\text{H}_2\text{O},g}^\theta(T_{\text{gasifier}}) - \Delta h_{\text{H}_2\text{O},g}^\theta(100^\circ\text{C})) \quad (\text{A.8})$$

Air preheating

$$Q_{\text{air}} T_0^{\text{gasifier}} = G_{\text{air}} [x_{\text{O}_2,\text{air}} (\Delta h_{\text{O}_2}^\theta(T_{\text{gasifier}}) - \Delta h_{\text{O}_2}^\theta(T_0)) + (1 - x_{\text{O}_2,\text{air}}) (\Delta h_{\text{N}_2}^\theta(T_{\text{gasifier}}) - \Delta h_{\text{N}_2}^\theta(T_0))] \quad (\text{A.9})$$

In the reaction zone, three calculations are solved sequentially. First, phenol flow and the inlet atom flow rates are calculated:

$$G_{\text{phenol}} = m_{\text{wood,dry}} w_{\text{tar,wood}} / M_{\text{phenol}} \quad (\text{A.10})$$

$$G_{\text{C}} = G_{\text{C,wood}} - 6G_{\text{phenol}} \quad (\text{A.11})$$

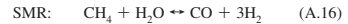
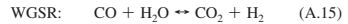
$$G_{\text{H}} = G_{\text{H,wood}} + 2G_{\text{steam}} - 6G_{\text{phenol}} \quad (\text{A.12})$$

$$G_{\text{O}} = G_{\text{O,wood}} + 2G_{\text{air}} x_{\text{O}_2,\text{air}} + G_{\text{steam}} - G_{\text{phenol}} \quad (\text{A.13})$$

$$G_{\text{N}} = G_{\text{N,wood}} + 2G_{\text{air}} (1 - x_{\text{O}_2,\text{air}}) \quad (\text{A.14})$$

where $w_{\text{tar,wood}}$ is the tar content of the wood (wt %).

If the amount of oxygen atom flow rate obtained from eqs A.13 is sufficient for the gasification process but less than needed for a complete combustion: $G_{\text{C}} - (1/4)G_{\text{H}} \leq G_{\text{O}} < 2(G_{\text{C}} + G_{\text{H}}/2)$, then the composition of the outlet stream is calculated based on chemical equilibrium with respect to the water–gas shift reaction (eq A.15) and the steam methane reforming (eq A.16). Otherwise, the calculation is ended and the process is infeasible.



The law of mass action of both reactions must be fulfilled:

$$\exp(-\Delta_r g_{\text{WGSR}}^\theta / RT_{\text{gasifier}}) = \frac{G_{\text{CO}_2,\text{out}} G_{\text{H}_2,\text{out}}}{G_{\text{CO},\text{out}} G_{\text{H}_2\text{O},\text{out}}} \quad (\text{A.17})$$

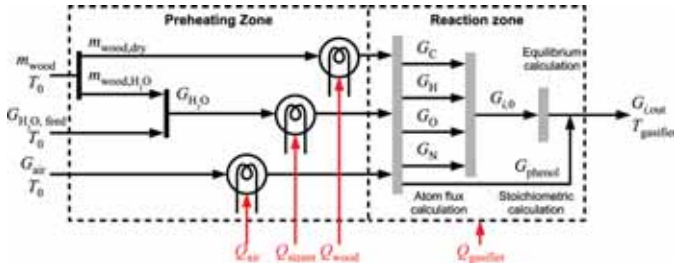


Figure 16. Mass and heat flow scheme of the gasifier model.

$$\exp\left(\frac{-\Delta_r G_{\text{GSR}}^{\theta}}{RT_{\text{gasifier}}}\right) = \frac{G_{\text{CO}_2, \text{out}} G_{\text{H}_2, \text{out}}}{G_{\text{CO}, \text{out}} G_{\text{H}_2\text{O}, \text{out}}} \quad (\text{A.18})$$

where the Gibbs enthalpies of both reactions are calculated as

$$\Delta_r G_{\text{WGSR}}^{\theta}(T_{\text{gasifier}}) = \Delta_r h(T_{\text{gasifier}}) - T_{\text{gasifier}} \Delta_r s(T_{\text{gasifier}}) \quad (\text{A.19})$$

$$\Delta_r G_{\text{SMR}}^{\theta}(T_{\text{gasifier}}) = (\Delta_r h(T_{\text{gasifier}}) - T_{\text{gasifier}} \Delta_r s(T_{\text{gasifier}})) + \alpha \quad (\text{A.20})$$

Because the SMR equilibrium is only approximately reached, the equilibrium constant of SMR has to be modified by adding a constant α to the Gibbs enthalpy (eq A.20). This constant has been fitted to the experiment results²⁰ and was found to be +10 kJ·mol⁻¹.

In addition, four atom balances have to be fulfilled:

$$G_C = G_{\text{CO}, \text{out}} + G_{\text{CO}_2, \text{out}} + G_{\text{CH}_4, \text{out}} \quad (\text{A.21})$$

$$G_H = 2G_{\text{H}_2, \text{out}} + 2G_{\text{H}_2\text{O}, \text{out}} + 4G_{\text{CH}_4, \text{out}} \quad (\text{A.22})$$

$$G_O = G_{\text{CO}, \text{out}} + 2G_{\text{CO}_2, \text{out}} + G_{\text{H}_2\text{O}, \text{out}} \quad (\text{A.23})$$

$$G_N = 2G_{\text{N}_2, \text{out}} \quad (\text{A.24})$$

Solving these six equations (eqs A.17, A.18, and A.21–A.24) gives the molar flows of CO, CO₂, H₂, H₂O, CH₄, and N₂ at the gasifier outlet. At the outlet stream, no O₂ can be found because all oxygen atoms are completely utilized and phenol flow rate is computed by eq A.10.

The heat required or produced by the gasifier is the difference between all incoming enthalpy fluxes (air, steam, and wood) at gasifier temperature and outgoing enthalpy flux (outlet gas) also at gasifier temperature:

$$H_{\text{wood}} = m_{\text{wood}, \text{dry}} (\Delta_r h_{\text{wood}}^{\theta} + C_{p, \text{wood}} (T_{\text{gasifier}} - T_0)) \quad (\text{A.25})$$

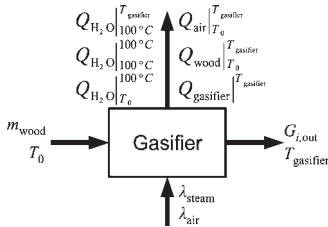


Figure 17. Inlet and outlet streams, control variable, and outlet variable of the gasifier model.

$$H_{\text{steam}} = G_{\text{H}_2\text{O}} \Delta_r h_{\text{H}_2\text{O}, \text{g}}^{\theta}(T_{\text{gasifier}}) \quad (\text{A.26})$$

$$H_{\text{air}} = G_{\text{air}} [x_{\text{O}_2, \text{air}} \Delta_r h_{\text{O}_2}^{\theta}(T_{\text{gasifier}}) + (1 - x_{\text{O}_2, \text{air}}) \Delta_r h_{\text{N}_2}^{\theta}(T_{\text{gasifier}})] \quad (\text{A.27})$$

$$H_{\text{out}} = \sum_i G_{i, \text{out}} \Delta_r h_i^{\theta}(T_{\text{gasifier}}) \quad (\text{A.28})$$

$$Q_{\text{gasifier}}^{T_{\text{gasifier}}} = H_{\text{out}} - (H_{\text{wood}} + H_{\text{steam}} + H_{\text{air}}) \quad (\text{A.29})$$

To conclude, the input and output quantities of the gasifier model are illustrated in Figure 17.

Symbols

- $C_{p, \text{wood}}$ = heat capacity of dry wood, J·g⁻¹·K⁻¹
- f = fuel utilization factor, 1
- G_i = flow rate of gas component i , mol·s⁻¹
- $G_{i, \text{wood}}$ = flow rate of atom i (C, H, O, N) from dry wood, mol·s⁻¹
- H = enthalpy flux, MW
- K_{eq} = equilibrium constant, 1
- m_{wood} = mass flow rate of wet wood, g·s⁻¹
- $m_{\text{wood}, \text{dry}}$ = mass flow rate of dry wood, g·s⁻¹
- $m_{\text{wood}, \text{H}_2\text{O}}$ = mass flow rate of H₂O from wood moisture, g·s⁻¹
- M_i = molar mass of atom i (C, H, O, N), g·mol⁻¹
- p = pressure, bar
- P_{el} = electrical power produced or consumed, MW
- $P_{\text{th}, 600^\circ\text{C}}$ = heat power produced at 600 °C, MW
- $P_{\text{th}, \text{req}}$ = heat power required by the system, MW
- Q = heat flux, MW
- R = gas constant, J·mol⁻¹·K⁻¹
- T = temperature, K
- $w_{\text{H}_2\text{O}}$ = moisture content of wood, g·g⁻¹
- $w_{\text{tar}, \text{wood}}$ = tar content of wood, g·g⁻¹
- x_i = molar fraction of gas component i , mol·mol⁻¹
- $y_{\text{wood}, \text{dry}}$ = composition of wood on a dry basis, g·g⁻¹
- $\Delta_r h$ = enthalpy of formation, J·mol⁻¹
- $\Delta_r h_{\text{wood}}$ = enthalpy of formation of dry wood, J·g⁻¹
- $\Delta_r g$ = Gibbs enthalpy of reaction, J·mol⁻¹
- $\Delta_r h$ = enthalpy of reaction, J·mol⁻¹
- $\Delta_r s$ = entropy of reaction, J·mol⁻¹·K⁻¹
- ΔT_{min} = minimum temperature difference in heat exchangers, K
- α = fitting parameter of SMR equilibrium, J·mol⁻¹
- λ_{air} = air number 1
- λ_{steam} = steam number 1
- η_{el} = electrical efficiency 1
- η_{th} = thermal efficiency 1
- $\eta_{\text{fuel}, \text{SOFC}, \text{seq}}$ = fuel utilization of the SOFC in a sequential process 1

Superscripts

- θ = standard
- $*$ = modified

Subscripts

- in = inlet stream
- max = maximum
- out = outlet stream
- opt = optimal
- lim = limit

Abbreviations

- CHP = combined heat and power
- CWGSR = cyclic water–gas shift reactor

ECPrOx = electrochemical preferential oxidation

HHV = higher heating value

HT-/LT-SR = high temperature/low temperature shift reactor

HT-PEMFC = high temperature proton exchange membrane fuel cell

MBR = moving bed reactor

MCFC = molten carbonate fuel cell

PAFC = phosphoric acid fuel cell

PdM = palladium membrane

PEMFC = proton exchange membrane fuel cell

PrOx = preferential oxidation

PSA = pressure swing adsorption

SMR = steam methane reforming

SOFC = solid oxide fuel cell

WGSR = water–gas shift reaction

Literature Cited

- (1) Faaij, A. P. C. Bio-energy in Europe: changing technology choices. *Energy Policy* **2006**, *34*, 322.
- (2) Bridgewater, T. Review: Biomass for energy. *J. Sci. Food Agric.* **2006**, *86*, 1755.
- (3) Ersoz, A.; Ozdogan, S.; Caglayan, E.; Olgun, H. Simulation of biomass and/or coal gasification systems integrated with fuel cells. *J. Fuel Cell Sci. Technol.* **2006**, *3*, 422.
- (4) McIlveen-Wright, D. R.; Williams, B. C.; McMullan, J. T. Wood gasification integrated with fuel cells. *Renewable Energy* **2000**, *19*, 223.
- (5) Lobachyov, K. V.; Richter, H. J. An advanced integrated biomass gasification and molten fuel cell power system. *Energy Convers. Mgmt.* **1998**, *39*, 1931.
- (6) Panopoulos, K. D.; Fryda, L. E.; Karl, J.; Poulou, S.; Kakaras, E. High temperature solid oxide fuel cell integrated with novel allothermal biomass gasification. *J. Power Sources* **2006**, *159*, 570.
- (7) Jin, H.; Larson, E. D.; Celik, F. E. Performance and cost analysis of future, commercially mature gasification-based electric power generation from switch grass. *Biofuels, Bioprod. Biorefining* **2009**, *3*, 142.
- (8) Yokoo, M.; Take, T. Simulation analysis of a system combining solid oxide and polymer electrolyte fuel cells. *J. Power Sources* **2004**, *137*, 206.
- (9) Yokoo, M.; Watanabe, K.; Arakawa, M.; Yamazaki, Y. The effect of fuel feeding method on performance of SOFC-PEFC system. *J. Power Sources* **2006**, *159*, 836.
- (10) Herrmann, A.; Thomas, S.; Schotte, E. High temperature cleaning of fuel gas from biomass gasification. Presented at the 14th International Conference for Renewable Resources and Plant Biotechnology, Magdeburg, Germany, June 8–10, 2008.
- (11) Galvita, V.; Schröder, T.; Munder, B.; Sundmacher, K. Production of hydrogen with low CO₂-content for PEM fuel cells by cyclic water gas shift reactor. *Int. J. Hydrogen Energy* **2008**, *33*, 1354.
- (12) Hacker, V.; Fankhauser, R.; Faleschini, G.; Fuchs, H.; Friedrich, K.; Muhr, M.; Kordes, K. Hydrogen production by steam-iron process. *J. Power Sources* **2000**, *86*, 531.
- (13) Heidebrecht, P.; Sundmacher, K. Thermodynamic analysis of a cyclic water gas-shift reactor (CWGSR) for hydrogen production. *Chem. Eng. Sci.* **2009**, *64*, 5057.
- (14) Zhang, J.; Datta, R. Sustained potential oscillations in proton exchange membrane fuel cells with PtRu as anode catalyst. *J. Electrochem. Soc.* **2002**, *149*, A1423.
- (15) Zhang, J.; Datta, R. Electrochemical preferential oxidation of CO in reformate. *J. Electrochem. Soc.* **2005**, *152*, A1180.
- (16) Hanke-Rauschenbach, R.; Weinzierl, C.; Krasnyk, M.; Rihko-Struckmann, L.; Lu, H.; Sundmacher, K. Operating behavior and scale-up of an ECPrOx unit for CO removal from reformate for PEM fuel cell application. *J. Electrochem. Soc.* **2009**, *156*, B1267.
- (17) Lu, H.; Rihko-Struckmann, L.; Hanke-Rauschenbach, R.; Sundmacher, K. Improved electrochemical CO removal via potential oscillations in serially connected PEM fuel cells with PtRu anodes. *Electrochim. Acta* **2009**, *54*, 1184.
- (18) Steele, B. C. H.; Heinzel, A. Materials for fuel-cell technologies. *Nature* **2001**, *414*, 345.
- (19) Li, Q.; He, R.; Gao, J.; Jensen, J. O.; Bjerrum, N. J. The CO poisoning effect in PEMFCs operational at temperature up to 200 °C. *J. Electrochem. Soc.* **2003**, *150*, A1599.
- (20) Zhang, J.; Xie, Z.; Zhang, J.; Tang, Y.; Song, C.; Navessin, T.; Shi, Z.; Song, D.; Wang, H.; Wilkinson, D. P.; Liu, Z. S.; Holdcroft, S. Review: High temperature PEM fuel cells. *J. Power Sources* **2006**, *160*, 872.
- (21) He, L.; Schotte, E.; Thomas, S.; Schlinkert, A.; Herrmann, A.; Mosch, V.; Rajendran, V.; Heinrich, S. Wood gasification in a lab-scale bubbling fluidized bed: experiment and simulation. *Proceedings of the 4th European Combustion Meeting*, Vienna, 2009.
- (22) Narváez, I.; Orío, A.; Aznar, M. P.; Corella, J. Biomass gasification with air in an atmospheric bubbling fluidized bed. Effect of six operational variables on the quality of the produced raw gas. *Ind. Eng. Chem. Res.* **1996**, *35*, 2110.
- (23) Pröll, T.; Siefert, I. G.; Friedl, A.; Hofbauer, H. Removal of NH₃ from biomass gasification producer gas by water condensing in an organic solvent scrubber. *Ind. Eng. Chem. Res.* **2005**, *44*, 1576.
- (24) Ladebeck, J. R.; Wagner, J. P. Catalyst development for water-gas shift. In *Handbook of fuel cells: fundamentals, technology and applications*; Vielstich, W.; Lamm, A.; Gasteiger, H. A., Eds.; Wiley: Chichester, 2003; Vol. 3, pp 190–200.
- (25) Rhodes, C.; Hutchings, G. J.; Ward, A. M. Water-gas shift reaction: finding the mechanistic boundary. *Catal. Today* **1995**, *23*, 43.
- (26) Ritter, J. A.; Ebner, A. D. State-of-the-art adsorption and membrane separation processes for hydrogen production in the chemical and petrochemical industries. *Sep. Sci. Technol.* **2007**, *42*, 1123.
- (27) Sircar, S.; Golden, T. C. Purification of hydrogen by pressure swing adsorption. *Sep. Sci. Technol.* **2000**, *35*, 667.
- (28) Baker, R. W. *Membrane technology and applications*; 2nd ed.; Wiley-Blackwell: Chichester, 2004.
- (29) Brunetti, A.; Barbieri, G.; Drioli, E. A PEMFC and H₂ membrane purification integrated plant. *Chem. Eng. Process.* **2008**, *47*, 1081.
- (30) Bion, N.; Epron, F.; Moreno, M.; Mariño, F.; Duprez, D. Preferential oxidation of carbon monoxide in the presence of hydrogen (PROX) over noble metals and transition metal oxides: advantages and drawbacks. *Top. Catal.* **2008**, *51*, 76.
- (31) Shore, L.; Farrauto, R. J. PROX catalysts. In *Handbook of fuel cells: fundamentals, technology and applications*; Vielstich, W.; Lamm, A.; Gasteiger, H. A., Eds.; Wiley: Chichester, 2003; Vol. 3, pp 211–217.
- (32) Woosch, A.; Descombes, C.; Duprez, D. Preferential oxidation of carbon monoxide in the presence of hydrogen (PROX) over ceria-zirconia and alumina-supported Pt catalysts. *J. Catal.* **2004**, *225*, 259.
- (33) Chen, Y.; Peng, H. A segmented model for studying water transport in a PEMFC. *J. Power Sources* **2008**, *185*, 1179.
- (34) Hedström, L.; Tingelöf, T.; Alfvors, P.; Lindbergh, G. Experimental results from a 5 kW PEM fuel cell stack operated on simulated reformate from highly diluted hydrocarbon fuels: Efficiency, dilution, fuel utilization, CO poisoning and design criteria. *Int. J. Hydrogen Energy* **2009**, *34*, 1508.
- (35) Kuznetsov, M.; Otschik, P.; Eichler, K.; Trofimenko, N.; Megel, S. Development of planar SOFC stacks for CHP. *Electrochemical Society Proceedings*, Quebec City, Canada, May 15–20, 2005.
- (36) Kalschmitt, M.; Hartmann, H. *Energie aus Biomasse: Grundlagen, Techniken und Verfahren*; Springer-Verlag: Berlin, 2001.
- (37) Biegler, L. T.; Grossmann, I. E.; Westerberg, A. W. *Systematic methods of chemical process design*; Prentice Hall PTR: New Jersey, 1997.

Received for review February 24, 2010

Revised manuscript received May 17, 2010

Accepted May 19, 2010

IE100408N

[PH 7]

P. Heidebrecht, L.T. Biegler, K. Sundmacher

Optimal Design of Nonlinear Temperature Programmed
Reduction (N-TPR) Experiments

AIChE Journal 57 (2011), 2888-2901

Optimal Design of Nonlinear Temperature Programmed Reduction Experiments

Peter Heidebrecht

Physical and Chemical Process Engineering, Max Planck Institute, Sandtorstrasse 1, 39106 Magdeburg, Germany

Kai Sundmacher

Physical and Chemical Process Engineering, Max Planck Institute, Sandtorstrasse 1, 39106 Magdeburg, Germany

Lorenz T. Biegler

Dept. Chemical Engineering, Carnegie Mellon University, 5000 Forbes Avenue, Pittsburgh, PA 15213

DOI 10.1002/aic.12485

Published online January 19, 2011 in Wiley Online Library (wileyonlinelibrary.com).

We propose the application of nonconstant temperature gradients to improve the quality of temperature programmed reduction (TPR) experiments with respect to parameter estimation and model discrimination. This leads to TPR experiments with nonlinear temperature profiles (N-TPR). To determine optimal profiles for the temperature gradient, optimal control problems are set up and solved numerically. The results show that N-TPR experiments can be significantly better than traditional linear TPR experiments for many different scenarios. To implement these results in practice, we develop and demonstrate reduced optimization problem formulations, which can be solved faster and more reliably than the original formulation, with very similar results.

© 2011 American Institute of Chemical Engineers *AIChE J.* 57: 2888–2901, 2011

Keywords: temperature programmed reduction, experimental design, optimal control, model reduction

Introduction

Temperature Programmed Reduction (TPR) is an experimental method that is widely used for the estimation of kinetic parameters of metal oxide reduction reactions.^{1,2} Its working principle is simple (Figure 1); hydrogen (or some other reducing gas) flows continuously through a small sample of the metal oxide powder. The metal oxide is reduced in the hydrogen atmosphere, converting part of the hydrogen to steam. The concentration of steam in the exhaust gas is proportional to the reaction rate in the sample and is measured in short time inter-

vals (about one measurement per second). The reduction process may include several reaction steps in which the steam fraction is proportional to the cumulated rates of all reactions. The sample temperature starts at low values (ambient temperature up to 500 K), is increased at a constant rate, and follows a linear profile over time. Typical temperature gradients are between 5 and 25 K/min. At initial time, due to the low temperatures, reaction rates are virtually zero. With increasing temperature, the reaction rates increase and eventually, reactions reach complete conversion. As soon as full reduction conversion is reached, the reaction rates approach zero again, and the TPR run ends. The resulting measurement signal is used to estimate kinetic parameters. It may also be applied to discriminate rivaling models.^{3–5}

The only control variable that can be changed from one TPR experiment to another is the applied temperature

Correspondence concerning this article should be addressed to P. Heidebrecht at heidebrecht@mpi-magdeburg.mpg.de.

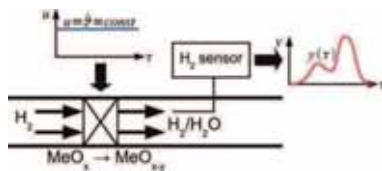


Figure 1. Principle of a TPR experiment.

[Color figure can be viewed in the online issue, which is available at www.interscience.wiley.com.]

gradient. Typically, a series of three to five TPR experiments is carried out with different temperature gradients and the whole ensemble of measured profiles is used for the parameter estimation. In a system with three reactions [e.g., the reduction of hematite (Fe_2O_3)], 12 parameters need to be estimated from these few experiments: the reaction rate constants, the activation energies, the orders of reaction, and the fractions of convertible material in the sample.

With 12 unknown parameters and only one single control parameter, the TPR method has very limited options to control the experiment. This can also be seen in a contribution by Pineau et al.,⁶ where they present a compilation of TPR studies on the reaction kinetics of iron oxide reduction carried out by various authors. Essentially, they show that estimates of the activation energies of reduction reactions vary significantly, even though they were obtained under comparable conditions. While some of these differences may be attributed to morphological differences in the sample materials, this result indicates that the parameter estimates have a large uncertainty. Moreover, with regard to model discrimination, we have shown³ that the classical TPR method is not well suited to identify the reaction scheme or the type of reaction kinetics of systems with multiple reactions; the data from a series of TPR experiments could be fitted equally well by very different models.

One option to amend these deficits of the TPR method is to extend its control options. This can be achieved by lifting the restriction of a constant temperature gradient and thereby turning it into a function of time. Because this leads to experiments with nonlinear temperature profiles, we propose to call this method N-TPR (Nonlinear Temperature Programmed Reduction). The control function, namely the temperature gradient, can then be designed in such a way that the resulting measurement function becomes optimal for the goals of the experiment. This leads to formulation of optimal control problems, which are developed and described in Section "Problem Formulation." These are solved numerically, and some exemplary solutions are shown in Section "Optimal N-TPR Experiments." With respect to better applicability of N-TPR, we propose to use reduced optimization problems, which can be solved reliably and quickly. They are introduced and discussed in Section "Reduced Problem Formulation."

Problem Formulation

In this study, we develop optimization problem formulations for two different purposes: to design optimal N-TPR

experiments for parameter estimation (Section "Optimal control problem for improved parameter estimation") and to discriminate among competing models (Section "Optimal control problem for model discrimination"). Because the dynamic model equations of a TPR system are common to both problems, we introduce them in the next section.

The TPR model

The TPR model describes the relation between the input and the output of a TPR experiment (Figure 2). The only input variable is the temperature gradient. In traditional TPR, this is a constant, while in N-TPR, it is time dependent. The output variable is the measurement signal that essentially corresponds to the cumulative reaction rate in the sample. The model states comprise the sample composition, x , and temperature, ϑ , which we normalize by a fixed standard temperature.

The model is formulated in terms of the following dimensionless parameters, p (see Heidebrecht et al.³ for a more detailed derivation):

- The Damköhler number, Da_j , corresponds to the reaction rate constant of reaction j at reference temperature, ϑ_j^{ref} .
- The Arrhenius number, $\text{Arr}_j = E_j/\text{RT}^0$, corresponds to the activation energy of reaction j .
- The oxygen capacity, Θ_j , corresponds to the fraction of oxygen that is released by reaction j , related to the total amount of reducible oxygen in the fully oxidized material.
- The order of the reaction, n .

In addition, we define the rate of reaction j , that is, $R_j(x, \vartheta, p)$ as well as the temperature gradient, u . The model equations include the mass balance, which comprises the reaction rates, $\text{Da}_j R_j$, divided by the oxygen capacity, Θ_j and multiplied by the stoichiometric coefficients, $\nu_{i,j}$. This balance describes the change in the sample composition, x :

$$\dot{x}_i = f(x, \vartheta, p) = \sum_{j=1}^{N_r} \nu_{i,j} \cdot \frac{\text{Da}_j}{\Theta_j} \cdot R_j(x, \vartheta, p); \quad i = 1 \dots N_s \quad (1)$$

with N_s denoting the number of reducible species and N_r the number of reactions in the system. The initial conditions for these ODEs are

$$x(\tau = 0) = x_0 \quad (2)$$

The temperature is increased according to the temperature gradient:

$$\dot{\vartheta} = u(\tau) \quad (3)$$

with the initial temperature

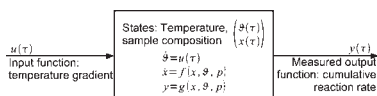


Figure 2. Input-output scheme of a TPR experiment.

$$\vartheta(\tau = 0) = \vartheta_0 \quad (4)$$

The measured output signal is the sum of all reaction rates:

$$y = g(x, \vartheta, p) = \sum_{j=1}^{N_r} \text{Da}_j \cdot R_j(x, \vartheta, p) \quad (5)$$

The reaction kinetics comprise an Arrhenius term, considering the effect of temperature on the reaction rate, as well as a composition dependent function. The latter depends on the mole fraction of the reactant species of reaction j , x_j , and has the reaction order n_j .

$$R_j = \exp \left(\text{Arr}_j \cdot \left(\frac{1}{\vartheta^{\text{ref}}} - \frac{1}{\vartheta} \right) \right) \cdot r_j(x_j, n_j); \quad j = 1 \dots N_r \quad (6)$$

In solid state reactions, three kinetic laws are commonly applied: Power law, Avramy-Erofeev, and diffusion-limited kinetics.⁷⁻⁸ Additional kinetic models such as the shrinking core or the cracking core models⁹ may be applied, but are not considered here.

- *Power law kinetics*

$$r_j = x_j^{n_j}; \quad 0.5 \leq n_j \leq 2.0 \quad (7)$$

Strictly speaking, the physical motivation behind the power law kinetics—the probability of n_j reactant molecules meeting at a reaction site at the same time—does not apply to solid phase conversions.^{4,10} However, due to its simplicity and effectiveness in practical applications, power law kinetics are frequently used to describe reduction processes. The bounds on the reaction order in Eq. 7 are arbitrary, but they reflect a typical span for these kinetics.

- *Avramy-Erofeev kinetics*

$$r_j = \frac{x_j \cdot \left[-\log(x_j) \right]^{n_j}}{1 - n_j}; \quad \frac{1}{2} \leq n_j \leq \frac{3}{4} \quad (8)$$

The Avramy-Erofeev kinetics result from a simplification of a rather complex model that considers populations of nucleates of product species, each of a different size, in combination with a growth rate at the boundaries of nucleates, where product and reactant phase are in contact with each other. Equation 8 is derived for a single reaction system, with pure reactants as initial conditions.^{11,12}

- *Diffusion limited kinetics*

$$r_j = \frac{x_j^{1-1/n_j}}{1 - x_j^{1/n_j}}; \quad 1 \leq n_j \leq 3 \quad (9)$$

Similar to Avramy-Erofeev kinetics, diffusion limited kinetics are derived with the assumption of pure reactants at initial time,⁹ so its physical motivation is only valid for a single reaction system. At initial time, the reaction rate (Eq. 9) according to this formulation reaches infinite values. The overall rate (Eq. 6) remains bounded by choosing a zero ini-

tial temperature, and, consequently, zero Arrhenius term at initial time.

Optimal control problem for improved parameter estimation

Objective function We first consider N-TPR optimization problems that maximize the quality of the parameter estimates. The idea is to determine a control profile [the temperature gradient, $u(\tau)$], which results in a measurement signal [the cumulative reaction rate, $y(\tau)$] that offers the best covariance matrix of the estimated parameters. This matrix includes variances of individual parameters, as well as the pairwise correlation of different parameters, representing the interdependence of these estimates.

Several optimality criteria have been derived in an effort to define the “best” covariance matrix^{13,14}:

- A-optimality criterion minimizes the trace of the covariance matrix. Thus, the individual estimates of the parameters are improved, but the off-diagonal elements describing the covariance between different parameters are ignored.
- C-optimality criterion minimizes the variance of an estimator of a linear function of the parameters. As with the A-optimality criterion, off-diagonal elements are not considered.
- D-optimality criterion minimizes the determinant of the covariance matrix. Thus, the interdependence of the estimated parameters is considered in this criterion.

- E-optimality criterion minimizes the largest eigenvalue of the covariance matrix. All other properties of the covariance matrix are disregarded. This criterion corresponds to minimizing the largest diameter of the parameter confidence region. The objective function may not be continuously differentiable at all points.

The D-optimality criterion considers the covariance elements of the matrix, reducing variances, and covariances alike, and is a continuously differentiable function. Moreover, by modifying the original D-optimality criterion, one can also choose to design experiments that minimize the variances of specific parameters or reduce the covariance of a certain pair of parameters. Because this criterion offers greater flexibility, it is the criterion that we consider in this study.

The objective function according to the D-optimality criterion is given by (see Bard,¹⁵ Chapter 10):

$$\max \det(V_0^{-1} + B^T \Pi^{-1} B) \quad (10)$$

In this function, V_0 denotes the *a priori* covariance matrix of the parameters from previous estimates, Π denotes the expected covariance matrix of the measurements in the planned experiment, and B describes the expected sensitivity of the measurements with respect to the parameters in the planned experiment.

In the case of N-TPR, this objective function can be further modified according to the following assumptions. First, we note that *prior* parameter values as well as the covariance matrix, V_0 , have to be estimated from previous experiments, which may be traditional linear or nonlinear TPR experiments. One can expect that *prior* parameter values of the model have a strong impact on the optimal design.

However, if V_0 is unknown it requires many optimizations to be conducted to cover a wide space of possible parameter values. Including the dependence of the optimal experiments on the *a priori* covariance matrix would increase the multitude of the necessary calculations. Therefore, to keep the number of cases to be solved to a reasonable level, we omit this matrix from the objective function. Of course, if V_0 is known *a priori*, it can easily be included in the objective function.

Second, the covariance matrix of the measurements, Π , is difficult to obtain because (a) the measurement error is not independent of the measured value and (b) the measurements in a single TPR run are not statistically independent. Thus, diagonal elements are of different magnitudes and off-diagonal elements in Π are non-zero. Because this is the *a priori* covariance matrix of the measurements, one would need a good model to predict it for TPR experiment, which is not available. Instead, for the purpose of planning the experiments, we replace the unknown matrix Π by an identity matrix. This essentially ignores the statistical properties of the measurements and, instead, focuses on the sensitivities from the postulated model. With that, we end up with a reduced objective function:

$$\max \det(B^T B) \quad (11)$$

This essentially tells us to design the experiment in such a way that its outcome is as sensitive with respect to the model parameters as possible.

The sensitivity matrix, B , comprises the sensitivities of the measurement signal with respect to the estimated parameters, p , at the designed experimental conditions (Bard,¹⁵ Chapter 7–51). To account for different orders of magnitude of the parameters, the sensitivities are normalized by the actual value of the corresponding parameter. Let n be the number of measurements taken during a TPR run, τ_i the time when the i -th measurement is taken, and m the number of model parameters to be estimated from the TPR experiment. Then, the sensitivity matrix B can be estimated using the parameter sensitivities of the model output at each measurement point:

$$B \approx \begin{pmatrix} \left. \frac{\partial y}{\partial p_1} \right|_{\tau_1} \cdot p_1 & \cdots & \left. \frac{\partial y}{\partial p_m} \right|_{\tau_1} \cdot p_m \\ \vdots & & \vdots \\ \left. \frac{\partial y}{\partial p_1} \right|_{\tau_n} \cdot p_1 & \cdots & \left. \frac{\partial y}{\partial p_m} \right|_{\tau_n} \cdot p_m \end{pmatrix} = \begin{pmatrix} y_{p_1}(\tau_1) & \cdots & y_{p_m}(\tau_1) \\ \vdots & & \vdots \\ y_{p_1}(\tau_n) & \cdots & y_{p_m}(\tau_n) \end{pmatrix} \quad (12)$$

With this, the objective function reads:

$$\max \det B^T B \approx \begin{pmatrix} \sum_i y_{p_1}(\tau_i) \cdot y_{p_1}(\tau_i) & \cdots & \sum_i y_{p_1}(\tau_i) \cdot y_{p_m}(\tau_i) \\ \vdots & & \vdots \\ \sum_i y_{p_m}(\tau_i) \cdot y_{p_1}(\tau_i) & \cdots & \sum_i y_{p_m}(\tau_i) \cdot y_{p_m}(\tau_i) \end{pmatrix} \quad (13)$$

To adapt to continuous measurement signals, we shift from discrete, equidistant points in time to a continuous for-

mulation. Thus, the summations are replaced by integrals over the whole duration, ($\tau = 0 \cdots \tau_e$), of the TPR run:

$$\max \det \int_{\tau=0}^{\tau_e} y_p \cdot y_p^T d\tau \quad (14)$$

where

$$p = (p_1, \dots, p_m)^T \\ = (\text{Da}_1, \text{Arr}_1, n_1, \Theta_1, \dots, \text{Da}_{N_r}, \text{Arr}_{N_r}, n_{N_r}, \Theta_{N_r})^T$$

Optimal control problem The time dependent sensitivity functions, $y_p(\tau)$, are obtained from direct sensitivity equations, the Jacobian ODEs, which pose additional constraints to the optimization problem. In addition to these ordinary differential equations and algebraic equations (DAEs), several inequality constraints are also imposed. The resulting optimization problem is given below, with N_s as the number of reducible species in the reaction system and N_p as the number of model parameters:

$$\max_{u(\tau)} \det \int_{\tau=0}^{\tau_e} y_p \cdot y_p^T d\tau \quad \text{Objective function} \quad (15)$$

$$\dot{x} = f(x, \vartheta, p) \quad \text{ODE constraint, sample composition} \in \mathbb{R}^{N_s} \quad (16)$$

$$\dot{\vartheta} = u(\tau) \quad \text{ODE constraint, temperature} \in \mathbb{R}^1 \quad (17)$$

$$\dot{J} = f_x \cdot J + f_p \quad \text{ODE constraint, Jacobian} \in \mathbb{R}^{N_s \times N_p} \quad (18)$$

$$y = g(x, \vartheta, p) \quad \text{AE constraint, output signal} \in \mathbb{R}^1 \quad (19)$$

$$y_p = (g_x \cdot J + g_p) \cdot p \quad \text{AE constraints, sensitivities} \in \mathbb{R}^{N_p} \quad (20)$$

$$x(\tau = 0) = x_0 \quad \text{Initial condition, Eq. 16} \in \mathbb{R}^{N_s} \quad (21)$$

$$\vartheta(\tau = 0) = \vartheta_0 \quad \text{Initial condition, Eq. 17} \in \mathbb{R}^1 \quad (22)$$

$$J(\tau = 0) = 0 \quad \text{Initial condition, Eq. 18} \in \mathbb{R}^{N_s \times N_p} \quad (23)$$

$$u_{\min} \leq u \leq u_{\max} \quad \text{Bounds on control variable} \in \mathbb{R}^1 \quad (24)$$

$$\vartheta_{\min} \leq \vartheta \leq \vartheta_{\max} \quad \text{Bounds on temperature} \in \mathbb{R}^1 \quad (25)$$

$$x(\tau_e) \leq x_{e,\max} \quad \text{Complete conversion at end time} \in \mathbb{R}^{N_s} \quad (26)$$

With regard to real experimental systems, which cannot realize arbitrarily high temperature gradients, an upper bound and a lower bound is imposed on the control variable in Eq. 24. The temperature itself is also limited. TPR devices usually do not have a cooling device, so the lowest applicable temperature is ambient temperature. Due to limited material stability, an upper bound is also imposed in Eq. 25. To ensure that the reduction has reached virtually complete conversion after the given duration of the run, τ_e , additional

lower bounds are introduced in Eq. 26 with a typical value of $x_{e,\max} = 10^{-3}$.

For a system with three reactions, where 12 parameters have to be estimated, this optimal control problem has 40 ODEs and 13 AEs. Because of the Arrhenius terms, the state equations are nonlinear. The control profile, however, appears linearly in (Eq. 17). This leads to a so-called singular optimal control problem, which poses a number of challenges that will be explored in Section “Reduced Problem Formulation.” To handle these problems, we first describe the following solution strategy.

Numerical treatment To solve the optimal control problem (Eqs. 15–26), the DAEs are discretized in time according to the method of orthogonal collocation on finite elements (see, e.g., Biegler¹⁶). Here, three collocation points are chosen per finite element, and the number of finite elements is varied between 100 and 300. To reduce the number of degrees of freedom, the optimization variable, $u(\tau)$ is assumed constant over each finite element. With that, a typical optimization problem for an N-TPR has about 10,000 variables and 100 degrees of freedom. The discretized problem is implemented in AMPL¹⁷ and solved using the optimization algorithms CONOPT and IPOPT.¹⁸

Only for some parameter configurations, the optimization algorithm converges towards an optimum from any arbitrary initial point. Thus, the following procedure is proposed to enhance convergence:

- Initialization: The constraint equations are solved for some constant temperature gradient, that is, with no degrees of freedom. This is achieved by setting identical lower and upper bounds for the temperature gradients.
- Define the objective function and impose an inequality constraint for complete conversion (Eq. 26).
- Specify the upper and lower bounds on the temperature gradient in a sequence of relaxations. Each time one or both bounds are changed, the problem is solved again. This is a “trial and error” procedure and the algorithms IPOPT and CONOPT tend to work well in different cases, although performance of each is hard to predict in advance. If both algorithms fail, the whole procedure is started again, but with a more conservative relaxation of the bounds.
- An optimization run is usually performed for a given duration of the TPR experiment. Starting from an initial profile that stretches the TPR curve over the whole time span may be advantageous. Cases have been observed where starting from a profile with a maximum temperature gradient (and thus a very short TPR curve) do not converge to an optimum, but starting from a lower temperature gradient (with a TPR curve using almost the whole given time span) would end up in an optimum.
- Using up to six relaxation steps, the bounds reach the desired values and an optimal solution is obtained.

Typical solution times on a standard PC (Intel Core2 Duo CPU E6850, 3.00 GHz) is between 5 and 30 CPU minutes, depending on the number of relaxation steps required to achieve convergence.

Application strategy We expect N-TPR experiments to be applied in a campaign to estimate kinetic parameters for a given reaction system. Initially, when no estimates of the parameters are available, a few linear TPR experiments are conducted, so that a first estimate of the parameters can be

obtained, together with a covariance matrix (V_0) of these estimates. If the covariances are larger than desired, then an N-TPR experiment is designed from the optimal control problem, based on these parameter estimates and their covariance. After conducting this experiment, new estimates are obtained from the data of the linear and the nonlinear experiments and the covariance of this estimate should be smaller than the one before. The design, execution, and evaluation of N-TPR experiments are repeated until the desired quality of the parameter covariance matrix is obtained.

Optimal control problem for model discrimination

Objective function and optimal control problem To design N-TPR experiments for the purpose of model discrimination, we propose an objective function based on the T-optimality criterion.¹⁹ This criterion assumes that two models, M_1 and M_2 , exist and the aim is to design an experiment that maximizes the ability to discriminate between both of them. In our implementation, we assume that parameter estimates are available for both models and we propose the following objective:

$$\max_{u(\tau)} \int_{\tau=0}^{\tau_f} \left(y^{(1)}(u(\tau)) - y^{(2)}(u(\tau)) \right)^2 d\tau. \quad (27)$$

Thus, the optimal N-TPR experiment should give the maximum difference between the output of both rivaling models, $y^{(1)}$ and $y^{(2)}$, and thereby allow to discriminate between both. The resulting optimization problem is given below. Note that it is simpler than the parameter estimation problem in the previous section, especially since sensitivity terms are not needed in the objective function.

$$\max_{u(\tau)} \int_{\tau=0}^{\tau_f} \left(y^{(1)}(\tau) - y^{(2)}(\tau) \right)^2 d\tau$$

Objective function (28)

$$\dot{x}^{(1)} = f^{(1)}\left(x^{(1)}, \vartheta, p^{(1)}\right)$$

ODE constraint, sample comp., model $M_1 \in \mathfrak{R}^{M_1^{(1)}} \quad (29)$

$$\dot{x}^{(2)} = f^{(2)}\left(x^{(2)}, \vartheta, p^{(2)}\right)$$

ODE constraint, sample comp., model $M_2 \in \mathfrak{R}^{M_2^{(2)}} \quad (30)$

$$\dot{\vartheta} = u(\tau)$$

ODE constraint, temperature $\in \mathfrak{R}^1 \quad (31)$

$$y^{(1)} = g^{(1)}\left(x^{(1)}, \vartheta, p^{(1)}\right)$$

AE constraint, output signal, model $M_1 \in \mathfrak{R}^1 \quad (32)$

$$y^{(2)} = g^{(2)}\left(x^{(2)}, \vartheta, p^{(2)}\right)$$

AE constraint, output signal, model $M_2 \in \mathfrak{R}^1 \quad (33)$

$$x^{(1)}(\tau = 0) = x_0^{(1)}$$

Initial condition, Eq. 29 $\in \mathfrak{R}^{M_1^{(1)}} \quad (34)$

$$x^{(2)}(\tau = 0) = x_0^{(2)} \quad \text{Initial condition, Eq. 30} \quad \in \mathbb{R}^{N_s^{(2)}} \quad (35)$$

$$\vartheta(\tau = 0) = \vartheta_0 \quad \text{Initial condition, Eq. 31} \quad \in \mathbb{R}^1 \quad (36)$$

$$u_{\min} \leq u \leq u_{\max} \quad \text{Bounds on control variable} \quad \in \mathbb{R}^1 \quad (37)$$

$$\vartheta_{\min} \leq \vartheta \leq \vartheta_{\max} \quad \text{Bounds on temperature} \quad \in \mathbb{R}^1 \quad (38)$$

$$x^{(1)}(\tau_e) \leq x_{e,\max}$$

$$\text{Complete conversion at end time, model } M_1 \quad \in \mathbb{R}^{N^{(1)}} \quad (39)$$

$$x^{(2)}(\tau_e) \leq x_{e,\max}$$

$$\text{Complete conversion at end time, model } M_2 \quad \in \mathbb{R}^{N_s^{(2)}} \quad (40)$$

This optimization can be used to discriminate between rivaling models that differ with respect to the assumed reaction mechanisms and the number of reactions or the sequence of reactions (parallel or sequential reaction schemes) in systems with single or multiple reactions. In this study, we focus on the discrimination of reaction kinetic laws in systems with a single reaction.

Numerical treatment As with the optimization problem in Section “Optimal control problem for improved parameter estimation,” we discretize the DAEs (Eqs. 29–33) according to the orthogonal collocation method on finite elements. Three collocation points per finite element are applied, and the number of elements range between 100 and 300. The discretized problem is implemented in AMPL, and IPOPT and CONOPT are used to solve it. Numerous cases have been solved for competing kinetic models with variations of the parameters of the model M_1 .

The optimization procedure is as follows:

- The output signal of the first model, M_1 , with given parameters is calculated for a linear TPR experiment with maximum temperature gradient.

- The parameters of the second model, M_2 , are estimated by minimizing the squared error between the outputs of both models at the maximum temperature gradient. In this minimization, upper and lower bounds for the parameter values are imposed. The parameters of both models are kept constant throughout the following optimization of the N-TPR experiment.

- Next, a linear TPR experiment is designed by solving Eqs. 28–40 in discretized form with a constant temperature gradient. This yields the best possible linear TPR experiment.

- As a final step, the assumption of a constant temperature gradient is relaxed and an N-TPR experiment is designed using Eqs. 28–40 in discretized form.

Application strategy These N-TPR experiments are used to discriminate between two models with known or estimated parameters. If no parameter estimates exist, then they may be obtained from a priori TPR experiments, which may follow linear temperature profiles or nonlinear TPRs determined in Section “Optimal control problem for improved parameter estimation.” Once the parameter values are available, an N-TPR experiment can be designed using Eqs. 28–40 to discriminate between two models. After executing the designed experiment, one should be able to rule out one of

the two models. If this N-TPR experiment is not sufficient to statistically disqualify one of both models, then discrimination between these models is not possible with the TPR method alone.

Optimal N-TPR Experiments

The solutions of both optimal control problems are dependent on the choice of model parameters. Therefore, in this study optimizations were carried out over a wide range of parameter combinations. For the sake of brevity, only a few representative solutions are discussed in this section.

Optimal N-TPR experiments for improved parameter estimation

Systems with one reaction—analytical solution Generally, the model equations in Section “The TPR model” cannot be solved analytically. However, for systems with a single reaction, one can manipulate the optimal control problem stated in Section “Optimal control problem” such that some information on the optimal control profile can be obtained. If we assume a system with a single reaction following power law kinetics, then applying Eqs. 15–23 and introducing the variable

$$T = \exp\left(\text{Arr} \cdot \left(\frac{1}{\vartheta_{\text{ref}}} - \frac{1}{\vartheta}\right)\right) \quad (41)$$

gives the following formulation:

$$\max_{u(\tau)} \det \int_{\tau=0}^{\tau_e} y_p \cdot y_p^T d\tau; \quad p = \{\text{Da}, \text{Arr}, n, \Theta\} \quad (42)$$

$$\dot{x} = -\frac{\text{Da}}{\Theta} \cdot T \cdot x^n \quad (43)$$

$$\dot{\vartheta} = u \quad (44)$$

$$y = \text{Da} \cdot T \cdot x^n \quad (45)$$

$$\dot{J}_{\text{Da}} = -\frac{\text{Da}}{\Theta} \cdot T \cdot n \cdot x^{n-1} \cdot J_{\text{Da}} - \frac{1}{\Theta} \cdot T \cdot x^n \quad (46)$$

$$\dot{J}_{\text{Arr}} = -\frac{\text{Da}}{\Theta} \cdot T \cdot n \cdot x^{n-1} \cdot J_{\text{Arr}} - \frac{\text{Da}}{\Theta} \cdot T \cdot \frac{\log T}{\text{Arr}} \cdot x^n \quad (47)$$

$$\dot{J}_n = -\frac{\text{Da}}{\Theta} \cdot T \cdot n \cdot x^{n-1} \cdot J_n - \frac{\text{Da}}{\Theta} \cdot T \cdot x^n \cdot \log x \quad (48)$$

$$\dot{J}_{\Theta} = -\frac{\text{Da}}{\Theta} \cdot T \cdot n \cdot x^{n-1} \cdot J_{\Theta} + \frac{\text{Da}}{\Theta^2} \cdot T \cdot x^n \quad (49)$$

$$y_{\text{Da}} = [\text{Da} \cdot n \cdot x^{n-1} \cdot J_{\text{Da}} + x^n] \cdot T \cdot \text{Da} \quad (50)$$

$$y_{\text{Arr}} = \left[\text{Da} \cdot n \cdot x^{n-1} \cdot J_{\text{Arr}} + \text{Da} \cdot \frac{\ln T}{\text{Arr}} \cdot x^n \right] \cdot T \cdot \text{Arr} \quad (51)$$

$$y_n = [\text{Da} \cdot n \cdot x^{n-1} \cdot J_n + \text{Da} \cdot x^n \cdot \log x] \cdot T \cdot n \quad (52)$$

$$y_{\Theta} = [\text{Da} \cdot n \cdot x^{n-1} \cdot J_{\Theta} + 0] \cdot T \cdot \Theta \quad (53)$$

The term Arrhenius, T , occurs linearly in most of the ODEs, so we introduce a new time coordinate, t :

$$\frac{dt}{d\tau} = T \quad (54)$$

This transformed time may be interpreted as a decelerated time, because the reaction and the evolution of all sensitivity functions are accelerated by the Arrhenius term, in the actual time domain. Derivatives with respect to the decelerated time coordinate are noted as x' . The optimization problem in the decelerated time coordinate reads:

$$\max_{u(t)} \det \int_{t=0}^{t_f} \left(\frac{y_p}{T} \right) \cdot \left(\frac{y_p}{T} \right)^T \cdot T \, dt \quad (55)$$

$$x' = -\frac{Da}{\Theta} \cdot x^n \quad (56)$$

$$\dot{y}' = \frac{u}{T} \quad (57)$$

$$J'_{Da} = -\frac{Da}{\Theta} \cdot n \cdot x^{n-1} \cdot J_{Da} - \frac{1}{\Theta} \cdot x^n \quad (58)$$

$$J'_{Arr} = -\frac{Da}{\Theta} \cdot n \cdot x^{n-1} \cdot J_{Arr} - \frac{Da}{\Theta} \cdot \frac{\log T}{Arr} \cdot x^n \quad (59)$$

$$J'_n = -\frac{Da}{\Theta} \cdot n \cdot x^{n-1} \cdot J_n - \frac{Da}{\Theta} \cdot x^n \cdot \log x \quad (60)$$

$$J'_\Theta = -\frac{Da}{\Theta} \cdot n \cdot x^{n-1} \cdot J_\Theta + \frac{Da}{\Theta^2} \cdot x^n \quad (61)$$

$$\frac{y_{Da}}{T} = [Da \cdot n \cdot x^{n-1} \cdot J_{Da} + x^n] \cdot Da \quad (62)$$

$$\frac{y_{Arr}}{T} = \left[Da \cdot n \cdot x^{n-1} \cdot J_{Arr} + Da \cdot \frac{\ln T}{Arr} \right] \cdot Arr \quad (63)$$

$$\frac{y_n}{T} = [Da \cdot n \cdot x^{n-1} \cdot J_n + Da \cdot x^n \cdot \log x] \cdot n \quad (64)$$

$$\frac{y_\Theta}{T} = [Da \cdot n \cdot x^{n-1} \cdot J_\Theta + 0] \cdot \Theta \quad (65)$$

Except for Eqs. 57, 59, and 63, these equations can be solved analytically and all sensitivities except y_{Arr} are independent of $T(t)$, which represents the chosen temperature profile. Thus, as long as the sensitivities with respect to the Arrhenius number are neglected, the first two factors of the integrand in the objective function (Eq. 55) are independent of the control variable, u . Moreover, maximizing the objective function is achieved by setting the factor $T(t)$ to its upper bound, by applying the maximum possible temperature gradient. Thus, when the activation energy is not of interest, the highest possible temperature gradient should be applied in single reaction systems.

This result for power law kinetics also applies to single reaction systems with other reaction kinetics in a similar way, and leads to the same maximum temperature gradient policy.

Systems with one reaction—numerical solutions Here we apply the optimization algorithms from Section “Optimal control problem for improved parameter estimation.” For a single reaction system, the relative oxygen capacity is always equal to one, so its sensitivity can be omitted from

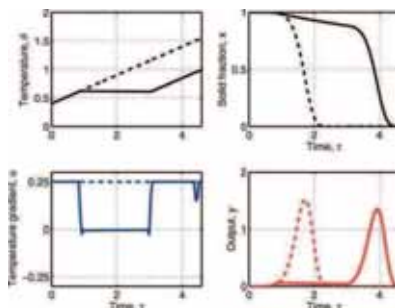


Figure 3. Optimal N-TPR experiment for a single reaction system (power law) with $Da = 1.0$; $Arr = 10$; $n = 1.0$; $g^{ref} = 0.75$.

Dashed lines: profiles from the linear TPR run with maximum temperature gradient. Solid lines: Optimal N-TPR run. [Color figure can be viewed in the online issue, which is available at [wileyonlinelibrary.com](http://www.interscience.wiley.com).]

the objective function. We consider only power law kinetics here. In principle, these examinations can be extended to other reaction kinetics as well, and the results are expected to be similar.

The optimization results are expected to depend on the model parameters selected a priori. Among these, the Damköhler number simply has the effect of shifting the whole TPR signal forward or backward in time. Because this has no qualitative effect on the optimal control profile, we always set this parameter to unity. Also, for single reactions, the oxygen capacity in a single reaction system is also always equal to unity. The two remaining parameters, the Arrhenius number and the order of reaction, are varied systematically in several cases (see Appendix Table A1). Furthermore, several additional cases have been solved to evaluate the impact of parameters such as the number of finite elements, the duration of the N-TPR run and extreme values of the order of reaction. Here, we set the duration of the N-TPR experiment to twice the duration of the linear experiment with maximum temperature gradient.

A typical solution of the optimal control problem is shown in Figure 3. In this example, $Arr = 10$, which corresponds to an activation energy of 81 kJ/mol, and the order of reaction is equal to unity. The solution is qualitatively similar in most of the other cases. The optimal control profile (lower left diagram) shows that the temperature gradient is at its upper bound, except during a certain time span, where it is close to zero. This isothermal segment is located at the ascending flank of the TPR peak and it delays the occurrence of the peak. Therefore, we refer to this time span of reduced temperature gradient as the “delay phase.”

The best possible linear TPR run, which is at maximum temperature gradient, has an objective function value of $F_{lin} = 9.05 \times 10^{-3}$. The optimal N-TPR experiment has an

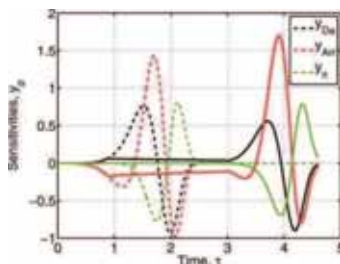


Figure 4. Sensitivity functions for a single reaction system (power law) with $Da = 1.0$; $Arr = 10$; $n = 1.0$; $g^{ref} = 0.75$. Dashed lines: profiles from the linear TPR run with maximum temperature gradient.

Solid lines: Optimal N-TPR run. [Color figure can be viewed in the online issue, which is available at www.interscience.wiley.com.]

objective function value of $F^* = 1.15 \times 10^{-2}$. This is an increase by 27%. In other cases, where different values of Arr and n are assumed, the improvement in the objective function from a linear TPR run with maximum temperature to the optimal N-TPR varies between 10 and 70%. Taking into account that the doubling of the TPR run time means an increase of the experiment duration by approximately 25% (including pretreatment, equilibration and cool down phases), this improvement justifies the additional effort.

The improvement of the objective function is due mainly from an increase of the sensitivity with respect to the Arrhenius number, Arr . This corresponds to the expectations that were concluded from the analytical solution in the previous section. The sensitivity functions with respect to the three model parameters (Da , Arr , and n) in the nonlinear and the linear TPR runs are shown in Figure 4. Note that the peak heights of y_n stay almost constant, the peak heights of y_{Da} are slightly lower in the nonlinear run, and the peak heights of y_{Arr} are increased. Although this trend does not seem to be significant, we note that these sensitivity functions are squared and integrated. Thus, a small increase in peak height, especially if the peak is already high, has a significant impact on the objective function value.

In most cases, the typical optimal control profile shows maximum temperature gradients except during a certain period of time at the ascending flank of the TPR peak. For high orders of reaction ($n > 1.5$), a different type of optimal control profile is observed: the delay phase is located at the descending flank of the TPR peak and it is divided into two parts. First, a strongly negative temperature gradient over a short time period is followed by a longer period with almost zero gradient. More detailed investigations have shown that indeed two local optima exist for high orders of reaction: one with a delay phase at the ascending flank and one with a delay phase at the descending flank. For orders of reaction with $n > 1.7$, the profile with the delay phase at the descending flank is better, otherwise the delay phase at the

ascending flank (as shown, for example, in Figure 3) leads to a better objective function.

Systems with two reactions To illustrate optimal N-TPR control profiles for systems with multiple reactions, we focus on a system with two consecutive reactions, each with power law kinetics. We assume that both reaction peaks are only about 100°C apart: their reference temperatures are $g_1^{ref} = 0.75$ and $g_2^{ref} = 0.85$. Such a system describes any metal oxide that is reduced in two subsequent steps. It has a total of eight parameters that need to be estimated: two Damköhler numbers, two Arrhenius numbers, two orders of reaction, and two oxygen capacities. Usually, one would like to use the determinant of the full sensitivity matrix as the objective function. To simplify the formulation, solution and interpretation of the D-optimal optimum, only the determinant of the sensitivities with respect to both Damköhler numbers and both Arrhenius numbers is considered here. Although this is not the complete determinant, this objective function may still be relevant, as it can be applied to improve the variances and covariances of these four parameters.

$$\max_{u(\tau)} \det \int_{\tau=0}^{\tau_f} y_p \cdot y_p^T d\tau; \quad p = (Da_1, Da_2, Arr_1, Arr_2)^T \quad (66)$$

A variety of such cases has been solved with varying Arrhenius numbers and orders of reaction (Appendix Table A2). In addition, the reference temperatures of the reactions were changed in some cases.

As with the single reaction systems, the condition of complete conversion was imposed, Eq. 26, and the end time was set to twice the duration of the corresponding linear run with maximum temperature gradient.

A typical solution of these problems is shown in Figure 5. In this example, the control variable (bottom left diagram) starts at its upper bound, so temperature is increasing (top left diagram) and the first reaction takes place (top right diagram). At about $\tau = 1.7$, when the first reaction's peak is over (see bottom right diagram) and the second reaction rate begins to increase, the control variable is changed to its lower bound for a short period of time, so temperature is decreased. After this, at about $\tau = 2$, the gradient is changed to almost zero for some time. Because the temperature has been decreased previously, the first reaction continues to proceed at low rate during this isothermal phase and reaches almost complete conversion, while the second reaction comes almost to a halt. Towards the end of the TPR run, at about $\tau = 3.9$, the temperature gradient is set back to its maximum value. As a consequence, the TPR peak occurs for the second reaction. The objective function value increases from $F_{lin} = 5.97 \times 10^{-5}$ for the linear TPR run with maximum gradient to $F_{opt} = 7.15 \times 10^{-5}$ for the N-TPR run.

Moreover, the effect of this two-staged delay phase leads to a separation of the signal peaks for the two reactions along the time coordinate. This is also reflected by the elements of the integrated sensitivity product. In the linear experiment with maximum gradient, the determinant is 5.97×10^{-5} and the corresponding matrix is given by:

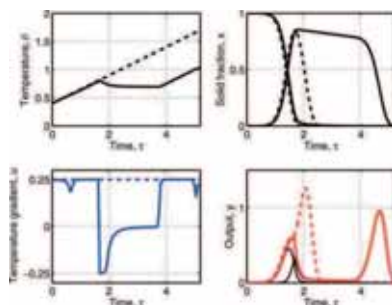


Figure 5. Optimal N-TPR experiment for a system with two reactions (both power law kinetics) with $Da = [1.0, 1.0]$; $Arr = [10, 13]$; $n = [1.0, 1.0]$; $\Theta = [0.75, 0.25]$; $g^{ref} = [0.75, 0.85]$.

Dashed lines: profiles from the linear TPR run with maximum temperature gradient. Solid lines: Optimal N-TPR run. [Color figure can be viewed in the online issue, which is available at www.interscience.wiley.com.]

$$\int_{\tau=0}^{\tau_c} y_p \cdot y_p^T d\tau = \int_{\tau=0}^{\tau_c} \begin{pmatrix} y_{Da1} \\ y_{Da2} \\ y_{Arr1} \\ y_{Arr2} \end{pmatrix} \cdot \begin{pmatrix} y_{Da1} \\ y_{Da2} \\ y_{Arr1} \\ y_{Arr2} \end{pmatrix}^T d\tau$$

$$= \begin{pmatrix} 0.027 & -0.022 & -0.012 & -0.014 \\ -0.022 & 0.253 & 0.015 & 0.130 \\ -0.012 & 0.015 & 0.043 & -0.018 \\ -0.014 & 0.130 & -0.018 & 0.329 \end{pmatrix} \quad (67)$$

For the optimal N-TPR run, the determinant is 7.15×10^{-5} and the corresponding matrix is given by:

$$\int_{\tau=0}^{\tau_c} y_p \cdot y_p^T d\tau = \begin{pmatrix} 0.024 & -0.007 & -0.011 & -0.008 \\ -0.007 & 0.156 & 0.013 & 0.006 \\ -0.011 & 0.013 & 0.043 & -0.011 \\ -0.008 & 0.006 & -0.011 & 0.520 \end{pmatrix} \quad (68)$$

While some of the main-diagonal elements have decreased, instead of increasing, one can determine that the improvements in the objective function are mainly obtained due to the decreases in off-diagonal elements, including $y_{Da2} \cdot y_{Arr2}$ and combined elements of parameters from both reactions, $y_{Da1} \cdot y_{Da2}$, and $y_{Da1} \cdot y_{Arr2}$.

However, such a peak separation was not obtained in all cases (see Appendix Table A2). For certain combinations of n_1 and n_2 , a linear TPR run with maximum temperature gradient is optimal, while a secondary delay phase can be observed, for example, in the case shown in Figure 5. Here,

the temperature gradient is decreased for a very short period of time at the ascending flank of the first reaction's peak. That indicates that the delay phase, which was optimal in the single reaction systems is still present here, but it is not dominant.

Optimal N-TPR experiments for model discrimination

We now consider the optimization strategy in Section "Optimal control problem for model discrimination" to design N-TPR experiments to discriminate between rivaling single reaction models with different kinetics. With three different reaction kinetics (power law, Avramy-Erofeev and diffusion limitation from Section "The TPR model"), six (ordered) pairs of rival models are possible. The optimization problems for these different model combinations are solved for varying Arrhenius numbers and reaction orders of the first model, M_1 (see Appendix Table A3). All other parameters are set constant: $Da^{(1)} = 1$, $\Theta^{(1)} = 1$, and $g^{ref(1)} = 0.75$.

The optimization results show two different types of optimal control profiles. In some cases, a short delay phase with a strongly negative gradient followed by a longer phase with constant gradient is observed. These control profiles are similar in shape to the peak separating delay phase in Figure 5. In many other cases, the optimal control profile simply has a delay phase with almost zero temperature gradient. Figure 6 shows a typical example of this type of control profile.

The upper right diagram shows the simulated outputs of both models from two linear TPR runs. The output signal of the model M_1 at its maximum temperature gradient is a clean sharp peak ending at about $\tau = 2.2$. Because the parameters of the model M_2 are fitted to this signal, the output profiles of both models are practically identical and the difference between both curves, given by the objective (Eq. 28), is only $F_{lin,ini} = 3.02 \times 10^{-5}$.

The best possible linear TPR run is obtained at $u = 0.107$, where the difference between both output profiles increases to $F_{lin,opt} = 0.165$. The two output signals are also shown as the two broader peaks in the upper right diagram. This is a constrained optimum, with an active inequality constraint for complete conversion (Eq. 39); further increasing the experiment time would lead to lower temperature gradients and additional improvement of the objective function value. Although a lower temperature gradient increases the difference between the two profiles by several orders of magnitude, both output signals are still very similar in shape. Conducting such a linear TPR run may produce a measured signal somewhere in between these calculated profiles. Such an experimental result would not allow us to discriminate between the two models.

The output signals of both models from the optimal N-TPR run are shown in the bottom right diagram, with the control profile represented by the solid line in the bottom left. Note that the control profile is at maximum temperature gradient, except during a long delay phase during the middle of the experiment. This leads to an objective function value of $F^* = 0.552$. The N-TPR run not only increases the objective function value by an additional factor of about 3, but also produces two profiles with qualitatively different shapes. Conducting such an experiment should provide a measured signal that allows us to discard one of the two models.

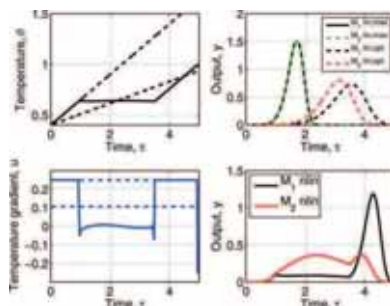


Figure 6. Optimal N-TPR experiment for model discrimination (power law vs. Avramy-Erofeev kinetics).

Upper right corner: Model outputs from linear TPR runs with maximum and optimal temperature gradient; Lower right corner: Model outputs from optimal N-TPR run. The optimal control profile is the blue solid line in the lower left diagram. $Da^{(1,2)} = [1.0, 1.12]$; $Arr^{(1,2)} = [10, 4.27]$; $n^{(1,2)} = [1.0, 0.5]$; $\phi^{(1,2)} = [1, 1]$; $g^{en(1,2)} = [0.75, 0.75]$.

[Color figure can be viewed in the online issue, which is available at www.interscience.wiley.com.]

Reduced Problem Formulation

Because of the linear dependence of $u(\tau)$ in Eqs. 17 and 31, both optimization formulations are singular control problems. These ill-conditioned problems are characterized by shallow response surfaces. If the optimal temperature gradient is not at its bounds, then $u(\tau)$ consists of singular arcs. Unique solutions of these profiles are difficult to determine within numerical precision.

Consequently, solving the optimal control problem for an N-TPR experiment is not an easy task, even with advanced methods and an experienced user. The procedure that is necessary to converge towards a useful solution is difficult and not identical for all cases. Initially guessed profiles that work well for some cases may fail for others.

With these characteristics this approach is difficult to implement and automate in a laboratory environment. Nevertheless, from the nature of singular control problems and the solutions in the previous section, we adopt two guidelines for the development of reduced problem formulations.

- Singular control problems can be regularized through the addition of quadratic penalty terms or coarse discretizations of the control profile. Either modification improves the likelihood for better conditioned problems, unique solutions, and faster convergence.
- The solution profiles $u(\tau)$ in Section "Optimal N-TPR Experiments" can be captured reasonably accurately by piecewise constant elements. Choosing such a discretization also leads to better conditioned problem formulations with fewer degrees of freedom.

These guidelines are applied for the following problem cases.

Reduced problems for parameter estimation

Systems with one reaction The optimal control function for systems with one single reaction typically applies a maximum temperature gradient except during a delay phase, where the temperature gradient is virtually constant but not at its upper bound (see Section "Systems with one reaction—numerical solutions"). These profiles can be approximated by a piecewise constant function, as shown in Figure 7, with three variables: times at the beginning and at the end of the delay phase, τ_1 and τ_2 , and the value of the control variable during the delay phase, u_1 .

This reduced optimization problem has far fewer degrees of freedom and may be solved with standard software such as MATLAB. In this environment, the DAE constraints are integrated numerically at each function evaluation. In our implementation, we approximate the gradients by finite differences and use the MATLAB function "fmincon," which uses an SQP algorithm with a BFGS update of the Hessian. It allows implementing the upper and lower bounds of the optimization variables as inequality constraints.

The integration of the ODE constraints is conducted using *ode15s*, an implicit Runge-Kutta algorithm of variable order. It uses an adapted step width in time, and the resulting discretization in time is a bit finer than in the solution of the full problems. Due to these different discretization schemes, the objective function values in the full and in the reduced problem may differ, but optimal profiles can be compared directly.

The reduced problems are typically solved within 30–50 optimization steps, which usually takes a few CPU minutes (Intel Core2 Duo CPU E6850, 3.00 GHz). Convergence is reliable in more than 90% of the cases; only the choice of the initial point requires some input by the user.

The reduced problems have been solved for the same combinations of the Arrhenius number and the order of reaction as for the full problem. In most of the cases, the optimal control profiles obtained from the reduced problem is very similar to the results from the corresponding full problem, and the nonlinear experiments show similar improvements compared to their linear counterparts. In particular, the delay phase is always located at the beginning of the ascending flank of the TPR signal.

For illustration, we reconsider the case from Section "Systems with one reaction—numerical solutions." Here, the solid lines in Figure 8 show a typical result for the reduced problem formulation. For comparison, the solution from the corresponding full problem is shown in dashed lines and the two solutions have outputs and temperature profiles that are almost identical. This observation applies to the majority of the solved cases, so this problem reduction seems to be appropriate. For this case the objective function for the full problem increases by 27%, from $F_{\text{lin}} = 9.05 \times 10^{-3}$ to $F^* = 1.15 \times 10^{-2}$. For the reduced problem, it increases by 45%, from $F_{\text{lin}} = 1.39 \times 10^{-2}$ and $F^* = 2.02 \times 10^{-2}$.

Systems with two reactions The shape of the delay phase that separates the two peaks is different from the typical shape of the delay phase found with single reaction systems

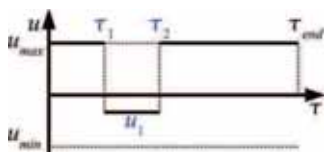


Figure 7. Schematic control profile for the reduced problem for single reaction systems.

[Color figure can be viewed in the online issue, which is available at wileyonlinelibrary.com.]

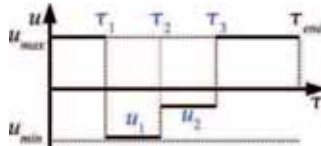


Figure 9. Schematic control profile for the reduced problem for systems with two reactions.

[Color figure can be viewed in the online issue, which is available at wileyonlinelibrary.com.]

(Section “Systems with one reaction—numerical solutions”). The profile in Figure 5 includes a strongly negative temperature gradient followed by a temperature gradient close to zero. Therefore, the delay phase is split into two parts, introducing one new segment to the reduced problem. This profile is depicted in Figure 9 with segments u_1 and u_2 , respectively.

As shown in Appendix Table A2, many reduced problem cases have been solved, using the same parameter combinations that were applied in the solutions of the full problem. A typical solution for a system with $\text{Arr} = [10, 10]$, $n = [1.0, 1.0]$ is shown in Figure 10 (right). It has a delay phase with a cooling period located between the two peaks. The control profile and the output signal closely approximate the typical peak separating solution of the corresponding full problem, which is shown in dotted lines in the diagram. Similar solutions are observed in many cases with different parameters.

However, depending on the initially chosen control profile, the optimization converges to a second local optimum (Figure 10, left). This optimal control profile has a delay phase

at the ascending flank of the first peak. No such delay phase was observed in the solutions of the full problems, so this second local optimum occurs due to the reduction of the control profile. With regard to the objective function, the control profile without peak separation (Figure 10 left) is better than the solution with peak separation (right diagram). This applies to many other cases in Appendix Table A2.

With two locally optimal solutions, the question arises, which of both solutions should be applied in an N-TPR experiment. At first glance, it seems to be reasonable to apply the control profile which gives the better objective function value. In the case in Figure 10 that would be the solution shown in the left diagram. There is, however, another practical aspect that needs to be considered: the sensitivity or robustness of the solution. In practice, the system parameters are not exactly known, and the control profile cannot be realized precisely as described in the optimal solution, even if obtained from a reduced problem. If the objective function is very sensitive to changes in the control profile, then it is very likely that small errors in the experimental procedure will result in a very bad experiment. Thus, it is advantageous if the applied solution has a low sensitivity with respect to the control profile. These sensitivities are represented by the eigenvalues of the Hessian matrix of the solution. They are listed in Table 1 for the two solutions shown in Figure 10. Obviously, the solution with a delay phase at the first peak is much more sensitive than the solution with peak separation. This argument advocates the application of the peak separating solution in the right diagram, because it is more robust, although it may not be globally optimal in all cases. Because in such uncertain systems robustness may be an important issue, it should be considered in the optimization, for example, through a robustness term in the objective function. This aspect needs further detailed consideration and is left as a subject for future studies.

Another approach to solve the problem of multiple optima is to apply more complex control profiles. In the case here, a control profile with two distinct delay phases could be chosen. The first delay phase is supposed to be located at the ascending flank of the first peak, and the second delay phase, which should have a cooling phase and an approximately isothermal phase, should separate the two peaks. This control profile combines the two optimal profiles in Figure 10 and should lead to unique optima. Further investigation will be considered in future studies.

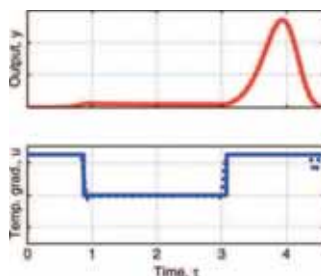


Figure 8. Optimal N-TPR experiments for a single reaction system (power law) with $\text{Da} = 1.0$; $\text{Arr} = 10$; $n = 1.0$; $y^{\text{ref}} = 0.75$ (c.f. Section “Systems with one reaction—numerical solutions”).

Dashed lines: solution of the full problem; solid lines: Solution of the reduced problem. [Color figure can be viewed in the online issue, which is available at wileyonlinelibrary.com.]

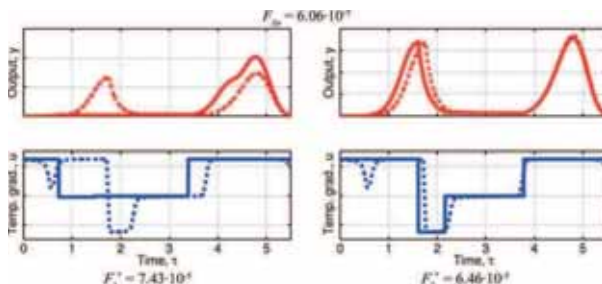


Figure 10. Example of two local optima of the reduced problem.

The dotted lines indicate the solution of the full problem and the solid lines are the solutions of the reduced problems. Da = [1.0, 1.0], Arr = [10, 10], n = [1.0, 1.0], Θ = [0.75, 0.25], θ^{ref} = [0.75, 0.85]. [Color figure can be viewed in the online issue, which is available at www.interscience.wiley.com.]

Reduced problems for model discrimination

The solutions of the full problems for model discrimination in Section "Optimal N-TPR experiments for model discrimination," typically show a control profile with a single delay phase where the temperature gradient is close to zero. In some cases, an additional delay phase is also included with a strongly negative temperature gradient. In the reduced problem, we ignore the possible occurrence of this cooling phase and instead favor a simple profile with only one delay phase, as shown in Figure 7.

A typical solution of the reduced problem is shown in Figure 11 together with the solution of the corresponding full problem. The objective function value is increased from $F_{lin,ini} = 3.03 \times 10^{-5}$ for a linear TPR run with maximum temperature gradient to $F^* = 0.543$ at the solution of the reduced problem. The function values are usually very similar to those obtained from the full problems. This is aided by the absence of sensitivity terms in the objective function; these may have very strong curvature and are therefore sensitive to discretization errors.

The results for other combinations of models show similar trends and are not shown here. Also in those cases, where the full solution shows a double delay phase, the output signals and the objective function values of the full and the corresponding reduced problem are very similar. This means that the proposed problem reduction is appropriate. Even in some cases, where no solution could be found for the full problem (see Appendix Table A3), the reduced problem was solved successfully. However, as seen in Appendix Tables A1–A3 some cases remain where no nonlinear solution could be found. This suggests that in these cases, no improvement of the objective function value is possible and a linear TPR experiment is optimal.

The initialization of the optimization problem is simple and reliable in most cases. A good initial guess is any control profile with a delay phase where the temperature gradient is close to zero and which has a higher objective function value than the linear experiment with maximum gradi-

ent. If such an initial solution can be found, the optimization converges within 10–20 optimization steps. These problems are usually solved within a few minutes of CPU time.

Conclusions

Optimal control problems for the design of nonlinear TPR experiments have been set up and solved for a wide range of parameters and for several different kinds of systems. Selected examples of their solutions are presented in Section "Optimal N-TPR Experiments." They show that N-TPR can improve the quality of parameter estimates obtained from TPR experiments. In some cases, the improvements are significant, while in other, they are only small and a linear TPR experiment is almost as good. For systems with more than one reaction, optimal control profiles often yield so-called peak separation, where the measurement signals of both reactions are separated in time. This reduces the covariances of the parameter estimates. The design of optimal N-TPR experiments for model discrimination yields strong improvements in model discrimination capabilities.

The full problem formulation is a singular control problem that may be difficult to solve. Nevertheless, the optimal control profiles can often be approximated by piecewise constant functions. In accordance with the analytical solution in Section "Systems with one reaction—analytical solution," the control variable is usually at its upper bound, except during

Table 1. Eigenvalues of the Hessian Matrices of the Solutions Shown in Figure 10

Position of delay phase	Ascending flank of first peak	Between both peaks
Eigenvalues of Hessian matrix	$\lambda = \begin{pmatrix} 5.2 \cdot 10^3 \\ 3.7 \cdot 10^5 \\ 2.5 \cdot 10^6 \\ 9.5 \cdot 10^6 \\ 1.7 \cdot 10^{14} \end{pmatrix}$	$\lambda = \begin{pmatrix} 1.3 \cdot 10^{-3} \\ 6.5 \cdot 10^1 \\ 1.5 \cdot 10^2 \\ 9.0 \cdot 10^2 \\ 1.7 \cdot 10^4 \end{pmatrix}$

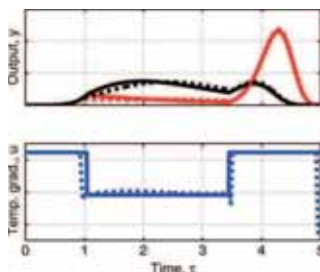


Figure 11. Solution of the reduced problem for model discrimination (power law vs. Avramy-Erofeev kinetics).

Dotted lines: Solution of the corresponding full problem (see Figure 6); solid lines: Solution of the reduced optimization problem; Black lines: Output model M_1 ; Red lines: output model M_2 ; Blue lines: control profiles. $Da = [1.0, 1.12]$; $Arr = [10, 4.27]$; $n = [1.0, 0.5]$; $\Theta = [1, 1]$; $\vartheta^{ref} = [0.75, 0.75]$. [Color figure can be viewed in the online issue, which is available at [wileyonlinelibrary.com](http://www.interscience.wiley.com).]

so-called delay phases, where it is close to zero or near its lower bound. Consequently, the reduction of the optimal control problems to optimization problems of lower dimension is possible and successful in most cases. The solutions of the reduced problems usually approximate the solutions of the corresponding full problems very well. In addition, for many parameter combinations that could not be solved in the full formulation, a good reduced solution could be obtained.

In one group of cases, the reduced problems had at least two local optima. This was not observed with the solutions of the corresponding full problems. This point may be amended by applying different, more complex control profile schemes with more than two delay phases.

Numerical convergence of the optimization algorithm for the reduced problems is quite reliable. The only critical point is the identification of a suitable initial guess for the profiles. In some cases, this may be difficult and require some additional input by the user. Besides this, the procedure can be made to work in a fully automated way.

The solutions of the reduced problem are control profiles with piecewise constant temperature gradients. They resemble a sequence of linear TPR experiments, which, in principle, can be applied in TPR devices. Nevertheless, depending on the device, changes to the control software may be necessary so that sequences of linear temperature profiles can be applied. Moreover, to realize negative temperature gradients, as needed for multireaction systems (see Figure 10 right), an appropriate cooling device is required.

Finally, imperfections such as inhomogeneous spatial temperature distribution or nonideal temperature control lead to deviations from the desired, optimal temperature profile. This affects both linear and nonlinear TPR experiments alike, so the N-TPR experiments are still expected to be superior. A deeper analysis of this issue, which concerns the robustness of the optimal nonlinear control profiles, is left as subject for further studies.

Acknowledgment

A part of this work was supported by a fellowship within the Postdoc-Programme of the German Academic Exchange Service (DAAD).

Notation

The formulation of the optimization problems and the presentation of their results have been done in terms of dimensionless parameters.

- Arr_j = Arrhenius number of reaction j
- B = sensitivity matrix of measurements
- Da_j = Damköhler number of reaction j
- E_j = activation energy of reaction j , [J/mol]
- f = right-hand side of state equation (Eq. 1)
- g = right-hand side of output equation (Eq. 5)
- J = Jacobian, parameter sensitivity of states
- n_j = order of reaction j
- N_s = number of species
- N_p = number of model parameters
- p = vector of model parameters to be estimated
- R = universal gas constant, [J/mol/K]
- R_j = rate of reaction j
- r_j = concentration dependent term of R_j
- T = Arrhenius term
- T^0 = reference temperature, [K]
- t = decelerated time
- u = control variable, temperature gradient
- V_0 = a priori covariance of parameter estimates
- x_i = fraction of solid species i
- y = output variable, measurement signal
- y_p = parameter sensitivity of output variable
- Θ_j = relative oxygen capacity of reaction j
- ϑ = temperature
- λ_i = Eigenvalues of Hessian matrix
- ν_{ij} = stoichiometric coefficient of species i in reaction j
- Π = covariance matrix of measurements
- τ = Time

Subscripts

- i = solid species
- ini = initial profile
- j = reaction
- lin = linear TPR experiment
- min = lower bound
- max = upper bound
- p = derivative w.r.t. model parameters
- x = state
- 0 = initial value at $\tau = 0$

Superscript

- ref = reference
- (1),(2) = model 1, 2
- \emptyset = standard
- $*$ = optimum

Literature Cited

- Kissinger HE. Reaction Kinetics in Differential Thermal Analysis. *Anal Chem.* 1957;29:1702–1706.
- Hurst NW, Gentry SJ, Jones A. Temperature Programmed Reduction. *Catal Rev—Sci Eng.* 1982;24:233–309.
- Heidebrecht P, Galvita V, Sundmacher K. An alternative Method for Parameter Identification from Temperature Programmed Reduction (TPR) data. *Chem Eng Sci.* 2008;63:4776–4788.
- Wimmers OJ, Arnoldy P, Moulijn JA. Determination of the Reduction Mechanism by Temperature-Programmed Reduction: Application to small Fe₃O₄ Particles. *J Phys Chem.* 1986;90:1331–1337.
- Piotrowski K, Mondal K, Lorethova H, Stonawski L, Szymański T, Wiltowski T. Effect of Gas Composition on the Kinetics of Iron Oxide Reduction in a Hydrogen Production Process. *Int J Hydrogen Energy.* 2005;30:1543–1554.

6. Pineau A, Kanari N, Gaballah I. Kinetics of Reduction of Iron Oxides by H₂ – Part I: Low Temperature Reduction of Hematite. *Thermochim Acta*. 2006;447:89–100.

7. Vyazovkin S, Dollimore D. Linear and Nonlinear Procedures in Iso-conversional Computations of the Activation Energy of Nonisothermal Reactions in Solids. *J Chem Inf Sci*. 1996;36:42–45.

8. Wimmers OJ. Analytical Expressions for Temperature Programmed Patterns using Solid-State Kinetics. *Thermochim Acta*. 1985;95:67–72.

9. Levenspiel O. *The Chemical Reactor Omnibook*. Corvallis: OSU Book Stores, 1996.

10. Vyazovkin S, Wight CA. Kinetics in Solids. *Annu Rev Phys Chem*. 1997;48:125–149.

11. Avrami M. Kinetics of phase change I – General theory. *J Chem Phys*. 1939; 7:1103–1112.

12. Kanervo JM, Krause AO. Kinetic Analysis of Temperature-Programmed Reduction: Behavior of a CrO₃/Al₂O₃ Catalyst. *J Phys Chem B*. 2001;105:9778–9784.

13. Pukelsheim F. *Optimal design of experiments*. New York: Wiley, 1993.

14. Atkinson AC, Donev AN, Tobias RD. *Optimum experimental design*. Oxford: Oxford University Press, 2007.

15. Bard Y. *Nonlinear parameter estimation*. London: Academic Press, 1974.

16. Biegler LT. *Nonlinear programming: concepts, algorithms and applications to Chemical Processes*. Philadelphia: SIAM, 2010.

17. Fourer R, Gay DM, Kernighan BW. *AMPL: a modeling language for mathematical programming*, 2nd ed. Pacific Grove: Brooks/Cole – Thomson, 2003.

18. Wächter A, Biegler LT. On the implementation of an interior-point filter line-search algorithm for large-scale nonlinear programming. *Math Program*. 2006;106:25–57.

19. Atkinson AC, Fedorov VV. Optimal design: experiments for discrimination between several Models. *Biometrika*. 1975;62:289–303.

Appendix

Table A1. Solved Cases for a System with One Single Reaction

n	0.7	1.0	1.5
Arr			
5	+	+	+
10	+	+	+
15	+	+	+

“+”: cases where the optimization converged to an optimum.

Table A2. Solved Cases for a System with Two Reactions

		n ₁ ln ₂				
		1.01.0	1.01.5	1.511.0	1.00.7	0.711.0
Arr ₁ lArr ₂	1010	+	–	+	–	–
	1013	+	–	+	–	+
	1310	–	–	+	–	–
g ₂ ^{def} = 0.95						
Arr ₁ lArr ₂	1013	+	+	+	–	+

“+”: cases where the optimization converged to an optimum with peak separation; “–”: cases where no convergence was obtained and the linear TPR experiment is optimal or nearly optimal.

Table A3. Solved Cases for Model Discrimination

M ₁ : Power law M ₂ : Avramy-Erofeev			
n ₁	0.5	1.0	1.5
Arr ₁			
5	+	+	+
10	+	+	+
15	+	+	+
M ₁ : Avramy-Erofeev M ₂ : Power law			
n ₁	1/2	2/3	3/4
Arr ₁			
5	+	+	+
10	+	+	+
15	lin	lin	lin
M ₁ : Diffusion limited M ₂ : Power law			
n ₁	1.5	2.0	3.0
Arr ₁			
5	+	+	+
10	+	+	+
15	+	–	–

“+”: cases where the optimization converged to an optimum; “–”: cases where no convergence was achieved; “lin”: cases where a linear experiment is optimal.

Manuscript received July 2, 2010, and revision received Oct. 19, 2010.

[PH 8]

B. Hartono, P. Heidebrecht, K. Sundmacher

Mass Integration of High Temperature Fuel Cell Plants

International Journal of Hydrogen Energy 36 (2011),
7240-7250.

Available at www.sciencedirect.comjournal homepage: www.elsevier.com/locate/he

A mass integration concept for high temperature fuel cell plants

Benny Hartono^a, Peter Heidebrecht^{a,*}, Kai Sundmacher^{a,b}

^a Max Planck Institute for Dynamics of Complex Technical Systems, Physical and Chemical Process Engineering, Sandtorstrasse 1, 39106 Magdeburg, Germany

^b Otto von Guericke University, Process Systems Engineering, Universitätsplatz 2, 39106 Magdeburg, Germany

ARTICLE INFO

Article history:

Received 17 December 2010

Received in revised form

1 March 2011

Accepted 5 March 2011

Available online 22 April 2011

Keywords:

Mass integration

SOFC

MCFC

Recycle ratio

ABSTRACT

We investigate the utilization of anode exhaust gas from high temperature fuel cells as gasification or reforming agent in Solid Oxide Fuel Cell (SOFC) and Molten Carbonate Fuel Cell (MCFC) power plants. The minimal anodic recirculation ratio is determined by two approaches: based on stoichiometric considerations and using detailed modeling of all process units. In the latter case, the risk of carbon formation and system heat integration are considered. The results indicate that the stoichiometric approach can be used as a shortcut method only for the SOFC systems due to good agreements with the detailed calculations. Furthermore, the mass integration concept is a feasible option for a wide variety of fuels in SOFC plants thanks to their relatively high operating temperatures. In MCFC systems, significantly higher recycle ratios are required to suppress carbon deposition which makes this concept unattractive.

Copyright © 2011, Hydrogen Energy Publications, LLC. Published by Elsevier Ltd. All rights reserved.

1. Introduction

Stationary power plants based on high temperature fuel cells (MCFC or SOFC) can utilize a wide range of fuels [1–5]. This is basically because these fuel cells are tolerant to carbon monoxide [6]. Such plants typically include a fuel processor (reformer or gasifier), a purification unit (sulphur, dust and tar removal), the fuel cell and a burner (Fig. 1). The fuel processor requires a certain amount of oxygen atoms in order to transform the raw fuel into a fuel gas mixture. Three options are conventionally used for this purpose:

- **Air feed:** the fuel is partially burned with an under-stoichiometric amount of air. The feeding system is simple (no air cleaning necessary) and no additional heat is required in the fuel processor. However, a part of the fuel is consumed

and the product gas mixture is significantly diluted by nitrogen, penalizing the fuel utilization in the fuel cells.

- **Steam (or carbon dioxide) feed:** steam is fed to the fuel processor as gasification/reforming agent. The necessary pretreatment steps for the water increases the complexity of the system and a large amount of heat is required due to the endothermic reactions. On the other hand, it produces energy-rich gas mixture which allows high fuel utilization. Alternatively, carbon dioxide may be used instead of steam.
- **Autothermal:** a hybrid system between air and steam feed where the process is operated thermally autonomous. Although no external heat is needed, the water pretreatment steps are necessary and the product gas is diluted by nitrogen.

In systems with high temperature fuel cells such as an MCFC or an SOFC, the anode outlet stream has been oxidized

* Corresponding author. Tel.: +49 391 6110 285; fax: +49 391 6110 545.

E-mail address: heidebrecht@mpi-magdeburg.mpg.de (P. Heidebrecht).

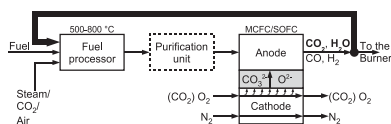


Fig. 1 – Principle of the mass-integrated high temperature fuel cell plant.

to a large extent. It leaves the fuel cell at high temperature and contains large fractions of carbon dioxide and steam. These two properties make the anode outlet stream applicable as an alternative to the conventional feeds by recirculating a part of it back to the fuel processor unit (Fig. 1, bold line). Such a system integrates the fuel cell and the fuel processor with respect to mass and heat and, thus, needs no pretreatment units. However, the gas flow rate is also increased, resulting in higher power consumption by the blower. In Table 1, the features of this system are compared with the properties of the conventional systems.

Therefore, the idea of mass integration raises two questions.

1. The influence of the recycle stream on the system efficiency.
2. The minimal recycle ratio required to satisfy the oxygen demand of the fuel processor.

In the past, several studies were focused on the first question. Fellows analyzed the effect of different recycle ratios on the system efficiency in direct internal reforming (DIR)-MCFC and SOFC plants [7,8]. He stated that an increase of anode recycle results in slightly higher system efficiency, but this advantage is cancelled out by the increased power consumption of the recycle blower. Lisbona et al. performed a theoretical research in a reformer-SOFC system with methane as feed [9]. They found that a high anodic recirculation ratio results in low system efficiency due to the dilution of the anodic inlet gas. Nearly the same conclusion was also found by Colpan et al., who came to a conclusion that a high recirculation ratio is undesirable due to the increase of the system's complexity [1]. Another study by Yi et al. studied the same issue on the reformer-SOFC system and considered the possibility of carbon formation for different types of fuel [10]. They concluded that the maximum system efficiency is achieved by the lowest recycle ratio needed to avoid carbon deposition. This optimum recycle ratio depends on the fuel

composition. All publications mentioned agree that the system efficiency is optimal when the lowest possible anodic recycle ratio is applied. Thus, the focus of our study is to identify the minimal recycle ratio depending on the applied system and fuel. Besides taking into account the risk of carbon formation, we also consider two types of high temperature fuel cells, the conversion of primary fuel (e.g. solid coal or wood) to fuel gas mixture and the thermal integration of the system. Furthermore, the effect of fuel composition on the minimal recycle ratio required is analyzed.

We evaluate the minimal recycle ratio with two different approaches. First, the lowest recycle ratio needed to provide sufficient oxygen for the fuel conversion is determined stoichiometrically. Then, to consider aspects such as thermodynamic equilibria, carbon deposition, system heat integration and operating temperatures, more detailed unit models are applied. The calculation results of different high temperature plants with different primary fuels are compared and discussed in details.

2. Methodology

In the present work, five different types of primary fuels are considered in order to analyze the influence of the fuel composition. These fuels are listed in Table 2 together with their atomic ratios. Gaseous and liquid fuels are assumed to be pure compounds, while solid fuels are assumed to be free of moisture. In order to compare fully integrated to non-integrated systems and for the sake of simplicity, only steam feed ($G_{\text{CO}_2}^{\text{feed}}$) is considered in the calculation.

2.1. Stoichiometric calculation

To derive a relation for the recycle ratio necessary for stoichiometric conversion, the plant is reduced to two units, namely the fuel processor and the fuel cell (Fig. 2). Because we take a purely stoichiometric approach, unit temperatures or energy balances are not considered.

In this derivation, the fuel composition is described as indicated in Fig. 2 by indexes x , y and z , denoting the amount of carbon, hydrogen and oxygen in the fuel. At stoichiometric dosing of the steam feed or recycle stream, the outlet stream of the fuel processor ($G_{\text{out,FP}}^{\text{out}}$) contains only carbon monoxide and hydrogen. The carbon and oxygen atom balances around the fuel processor (Fig. 2, balance boundary B_1) can be written as:

$$G_{\text{CO}_2}^{\text{rec}} + G_{\text{CO}}^{\text{rec}} + x \cdot G^{\text{fuel}} = G_{\text{CO}}^{\text{out,FP}} \quad (1)$$

Table 1 – Comparison of different oxygen feeding systems in high temperature fuel cell plants.

	Air feed	Steam or carbon dioxide feed	Autothermal	Anodic recycle
Energy density of fuel gas mixture	Low (–)	High (+)	Medium (0)	High (+)
Heat demand by fuel processor	No (+)	High (–)	No (+)	Medium (0)
Pretreatment units	Not required (+)	Required (–)	Required (–)	Not required (+)
Pressure drop	High (–)	Low (+)	Medium (0)	Medium (0)

Table 2 – Atomic ratios of fuels examined in this study.

Primary fuel $C_xH_yO_z$	Atomic ratio	
	$Y = y/x$ (H/C)	$Z = z/x$ (O/C)
Methane (g)	4	0
Ethanol (l)	3	0.5
Methanol (l)	4	1
Wood (s) [20]	1.5075	0.6512
Anthractite (s) [21]	0.4673	0.0204

$$G_{H_2O}^{rec} + 2 \cdot G_{CO_2}^{rec} + G_{CO}^{rec} + z \cdot G^{fuel} + G_{CO}^{feed} = G_{CO}^{out,FP} \quad (2)$$

Combining Eqs. (1) and (2), we obtain

$$(x - z) \cdot G^{fuel} = G_{H_2O}^{feed} + G_{CO_2}^{rec} + G_{H_2O}^{rec} \quad (3)$$

where the left-hand side of the equation corresponds to the oxygen required to convert the primary fuel to carbon monoxide and hydrogen and the right-hand side denotes the amount of available oxygen for gasification or reforming from the steam feed and the recycle stream.

Defining the steam-to-carbon ratio, S/C , as the ratio of steam feed rate and the flow rate of carbon from the fuel, we can write:

$$G_{H_2O}^{feed} = S/C \cdot x \cdot G^{fuel} \quad (4)$$

According to the definition of the recycle ratio

$$RR = \frac{G_{CO_2}^{rec}}{G_{CO_2}^{out,FC}} \quad (5)$$

we also have

$$G_{CO_2}^{rec} = RR \cdot G_{CO_2}^{out,FC} \quad (6)$$

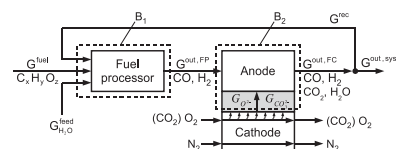
$$G_{H_2O}^{rec} = RR \cdot G_{H_2O}^{out,FC} \quad (7)$$

Inserting Eqs. (4), (6) and (7) into Eq. (3), the following relation is obtained:

$$(x - z) \cdot G^{fuel} = S/C \cdot x \cdot G^{fuel} + RR \cdot (G_{CO_2}^{out,FC} + G_{H_2O}^{out,FC}) \quad (8)$$

The amounts of carbon dioxide and steam leaving the fuel cell ($G_{CO_2}^{out,FC}$, $G_{H_2O}^{out,FC}$) depend on the fuel utilization applied at the cell. Fuel utilization, η_{fuel} , is defined as the ratio of the given electric current and the stoichiometrically possible current:

$$\eta_{fuel} = \frac{I}{I_{max}} \quad (9)$$

**Fig. 2 – Simplified HT-plant scheme for stoichiometric calculations.**

The electric currents need to be calculated differently for SOFC and MCFC systems due to different types of anions being transferred through the electrolyte, thus the further derivation is done separately for each type of fuel cell.

2.1.1. SOFC system

In an SOFC, the electric current is connected to the flux of oxygen anions (O^{2-}):

$$\eta_{fuel} = \frac{I}{I_{max}} = \frac{G_{O^{2-}}}{G_{O^{2-}}^{max}} \quad (10)$$

The maximum possible anion flow rate depends on the fuel composition. Two oxygen ions are required to completely oxidize a carbon atom and one oxygen ion can oxidize two hydrogen atoms. Each oxygen atom that is present in the fuel reduces the maximum rate of anion flux:

$$G_{O^{2-}}^{max} = (2x + 1/2 y - z) \cdot G^{fuel} \quad (11)$$

Oxygen ions are completely used up to oxidize carbon monoxide or hydrogen according to the following two electrochemical reactions:



According to the assumption of stoichiometric operation in the fuel converter, only carbon monoxide and hydrogen are fed to the SOFC. The combined molar mass balance of carbon and oxygen at the fuel cell anode (Fig. 2, boundary B_2) yields:

$$G_{O^{2-}} = G_{H_2O}^{out,FC} + G_{CO_2}^{out,FC} \quad (14)$$

Inserting Eqs. (10), (11) and (14) into Eq. (8) yields, after a few simple manipulations, the following equation for the stoichiometric recycle ratio:

$$RR^{SOFC} = \frac{x - z - x \cdot S/C}{\eta_{fuel} \cdot (2x + 1/2 y - z)} \quad (15)$$

Finally, introducing the ratios $y/x = Y$ and $z/x = Z$ (see Table 2), we can also write:

$$RR^{SOFC} = \frac{1 - Z - S/C}{\eta_{fuel} \cdot (2 + 1/2 Y - Z)} \quad (16)$$

2.1.2. MCFC system

In an MCFC, the electric current is connected to a flux of carbonate anions (CO_3^{2-}), thus

$$\eta_{fuel} = \frac{I}{I_{max}} = \frac{G_{CO_3^{2-}}}{G_{CO_3^{2-}}^{max}} \quad (17)$$

where

$$G_{CO_3^{2-}}^{max} = (2x + 1/2 y - z) \cdot G^{fuel} \quad (18)$$

Carbonate ions are consumed in the following two reactions:



With zero feed of carbon dioxide and steam, the combined molar mass balance of carbon and oxygen at the fuel cell reads:

$$2 \cdot G_{\text{CO}_2} = G_{\text{H}_2\text{O}}^{\text{out,FC}} + G_{\text{CO}_2}^{\text{out,FC}} \quad (21)$$

Inserting Eqs. (17), (18) and (21) into Eq. (8) yields

$$\text{RR}_{\text{stol}}^{\text{MCFC}} = \frac{x - z - x \cdot S/C}{2 \cdot \eta_{\text{fuel}} \cdot (2x + 1/2 y - z)} \quad (22)$$

which may also be re-written as:

$$\text{RR}_{\text{stol}}^{\text{MCFC}} = \frac{1 - Z - S/C}{2 \cdot \eta_{\text{fuel}} \cdot (Z + 1/2 Y - Z)} \quad (23)$$

This is exactly half the recycle ratio of the SOFC (Eq. (16)). As can be seen from the derivation, this is entirely due to the different type of ions involved in the electrochemical reactions. The carbonate ion contributes one of its oxygen atoms to the oxidation of carbon monoxide or hydrogen and adds another molecule of carbon dioxide to the anode gas. Thus, the MCFC anode exhaust gas contains two times as much fully oxidized species compared to the SOFC system, which leads to lower recycle ratios. Nevertheless, it should be noted that Eqs. (16) and (23) are derived without consideration of heat integration and risk of carbon formation. From a stoichiometric point of view, the MCFC system is therefore more advantageous than the SOFC system.

2.2. Detailed calculation

To take into account aspects such as carbon formation and heat integration, more detailed process unit models were applied.

2.2.1. Unit models

Five process unit models were developed to assemble complete high temperature plants (Fig. 1). These models must be able to compute each component's molar flow rate of product gas and the amount of heat needed or produced from the unit with its corresponding temperature. Thus, lumped steady state models have been derived based on balances of mass and energy.

Although these unit models were derived individually, several general assumptions apply to all of them.

- Isothermal condition.
- Ideal gas behavior.
- Heat loss to the environment is neglected.
- Minimum temperature difference in heat exchangers, $\Delta T_{\text{min}} = 10^\circ\text{C}$.
- Air components other than O_2 and N_2 are neglected.

Each of the unit models receives information about the molar flows of all chemical species entering this unit. The output of each model contains information about the molar outlet flows of each species, which is usually passed on to the subsequent unit. Energy balances yield the amount of heat required or released by each unit. The heat flux together with its corresponding temperature level is also passed on as a model output and is used to evaluate the heat integration of the system (see Section 2.2.2). In the following, some more details about the unit models are given.

2.2.1.1. Fuel processor. Two types of fuel processor are considered: the gasifier [11,12] and the reformer [9,13]. Both units typically work at 800°C , but the reformer is also able to operate at significantly lower temperatures. It is assumed that the primary fuel is converted to carbon monoxide, carbon dioxide, hydrogen, steam and methane. The outlet gas composition is in chemical equilibrium with respect to the water gas shift reaction (WGSR) and the steam methane reforming (SMR) at given temperature of the fuel processor. More details about the fuel processor model can be found in [11].

The product gas of the fuel processor may contain impurities which can poison the fuel cells and which have to be removed in a purification unit. The practical design of this purification sequence depends on the type and concentration of impurities that need to be removed. A very favorable option, especially in combination with high temperature fuel cells, is the application of units operating at similar temperatures as the fuel converter and the fuel cells [11]. Herrmann et al. proposed a moving bed reactor working at temperatures of about 700°C that may be applied here [14]. However, in order to keep the complexity of this study at a reasonable level, we consider the fuel purification unit implicitly in the fuel processor models, so the product gas is free from poisonous impurities.

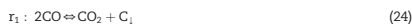
2.2.1.2. High temperature fuel cell. Two types of high temperature fuel cell are considered here: SOFC [15] and MCFC [16] (see Section 1). Both fuel cells have some similarities, e.g. they are insensitive to carbon monoxide, operate at ambient pressure and feature internal reforming. Thus, it is assumed in both units' models that the anode feed gas is completely reformed to H_2 before being converted electrochemically. Both cells operate at a cell voltage of 0.7 V and the current is determined via the fuel utilization, which is an input parameter. The anode outlet gas composition is in chemical equilibrium with respect to the WGSR. Besides the type of anion transferred through the electrolyte, the essential difference between SOFC and MCFC is their operating temperature. The SOFC typically works at 850°C , while the MCFC operates at 600°C . More detailed information about the SOFC model is provided in the Appendix.

2.2.1.3. Burner. The anode exhaust gas, which still has some heating value, is fed to a burner to generate some heat. The burner is assumed to operate at 900°C and all fuel components are completely oxidized to steam and carbon monoxide. Air is added according to an air number of 2.5.

2.2.2. Constraints

In the detailed simulation, a feasible operating point is required to fulfill two constraints: carbonization should be avoided and the system should be fully heat integrated.

2.2.2.1. Carbonization. The deposition of solid carbon in any of the units must be avoided. It can occur in a high temperature unit if the gas mixture contains a large fraction of carbon monoxide. Since almost all streams in the considered plants carry a certain amount of carbon monoxide, the risk of carbon formation has to be considered in each unit. Carbonization may take place according to the following reactions:



To determine whether carbonization tends to occur or not, we use a thermodynamic criterion: as long as the equilibrium of at least one carbonization reaction favors the educts and not the formation of solid carbon, there exists a mechanism of carbon removal and thus a carbon-free process is feasible. In mathematical form, this can be expressed as:

$$\Delta_r g_1 > 0 \quad \vee \quad \Delta_r g_2 > 0 \quad (26)$$

where

$$\Delta_r g_1 = \Delta_r g_1^\circ(T) + R \cdot T \cdot \ln \left\{ \frac{x_{\text{CO}_2} p^\circ}{x_{\text{CO}}^2 p} \right\} \quad (27)$$

and

$$\Delta_r g_2 = \Delta_r g_2^\circ(T) + R \cdot T \cdot \ln \left\{ \frac{x_{\text{H}_2\text{O}} p^\circ}{x_{\text{H}_2} x_{\text{CO}} p} \right\} \quad (28)$$

2.2.2.2. Heat integration. Each system produces or requires heat at different temperature levels. This information is provided by the output variables of each unit (heat flux and corresponding temperature). All of these heat fluxes are integrated in composite curves and a pinch analysis is applied to determine whether the system requires additional heat or provides heat as an energetic product. The details of the pinch analysis method used in this study can be found in Biegler et al. [17]. We demand that the process is thermally autonomous, meaning that all heat necessities can be satisfied by hot streams within the process. In other words, this constraint is fulfilled if the result of the pinch analysis shows that the system requires no additional heat. In the discussed systems, heat is mainly generated by the fuel cell and the burner. Since only steam feed is considered (as mentioned in the beginning of this chapter), the most important heat sink is the fuel processor due to its strong endothermic reaction.

3. Results and discussion

In this chapter, the results of the stoichiometric calculation and detailed simulation for the SOFC system are presented first with a methane-fed SOFC system as an example. Then, the outcomes from different primary fuels in the SOFC plant are summarized and the influence of fuel composition to the recycle ratio required is discussed. Nevertheless, some selected results for the MCFC system as well as some variations of working parameters are shown and explained.

3.1. Solid oxide fuel cell (SOFC) systems

3.1.1. Stoichiometric calculation

We apply Eq. (16) to an SOFC system with methane as the primary feed (Fig. 3a). It comprises a reforming reactor as fuel processor, the SOFC and the burner. This system corresponds to a typical SOFC plant operated with natural gas.

The gray plane in Fig. 3b indicates the recycle ratio required by the system for stoichiometric operation. In general, the

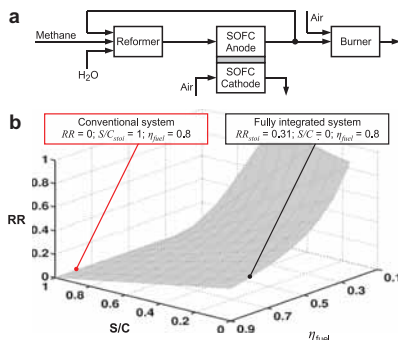


Fig. 3 – SOFC system fueled with methane. (a) Process structure. (b) Stoichiometric RR_{stoi} as function of fuel utilization (η_{fuel}) and steam-to-carbon (S/C) ratio.

amount of carbon dioxide and steam produced in the anode depends linearly on fuel utilization (η_{fuel}). At higher values of fuel utilization, more carbon dioxide and steam are available in the anode exhaust gas, thus a lower recycle ratio can be applied. To make the comparison of different systems easier, two characteristic operating points are defined (see Fig. 3b). The first characteristic operating point represents a conventional system without any recycle stream ($RR=0$), where the reforming agent is supplied via steam feed. The second operating point is where the system operates fully integrated with a recycle stream and the steam feed is not used ($S/C=0$). For both points, a fuel utilization of 80% is assumed, which is a typical value for SOFCs. In case this fuel utilization is infeasible, the highest possible fuel utilization is chosen for the characteristic operating point.

According to the first operating point, the conventional system requires a steam-to-carbon ratio of $S/C=1$, which is an obvious result for methane as fuel. At the second point, the steam feed can be substituted completely by the anode recycle stream with a relatively low recycle ratio of $RR=0.31$. If the fuel cell is operated fully integrated at a lower fuel utilization, for example in order to produce more heat in favor of electrical energy, the stoichiometric recycle ratio increases quickly. At $\eta_{\text{fuel}}=25\%$, the recycle ratio reaches its upper limit, $RR_{\text{stoi}}=1$, which is a practically infeasible operating point. At fuel utilization equal or less than this value, the oxygen flux through the electrolyte of the fuel cell is not sufficient to convert methane into reformat gas. Thus, if lower fuel utilization is desired, an additional feed of steam is necessary.

The explicit equation for RR_{stoi} derived in Section 2.1 is very helpful to estimate the recycle ratio required to integrate an SOFC plant as function of three parameters: fuel utilization (η_{fuel}), steam-to-carbon ratio (S/C) and fuel composition. For a system like the one shown in Fig. 3, complete mass integration is feasible at relatively low recycle ratios, as long as fuel utilization in the fuel cell is high. However, this

stoichiometric model does not consider any risk of carbon formation or the feasibility of thermal integration.

3.1.2. Nonstoichiometric calculations

In the following, more detailed unit models are used to identify the minimal recycle ratio required for mass integration of SOFC plants, considering the carbonization and heat integration constraints. Simulations are conducted for all five primary fuels listed in Table 2. However, since the results of all SOFC plants behave similar, only the outcomes from the methane feed system are shown and discussed in details.

3.1.2.1. SOFC system fueled with methane. This system is analogous to the system discussed in the previous section. The dark gray/colored plane in Fig. 4b represents the minimal recycle ratio that satisfies the carbonization constraint as a function of fuel utilization and steam-to-carbon ratio. This recycle ratio is only slightly higher than the stoichiometric recycle ratio (the gray plane). For instance, at 80% fuel utilization, the fully integrated system demands a recycle ratio of 0.31 for stoichiometric operation, and $RR = 0.34$ to avoid carbon deposition. This small increase of the recycle ratio raises the steam and carbon dioxide content of the reformer product gas sufficiently in order to suppress carbon deposition.

This outcome agrees well with the findings of Yi et al. [10], who calculated a minimal recycle ratio of 0.4 for a similar SOFC system (fully integrated system, 82% fuel utilization, 750 °C reformer temperature). Their system requires a slightly higher recycle ratio due to the lower reformer temperature. Applying the same conditions to our model yields a minimal recycle ratio of $RR = 0.36$, which corresponds well to their results. Because carbonization is easily suppressed due to the high operating temperatures, the second characteristic operating point ($RR = 0$, $\eta_{\text{fuel}} = 0.8$) applies a steam-to-carbon ratio of $S/C = 1.05$, which is only slightly higher than at stoichiometric operation.

The overall shape of the profiles obtained from the stoichiometric and the detailed simulation are very similar. Like

the stoichiometric model, the detailed calculation also shows an infeasible region of operation at low fuel utilization. Fuel reforming with steam or carbon dioxide is a highly endothermic process. The heat required by this process is covered by the heat generated by the SOFC and the burner. At higher fuel utilization, a larger fraction of the fuel's heating value is converted into electrical energy in the SOFC. Consequently, less heat is generated in the SOFC and the burner. The vertical transparent surface in Fig. 4b indicates the maximum fuel utilization which can be applied in the methane-fed SOFC system, so that it operates autothermally, i.e. no external heat input is needed. Operating at fuel utilization beyond this boundary ($\eta_{\text{fuel}} > 85\%$) means that external heat input is required, hence the process is considered infeasible.

To summarize, the mass integration of this high temperature fuel cell system can be accomplished with relatively small recycle flows. The heat integration constraint limits the fuel utilization to values below 85%, which is acceptable. At reduced fuel utilization, the required recycle ratio increases, so additional steam feed may be preferable at such operating conditions.

3.1.3. Summary of the evaluated SOFC systems

The results from the characteristic operating points of both the stoichiometric and the detailed computations of different SOFC systems are summarized in a Van Krevelen diagram (Fig. 5). It shows that the recycle ratio required to suppress carbon deposition is only slightly higher than the value that is obtained from the stoichiometric calculation. The difference is small basically due to the high operating temperature of the fuel processor unit and the SOFC. It is much easier to suppress carbonization thermodynamically at elevated temperature, hence a small increase of the recycle ratio or steam feed from the stoichiometric demand is sufficient to avoid carbon formation. This fact makes Eq. (16) suitable as a shortcut formula to estimate the minimal recycle ratio as well as the minimal steam-to-carbon ratio in SOFC systems.

It can be seen also from Fig. 5 that the minimal recycle ratios of SOFC system fueled with methanol (CH_3OH) are very small. This comes from the fact that the oxygen-to-carbon ratio of methanol already equals unity, meaning that,

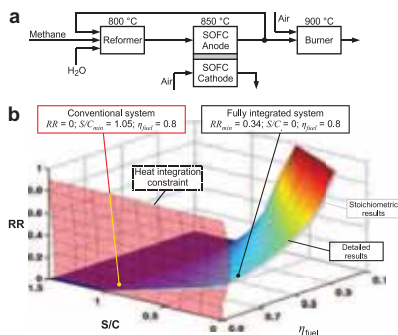


Fig. 4 – SOFC system fueled with methane. (a) Process structure. (b) RR_{\min} as function of fuel utilization (η_{fuel}) and steam-to-carbon (S/C) ratio.

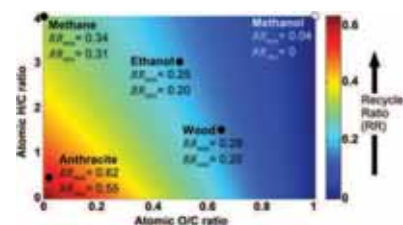


Fig. 5 – Van Krevelen diagram for various fuels with their feasible operating conditions in the SOFC plant. The color indicates the stoichiometric recycle ratio at $\eta_{\text{fuel}} = 80\%$ and $S/C = 0$. (For interpretation of the references to colour in this figure legend, the reader is referred to the web version of this article).

stoichiometrically, methanol can decompose into gaseous compounds without any addition of a reforming agent:



Thus, from a stoichiometric point of view, there is no oxygen demand for the reforming of methanol ($\text{RR}_{\text{stoi}} = 0$), but a certain amount of steam and/or carbon dioxide is still required to prevent carbon deposition. This leads to a minimal recycle ratio of 0.05 for the fully integrated system.

The minimal recycle ratio decreases with increasing oxygen and hydrogen content of the fuel. A high oxygen content of the fuel reduces the demand for additional oxygen in the primary fuel conversion process. A large fraction of fuel-bound hydrogen leads to a large amount of steam in the anode exhaust gas, which in turn means that a lower recycle ratio is required to satisfy the oxygen demand in the fuel converter. This is also indicated by Eq. (16); assuming full integration ($\text{S/C} = 0$) and a fixed fuel utilization (e.g. $\eta_{\text{fuel}} = 0.8$), one can see that the increase of both fuel composition parameters, oxygen and hydrogen content, decreases the stoichiometric recycle ratio. These results are represented by different darkness/colors in Fig. 5.

It should be noted that these results are very sensitive with respect to operating temperatures. A decrease in the gasifier or SOFC temperature by 50 °C increases the required recycle ratio by about 3% due to the shifted equilibrium of the carbonization reactions. These results are also only valid if a high temperature purification unit is applied. Using a purification unit operating at a significantly lower temperature not only increases the risk of carbon deposition, but it also causes a loss of exergy which penalizes the system heat integration [11].

According to these results, the anodic recirculation might be a potential replacement for the conventional steam feed in SOFC plants. Except for the coal feed system, recycle ratios are lower than $\text{RR} = 0.34$, which may be considered acceptable. Whether or not mass integration is really favorable in a specific system strongly depends on design details such as the additional power demand due to increased gas flow rates, and the cost of a water desalinization and evaporation system. Thus, the question whether this process option should be applied or not can only be answered individually for each system.

3.2. Molten carbonate fuel cell (MCFC) systems

The second type of high temperature fuel cell considered in this work is the MCFC. Similar to the SOFC system, the calculation of the minimal recycle ratio is differentiated into stoichiometric and detailed simulations. Only the results for the MCFC systems fed with methane and wood are presented here.

3.2.1. Stoichiometric calculation

In an MCFC, carbonate anions are transferred from the cathode to the anode. This makes the minimal recycle ratio for MCFC system only half as large as the minimal recycle ratio for an SOFC system (see Section 2.1). As an example, for stoichiometric operation of an MCFC system fed with methane at a fuel utilization of 80%, a recycle ratio of only $\text{RR} = 0.16$ is required, whereas a recycle ratio of $\text{RR} = 0.31$ is required for the equivalent SOFC system (Fig. 4b).

3.2.2. Nonstoichiometric calculations

Caused by different kinds of anions migrating through the electrolyte, the MCFC has a significantly lower operating temperature ($T = 600^\circ\text{C}$) than the SOFC. Lower temperatures favor the products of the carbonization reactions (Eqs. (24) and (25)). Thus, one can expect that a higher amount of steam feed or recycle ratio is necessary to suppress carbon deposition.

The low operating temperature of the MCFC also affects the heat integration. The main heat sources of the plant are the fuel cell and the burner, while the main heat sink is the fuel conversion unit. If the fuel processor temperature is higher than the fuel cell temperature, only the heat released from the burner can be used to cover the heat demand. Hence, a certain amount of fuel has to be available for the burner which limits the fuel utilization in the fuel cell. In practice, the burner of an MCFC is often integrated with the fuel cells in a common housing, so the burner temperature is similar to the cell temperature (see Hot Module concept by MTU Onsite Energy [18]). In order to operate the burner at a significantly higher temperature than the fuel cell, it must be placed separately from the fuel cells.

3.2.2.1. MCFC system fueled with methane. Fig. 6a depicts the flow sheet of an MCFC process with methane as fuel. The process design is similar to the SOFC system (Fig. 4a). In a typical MCFC plant, the reforming unit is heated by the off-gases from the fuel cell, so we assume a reformer temperature that is lower than the fuel cell temperature. Another difference between this system and the SOFC system is that the exhaust gas of the burner is fed to the cathode channel, which is a special feature of MCFC technology, but it has no influence on the determination of anode recycle ratio. Air is added to the burner according to an air number of 2.5.

Fig. 6b shows that the non-integrated MCFC requires a steam-to-carbon ratio of $\text{S/C} = 2$ in order to suppress carbon deposition. This is a typical value for MCFC operation. However, the integrated system requires a recycle ratio of $\text{RR} = 0.86$, which increases the anodic gas flow rate by a factor of 7. This high recycle ratio is necessary in order to avoid

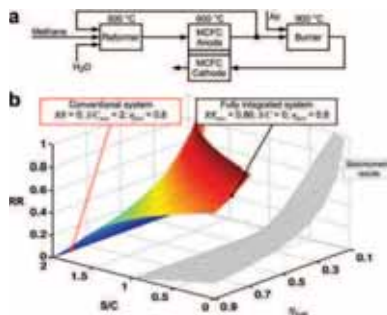


Fig. 6 – MCFC system fueled with methane. (a) Process structure. (b) RR_{min} as function of fuel utilization (η_{fuel}) and steam-to-carbon (S/C) ratio.

carbon deposition in the low temperature reforming unit. Moreover, the infeasible operating area is large, e.g. for a fully integrated system, the fuel utilization cannot be decreased below 70%, otherwise additional steam is required. All these facts clearly indicate that mass integration is not an attractive option in such a system.

The profile obtained from the stoichiometric calculation and the result from the detailed simulation strongly deviate. Contrary to the SOFC systems, the stoichiometric calculation does not yield a reliable approximation for the required recycle ratio.

3.2.2.2. MCFC system fueled with wood. The results for an MCFC plant based on wood are shown in Fig. 7. Because the gasifier works at temperature higher than the MCFC temperature, the heat from the fuel cell cannot be used to compensate the heat demands in the gasifier, and heat integration becomes a limiting constraint for fuel utilization. This leads to an upper bound of the fuel utilization of 77% for the fully integrated system. In order to suppress carbon deposition in the fuel cell at this operating point, a high recycle ratio of $RR = 0.7$ is needed. The integrated system becomes infeasible at fuel utilizations lower than 50% because of the carbonization constraint in the fuel cell. Obviously, this is not an attractive option, either.

The non-integrated system is constrained to fuel utilizations less than 65% due to the heat integration constraint, but it works at a moderate steam-to-carbon ratio of $S/C = 2.2$.

3.2.3. Parameter sensitivity analysis in the MCFC plant

As shown in the previous chapter, the limitations in the MCFC systems are strongly connected to the temperatures of the fuel processor and the fuel cell. In order to evaluate the sensitivity of the limitations with respect to these temperatures, we simulate a hypothetical MCFC system based on wood with a decreased gasifier temperature and an increased MCFC temperature (see Fig. 8a).

We assume an MCFC operating temperature of 700 °C and a slightly lower gasifier temperature of 650 °C. This shifts the heat integration constraint far enough so that the fully integrated system can be operated at 80% fuel utilization (Fig. 8b). This operating point requires a recycle ratio of $RR = 0.41$. The open system may reach 76% fuel utilization and operates at $S/C = 0.9$. This situation is roughly comparable with the SOFC plant fueled with methane.

Obviously, the two measures proposed here are not easily realized. Typical gasifier temperatures are between 700 °C and 1000 °C [19]. A gasifier operating at 650 °C is likely to produce significant amounts of tar, especially if wood is used as fuel. An MCFC usually works at temperatures between 600 °C to 650 °C, at which degradation rates are still tolerable [18]. In order to achieve long system life time at 700 °C, different materials would be needed for the electrode and probably even the electrolyte materials in this fuel cell. Thus, such a high temperature MCFC would be significantly different from today's MCFCs.

These results show that, only with strong changes in the temperature levels, the mass integration concept in MCFC systems is attractive.

3.2.4. Summary of MCFC systems

Although from the stoichiometric point of view, mass integration seems to be more attractive for MCFC than for SOFC systems, the MCFC requires significantly higher recycle ratios in order to suppress carbon deposition. In addition, the heat integration is a severely limiting constraint in many MCFC systems. This leads to small windows of feasible operating conditions for fully integrated systems. Only if the temperature levels of the gasifier and the fuel cell are significantly changed, the integrated MCFC system can be operated at acceptable recycle ratios.

The results obtained from the stoichiometric and the detailed calculations strongly deviate for all considered MCFC system configurations. The first reason is that the basic

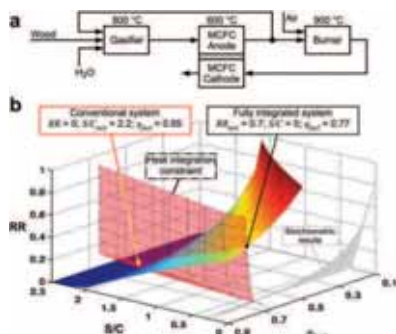


Fig. 7 – MCFC system fueled with wood. (a) Process structure. (b) RR_{\min} as function of fuel utilization (η_{fuel}) and steam-to-carbon (S/C) ratio.

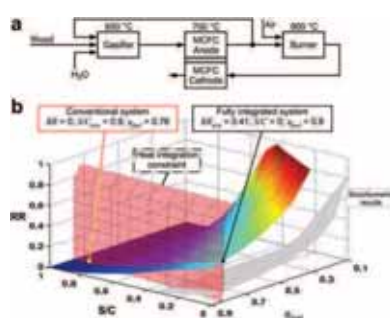


Fig. 8 – MCFC plant with high temperature MCFC and low temperature gasifier fueled with wood. (a) Process structure. (b) RR_{\min} as function of fuel utilization (η_{fuel}) and steam-to-carbon (S/C) ratio.

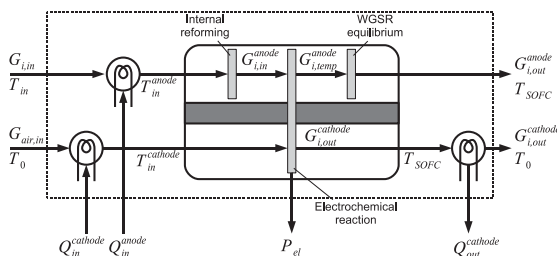


Fig. 9 – Mass and heat flow scheme of the SOFC model.

assumption of the stoichiometric model, which postulates that the fuel processor produces only carbon monoxide and hydrogen, is only fulfilled in MCFC systems if the fuel processor operates at high temperature. The second reason is that due to the low fuel cell temperature, a feed gas mixture of carbon monoxide and hydrogen is far inside the carbonization region, and a strong increase in steam feed or recycle ratio compared to the stoichiometric result is required to avoid carbon formation. This means also that Eq. (23) is not appropriate as a shortcut model for the MCFC system.

4. Conclusions

The mass integration concept has been evaluated on two types of high temperature fuel cell plants. In the SOFC plants, apart from the coal feed system, the recirculation of oxygen-rich anode exhaust gas is an attractive option to replace the steam or air feed as reforming agent, leading to a significant simplification of the system design. The fully integrated system works at acceptable levels of recycle ratio depending on the type of fuel used (see Fig. 5) in which two important constraints, namely carbon formation and system wide heat integration, are already considered.

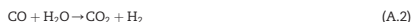
Although the stoichiometric calculations indicate that this process option is more attractive for the MCFC than the SOFC, the results from the detailed simulations show reversely. Unless drastic measures are applied, the fully mass-integrated MCFC systems are hardly feasible.

Eq. (16) can be used as a shortcut tool for the SOFC systems since the results from the stoichiometric approach are in a good agreement with the outcomes from the detailed calculations. It is very practical because it can predict not only the lower bound of recycle ratio required, but also the minimal steam-to-carbon ratio for the conventional plant.

Appendix. SOFC model

The SOFC is one of the two types of high temperature fuel cells considered in this study. Its model is illustrated in Fig. 9. Several assumptions are applied in this model.

1. The SOFC operates at 850 °C.
2. The anode inlet temperature, T_{in}^{anode} , is 820 °C. The fuel gas is heated and brought to this temperature using the heat flux Q_{in}^{anode} .
3. In the anode channel, the SMR (Eq. (A.1)) and the WGSR (Eq. (A.2)) occur:



Because these reactions typically attain virtually complete conversion in the anode channel, we assume complete reforming conversion at the inlet of the anode channel.

4. The product of the reforming process is converted electrochemically at the anode according to



5. Because only very small amounts of methane are expected at the anode outlet, the anode exhaust gas is assumed to be in chemical equilibrium with respect only to the WGSR.
6. The air feed to the cathode is adjusted so that the system is kept at its operating temperature of 850 °C (see assumption 1). This flow rate is usually sufficiently high to provide the required oxygen for the cathode reaction.
7. The air feed temperature, $T_{in}^{cathode}$, is 650 °C. The air is heated up from ambient temperature to this temperature level using the heat flux $Q_{in}^{cathode}$ before being fed into the cathode channel. The exhaust air is cooled down to ambient temperature, providing the heat flux $Q_{out}^{cathode}$.
8. At the cathode, oxygen is reduced according to



9. The fuel cell is designed sufficiently large so that a given fuel utilization, η_{fuel} , can always be achieved with a cell voltage, U_{cell} , of 0.7 V, as long as the Nernst voltage of the fuel gas and air is above this value.

10. Six gas components are considered: CH_4 , H_2 , CO , H_2O , CO_2 and N_2 (inert).

These assumptions lead to the following model equations.

Anode channel

At the anode inlet (molar flow rates $G_{i,\text{in}}$), the fuel gas is completely reformed. The resulting component's flow rates, $G_{i,\text{in}}^{\text{anode}}$, are calculated as follows:

$$G_{i,\text{in}}^{\text{anode}} = 0 \quad \forall i \in \{\text{CO}, \text{CH}_4\} \quad (\text{A.5})$$

$$G_{\text{CO}_2,\text{in}}^{\text{anode}} = G_{\text{CO}_2,\text{in}} + G_{\text{CO},\text{in}} + G_{\text{CH}_4,\text{in}} \quad (\text{A.6})$$

$$G_{\text{H}_2,\text{in}}^{\text{anode}} = G_{\text{H}_2,\text{in}} + G_{\text{CO},\text{in}} + 4 \cdot G_{\text{CH}_4,\text{in}} \quad (\text{A.7})$$

$$G_{\text{H}_2\text{O},\text{in}}^{\text{anode}} = G_{\text{H}_2\text{O},\text{in}} - G_{\text{CO},\text{in}} - 2 \cdot G_{\text{CH}_4,\text{in}} \quad (\text{A.8})$$

$$G_{\text{N}_2,\text{in}}^{\text{anode}} = G_{\text{N}_2,\text{in}} \quad (\text{A.9})$$

The conversion of the electrochemical process is characterized by the fuel utilization. The system wide fuel utilization is the ratio between the electrical cell current and the stoichiometrically possible current from the fuel that is fed into the system:

$$\eta_{\text{fuel}} = \frac{I}{2F \cdot (2x + 1/2 y - z) \cdot G_{\text{fuel}}} \quad (\text{A.10})$$

This is an input parameter of the system, and it can be found on one of the horizontal axes in Figs. 3 and 4 and 6–8. For practical calculations, we define the single pass utilization as the ratio of the electrical current and the stoichiometrically possible current from the completely reformed inlet gas flux:

$$\eta_{\text{fuel}}^{\text{sp}} = \frac{I}{2F \cdot G_{\text{H}_2,\text{in}}^{\text{anode}}} \quad (\text{A.11})$$

Combining both equations yields

$$\eta_{\text{fuel}}^{\text{sp}} = \eta_{\text{fuel}} \cdot \frac{(2x + 1/2 y - z) \cdot G_{\text{fuel}}}{G_{\text{H}_2,\text{in}}^{\text{anode}}} \quad (\text{A.12})$$

With the definition above, the component fluxes after the electrochemical reactions can be calculated:

$$G_{\text{H}_2,\text{temp}}^{\text{anode}} = \left(1 - \eta_{\text{fuel}}^{\text{sp}}\right) \cdot G_{\text{H}_2,\text{in}}^{\text{anode}} \quad (\text{A.13})$$

$$G_{\text{H}_2\text{O},\text{temp}}^{\text{anode}} = G_{\text{H}_2\text{O},\text{in}}^{\text{anode}} + \eta_{\text{fuel}}^{\text{sp}} \cdot G_{\text{H}_2,\text{in}}^{\text{anode}} \quad (\text{A.14})$$

$$G_{i,\text{temp}}^{\text{anode}} = G_{i,\text{in}}^{\text{anode}} \quad \forall i \in \{\text{CO}, \text{CO}_2, \text{CH}_4, \text{N}_2\} \quad (\text{A.15})$$

as well as the electrical power output:

$$P_{\text{el}} = \eta \cdot F \cdot U_{\text{cell}} \cdot \eta_{\text{fuel}}^{\text{sp}} \cdot G_{\text{H}_2,\text{in}}^{\text{anode}} \quad (\text{A.16})$$

These fluxes, $G_{i,\text{temp}}^{\text{anode}}$, are used as the initial values for the exhaust gas which is in equilibrium with respect to the WGSR. Since only four components, i.e. CO, CO₂, H₂ and H₂O, are involved in this reaction, the outlet molar flows of CH₄ and N₂ are equal to the results from the electrochemical calculations.

$$G_{i,\text{out}}^{\text{anode}} = G_{i,\text{temp}}^{\text{anode}} \quad \forall i \in \{\text{CH}_4, \text{N}_2\} \quad (\text{A.17})$$

The law of mass action of the WGSR must be fulfilled at the anode exhaust:

$$\exp\left(\frac{-\Delta_r G_{\text{WGSR}}}{R \cdot T_{\text{SOFC}}}\right) = \frac{G_{\text{CO}_2,\text{out}}^{\text{anode}} \cdot G_{\text{H}_2,\text{out}}^{\text{anode}}}{G_{\text{CO},\text{out}}^{\text{anode}} \cdot G_{\text{H}_2\text{O},\text{out}}^{\text{anode}}} \quad (\text{A.18})$$

where $\Delta_r G_{\text{WGSR}}(T_{\text{SOFC}})$ is the Gibbs enthalpy of this reaction.

In addition, three atom balances have to be satisfied:

$$\text{C-balance: } G_{\text{CO}_2,\text{out}}^{\text{anode}} + G_{\text{CO}_2,\text{out}}^{\text{anode}} = G_{\text{CO}_2,\text{temp}}^{\text{anode}} + G_{\text{CO}_2,\text{temp}}^{\text{anode}} \quad (\text{A.19})$$

$$\text{H-balance: } G_{\text{H}_2,\text{out}}^{\text{anode}} + G_{\text{H}_2\text{O},\text{out}}^{\text{anode}} = G_{\text{H}_2,\text{temp}}^{\text{anode}} + G_{\text{H}_2\text{O},\text{temp}}^{\text{anode}} \quad (\text{A.20})$$

$$\begin{aligned} \text{O-balance: } G_{\text{CO}_2,\text{out}}^{\text{anode}} + G_{\text{CO}_2,\text{out}}^{\text{anode}} + G_{\text{H}_2\text{O},\text{out}}^{\text{anode}} \\ = G_{\text{CO}_2,\text{temp}}^{\text{anode}} + G_{\text{CO}_2,\text{temp}}^{\text{anode}} + G_{\text{H}_2\text{O},\text{temp}}^{\text{anode}} \end{aligned} \quad (\text{A.21})$$

Solving these four equations (Eqs. (A.18)–(A.21)) gives the molar flow rates of CO, CO₂, H₂, H₂O at the anode outlet.

Cathode channel

The air flow rate in an SOFC is typically used to adjust the fuel cell temperature. It is determined via the enthalpy balance around the fuel cell, which reads

$$H_{\text{in}}^{\text{anode}} + H_{\text{in}}^{\text{cathode}} - P_{\text{el}} - H_{\text{out}}^{\text{anode}} - H_{\text{out}}^{\text{cathode}} = 0 \quad (\text{A.22})$$

where

$$H_{\text{in}}^{\text{anode}} = \sum_i G_{i,\text{in}}^{\text{anode}} \cdot \Delta_r h_i^f(T_{\text{in}}^{\text{anode}}) \quad (\text{A.23})$$

$$H_{\text{out}}^{\text{anode}} = \sum_i G_{i,\text{out}}^{\text{anode}} \cdot \Delta_r h_i^f(T_{\text{SOFC}}) \quad (\text{A.24})$$

$$\begin{aligned} H_{\text{in}}^{\text{cathode}} = & G_{\text{air},\text{in}} \cdot (x_{\text{O}_2,\text{air}} \cdot \Delta_r h_{\text{O}_2}^f(T_{\text{in}}^{\text{cathode}}) \\ & + (1 - x_{\text{O}_2,\text{air}}) \cdot \Delta_r h_{\text{N}_2}^f(T_{\text{in}}^{\text{cathode}})) \end{aligned} \quad (\text{A.25})$$

$$\begin{aligned} H_{\text{out}}^{\text{cathode}} = & \left(G_{\text{air},\text{in}} \cdot x_{\text{O}_2,\text{air}} - \frac{1}{2} \cdot \eta_{\text{fuel}}^{\text{sp}} \cdot G_{\text{H}_2,\text{in}}^{\text{anode}}\right) \cdot \Delta_r h_{\text{O}_2}^f(T_{\text{SOFC}}) \\ & + G_{\text{air},\text{in}} \cdot (1 - x_{\text{O}_2,\text{air}}) \cdot \Delta_r h_{\text{N}_2}^f(T_{\text{SOFC}}) \end{aligned} \quad (\text{A.26})$$

From this enthalpy balance, together with the given inlet temperatures and the given fuel cell temperature, the air flow rate at the cathode channel, $G_{\text{air},\text{in}}$, is determined.

The outlet flow rates from the cathode channel can then be obtained as:

$$G_{\text{O}_2,\text{out}}^{\text{cathode}} = G_{\text{air},\text{in}} \cdot x_{\text{O}_2,\text{air}} - \frac{1}{2} \cdot \eta_{\text{fuel}}^{\text{sp}} \cdot G_{\text{H}_2,\text{in}}^{\text{anode}} \quad (\text{A.27})$$

$$G_{\text{N}_2,\text{out}}^{\text{cathode}} = G_{\text{air},\text{in}} \cdot (1 - x_{\text{O}_2,\text{air}}) \quad (\text{A.28})$$

Heat exchangers

The heat fluxes entering and leaving the SOFC are output quantities of the model which are required for the pinch analysis. These heat fluxes describe the amount of heat needed to heat up the fuel gas at the anode and the air at the

cathode as well as the heat that is obtained from cooling down the cathode exhaust gas to ambient temperature:

$$Q_{in}^{anode} \bigg|_{T_{in}}^{T_{anode}} = \sum_i G_{i,in} \cdot (\Delta_r h_i^0(T_{in}^{anode}) - \Delta_r h_i^0(T_{in})) \quad (A.29)$$

$$Q_{in}^{cathode} \bigg|_{T_0}^{T_{cathode}} = \sum_i G_{i,air,in} \cdot (\Delta_r h_i^0(T_{in}^{cathode}) - \Delta_r h_i^0(T_0)) \quad (A.30)$$

$$Q_{out}^{cathode} \bigg|_{T_{sorc}}^{T_0} = \sum_i G_{i,out}^{cathode} \cdot (\Delta_r h_i^0(T_0) - \Delta_r h_i^0(T_{sorc})) \quad (A.31)$$

Nomenclature

Latin symbols

F	Faraday constant, C mol ⁻¹
G	total molar flow rate, mol s ⁻¹
G _i	molar flow rate of species i, mol s ⁻¹
H	enthalpy flux, MW
I	electric cell current, A
p; p ^o	pressure; standard pressure, N m ⁻²
P	electrical power produced, MW
Q	heat flux, MW
R	gas constant, J mol ⁻¹ K ⁻¹
RR	recycle ratio, 1
S/C	steam-to-carbon ratio, 1
T	temperature, K
U	cell voltage, V
x	fuel composition: amount of C per mole of fuel, 1
y	fuel composition: amount of H per mole of fuel, 1
Y	relative fuel composition: mole H per mole C, 1
z	fuel composition: amount of O per mole of fuel, 1
Z	relative fuel composition: mole O per mole C, 1

Greek symbols

$\Delta \cdot g_{WGR}^0(T)$	standard Gibbs enthalpy of WGR, J mol ⁻¹
$\Delta_r h_i^0(T)$	standard enthalpy of formation of component i, J mol ⁻¹
η_{fuel}^{fuel}	system wide fuel utilization, 1
η_{fuel}^{sp}	single pass fuel utilization, 1

Indices, upper

fuel	fuel flow into the fuel processor
MCFC	related to molten carbonate fuel cells
out,FC	outlet flow from the fuel cell
out,FP	outlet flow from the fuel processor
out,sys	exhaust flow leaving the system
rec	recycle flow
SOFC	related to solid oxide fuel cells

Indices, lower

max	highest possible value
min	lowest possible value
stoi	stoichiometric value

Acronyms

SMR	steam methane reforming
WGR	water gas shift reaction

REFERENCES

- [1] Colpan CO, Dincer I, Hamdullahpur F. Thermodynamic modeling of direct internal reforming solid oxide fuel cells operating with syngas. *Int J Hydrogen Energy* 2007;32:787–95.
- [2] Assabumrungrat S, Laosiripojana N, Pavarajarn V, Sangtongkitcharoen W, Tangitmatee A, Praserttham P. Thermodynamic analysis of carbon formation in a solid oxide fuel cell with a direct internal reformer fuelled by methanol. *J Power Sources* 2005;139:55–60.
- [3] Assabumrungrat S, Pavarajarn V, Charojrochkul S, Laosiripojana N. Thermodynamic analysis for a solid oxide fuel cell with direct internal reforming fueled by ethanol. *Chem Eng Sci* 2004;59:6015–20.
- [4] Douvartzides SL, Coutelieres FA, Demin AK, Tsiakaras PE. Fuel options for solid oxide fuel cells: a thermodynamic analysis. *AIChE J* 2003;49:248–57.
- [5] Sasaki K, Watanabe K, Teraoka Y. Direct-alcohol SOFCs: current–voltage characteristics and fuel gas compositions. *J Electrochem Soc* 2004;151:A965–70.
- [6] Steele BCH. Fuel-cell technology – running on natural gas. *Nature* 1999;400:619–21.
- [7] Fellows R. The effect of fuel cell operating conditions on DIR-MCFC system selection. *J Power Sources* 1996;61:213–8.
- [8] Fellows R. A novel configuration for direct internal reforming stacks. *J Power Sources* 1998;71:281–7.
- [9] Lisbona P, Corradetti A, Bove R, Lunghi P. Analysis of a solid oxide fuel cell system for combined heat and power applications under non-nominal conditions. *Electrochim Acta* 2007;53:1920–30.
- [10] Yi YF, Rao AD, Brouwer J, Samuelsen GS. Fuel flexibility study of an integrated 25 kW SOFC reformer system. *J Power Sources* 2005;144:67–76.
- [11] Heidebrecht P, Hartono B, Hertel K, Sundmacher GS. Biomass-based fuel cell power plants: evaluation of novel reactors and process designs. *Ind Eng Chem Res*; 2010.
- [12] He I, Schotte E, Thomas S, Schlinkert A, Herrmann A, Mosch V, et al. Wood gasification in a lab-scale bubbling fluidized bed: experiment and simulation. In: Fourth European combustion meeting, Vienna, Austria; 2009.
- [13] Song CS. Fuel processing for low-temperature and high-temperature fuel cells – challenges, and opportunities for sustainable development in the 21st century. *Catal Today* 2002;77:17–49.
- [14] Herrmann A, Thomas S, Schotte E. High temperature cleaning of fuel gas from biomass gasification. In: 14th International conference for renewable resources and plant biotechnology, Magdeburg, Germany; June 8–10, 2008.
- [15] Kuznecov M, Otschik P, Eichler K, Trofimenko N, Megel S. Development of planar SOFC stacks for CHP. In: Electrochemical society proceedings, Quebec City, Canada; 2005.
- [16] Heidebrecht P, Sundmacher K. Molten carbonate fuel cell (MCFC) with internal reforming: model-based analysis of cell dynamics. *Chem Eng Sci* 2003;58:1029–36.
- [17] Biegler LT, Grossmann IE, Westerberg AW. Systematic methods of chemical process design. Upper Saddle River, New Jersey: Prentice Hall; 1997.
- [18] Bischoff M. Molten carbonate fuel cells: a high temperature fuel cell on the edge to commercialization. *J Power Sources* 2006;160:842–5.
- [19] Bridgwater AV. The technical and economic feasibility of biomass gasification for power generation. *Fuel* 1995;74:631–53.
- [20] Kaltschmitt M, Hartmann H. *Energie aus Biomasse: Grundlagen, Techniken und Verfahren*. Berlin: Springer Verlag; 2001.
- [21] Perry RH, Green DW. *Perry's chemical engineer's handbook*. 8th ed. New York: McGraw-Hill; 2008.

[PH 9]

P. Heidebrecht, M. Pfafferoth, K. Sundmacher

Hierarchical Modeling Strategy for Structured Reactors

Chemical Engineering Science 66 (2011), 4389-4402.



Multiscale modelling strategy for structured catalytic reactors

Peter Heidebrecht^a, Matthias Pfafferoth^b, Kai Sundmacher^{a,b,*}

^a Max Planck Institute for Dynamics of Complex Technical Systems, Sandtorstrasse 1, 39106 Magdeburg, Germany

^b Otto von Guericke University, Process Systems Engineering, Universitätsplatz 2, 39106 Magdeburg, Germany

ARTICLE INFO

Article history:

Received 16 November 2010

Received in revised form

26 January 2011

Accepted 25 March 2011

Available online 31 March 2011

Keywords:

Model hierarchy

Structured packing

Reactor design

Model reduction

Multiscale

Mass transport limitation

ABSTRACT

Structured reactors, and especially arranged reactors, are multiscale systems, in which the design on the small scale essentially determines the macroscopic reactor behaviour. In the present contribution, we propose a modelling strategy for the design and optimisation of an arranged flat-bed reforming reactor. It consists of three model levels, each describing the structure of the reactor on a different scale and detail level. The elements of this hierarchy are consistent and compatible, which means that results obtained with one model can be transferred to the other models. The possible applications of this model hierarchy range from estimation of pressure drop coefficients up to the integration of the structured reactor into a process plant.

© 2011 Elsevier Ltd. All rights reserved.

1. Introduction

Structured reactors play a key role in the design of intensified multiphase processes in chemical engineering (Pangarkar et al., 2008). In contrast to classical fixed beds, which are random packings of catalytically active particles, structured reactors can be purposefully designed on all scales from the catalyst level up to the reactor level (Kreutzer et al., 2006). For, say, spherical non-porous catalyst particles, the structure of a fixed bed has only one design parameter, which is the size of the particles. It determines the size of the available catalyst surface and thereby the reaction rate and catalyst efficiency; small particles are preferred here. The particle size also determines the interparticle length, which has a strong impact on the total pressure drop of the reactor; large particles are preferred in order to keep the pressure loss low. Selecting the particle size therefore is a compromise between maximising the catalyst efficiency and minimising the pressure loss. Application of porous or non-spherical particles adds some degrees of freedom to the design, but it does not allow to design mass transport and reaction independently.

In a structured packing, the design of the structure introduces many new degrees of freedom for reactor design, allowing to decouple the hydrodynamic state (pressure drop), the reaction rate (catalyst efficiency) and the transport of heat and mass (reaction control) to a wide extent (Pangarkar et al., 2008). Thus, in a structured reactor these processes can be adjusted in order to

control the temperature and concentration profiles along the flow path, thereby improving selectivity and conversion, and avoiding local temperature peaks.

According to Cybulski and Moulijn, (2006), structured reactors can be categorised into monolithic reactors, membrane reactors and arranged reactors (see Fig. 1). Numerous contributions about the modelling and simulation of monolithic reactors have been published, including modelling of specific details and simulations of complete reactors (e.g. Chen et al., 2008; Tischer and Deutschmann, 2002). Also, a wide range of contributions on modelling of membrane reactors is available (e.g. Marcano and Tsotsis, 2002). With regard to arranged reactors, many contributions treat the modelling of gas–liquid systems in structured packings (see Pangarkar et al., 2008), which are widely applied, for example in reactive distillation. However, only a few publications treat arranged reactors for heterogeneously catalysed gas–phase reactions. von Scala et al. (1999) investigated flow paths in Katapak-M packings and estimated pressure drops from CFD simulations of the structure for single phase flow. Their model-based results correspond very well with experimental data. Petre et al. (2003) proposed a computational method for a priori estimation of the pressure drop in a structured packing by analysis of dissipation rates in recurrent structure elements. Calis et al. (2001) focussed on regular fixed bed channels with very low tube-to-particle-diameter ratio. They applied CFD simulations to predict pressure drop correlations, which showed reasonable agreement with experimental results. However, none of these contributions treats mass and heat transfer in arranged, parallel passage reactors, which is the focus of this work.

Like all structured reactors, arranged reactors are multiscale systems; the geometrical design of the structure determines the

* Corresponding author at: Max Planck Institute for Dynamics of Complex Technical Systems, Sandtorstrasse 1, 39106 Magdeburg, Germany.
E-mail address: sundmacher@mpi-magdeburg.mpg.de (K. Sundmacher).

processes of transport and reaction on this scale and has a strong impact on the behaviour of the complete reactor on a larger scale. Thus, the ability to describe the processes on a small scale and transfer this knowledge to the reactor scale is a prerequisite for a purposeful reactor design. While the simulation of the processes on the scale of the repeating structures can be done with established methods such as computational fluid dynamics (CFD), the same level of detail cannot be applied to the description of the whole reactor due to high computational costs. Instead, reduced reactor models are required, which reflect the essential behaviour on the small scale, but which are computationally cheap and thus applicable to the simulation of the complete reactor.

In this contribution, we propose a multiscale hierarchy of three model levels for the design and analysis of structured reactors (Fig. 2). Each model describes the reactor or a part of it on a different level of detail and is tailored for specific tasks:

- The *detailed model* describes one or several repeating sections of the structure in all geometric details. It is not only

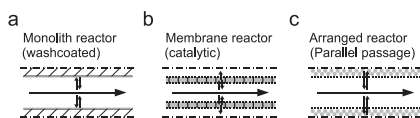


Fig. 1. Classes of structured reactors according to Cybulski and Moulijn (2006).

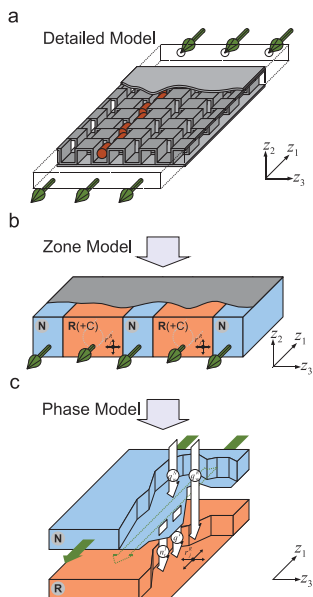


Fig. 2. Proposed model hierarchy for structured reactors. N, R: non-reactive and reactive zone or phase; C: catalyst phase, n_i , q_i : molar fluxes and heat flux, respectively. Drawings are not to scale.

applicable for the analysis and design of the structure, but it also allows to estimate heat and mass transport parameters needed to transfer the essential characteristics of the structure to the reduced models (see below).

- The *zone model* neglects exact geometrical details. Instead, it considers discrete volumes in which the reaction takes place. It is useful, e.g. for designing the reactor-wide flow pattern.
- The *phase model* has spatially homogenised reactive and non-reactive phases, coupled by interphase mass and heat transfer. It is suitable to describe the spatially distributed reactor behaviour and its interaction with surrounding devices in a computationally efficient way. It can be applied for optimisation of the reactor and its integration into complex devices.

None of these models is entirely new. The novelty of this contribution is the hierarchy of coherent and compatible models; results obtained with one of the models can be transferred to other elements of the model hierarchy. Furthermore, the application of the models covers a wide spectrum of tasks ranging from the design of the structure up to the heat integration and optimal control of the complete reactor. It is the latter aspect, in particular, which makes the proposed hierarchy a powerful and useful tool.

In this contribution, we derive and discuss the three models illustrated in Fig. 2, thereby focussing on a flat bed reforming reactor that is used as an indirect internal reforming unit in high temperature molten carbonate fuel cell (MCFC) systems (Bischoff and Huppmann, 2002; Pfafferoth et al., 2010). Its purpose is to reform the fuel gas (usually a methane/steam mixture) to a certain conversion before the gas mixture is fed to the fuel cells. They are inserted into the fuel cell stack at certain intervals, so they absorb heat from the fuel cells they are attached to. The elementary cell of this arranged reactor is shown in Fig. 3 left. It consists of two corrugated metal sheets, which are aligned in a staggered way, forming small chambers. In some of these, cylindrical catalyst particles are inserted.

Because the derivations of the zone and the phase models are motivated by the simulation results obtained from their preceding models, we discuss the models directly together with their results and some examples of typical applications. The detailed model and the zone model have already been published elsewhere in detail (Pfafferoth et al., 2008). For the sake of completeness, we repeat the most important aspects of these models here, so the reader can follow the argumentation, and refer to the mentioned publications for further details. Because the phase model has not been published elsewhere, we discuss its derivation in detail.

In Section 5, we also discuss how this hierarchical modelling approach can be transferred to other arranged, parallel passage reactors such as Katapak structures.

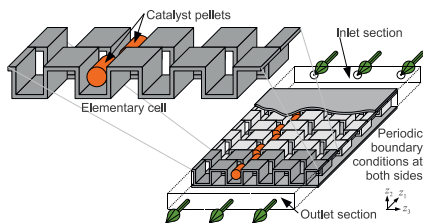


Fig. 3. Elementary cell and scheme of the detailed model of the reforming reactor (U.S.-Patent 6200696, not to scale).

2. The detailed model

This model describes the hydrodynamic and chemical behaviour in the elementary cell of the catalytic reactor on a small scale. It can be used to evaluate the performance of different geometrical structures. Furthermore, it is an important tool for the estimation of parameters that are required in the subsequently discussed zone and phase models. The class of detailed models is only briefly described here. For detailed information about the example, the reader is referred to the work of Pfafferoth et al. (2008).

2.1. Model definition

The CFD method is applied to describe the flow behaviour and the chemical reactions in the elementary cell. Independent from the modelled system, the detailed model reflects a cut-out section of the complete reactor, comprising several elementary cells (Fig. 3). Symmetry conditions are used in order to reduce the size of the model geometry and thereby decrease the necessary numerical effort. An inlet and an outlet section are added so that the gas flow can adapt smoothly from the uniform flow at the inlet boundary to the non-uniform flow pattern inside the structure, and vice versa. In addition, several elementary cells are aligned along the main direction of gas flow in order to obtain a representative flow pattern despite the effects at the inlet and outlet regions.

In general, laminar or turbulent flow equations are applied in detailed models, depending on the Reynolds number. Depending on the solid structure of the catalyst, the chemical reaction can be modelled as a surface reaction, or diffusion/reaction models (e.g. Levenspiel, 1996) can be used to describe the processes inside a porous catalyst. The boundary conditions define the gas flow (velocity, composition and temperature) into the model region at the inlet section, constant pressure level at the outlet, symmetry conditions at all symmetric faces and no-slip conditions on all solid surfaces. If applicable, boundary conditions with respect to temperature should be kept as simple as possible, for example with uniform temperature on all outer walls or adiabatic conditions.

In the case of the reforming reactor, seven elementary cells are aligned together with an inlet and an outlet section in the detailed model, so the catalyst pellets are allocated in a slightly staggered row (Fig. 3 right). Due to the high density of edges and obstacles in the geometry, which frequently cause laminar separation, Navier–Stokes equations with a $k-\epsilon$ -turbulence model are applied. The catalyst pellets are assumed to be highly active, so the reaction is modelled as a surface reaction with a high reaction rate coefficient. Two simultaneous reactions are considered, which are the methane steam reforming and the water gas shift reaction. The boundary conditions in this example comprise the flow rate, gas composition and temperature at the inlet, a constant pressure at the outlet surface, symmetric boundary conditions at the sides of the model, no-slip conditions at all internal surfaces, isothermal conditions at all outer surfaces of the top and bottom metal sheets and the aforementioned reaction rates at the pellet surfaces.

Note that virtually any structure can be modelled in a similar way. For example, von Scala et al. (1999) presented a detailed model of a Katapak-M packing. Their model represents a series of four identical packing elements, where all details of the geometrical structure are included. In contrast to the model presented here, they did not include any chemical reaction, but instead focused on the heat transfer between the reactor wall and the fluid. Calis et al. (2001) used similar models to evaluate the pressure drop across regular structured packings with very low

channel-to-particle-diameter ratio. Their model approach and the detailed model proposed in this contribution essentially follow the same guidelines.

The detailed model was implemented and solved with the CFX 10.0 software package. Typical numerical solution times of detailed models strongly depend on their individual complexity with regard to geometry and on the described physical and chemical processes. The detailed model of the reformer shown in Fig. 3 can usually be solved within 2.5–3 h CPU time (Dual Xeon CPU at 3.2 MHz), using up to 1.3 GB of RAM.

2.2. Simulation results

The detailed model of the reforming reactor considered here has been solved under the boundary conditions given in Table 1. The inlet conditions correspond to a gas mixture of methane and steam, which has been pre-reformed to a certain extent. The results in Fig. 4 indicate the existence of two zones in this reactor. In the vicinity of the catalyst pellets, the gas is almost stagnant due to the flow resistance caused by the catalyst pellets. The gas composition around the pellets is close to chemical equilibrium with respect to the methane steam reforming and the water gas shift reaction. Due to the overall endothermic character of the reforming process, the temperature is low there. At a certain distance from the catalyst pellets, the gas flows at high velocity and with low pressure drop, and its conversion is low. The two zones are designated as reactive zone (index R) and non-reactive zone (index N). Repeating cross-sectional profiles of the velocity and temperature evolve after a few pellets, and from there on, the rates of the reforming reactions are basically limited by mass

Table 1
Boundary conditions applied to the detailed model of the reforming reactor.

Parameter	Value
Feed conditions	
Mass flux	$6.00 \times 10^{-5} \text{ kg s}^{-1}$
Mass fraction CH_4	0.246 kg kg^{-1}
Mass fraction H_2O	0.554 kg kg^{-1}
Mass fraction H_2	0.031 kg kg^{-1}
Mass fraction CO	0.000 kg kg^{-1}
Mass fraction CO_2	0.169 kg kg^{-1}
Temperature	600°C
Walls	
Temperature	600°C

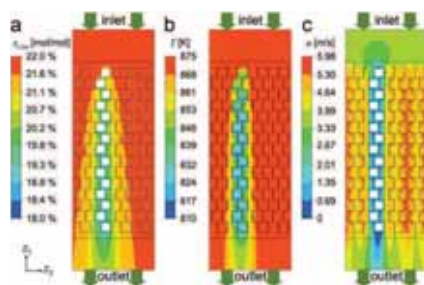


Fig. 4. Selected simulation results of the reforming reactor based on the detailed model. X_{CH_4} : Methane mole fraction, T : temperature and u : velocity. Profiles shown at half the reactor height.

transfer between both zones and by heat transport between the reactor walls and the reactive zone. Towards the end of the structure, the influence of the outlet boundary conditions perturbs the distributions of temperature, composition and velocity. Thus the flow pattern at the first and the last few pellets is not fully developed and cannot be considered as fully representative for the state inside such a reactor.

2.3. Applications

Besides the simulation of the gas velocity, composition and temperature profiles, the detailed model is suitable for a wide range of purposes. It can be used to compare the performance of different geometrical patterns, for example to evaluate the effect of a different placement of the catalytically active material. The model also serves to estimate parameters that are required in the following reduced models (Sections 3 and 4), including anisotropic gas permeabilities, effective mass and heat transfer coefficients between both zones, transfer coefficients between gas and wall and volumetric ratios of both zones. In the following, some of these applications are discussed in more detail.

2.3.1. Comparison of different geometrical structures

Structured reactors offer the opportunity to precisely design the surrounding of the catalyst, and thereby to control the state changes in the fluid volumes passing through. The detailed model is the tool for the comparison of different geometrical structures on the small scale. The variation may simply be a single parameter such as the width of a gap or the distance between catalyst pellets, which is modified in a systematic way to evaluate the effect of this parameter. The detailed model can also be applied to compare completely different structure designs, for example structures with straight channels versus geometries with a zigzag pattern.

Calis et al. (2001) demonstrated a similar comparison for structured packed beds with very low channel-to-particle-diameter ratio, focussing on the friction occurring in these structures. They solved CFD models of packed beds with a varying channel diameter at different Reynolds numbers in order to estimate the coefficients of the Ergun equation for each geometry individually.

In Fig. 5, three geometries of the reforming reactors are compared. They vary with respect to the pattern of catalyst pellets inserted into the structure. The states in these models strongly differ with respect to the conversion of the reforming process. The first structure (Fig. 5a) shows an overall conversion of 1.8%, the geometry with two catalyst rows has 3.6% and the geometry in Fig. 5(c) has the highest conversion, which is 5.5%. These results clearly show the impact of the catalyst allocation on the effective reaction rate in this structure. In addition, the profiles show that in each case, clearly separated reactive and the non-reactive zones are present, which confirms the finding from the previous Section 2.2.

The model hierarchy also allows comparing the performance of different geometrical structures on the reactor scale. As shown in the following sections, the detailed model can be applied to estimate parameters that are used in the reduced models, which then reveal the impact of design changes on the behaviour of the whole reactor.

2.3.2. Estimation of pressure drop coefficients

The detailed model can be applied to estimate coefficients for correlations of the pressure drop in structured reactors. Typically, correlations are used to describe the pressure drop (Δp) per length of the reactor (L) as a function of several geometrical

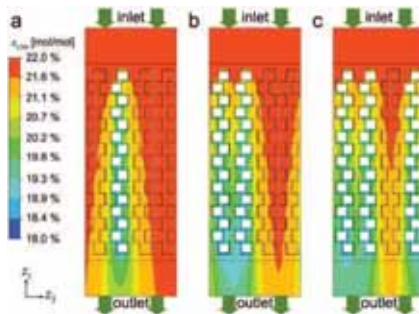


Fig. 5. Mole fractions of methane simulated by detailed models of the considered reforming reactor with three different catalyst patterns. Profiles shown at half the reactor height.

parameters (void fraction, ϵ , and lengths, d), fluid properties (viscosity, μ , and density, ρ) and operating conditions (superficial gas velocity, u_0):

$$\frac{\Delta p}{L} = f(u_0, \epsilon, d, \mu, \rho) \quad (1)$$

For the sake of simplicity, the following discussion is carried out for a one-dimensional system, although the results are applied later to three spatial dimensions. The friction function, f , may be chosen such that Eq. (1) becomes the Ergun equation (Ergun, 1952):

$$\frac{\Delta p}{L} = c_1 \frac{\mu u_0}{\epsilon d^2} + c_2 \frac{\rho u_0^2}{\epsilon^2 d} \quad (2)$$

or the Darcy's law (Bird et al., 2007):

$$\frac{\Delta p}{L} = \frac{u_0 \mu}{\kappa} \quad (3)$$

The detailed model can be used to estimate the fitting parameters in these correlations (the Ergun coefficients c_1 and c_2 , or the permeability κ). For this purpose, the operating parameters and fluid properties are varied over the whole range of expected conditions inside the reactor. In principle, the simulated pressure drop is then divided by the length, L , of the simulated structure to yield the pressure gradient.

Generally, one is interested to estimate the fitting parameters for a flow pattern, which represents the fully developed flow inside the structured reactor. In the detailed model, this condition is not nearly fulfilled near the inlet region and the outlet region. Only a certain part in the middle of the simulated geometry represents the typical pressure gradient in the structured reactor, provided that a sufficient number of elementary cells is used. In order to eliminate these effects caused by the boundary conditions, we propose the following approach. Assume that the total pressure drop over the simulated detailed model can be decomposed into the pressure drop over the inlet region, the outlet region and over the region of fully developed flow in between these:

$$\Delta p = \Delta p_{in} + \Delta p_{out} + \Delta p_{middle} \quad (4)$$

Equivalently, the length of the simulated geometry is decomposed:

$$L = L_{in} + L_{out} + L_{middle} \quad (5)$$

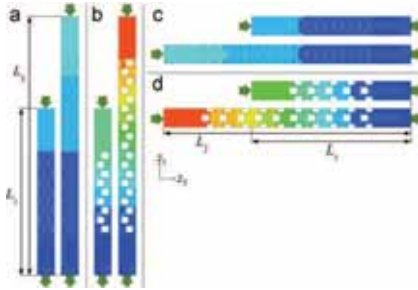


Fig. 6. Estimation of permeabilities in the reforming reactor using pressure profiles from different variants of the detailed model. (a) Permeability in main flow direction in the non-reactive zone, (b) main flow direction, reactive zone, (c) lateral flow, non-reactive zone and (d) lateral flow, reactive zone. Colours indicate simulated pressure level in the gas phase at half the height of the reactor.

Eq. (1) is applied to describe the pressure drop in the middle part, so

$$\Delta p_{\text{middle}} = L_{\text{middle}} f(u_0, \varepsilon, d, \mu, \rho) \quad (6)$$

and consequently

$$\Delta p - \Delta p_{\text{in}} - \Delta p_{\text{out}} = f(u_0, \varepsilon, d, \mu, \rho) (L - L_{\text{in}} - L_{\text{out}}) \quad (7)$$

Assume further that the pressure drops over the inlet and the outlet regions as well as the length of these regions only depend on the choice of operating conditions such as the gas velocity, its viscosity and density. Conducting two simulations at the same conditions but with different lengths of the detailed structure (L_1 and L_2) yields two simulated pressure drops (Δp_1 and Δp_2). As long as the fluid properties at the outlet are similar in both simulations, the pressure drops over the outlet region are the same in both cases. Forming the difference of the pressure drop obtained from these two simulations eliminates the unknown pressure drops and lengths at the inlet and outlet and yields the following equation, which can be used to estimate the unknown coefficients:

$$\frac{\Delta p_1 - \Delta p_2}{L_1 - L_2} = f(u_0, \varepsilon, d, \mu, \rho) \quad (8)$$

In our example, we apply the Darcy's law to represent the pressure drop in the reforming reactor. Due to the corrugated sheets (Fig. 3), the gas flow resistance along the main gas flow direction and perpendicular to it are expected to be very different, so anisotropic permeabilities are used to describe it. In three spatial dimensions, the permeability tensor is symmetrical and contains 3×3 elements. In the case considered here, the generalised eigenvectors of the permeability tensor coincide with the chosen axes of the Cartesian coordinate system, so all off-diagonal elements of the permeability tensor are zero. The pressure gradient with respect to the coordinate z_2 is considered to be negligible compared to the pressure gradients in the other two directions. Thus, the second element of the diagonal tensor, which describes the permeability along the height of the reactor, is set to an arbitrarily high value, leaving only the permeabilities along the main flow direction (z_1) and perpendicular to it (z_3) as unknown parameters. Because the permeabilities in the reactive zone are expected to deviate from those in the non-reactive zone, we need to determine permeabilities in both zones separately, so there is a total of four parameters to be estimated. Each of them is obtained from different versions of the detailed model as indicated in Fig. 6.

Table 2
Estimated Darcy permeability tensors in the two zones of the reforming reactor.

	Non-reactive zone			Reactive zone		
$\kappa \text{ (m}^2\text{)}$	1.5×10^{-7}	0	0	0.4×10^{-7}	0	0
	0	∞	0	0	∞	0
	0	0	0.43×10^{-7}	0	0	0.11×10^{-7}

Simulations with two different lengths of the model geometry are sufficient to estimate the permeabilities. Performing some additional simulations with identical boundary conditions but different lengths showed that the pressure drop is almost exactly linear to the length. This confirms the validity of Eq. (8).

Because the pressure drop is expected to depend on gas velocity and gas composition, two additional series of simulations were carried out. In the first series, the gas velocity at the inlet boundary was changed. In another series, the molar fractions at the inlet boundary were varied such that they represented typical gas compositions at the inlet, in the middle and at the outlet of the complete reactor. The effect of gas composition was found to be negligible compared to the dependency of the permeability on the gas velocity. Three of the four estimated permeabilities showed that they were roughly proportional to the inverse of the gas velocity. This indicates that the pressure drop is not linear to the gas velocity, as postulated by the Darcy's law (Eq. (3)). Instead, it is approximately proportional to the square of the gas velocity, which might better be described by the Ergun approach (Eq. (3)). Only the permeability along z_3 in the reactive phase (Fig. 6d) showed constant permeabilities for different gas velocities. However, the Darcy approach is still applicable as long as the velocity is approximately constant throughout the reactor. In that case, the permeability obtained at a typical velocity is sufficient to approximate the pressure drop over the reactor. Otherwise, velocity-dependent permeabilities can be used.

The estimates of the permeabilities are given in Table 2. Obviously, the lateral permeabilities are significantly lower than the longitudinal ones. Hence, unless strong pressure drops are applied in lateral direction, the gas flows mainly along z_1 . Furthermore, the reactive zone has far lower permeabilities than the non-reactive zone, which corresponds to the findings in the velocity profile (Fig. 4c).

The basic idea of the just discussed procedure can be transferred to other structured reactors, although some modifications such as non-zero off-diagonal elements may be necessary.

In principle, such estimates can be validated experimentally. Mahr and Mewes (2007) used a similar approach to estimate anisotropic permeabilities in a Sulzer Mellapak 250Y. They measured the pressure gradient along different directions in long, narrow cut-out sections of this packing. They found excellent agreement of the experimental data with theoretical results obtained from corresponding CFD simulations. This indicates that the proposed approach described here is a reasonable basis for model reduction.

Petre et al. (2003) proposed a similar method to estimate pressure drops of structured packings. They split the repeating structure into several repeating elementary units (REU), for which they determined dissipation rates over a wide range of operating conditions. The pressure loss over a certain structure can then be estimated as a combination of the dissipation in the REU that form the structure.

2.3.3. Estimation of volume fractions

Another parameter that is of importance for the subsequently presented reduced models is the volumetric ratio of the reactive and non-reactive zones. There is no general rule how to define the

boundary of the reactive zone from the detailed model. However, depending on the specific structure at hand, the boundary may be defined as the location where one or several of the states show a steep change. In the example of the reforming reactor, the gas velocity can be used as a criterion; it is almost constant in the non-reactive zone and changes quickly to lower values in the reactive zone (Fig. 4c). Another criterion might be the location of mass and heat transport barriers. The corrugated sheets around the catalyst pellets in the reformer pose a barrier for the transport processes between the catalyst pellets and the bulk of the gas. Hence, the boundary between both zones may be defined at this location. This approach may also be used in structured packings such as Katapak or Katamax, where the catalyst particles are placed inside pockets of corrugated wire gauze; the gauze can be seen as the interface between both zones.

Both approaches, using the velocity profile or the transport barrier, lead to essentially the same results for the reforming reactor.

2.3.4. Estimation of transport parameters

The results of the detailed model have shown that the transport of heat and mass between the catalyst and the bulk of the gas phase is important for the overall rate of reaction. Based on the detailed model, transfer coefficients between the reactive and the non-reactive zone can be estimated. These parameters are then applied in the phase model (Section 4). In the following, we exemplarily show the estimation procedure for the heat transfer coefficient.

We assume linear kinetics for the heat transfer between the two zones:

$$q' = k' (T^N - T^R) \quad (9)$$

where k' is the heat transfer coefficient, T^N and T^R are temperatures representative for the two zones and q' is the heat flux density across the interface between them. In order to estimate the heat transfer coefficient, information about the heat flux density and the temperature difference is needed. In a structured reactor, the local values of these quantities can vary strongly. This leads to locally varying estimates of the transfer coefficient, which is not desired. To obtain spatially averaged transfer coefficients, we apply integral values of the heat flux and average values of the temperature difference. For this purpose, we integrate Eq. (9) over the interface of a complete elementary cell (Fig. 3):

$$Q' = k' A' (T^N - T^R) \quad (10)$$

where A' is the interfacial area between the two zones in a single structure element, and Q' is the total heat flux across this interface.

In a detailed model with adiabatic boundary conditions, the heat flux across the interface of the elementary cell with fully developed flow can be approximated by the heat flux originating from the catalyst surface, which corresponds to the cumulative heat of reaction released in the reactive zone of this element:

$$Q' \approx Q_{cat} = \int_{A_{cat}} \sum_j \Delta_R h_j^0(T) r_j dA \quad (11)$$

The representative temperature in the non-reactive zone is its volume average:

$$T^N = \frac{1}{V^N} \int_{V^N} T dV \quad (12)$$

The most important process in the reactive zone is the chemical reaction. The representative temperature of this zone should therefore reflect the temperature at which the reactions occur. In the case of a surface reaction, this should be the average

temperature at the catalyst surface:

$$T^R = \frac{1}{A_{cat}} \int_{A_{cat}} T dA \quad (13)$$

If the reactions take place in a certain volume, say inside a porous catalyst particle, then the representative temperature should be the average temperature of this particle:

$$T^R = \frac{1}{V_{cat}} \int_{V_{cat}} T dV \quad (14)$$

The integrals in Eqs. 11, 12 and 13–14 can be obtained from the simulation results of the detailed model. The values are then inserted into Eq. (10) to yield estimates of the heat transfer coefficient, k' . This procedure is carried out for all elementary cells in the detailed model.

It can be expected that the estimates of the heat transfer coefficients obtained from structure elements close to the inlet or the outlet region are not representative for the hydrodynamically and thermally fully developed flow. Thus, it is important to apply sufficiently long domains of the detailed model, so that the gas flow can develop to a steadily repeating pattern well before the outlet.

As an example, the heat transfer coefficients estimated from the repeating structure elements of the detailed model of the reforming reactor are shown in Fig. 7. Because a portion of the gas in the inlet region is forced to enter the reactive zone, the heat transfer coefficient is relatively high in the first few elementary cells. After about three elements, the coefficient attains almost constant values, which can be seen as representative for the heat transfer in a hydrodynamically and thermally fully developed flow.

A similar approach can be used to estimate mass transfer coefficients. For this purpose, the mass flux rates are approximated by the mass source terms due to reaction, and the mass fractions in the reactive and the non-reactive zone are approximated by volume or surface averaged values. These values are then used to estimate mass transfer coefficients. However, in addition to diffusive transport, convective transport due to non-equimolar reactions has to be taken into account in this procedure.

2.3.5. Further applications

In addition to the applications shown in the previous sections, the detailed model can be applied for several other purposes. If

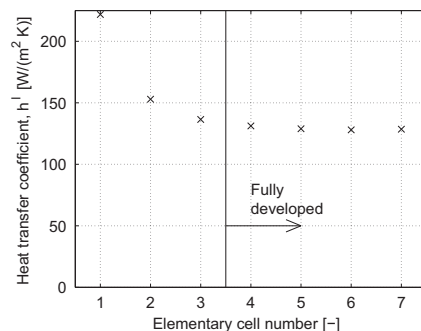


Fig. 7. Estimates of the heat transfer coefficient of the reformer, obtained at each elementary cell of the detailed model.

axial dispersion cannot be neglected in the structured reactor, the detailed model can be used to estimate dispersion coefficients. This has been demonstrated by Freund et al. (2005) based on a detailed model of a fixed bed, where they applied the particle tracking method to estimate axial and radial dispersion coefficients (Maier et al., 2000). The detailed model is also useful to obtain average heat transfer coefficients between the fluid and a reactor wall, in which case non-adiabatic conditions need to be applied to the reactor walls.

3. The zone model

The zone model is a reduced model that is based on the findings from the detailed model. It describes the processes on the scale of the structures in a reduced way. Thus, the complete reactor, or at least a large part of it, can be simulated. The zone model is suitable to design a complete structured reactor with respect to the flow field, catalyst distribution and pressure drop.

3.1. Model definition

The zone model is motivated by the existence of reactive and non-reactive zones in a structured reactor. The transition from the detailed model to the zone model is achieved in two steps:

- The gas volume around the catalyst particles, which is almost stagnant and close to chemical equilibrium, is defined as the reactive zone. The geometrical shape of the reactive zone may be as simple as a cuboid, for example in case of the reforming reactor (Fig. 2b). For reactors with other structures, for example with Katapak-S internals, the zones may be shaped as three-sided prisms. The reactions that occur on the surface or inside the catalyst particles are reflected as quasi-homogeneous reactions in the whole reactive zone.
- The detailed geometrical structure of the reactor internals is neglected. The resistance of the internals against convective gas flow is represented by introducing friction terms into the momentum balance. These friction terms may follow the Darcy's law or the Ergun equation, for example. If necessary, anisotropic transport parameters may be applied.

This approach has certain parallels to the concept of hydrodynamic analogy (e.g. Shilkin and Kenig, 2005). Both simplify the complex spatial distribution of different phases in order to obtain a reduced model formulation. However, the phases considered by Shilkin and Kenig are phases in a thermodynamic sense (liquid and gas), which exchange mass, energy and momentum across film layers, whereas we discriminate between two gas phases that are separated by solid obstacles. Furthermore, the zone model presented here is incorporated in a model hierarchy, which allows to transfer parameters and qualitative results from one detail level to another; this is not the case with the model proposed by Shilkin and Kenig.

The model resulting from the previously mentioned assumptions has a strongly simplified geometry compared to the detailed model. It is based on the Navier–Stokes equations in three spatial dimensions, including an additional friction term, so the momentum balance reads (with neglected gravity forces)

$$\frac{\partial}{\partial z_k} (\rho u_j u_k) = - \frac{\partial}{\partial z_k} (P' \delta_{jk} + \pi_{jk}) - \mu [\kappa^{-1}]_{jk} u_k \quad (15)$$

The reaction rate coefficients in the reactive phase can be obtained by relating the rate coefficients used in the detailed model to the reactive volume of one elementary structure element. In the case of a reaction taking place at the catalyst

surface, the volume-related rate coefficient can be calculated according to

$$k^V = \frac{k^A A_{cat}}{V^R} \quad (16)$$

where k^A is the surface-related reaction rate coefficient at the catalyst pellet, A_{cat} is the total catalyst surface inside a single elementary cell and V^R is the volume of the reactive zone in a cell. If reactions take place inside a porous catalyst particle and internal mass transport plays an important role, then an effective rate coefficient should be applied instead of $k^A A_{cat}$.

The boundary conditions of the zone model for the reforming reactor include inlet conditions at the feed position, a constant pressure at the outlet, no-slip conditions on all walls and isothermal conditions at the outside of all reactor walls. The zone model has been presented and discussed in more detail by Pfafferodt et al., 2008.

3.2. Simulation results

As an example, the zone model has been applied to simulate a complete reforming reactor. This reactor is subdivided into four sections (Fig. 8). The first section has no internals, the second section contains structures with a low catalyst loading and a horizontal main flow direction. The third section has a vertical main flow direction and a catalyst density as in the second section, and the fourth section has an increased catalyst density.

Fig. 8a shows the mole fraction of methane in this reactor under certain operating conditions and with isothermal boundary conditions at the top and bottom metal sheets. Funnel-like shapes can be observed around all the reactive zones. These shapes were already visible in the concentration profiles obtained from the detailed model (Fig. 4a), and they are well reflected in this reduced model.

3.3. Applications

The zone model is suitable for the analysis and optimisation of many issues related to the spatially distributed design of the complete reactor. It can be used to evaluate the effect of different internals on the reactor performance. The application of sections with different structures in a reactor is an interesting option to optimise the overall behaviour. The zone model also allows to elucidate the effect of applying zigzag shaped alignment of structured elements, and many more design options.

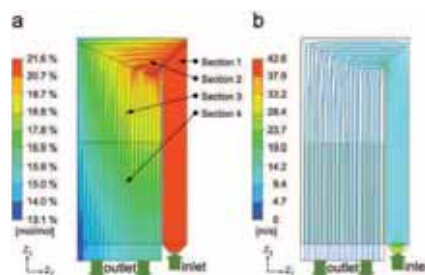


Fig. 8. Selected results from the zone model of the reforming reactor. Left: Distribution of the methane mole fraction in the complete reactor; right: flow lines through the reactor.

Furthermore, it can be used to analyse critical points regarding the reactor geometry. In the example in Fig. 8, two such points arise. The first critical area is near the upper end of the separating wall between the inlet section and section 3. Due to different lengths of gas flow paths, the gas velocity distribution in sections 3 and 4 might be strongly inhomogeneous, with low velocities on the left hand side and high velocities on the right hand side. The second point that needs closer investigation is the upper left corner, which may be a dead zone. Fig. 8b, which shows gas flow lines through the reactor, gives answers to both questions. The gas flow through sections 3 and 4 is evenly distributed, and the upper left corner is supplied with reactant gas, as can be seen by the almost equidistant pattern of the flow lines.

4. The phase model

The phase model represents the next reduction level of a structured reactor. Its derivation is based on the zone model, and it adopts the idea of two different zones present in the reactor. However, it is not necessary to set up and solve the zone model of a reactor in order to develop the corresponding phase model. This model can be applied to simulate spatially distributed states in a complete structured reactor in a very efficient way. It can also be coupled with models of other, neighbouring units to simulate coupled systems, such as fuel cell stacks (Pfafferoth et al., 2010).

4.1. Model derivation

To derive the equations of the phase model, we consider an elementary cell of the geometrical structure (see Fig. 9). The general mass balance of a chemical species i formulated in tensor notation (Tskov, 2009; Jischa, 1982) reads

$$\frac{\partial c_i}{\partial t} = -\frac{\partial}{\partial z_k} (g_{ik} + j_{ik}) + \sigma_i \quad (17)$$

where g_{ik} denotes the convective flux density of species i in the k th direction, j_{ik} is the diffusive flux density and σ_i is the volume related source density of species i due to reactions. For the sake of brevity, we introduce the flux density, n_{ik} , which is the sum of the convective and diffusive mass flux densities. We integrate this equation over the complete non-reactive zone that is contained in the considered repeating element:

$$\int_{V^N} \frac{\partial c_i}{\partial t} dV = - \int_{V^N} \frac{\partial n_{ik}}{\partial z_k} dV + \int_{V^N} \sigma_i dV \quad (18)$$

With the Gaussian integral theorem, the mass transport term can be converted from a volume integral into a surface integral, where m_k is the unit normal vector on the surface of the

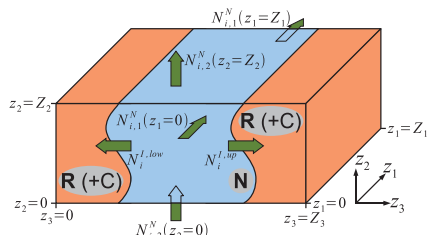


Fig. 9. Scheme of an elementary cell.

integration volume:

$$\int_{V^N} \frac{\partial c_i}{\partial t} dV = - \int_{A^N} n_{ik} m_k dA + \int_{V^N} \sigma_i dV \quad (19)$$

The surface integral can be split up into several terms, each considering the mass flux across a different part of the surface (Fig. 9):

$$\int_{V^N} \frac{\partial c_i}{\partial t} dV = N_{i,1}^N(z_1=0) - N_{i,1}^N(z_1=Z_1) + N_{i,2}^N(z_2=0) - N_{i,2}^N(z_2=Z_2) - N_{i,1}^{L,up} - N_{i,1}^{L,low} + \int_{V^N} \sigma_i dV \quad (20)$$

$N_{i,1}^{L,up}$ and $N_{i,1}^{L,low}$ are defined as the mass fluxes from the non-reactive zone into the reactive zone. Hence, their signs in this balance are negative. In order to evaluate the remaining integrals, we assume that the concentration and source densities are constant within the non-reactive volume:

$$c_i(z \in V^N, t) = c_i^N(t) \quad (21)$$

$$\sigma_i(z \in V^N, t) = \sigma_i^N(t) \quad (22)$$

An additional important assumption in this derivation is that net mass transport perpendicular to the non-reactive and the reactive zone (in z_2 -direction) can be neglected. This essentially means that $N_{i,2}^{L,up} = N_{i,2}^{L,low} = N_{i,2}^L$. Furthermore, we define the superficial molar flux densities:

$$n_{i,1}^N = \frac{N_{i,1}^N}{(Z_2 - Z_1)} \quad (23)$$

$$n_{i,2}^N = \frac{N_{i,2}^N}{(Z_1 - Z_3)} \quad (24)$$

Also, the interfacial mass transport is expressed by an area-related mass flux density:

$$n_i^L = \frac{N_i^L}{A^L} \quad (25)$$

These assumptions and definitions lead to

$$V^N \frac{dc_i^N}{dt} = -(n_{i,1}^N(z_1=Z_1) - n_{i,1}^N(z_1=0))Z_2Z_3 - (n_{i,2}^N(z_2=Z_2) - n_{i,2}^N(z_2=0))Z_1Z_3 - 2A^L n_i^L + V^N \sigma_i^N \quad (26)$$

Dividing this equation by the total volume of the repeating volume $V = Z_1 Z_2 Z_3$ and introducing the volumetric fraction of the non-reactive phase, $\epsilon^N = V^N/V$, and the specific volume-related exchange area, $a^L = 2A^L/V$, yields

$$\epsilon^N \frac{dc_i^N}{dt} = - \frac{(n_{i,1}^N(z_1=Z_1) - n_{i,1}^N(z_1=0))}{Z_1} - \frac{(n_{i,2}^N(z_2=Z_2) - n_{i,2}^N(z_2=0))}{Z_2} - a^L n_i^L + \epsilon^N \sigma_i^N \quad (27)$$

The limit of this difference quotient with Z_1 and Z_2 approaching zero reads

$$\epsilon^N \frac{dc_i^N}{dt} = - \frac{\partial n_{i,1}^N}{\partial z_1} - \frac{\partial n_{i,2}^N}{\partial z_2} - a^L n_i^L + \epsilon^N \sigma_i^N \quad (28)$$

The superficial mass transport density is split again into a convective and a diffusive part:

$$n_{i,k}^N = \epsilon^N (g_{ik}^N + j_{ik}^N) = \epsilon^N (u_k^N c_i^N + j_{ik}^N) \quad (29)$$

In addition, the source term is zero in the non-reactive zone, so the final balance equation reads

$$\epsilon^N \frac{dc_i^N}{dt} = - \frac{\partial(\epsilon^N u_1^N c_i^N + \epsilon^N j_{i,1}^N)}{\partial z_1} - \frac{\partial(\epsilon^N u_2^N c_i^N + \epsilon^N j_{i,2}^N)}{\partial z_2} - a^L n_i^L \quad (30)$$

To describe the concentrations inside the reactive zone, Eq. 17 is integrated over the volume of the reactive zone. The procedure is similar to the one just introduced for the non-reactive zone. Instead of Eq. (20), we obtain for the reactive zone:

$$\int_{V_R} \frac{\partial C_i}{\partial t} dV = N_{1,1}^R(z_1=0) - N_{1,1}^R(z_1=Z_1) + N_{1,2}^R(z_2=0) - N_{1,2}^R(z_2=Z_2) + N_{1,3}^R(z_3=0) - N_{1,3}^R(z_3=Z_3) + N_i^{l,up} + N_i^{l,low} + \int_{V_R} \sigma_i dV \quad (31)$$

The assumption that no mass transport occurs across the reactive zone means that the mass fluxes across the boundaries in z_3 -direction vanish. After some manipulations, the balance equation of the reduced model reads

$$e^R \frac{\partial C_i^R}{\partial t} = - \frac{\partial(e^R u_1^R C_i^R + e^R J_{1,1}^R)}{\partial z_1} - \frac{\partial(e^R u_2^R C_i^R + e^R J_{1,2}^R)}{\partial z_2} + a^l n_i^l + e^R \sigma_i^R \quad (32)$$

With the additional assumption of stagnant gases in the reactive zone, this equation can be further reduced to

$$e^R \frac{\partial C_i^R}{\partial t} = a^l n_i^l + e^R \sigma_i^R \quad (33)$$

Eqs. (30) and (33) are sufficient to discuss the main features of the reduced model. The two zones are no longer present at discrete spatial positions, but representative states of both zones (gas compositions, temperatures, etc.) are described throughout the whole model domain by continuous gradients. The zones are homogenised and now rather resemble two phases: both are present everywhere in the reactor, and mass, energy and momentum are transferred between them (see Fig. 2c). That is why we refer to this as the phase model.

The phase model is not essentially new. Models with a similar structure and physical motivation have been applied to reflect the behaviour of monolith reactors. Groppi et al. (1995) compared results from a three-dimensional model of a monolith reactor with those obtained from a spatially one-dimensional model, which consists of very similar equations as shown here. Piironen et al. (2001) used the same idea to motivate their model of a gas–liquid reactor with Katapak structures. Schönfelder et al. (1996) proposed a two-phase model for a circulating fluidized bed reactor. In their system, one phase represents gas with a low concentration of solid material, which is ascending in the reactor, and the second phase describes clusters of solid material, which are moving downwards. Mass and energy are transferred between both phases. A similar approach was proposed, e.g. by Krishna et al. (1996) for the simulation of slurry reactors, and by van Hasselt et al. (1999) for trickle bed reactors. This shows that the basic idea of this reduction method is applicable to a wide range of processes that show reactive and non-reactive zones.

The kinetic models for the mass flux density across the interface, n_i^l , need to be discussed briefly. This mass flux includes all convective and diffusive contributions to the mass flow of component i across the interface. In order to describe the total convective flux, the pressure difference between both phases may be used, together with an effective transfer coefficient, which can be estimated from the detailed model. An alternative that can be applied at steady state follows from the summation of Eq. 33 over all chemical species involved. It basically states that the net molar flux across the interface must compensate the change of the total number of moles caused by the reaction:

$$a^l n_i^l = e^R \sum_j \sigma_j^R \quad (34)$$

This equation can be used to calculate the total flux across the interface. The diffusive transfer rates can be described by Fick's

diffusion kinetics or by the Maxwell–Stefan approach. Also in these cases, the required effective transfer coefficients can be estimated from the detailed model.

In order to complete the set of equations of the phase model, the remaining balance equations such as the total mass balance, the enthalpy balance and the momentum balance in z_1 -direction need to be integrated over each zone in a similar way. The result of these derivations strongly depends on several decisions, for example whether some diffusion fluxes should be neglected, whether a Darcy term should be introduced into the momentum balance, or whether isobaric conditions should be applied.

The derivation of the phase model of the reformer follows the approach shown above, but some additional reductions are applied. The most important is that due to the very low height-to-length ratio, we neglect all gradients w.r.t. the z_2 -coordinate, which represents the height of the reactor (Fig. 9). More precisely, all partial differential equations are integrated w.r.t. the z_2 -coordinate. Because all mass fluxes vanish at the z_2 -boundaries of this integration, the derivatives with respect to this coordinate simply disappear. In the enthalpy balance, the heat transfer flux densities across the top and bottom sheets (see Fig. 3) occur as source terms after the z_2 -integration. Further reductions are the neglect of diffusive transport terms in z_1 -direction, the neglect of heat conduction in the gas in any direction and the assumption of isobaric conditions.

A brief outline of the derivation of these equations is given in the Appendix. The governing equations are presented in the following. The mole fraction in the non-reactive phase, x_i^N , is determined by convective transport along the main flow direction and by mass transport to and from the reactive phase:

$$e^N x_i^N \frac{\partial C_i^N}{\partial t} = -e^N g_i^N \frac{\partial x_i^N}{\partial z_1} - a^l (n_i^l - x_i^N n_i^l) \quad (35)$$

The enthalpy balance in temperature form considers a convective term in z_1 -direction, heat transfer to the reactive phase and heat transfer across the top and bottom walls:

$$e^N C_p^N \frac{\partial T^N}{\partial t} = -e^N g_i^N \frac{\partial T^N}{\partial z_1} - a^l \left[\sum_i C_{p,i} n_i^l (T^N - T^R) - q^l \right] + e^N \frac{q_w^N}{d_z} \quad (36)$$

In this equation, q_w^N represents the heat flux density through the reactor wall into the gas of the non-reactive phase. This flux can be assumed to be proportional to the temperature difference between the surrounding temperature (or the temperature of the neighbouring reactor unit) and T^N .

The molar gas flux density in the non-reactive phase, g_i^N , is calculated from Eq. (37). It is derived from the ideal gas law in combination with isobaric condition and the total mass balance (see the Appendix). It reflects the fact that the volumetric flow rate changes along z_1 due to temperature change and mass transfer between both phases:

$$0 = - \frac{\partial(e^N g_i^N T^N)}{\partial z_1} + \frac{1}{C_p^N} \left[a^l \left(\sum_i C_{p,i} n_i^l (T^N - T^R) - q^l \right) + e^N \frac{q_w^N}{d_z} \right] - a^l n_i^l T^N \quad (37)$$

In the reactive phase, we assume a stagnant gas phase. Hence, the gas composition is influenced by mass exchange with the non-reactive phase and by the reaction rates:

$$e^R C_i^R \frac{\partial x_i^R}{\partial t} = a^l (n_i^l - x_i^R n_i^l) + e^R \sum_j (v_{i,j} - x_i^R v_j)^R \quad (38)$$

The enthalpy balance considers heat transfer across the interface, the heat of reaction and heat transfer across the top and bottom walls. Note that the reactive phase is assumed to

surround the catalyst, so its surface fraction between the reactive phase and the wall is $(c^R + c^C)$

$$c^R c_p^R \frac{\partial T^R}{\partial t} = d' \left[\sum_i c_{p,i} n_i^{t+} (T^N - T^R) - q' \right] + c^R \sum_j (-\Delta_R h_j^R) r_j^R + (c^R + c^C) \frac{q_w^R}{d_2} \quad (39)$$

The heat flux across the reactor wall into the reactive phase is represented by q_w^R . The total mass balance yields the following equation which can be used to calculate the total molar flow density across the interface:

$$0 = d' n_i^R + c^R \sum_j \bar{v}_j r_j^R + \frac{1}{T^R c_p^R} \left[d' \left(\sum_i c_{p,i} n_i^{t+} \cdot (T^N - T^R) - q' \right) + c^R \sum_j (-\Delta_R h_j^R) r_j^R + (c^R + c^C) \frac{q_w^R}{d_2} \right] \quad (40)$$

More details about this model, such as initial and boundary conditions, the reaction rate kinetics and the transport kinetics across the interface can be found in a paper by Pfafferoth et al. (2010).

4.2. Simulation results

A typical application of the phase model is to simulate and optimise the coupling of the structured reactor with other units (see Section 4.3 for more applications). For example, the reforming reactor is usually placed inside a stack of high temperature fuel cells. The fuel gas passes through the reformer, where it is converted to a certain degree, and is then fed into the fuel cell, where it is converted electrochemically. A part of the heat from the electrochemical reactions in the fuel cells is transferred to the reformer via the reactor walls (described by q_w^R and q_w^C in Eqs. 36 and 39). This heat compensates some of the heat losses due to the endothermic reforming process in the reformer. In the simulations shown in this section, we combine a spatially two-dimensional phase model of an internal reformer with a 2-D fuel cell model. Because we focus on the results from the phase model, we do not discuss the fuel cell model here. For the reader who is interested in more details of the fuel cell model, we refer to the publication of Pfafferoth et al. (2010). In the context of the present work, the purpose of the fuel cell model is to provide a spatially distributed temperature profile of a unit that is attached to the reforming reactor.

Differing from the arrangement shown in Fig. 8, the phase model describes a reforming reactor with straight channels, without any bendings. The inlet is located at the upper boundary of the z_1 -coordinate and the gas flows straight through the reactor along this coordinate. In the downstream half section of the reactor, the density of catalyst pellets is increased, which leads to increased heat and mass transfer parameters in this section. This staging of catalyst is typically done in order to sustain high reaction rates at decreasing reactant concentration. The boundary conditions applied to the phase model are listed in Table 3.

The phase model was combined with the fuel cell model, implemented and solved by the numerical tool Consol Multiphysics Version 3.5 (2008). With a spatial discretization of 8×8 second order elements and starting from arbitrary initial states, the model is typically solved within 10 min on a Dual Xeon CPU (3.2 MHz) and takes up to 3 GB of RAM.

Figs. 10 and 11 show the mole fraction of methane and the temperature in both, the reactive and non-reactive phases of the structured reformer at steady state, respectively. Note that normalised spatial coordinates, ζ_1 and ζ_3 , are used in both figures instead of z_1 and z_3 . In the inlet region, near $\zeta_1 = 1$, the difference of the mole fraction in both phases is about 5 mol%. Because the

Table 3

Feed conditions applied in the phase model of the reforming reactor.

Feed conditions	Value
Mole flux density	52.0 mol m ⁻² s ⁻¹
Mole fraction CH ₄	0.235
Mole fraction H ₂ O	0.471
Mole fraction H ₂	0.235
Mole fraction CO	0.000
Mole fraction CO ₂	0.059
Temperature	600 °C

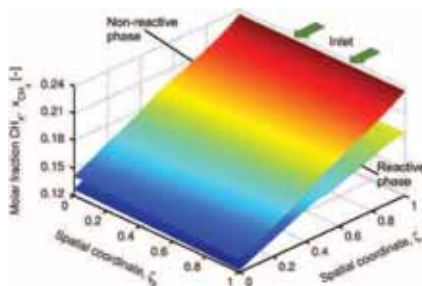


Fig. 10. Selected result from the phase model simulation of the reformer. Distributions of the mole fractions of methane in the reactive and the non-reactive phases.

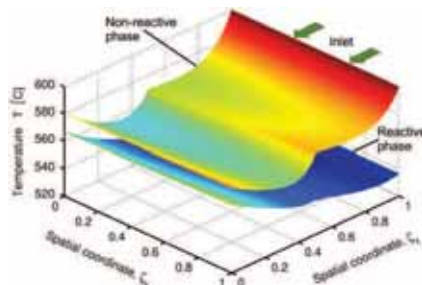


Fig. 11. Selected result from the phase model simulation of the reformer. Temperature distributions in the reactive and the non-reactive phases.

gas composition in the reactive phase is close to equilibrium there, the phase model clearly reflects the mass transport limitation of the reaction rate. The temperatures show a difference of 60 °C at the inlet, which quickly reduces to about 40 °C. Due to the significant mass transport limitation, the temperature drop near the inlet is roughly 30 °C, which is moderate compared to typical reforming reactors. Throughout the rest of the first section ($0.5 < \zeta_1 < 1$), the differences in temperature and gas composition stay almost constant. Because the reaction rate decreases slowly, and due to the heat flux from the neighbouring fuel cell, the temperature starts to increase slowly.

At $\zeta_1 = 0.5$, the gas enters the second section of the reactor, which has a higher catalyst density and therefore higher mass and

heat transfer parameter values. This leads to reduced differences in temperature and methane molar fraction in this section. Due to the increase of the transfer parameter values, the reaction rate is increased, and a second small temperature drop occurs. The staging of the catalyst provides an almost linear decrease of the methane fraction and thus a smooth distribution of the reaction rate. In addition, it leads to moderate temperature variations along the main flow direction, ζ_1 . This is a good example of how structured reactors can be used to purposefully control the spatial distribution of reaction rates and thereby control the temperature profile.

4.3. Applications

The phase model describes representative, spatially distributed states such as the gas composition and the temperature in the reactive and the non-reactive phases of a structured reactor. Due to its relatively low level of complexity (compared to the detailed model), it can be used to simulate a complete reactor at low computational costs. In the following, selected applications are discussed.

- The phase model can be applied to simulate spatial profiles of states and the overall performance of existing structured reactors. It delivers local information about reaction rates and gas compositions, which are difficult or impossible to measure in an experimental setup.
- If more than one geometrical structure is available for the design of a reactor, the effects of each structure on the spatial distribution of states and on the overall reactor performance (i.e. conversion and selectivity) can be analysed in order to identify the preferable structure.
- Structured reactors may include several different geometrical structures, which are applied in different parts of the reactor. A good example for this is shown in Fig. 8. The phase model can be used to evaluate such staged reactor designs. It can also be applied to optimise the spatial arrangement of the different structures in the reactor, either by manually applying changes to the exchange parameters or by numerical parameter optimisation.
- Operating conditions are usually applied as boundary conditions to the phase model. This allows to optimise the operating conditions applied to a structured reactor, for example with respect to conversion or selectivity. Additional constraints regarding the temperature or pressure drop may be applied.
- The traditional approach to design structured reactors is to choose a geometrical structure element and then to design a reactor based on the properties (transport parameters, etc.) of this element. The phase model, which contains all these properties, can be used to invert this approach. By varying the property parameters in the phase model, ideal structure properties can be identified. Once they are known, one can design elementary cells that approximate these desired properties. This approach may lead to very individual structure designs for different reactions and should improve control over the reaction with respect to concentration and temperature profiles.
- Because of the relatively low computational effort needed to solve the phase model equations, the model can be used to analyse structured reactors that are coupled with other process units. One example for this is shown in the previous section, where a reforming reactor is thermally coupled to a high temperature fuel cell, and their spatially distributed models are solved simultaneously. This tool can be used to improve the fuel cell's performance through optimisation of the reformer's design.

Another example is the autothermal reforming reactor described by Kolios et al. (2005), which thermally combines a tubular reforming reactor with a catalytic burner. Both parts of this integrated reactor, namely the reformer and the burner, could be designed as structured reactors in order to gain better control over the local reaction rates and to avoid temperature peaks. The phase model would be the tool of choice to optimise this coupled system with respect to operating conditions and the arrangement of the elementary cells.

All these applications have one aspect in common: the phase model is always applied to describe the complete reactor, be it in order to reflect its overall behaviour or to optimise the spatial distribution of states.

5. Conclusions

The proposed modelling strategy for arranged, parallel passage structured reactors covers a wide range of applications that are relevant for the design of such systems. The detailed model can be used to estimate important parameters of a given geometry of the elementary cells, for example coefficients of mass and energy transport or anisotropic permeabilities. This makes it a valuable tool for the design of the structure. The zone model describes a complete structured reactor or large parts of it. It can be utilised to analyse local phenomena such as temperature peaks and maldistribution of flow. The phase model is a strongly reduced model and is well suited to analyse and optimise complete structured reactors with respect to arrangement of structures, operating conditions and integration with neighbouring units. Thus, this hierarchy covers many applications ranging from the design of the structure elements up to the integration of the reactor with other processes.

The three elements of the model hierarchy are coherent. The reduced models were derived from the more complex ones; this was achieved partly by means of physical assumptions and partly by mathematical methods. Moreover, the results obtained from one model can be used in the others. For example, the estimates of the permeabilities from the detailed model are applied in the zone model; the transfer coefficients estimated from the detailed model are important parameters in the phase model; conditions calculated with the phase model at some place in the reactor can be used as boundary conditions in the detailed model in order to validate parameter estimates under these conditions. Thus, the results obtained with one model are not only valid and applicable in this specific model, but can be transferred to other levels of the hierarchy as well. Following the example of an internal reforming reactor in a high temperature fuel cell stack, we have demonstrated solutions and applications of these models.

In principle, analogous model hierarchies can be developed for other examples of arranged reactors. However, a comprehensive methodology for the model reduction of arranged reactors, which goes beyond the example discussed here, is not yet available. A good starting point for such a methodology are the works on volume averaging by Whitaker and Ochoa-Tapia (Whitaker, 1986, 1996; Ochoa-Tapia and Whitaker, 1995). They presented a rigorous approach for the reduction of flow models in porous media. Their applicability to reactors with spatially alternating properties (porosity, reaction rate constants, etc.) needs to be verified. If necessary, modifications of this method need to be developed. According to the works by Whitaker, the reduced model equations contain additional coefficients, e.g. permeabilities. Whitaker formulated closure problems that can be solved in order to determine these coefficients. An alternative to solving these rather complex problems is the estimation of these parameters from numerical experiments using detailed models, as shown for the permeabilities (see Section 2.3.2).

Nomenclature

a^l	Interfacial area between R/N-zone per volume (m^{-1})
A	Surface (m^2)
c_i	Concentration of species i (mol m^{-3})
c_{1, C_2}	Ergun coefficients (dimensionless)
c_t	Total concentration (mol m^{-3})
c_p	Average molar heat capacity ($\text{J mol}^{-1} \text{K}^{-1}$)
$c_{p,i}$	Molar heat capacity species i ($\text{J mol}^{-1} \text{K}^{-1}$)
d	Characteristic length (m)
d_2	Height of reforming reactor (m)
$f_{i,k}$	Volume force acting on species i (N mol^{-1})
g_i	Mass flux density of species i ($\text{mol m}^{-2} \text{s}^{-1}$)
h	Volumetric enthalpy density (J m^{-3})
h_i	Molar enthalpy species i (J mol^{-1})
h^l	Enthalpy flux density across interface ($\text{J m}^{-2} \text{s}^{-1}$)
h_k	Superficial enthalpy flux density ($\text{J m}^{-2} \text{s}^{-1}$)
j_i	Diffusive mass flux density of species i ($\text{mol m}^{-2} \text{s}^{-1}$)
k^l	Heat transfer coefficient across interface ($\text{J m}^{-2} \text{K}^{-1}$)
L	Length (m)
m_k	Normal vector (dimensionless)
n_i	Superficial mass flux density of species i ($\text{mol m}^{-2} \text{s}^{-1}$)
n_i^l	Mass flux density of species i across interface ($\text{mol m}^{-2} \text{s}^{-1}$)
n_t^l	Total mass flux density across interface ($\text{mol m}^{-2} \text{s}^{-1}$)
N_i	Mass flux of species i (mol s^{-1})
p	Pressure (static only) (N m^{-2})
p'	Pressure (static+turbulence term) (N m^{-2})
q	Heat flux density ($\text{J m}^{-2} \text{s}^{-1}$)
q_w	Heat flux density through wall ($\text{J m}^{-2} \text{s}^{-1}$)
\dot{q}	Superficial heat flux density ($\text{J m}^{-2} \text{s}^{-1}$)
Q	Heat flux (J s^{-1})
r_j	Rate of reaction j ($\text{mol m}^{-3} \text{s}^{-1}$)
R	Universal gas constant ($\text{J mol}^{-1} \text{K}^{-1}$)
t	Time coordinate (s)
T	Temperature (K)
u	Velocity (m s^{-1})
u_0	Superficial velocity (m s^{-1})
V	Volume (m^3)
x_i	Molar fraction of species i (1)
z_k	Spatial coordinate (m)
Z_1, Z_2, Z_3	Dimensions of repeating structure element (m)

Greek letters

Δp	Pressure difference (N m^{-2})
$\Delta_r h_j^l$	Enthalpy of reaction j (J mol^{-1})
ε	Volume fraction (1)
κ	Permeability tensor (m^2)
μ	Dynamic viscosity (N s m^{-2})
\bar{v}_{ij}	Net mole change of reaction j (1)
v_{ij}	Stoichiometric coefficient of species i in reaction j (1)
$\pi_{j,k}$	Stress tensor (N m^{-2})
ρ	Mass density (kg m^{-3})
σ_i	Source density of species i due to reaction ($\text{mol m}^{-3} \text{s}^{-1}$)

Subscripts

A	Area-related
C	Catalyst zone
I	Interface between reactive and non-reactive zone
N	Non-reactive zone
R	Reactive zone
V	Volume-related

Superscripts

cat	Catalyst
j	Reaction index
k	Spatial coordinate index
i	Chemical species index

Appendix

The equations of the phase model of the reforming reactor are derived based on the balances of mass and enthalpy. If isobaric conditions are assumed, the momentum balance can be disregarded. The derivation of Eqs. (35)–(37) (phase model equations, non-reactive phase) is shown in detail in the following sections. The equations for the reactive phase (Eqs. (38)–(40)) are derived analogously and are not discussed here.

A.1. Eq. (35): Component mass balance

The derivation of Eq. (35) starts from the component mass balances of the non-reactive phase (Eq. (30)):

$$e^N \frac{\partial c_i^N}{\partial t} = - \frac{\partial (e^N u_1^N c_i^N + e^N j_{i,1}^N)}{\partial z_1} - \frac{\partial (e^N u_2^N c_i^N + e^N j_{i,2}^N)}{\partial z_2} - a^l n_i^l \quad (\text{A.1})$$

We integrate over the height of the reactor (coordinate z_2 in Fig. 3), which essentially eliminates all derivatives along this coordinate. Furthermore, we neglect diffusion along the main flow direction, z_1 . Because we prefer to calculate molar flux densities and mole fractions we replace $u_1^N c_i^N$ by $g^N x_i^N$:

$$e^N \frac{\partial c_i^N}{\partial t} = - \frac{\partial (e^N g^N x_i^N)}{\partial z_1} - a^l n_i^l \quad (\text{A.2})$$

Summing this equation over all chemical species gives the total molar balance, with c_t^N being the total concentration and n_t^l the total molar flux density across the interface:

$$e^N \frac{\partial c_t^N}{\partial t} = - \frac{\partial (e^N g_t^N)}{\partial z_1} - a^l n_t^l \quad (\text{A.3})$$

The mole fraction of species i is defined as

$$x_i^N = \frac{c_i^N}{c_t^N} \quad (\text{A.4})$$

Its derivative with respect to time reads

$$\frac{\partial x_i^N}{\partial t} = \frac{1}{c_t^N} \frac{\partial c_i^N}{\partial t} + c_i^N \frac{\partial (c_t^N)^{-1}}{\partial t} = \frac{1}{c_t^N} \left(\frac{\partial c_i^N}{\partial t} - x_i^N \frac{\partial c_t^N}{\partial t} \right) \quad (\text{A.5})$$

Inserting the total and the component mass balance (Eqs. A.3 and A.2) into this equation yields after short manipulation:

$$c_t^N e^N \frac{\partial x_i^N}{\partial t} = - e^N g^N \frac{\partial x_i^N}{\partial z_1} - a^l (n_i^l - x_i^l n_t^l) \quad (\text{A.6})$$

which is identical to Eq. (35).

A.2. Eq. (36): Enthalpy balance in temperature form

The enthalpy balance in temperature form for the non-reactive phase is derived from the general form of the three-dimensional enthalpy balance (Jischa, 1982):

$$\frac{\partial h}{\partial t} - \frac{\partial p}{\partial t} = - \frac{\partial (u_k h + q_k + \sum_i h_j j_{i,k})}{\partial z_k} + u_k \frac{\partial p}{\partial z_k} + \sum_i f_{i,k} j_{i,k} - \pi_{j,k} \frac{\partial u_i}{\partial z_k} \quad (\text{A.7})$$

We apply isobaric conditions and neglect gravity and friction effects on the enthalpy balance, so the equation reduces to

$$\frac{\partial h}{\partial t} = - \frac{\partial (u_k h_k + q_k + \sum_i h_{j,i,k})}{\partial z_k} \quad (\text{A.8})$$

Describing the average enthalpy of the mixture, h , via the enthalpies of formation of the components ($h = \sum_i c_i h_i$), and defining the enthalpy flux density via mass flux and the mass related enthalpy ($h_k = \sum_i (u_k c_i + j_{i,k}) h_i$), yields

$$\frac{\partial h}{\partial t} = - \frac{\partial (h_k + q_k)}{\partial z_k} \quad (\text{A.9})$$

This equation is integrated over the non-reactive volume of an elementary cell. As with the derivation of the component mass balances (Eqs. (17)–(28)), the Gaussian integral theorem is applied, the surface integral is split into several parts and superficial transport densities, h_k^N and q_k^N , are defined. This leads to

$$\begin{aligned} \epsilon^N \frac{\partial h^N}{\partial t} = & - \frac{h_1^N(z_1 = Z_1) - h_1^N(z_1 = 0)}{Z_1} - \frac{h_2^N(z_2 = Z_2) - h_2^N(z_2 = 0)}{Z_2} - a' h' \\ & - \frac{\dot{q}_1^N(z_1 = Z_1) - \dot{q}_1^N(z_1 = 0)}{Z_1} - \frac{\dot{q}_2^N(z_2 = Z_2) - \dot{q}_2^N(z_2 = 0)}{Z_2} - a' q' \end{aligned} \quad (\text{A.10})$$

With Z_1 and Z_2 approaching zero, this gives

$$\epsilon^N \frac{\partial h^N}{\partial t} = - \frac{\partial (h_k + \dot{q}_k)}{\partial z_k} - a' (h' + q'); \quad k = 1, 2 \quad (\text{A.11})$$

The superficial fluxes are replaced by

$$h_k^N = \epsilon^N \sum_i (u_i^N c_i^N + j_{i,k}^N) h_i \quad (\text{A.12})$$

$$q_k^N = \epsilon^N \dot{q}_k^N \quad (\text{A.13})$$

and the volumetric enthalpy density is substituted by

$$h^N = \sum_i c_i^N h_i \quad (\text{A.14})$$

In the enthalpy exchange flux density ($h' = \sum_i n_i^N h_i(T_i)$) the enthalpy of each species crossing the interface needs to be evaluated at the temperature of the phase of its origin. For all species i moving from the reactive phase into the non-reactive phase ($n_i^N = n_i^R < 0$), the temperature of the reactive phase is used. For all species that are transported from the reactive phase into the non-reactive phase, ($n_i^N = n_i^R > 0$), the temperature of the non-reactive phase is applied.

Inserting these definitions and the component mass balances (Eq. (A.1)) yields the enthalpy balance in the temperature form:

$$\epsilon^N c_i^N c_p^N \frac{\partial T^N}{\partial t} = - \epsilon^N g_k^N c_p^N \frac{\partial T^N}{\partial z_k} - \frac{\partial q_k^N}{\partial z_k} - a' \left(\sum_i n_i^N c_{p,i} (T^R - T^N) + q' \right) \quad (\text{A.15})$$

For the reformer model, we neglect heat conduction in the main flow direction, ($q_1^N = 0$). In order to eliminate all gradients along z_2 , we integrate over this coordinate:

$$\begin{aligned} d_2 \epsilon^N c_i^N c_p^N \frac{\partial T^N}{\partial t} = & - d_2 \epsilon^N g_1^N c_p^N \frac{\partial T}{\partial z_1} - \int_{z_2=0}^{z_2=d} \epsilon^N g_2^N c_p^N \frac{\partial T}{\partial z_2} dz_2 \\ & - [q_2^N]_{z_2=0}^{z_2=d} = d_2 a' \left(\sum_i n_i^N c_{p,i} (T^R - T^N) + q' \right) \end{aligned} \quad (\text{A.16})$$

The convective term in z_2 -direction becomes zero at the integration boundaries. They correspond to the top and bottom metal sheets (see Fig. 3), and the mass fluxes are zero at these coordinates. However, the heat flux density in this direction is equal to the density of the heat flux through these metal sheets,

so $q_2^N(z_2 = 0) = -q_2^N(z_2 = d) = q_w^N$. With this, we obtain the enthalpy balance in temperature form for the non-reactive phase of the phase model, as given in Eq. (36).

A.3. Eq. (37): Total mass balance

The total concentration in the non-reactive phase must obey the ideal gas law. With isobaric conditions, this means for the gradient of the total concentration:

$$\frac{\partial c^N}{\partial t} = - \frac{\partial}{\partial t} \left(\frac{p}{RT^N} \right) = - \frac{c^N}{T^N} \frac{\partial T^N}{\partial t} \quad (\text{A.17})$$

According to Eq. (A.3), the total concentration must also follow the total mass balance:

$$\frac{\partial c^N}{\partial t} = - \frac{1}{\epsilon^N} \frac{\partial (\epsilon^N g_1^N)}{\partial z_1} - \frac{a'}{\epsilon^N} n_i^N \quad (\text{A.18})$$

Because both right hand sides must be equal, we may write

$$0 = T^N \frac{\partial (\epsilon^N g_1^N)}{\partial z_1} + a' n_i^N T^N - \epsilon^N c_i^N \frac{\partial T^N}{\partial t} \quad (\text{A.19})$$

Inserting Eq. (A.16) for the temperature gradient yields Eq. (37), which is used to compute the molar flux density.

References

- Bird, R.B., Stewart, W.E., Lightfoot, E.N., 2007. Transport Phenomena, Rev., 2nd Edn. Wiley, New York.
- Bischoff, M., Huppmann, G., 2002. Operating experience with a 250 kW_{el} molten carbonate fuel cell (MFC) power plant. *Journal of Power Sources* 105, 216–221.
- Calis, H.P.A., Nijenhuis, J., Paikert, B.B., Dautzenberg, F.M., van den Bleek, C.M., 2001. CFD modeling and experimental validation of pressure drop and flow profile in a novel structured catalytic reactor packing. *Chemical Engineering Science* 56, 1713–1720.
- Chen, J., Yang, H., Wang, N., Ring, Z., Dabros, T., 2008. Mathematical modeling of monolith catalysts and reactors for gas phase reactions. *Applied Catalysis A—General* 345, 1–11.
- Comsol Multiphysics Reference Manual (Version 3.4), 2008. Stockholm. <http://www.comsol.com>.
- Cybulski, A., Moulijn, J.A. (Eds.), 2006. 2nd Edn. Taylor & Francis, Boca Raton.
- Ergun, S., 1952. Fluid flow through packed columns. *Chemical Engineering Progress* 48, 89–94.
- Freund, H., Bauer, J., Zeiser, T., Emig, G., 2005. Detailed simulation of transport processes in fixed-beds. *Industrial & Engineering Chemistry Research* 44, 6423–6434.
- Groppi, G., Belloli, A., Tronconi, E., Forzatti, P., 1995. A comparison of lumped and distributed models of monolith catalytic combustors. *Chemical Engineering Science* 50, 2705–2715.
- van Hasselt, B.W., Lebens, B.W., Calis, H.P.A., Kapteijn, F., Sie, S.T., Moulijn, J.A., van den Bleek, C.M., 1999. A numerical comparison of alternative three-phase reactors with a conventional trickle-bed reactor. The advantages of counter-current flow for hydrodesulfurization. *Chemical Engineering Science* 54, 4791–4799.
- Itskov, M., 2009. Tensor Algebra and Tensor Analysis for Engineers: With Applications to Continuum Mechanics. Springer, Heidelberg.
- Jischke, M.F., 1982. Konvektiver Impuls-Wärme und Stoffaustausch. Vieweg, Brunswick.
- Kolios, G., Glöckler, B., Gritsch, A., Morillo, A., Eigenberger, G., 2005. Heat-integrated reactor concepts for hydrogen production by methane steam reforming. *Fuel Cells* 5, 52–65.
- Kreutzer, M.T., Kapteijn, F., Moulijn, J.A., 2006. Shouldn't catalysts shape up? Structured reactors in general and gas-liquid monolith reactors in particular. *Catalysis Today* 111, 111–118.
- Krishna, R., Ellenberger, J., Sie, S.T., 1996. Reactor development for conversion of natural gas to liquid fuels: a scale up strategy relying on hydrodynamic analogies. *Chemical Engineering Science* 51, 2041–2050.
- Levenspiel, O., 1996. The Chemical Reactor Omnibook. OSU Book Stores.
- Mahr, B., Mewes, D., 2007. CFD modelling and calculation of dynamic two-phase flow in columns equipped with structured packing. *Transactions IChemE Part A* 85, 1112–1122.
- Maier, R.S., Kroll, D.M., Bernard, R.S., Howington, S.E., Peters, J.F., Davis, H.T., 2000. Pore-scale simulation of dispersion. *Physics of Fluids* 12, 2065–2079.
- Marcano, J.C.S., Tsois, T.T., 2002. Catalytic Membranes and Catalytic Membrane Reactors. Wiley, New York.
- Ochoa-Tapia, J.A., Whitaker, S., 1995. Momentum transfer at the boundary between a porous medium and a homogeneous fluid—I. Theoretical development. *International Journal of Heat Mass Transfer* 38, 2635–2646.

- Pangarkar, K., Schildhauer, T.J., van Ommen, J.R., Nijenhuis, J., Kapteijn, F., Moulijn, J.A., 2008. Structured packings for multiphase catalytic reactors. *Industrial & Chemistry Engineering Research* 47, 3720–3751.
- Petre, C.F., Larachi, F., Illiuta, I., Grandjean, B.P.A., 2003. Pressure drop through structured packings: breakdown into the contributing mechanisms by CFD modeling. *Chemical Engineering Science* 58, 163–177.
- Pfafferodt, M., Heidebrecht, P., Sundmacher, K., Würtenberger, U., Bednarz, M., 2008. Multi-scale simulation of the indirect internal reforming unit (IIR) in a molten carbonate fuel cell (MCFC). *Industrial and Engineering Chemistry Research* 47, 4332–4341.
- Pfafferodt, M., Heidebrecht, P., Sundmacher, K., 2010. Stack modelling of a molten carbonate fuel cell (MCFC). *Fuel Cells* 10 (4), 619–635.
- Piironen, M., Haario, H., Turunen, I., 2001. Modelling of Katapak reactor for hydrogenation of anthraquinones. *Chemical Engineering Science* 56, 859–864.
- von Scala, C., Wehrli, M., Gaiser, G., 1999. Heat transfer measurements and simulation of Katapak-M catalyst supports. *Chemical Engineering Science* 54, 1375–1381.
- Schönfelder, H., Kruse, M., Werther, J., 1996. Two-dimensional model for circulating fluidized-bed reactors. *AIChE Journal* 42, 1875–1888.
- Shilkin, A., Kenig, E.Y., 2005. A new approach to fluid separation modelling in the columns equipped with structured packings. *Chemical Engineering Journal* 110, 87–100.
- Tischer, S., Deutschmann, O., 2002. Recent advances in numerical modeling of catalytic monolith reactors. *Catalysis Today* 105, 407–413.
- Whitaker, S., 1986. Flow in porous media I: a theoretical derivation of Darcy's law. *Transport in Porous Media* 1, 3–25.
- Whitaker, S., 1996. The Forchheimer equation: a theoretical development. *Transport in Porous Media* 25, 27–61.

